Compact electronic interface for opto-mechanical sensors

Houssein Elmi Dawale

THÈSE

Pour obtenir le grade de

DOCTEUR DE L'UNIVERSITÉ GRENOBLE ALPES

École doctorale : EEATS- Electronique, Electrotechnique, Automatique, Traitement du Signal.
Spécialité : Nano électronique et Nano technologies
Unité de recherche : CEA/LETI

Interface électronique compacte pour capteur opto-mécanique.

Compact electronic interface for opto-mechanical sensors

Présentée par :

Houssein ELMI DAWALE

Direction de thèse :

Franck BADETS — Directeur de thèse
Ingénieur de recherche HDR, CEA-LETI

Rapporteurs :

Jérôme JUILLARD
Professeur, Centrale Supélec
Hélène TAP
Professeure, Toulouse INP-ENSEEIHT

Thèse soutenue publiquement le **10 Janvier 2023**, devant le jury composé de :

Skandar BASROUR Professeur, Université Grenoble-Alpes	Président
Hélène TAP Professeure, Toulouse INP-ENSEEIHT	Rapporteuse
Jérôme JUILLARD Professeur, Centrale Supélec	Rapporteur
Edith KUSSENER Directrice Générale, ISBA TP Marseille	Examinatrice
Ivan FAVERO Directeur de recherche, Université de Paris	Examinateur
Franck BADETS Ingénieur de recherche HDR, CEA-LETI	Directeur de thèse

Remerciements

C’est l’occasion pour moi de remercier chaleureusement, toutes les personnes que j’ai pu rencontrer au cours de cette aventure. D’un point de vue personnel, ces trois années ont été une expérience incroyable. Les mots que je vais certainement employer ici me semblent faibles et ne reflètent pas totalement la profonde gratitude que je ressens.

En premier lieu, je voudrais remercier les membres du jury pour l’intérêt qu’ils ont porté à ces travaux et pour leur expertise qui ont contribué à une soutenance passionnante et riche en débats.

Je remercie sincèrement mon directeur de thèse Franck, pour sa direction. Malgré le large spectre du sujet et les nombreux facteurs exogènes (covid, pénurie de composant…) nous avons réussi à atteindre les objectifs qu’on s’était fixés. Merci à toi pour tous nos échanges et tes conseils, tu as su me tirer vers le haut. Un grand merci à Loïc et à Patrick, pour leur encadrement. J’ai beaucoup appris à vos côtés, en particulier lors de nos nombreuses réunions qui ont parfois duré tard le soir pendant le confinement par exemple ou encore lors de la correction d’un papier.

Je tiens particulièrement à remercier les permanents du laboratoire LGECA, à commencer par la cheffe Stéphanie pour m’avoir accueilli et facilité mon intégration. Merci à Gérard, Frédéric, Gaël, Yasser, Anass, Emmanuel, Yoann, Gwenaël, Thomas… aux anciens comme Anthony, Sylvain et Dominique, ou encore Guillaume R, Youcef, Anne, Mathieu pour toutes nos conversations en salle café.

Mes travaux ont été menés en étroite collaboration avec des permanents ou ex-permanents du laboratoire micro-systèmes capteurs que j’aimerais remercier ici. Merci à Sébastien H., Guillaume J. et Marc S. pour votre aide dans la compréhension des capteurs optomécaniques. Merci à Sébastien R., Thomas pour m’avoir aidé lors des expérimentations. J’ai beaucoup sollicité Renaud et Venceslas du laboratoire de test, un grand merci à eux deux aussi.

Je souhaite remercier les non-permanents (post-doctorants, doctorants, stagiaires, alternants) que j’ai eu la chance de fréquenter. Merci à Carlos, Quentin, Lucas, Brian, Thomas H., Emeric, Thomas B, Théo … pour tous ses beaux moments qu’on a partagés ensemble et qu’on partage toujours encore. J’ai apprécié discuter avec chacun d’entre vous que ça soit sur vos sujets de thèse respective ou lors de nos longues pauses ou en refaisait le monde à notre échelle. Je garde en mémoire nos parties Nintendo le vendredi soir ou encore le fait de partir manger à 11h30 pour éviter les longues files. Merci également aux anciens, à Adrien, Loïck, Nicolas, Jean-Baptiste, Paul pour m’avoir intégré à l’époque dans le carré des thésards. Je me souviens des beaux moments qu’on a partagé ensemble, des nombreux mèmes qu’on produit puis affiché fièrement au labo. Je n’oublie pas non plus, les non-permanents hors LGECA, merci à Roman, Valentin, Maxence ou encore Olivier F.

Enfin, j’aimerais saluer ici ma famille. Merci à mon binôme Hassan pour ton soutien durant toutes ces années. A ma sœur Khadira qui souhaiterait suivre mes traces, ne doute pas, tu as largement la motivation et les capacités requises. A mes deux frères Liban et Karim, je vous souhaite de suivre le même chemin que vos ainés. Pour finir, je remercie mes parents pour leur soutien sans relâche dans cette aventure.

List of Figures

List of Tables

Abbreviations

NEMS/MEMS nano-electromechanical and micro-electromechanical systems

OM optomechanical system

SOL self-oscillating loop

FLL frequency locked loop

PLL phase locked loop

LIA lock-in-amplifier

AH-FLL adjustable heterodyne frequency locked-loop

WGM whispering gallery mode

RBM radial breathing mode

SEM scanning electron microscope

PDMS polydimethylsiloxane

YIG yttrium iron garnet

BSA bovine serum albumin

OR optical resonator

MR mechanical resonator

NS nanowire sensor

FSR free spectral range

TE transverse electric

TL transverse magnetic

FEM finite element method

PML perfectly matched layer

RIN relative intensity noise

TIA transimpedance amplifier

FoM figure of merit

VCO voltage-controlled oscillator

AGC automatic gain control

PSD power spectral density

ADEV Allan deviation

AVAR Allan variance

PFD phase and frequency detector

IQ-FLL in phase and quadrature frequency locked loop

NEP noise equivalent power

PGA programmable gain amplifier

FPC fiber polarization controller

PD photodetector

Contents

Introduction

In recent decades, nano-electromechanical resonators (NEMS) or micro-electromechanical resonators (MEMS) have demonstrated their tremendous potential for sensing applications. Thanks to their electrical-mechanical coupling, they exhibit an excellent sensitivity. This permits them to be used in high precision applications such as mass spectrometry. Nowadays, these technologies appear mature and can detect atoms in vacuum. The mass resolution of a nano- and micromechanical resonator is proportional to its effective mass. The lower the mass of the resonators, the better the achieved resolution. Consequently, the resonators have been subject to a miniaturization campaign in order to reach the highest resolution possible. Nevertheless, this has led to fragile structures. Such devices are only used in unconstrained environments like vacuum or air. In a constrained environment such as liquid, the viscosity causes the beam-based micro and nano mechanical devices to break and not to resonate.

In the state of the art, more robust devices exist such as optomechanical disks. This kind of resonator hosts two resonance modes: optical and mechanical. A coupling called "optomechanical coupling" connects these two modes, which allows the interaction between light and a mechanical disk resonator at the low energy level. An optomechanical resonator is a device in which the propagation of light is modified (modulated) by its mechanical motion.

These devices are able to resonate in an unconstrained environment (vacuum, air) with excellent quality factor ($\boldsymbol{Q_{vacuum}}$ ≈10000 and $\boldsymbol{Q_{air}}$ ≈1500), as well as in a constrained environment like liquid with a moderate mechanical energy loss ($\boldsymbol{Q_{liquid}}$ ≈50). This makes them more interesting for the realization of mass sensors for a vast panel of applications such as biological and chemical detection. CEA-Leti develops this kind of disk resonator for mass applications. These resonators are based on silicon and have an excellent mass sensitivity of $\boldsymbol{1\ Hz/10^{-18}g}$.

This research project is part of the development of a mass measurement system based on an optomechanical resonator. The objective of the thesis is to develop electronics for the reading of an optomechanical resonator. The electronic to be designed must also be compatible with matrix reading. Over the past three years, we have focused on these objectives. We present in this work, a compact analytical model of the optomechanical resonator. Such a model is necessary to design a circuit. This allowed us to perform realistic and complete electrical simulations. We also propose a discussion on the ideal matrix configuration that will facilitate the design of a readout circuit. At last, to the best of our knowledge we report for the first time in this manuscript a reading circuit able to read accurately optomechanical resonators. Alone, the proposed circuit has a resolution of 20 ppb but when combined with the optomechanical sensor the resolution degrades and becomes 500 ppb.

Outline of the Thesis

Except the introduction and conclusion, this thesis manuscript is composed of five chapters:

- Chapter 1 - *Introduction to optomechanics*, is an outline of optomechanical cavities.

Part I presents the history and development of optomechanical resonators from the first experiments in the 17th century to the modern times. We introduce the operating principle of a basic optomechanical system (OM) by considering the optical resonance, the mechanical resonance and the optomechanical coupling. We will see the two main families of optomechanical resonators (photonic Crystal and circular cavity). Each kind of resonator is used in a variety of applications such as force detection, magnetic field detection, acoustic wave detection, mass detection, ... In the last part of the chapter, we will describe the optomechanical devices used for the mass detection. We will describe the optically actuated device and the electrostatically actuated device.

- Chapter 2 - *Optomechanical Sensor: Theory and Modeling*, describes analytically the behavior of optomechanical resonators. The optical and mechanical behavior of the disk is presented in the first section. We will examine the optomechanical coupling that links the two resonance modes. For each type of resonator (optically actuated and electrostatically actuated) we will present the equations describing the principle of operation. Based on these equations, we propose the development of a compact model in Verilog A. Then we validate the coherence of this model with respect to the experimental results.
- Chapter 3 - *Towards a matrix integration of optomechanical resonators*, suggests a new matrix configuration for optomechanical resonators. First, we will see the interest of such a structure for mass detection. Then the specifications on which we have based our design. The optomechanical matrix will be read sequentially, we will explain why. To allow this sequential reading we exploit the thermo-optical effect of the resonator. This consists in shifting the optical resonance to mask the mechanical response of the disk. We will show the means to exploit this effect. Finally, we will evaluate the complexity of manufacturing such a matrix.
- Chapter 4 - *Frequency tracking readout architectures*, is a review of readout architectures potentially applicable to the optomechanical resonator. We will examine closed-loop architectures such as the self-oscillating loop (SOL) and the frequency locked loop (FLL). We will also discuss open loop architectures such as the lock-in amplifier (LIA). For each architecture, a theoretical analysis of phase noise, mass resolution and loop stability are proposed. To read our optomechanical resonator, we have chosen an architecture based on the FLL, called AH-FLL for Adjustable Heterodyne Frequency Locked-Loop. The last part of the chapter describes the working principle and the specification of this AH-FLL architecture.
- Chapter 5 - *Practical realization and experimental validation*, presents the realization of the readout circuit based on the AH-FLL architecture. Firstly, we validate this architecture by stability studies and electrical simulations. Then, we illustrate the design steps of the circuit by explaining the different design constraints including the adaptation of the transmission lines. Lastly, we show the results of the demonstration of the discrete circuit with the optomechanical sensor. In this demonstration, we succeeded in reading and self-actuating the optomechanical disk with our circuit assembly. The resolution reached by the system (sensor and circuit) is 500 ppb.

Chapter 1

Introduction to optomechanics

Contents

This chapter presents the outline of optomechanical cavities. In the first part of the chapter, we will present the history and development of optomechanical resonators. Then we will explain the operating principle of a basic optomechanical system (OM) by considering the optical resonance, the mechanical resonance and the optomechanical coupling. We will present the two main families of optomechanical resonators (photonic crystals and circular cavity resonators). In the second part we will see a state of the art of optomechanical resonators and their applications. Today optomechanical devices are used in the detection of forces, magnetic fields or acoustic waves. They are also used to measure with great accuracy a mass or an acceleration. In the last part of the chapter, we will describe the optomechanical devices used for the mass detection. Precisely the optically actuated micro-disk and the electrostatically actuated resonator.

1.1. Background and context of optomechanics

Optomechanical cavities have in the last years experienced a very strong development in fundamental research to better understand the physical aspects (optical, mechanical and thermal). Indeed, the optical wave is extremely sensitive to small variations of force, mass, acceleration, and displacement [1]. Therefore, optomechanics becomes a privileged field of study to design ultra-sensitive, modern sensors with unequalled performances.

In this section, we propose to review the development of optomechanics since the first experiments. This history allows us to see the efforts made but also to see where the research and development of optomechanical cavities stand today. For that we will present a state of the art of the different types of optomechanical cavities currently existing. Then we will see their different applications.

1.1.1 Brief history

At the beginning of the 17th century, while observing comets, Kepler realized that their light tails were moving away from the sun [2]. He therefore assumes that light contains a quantity of movement giving rise to optical pressure forces. The first experimental demonstrations highlighting this optical pressure force were made by Lebedew [3]. Nichols and Hull realized in 1901 an experiment within a glass cavity demonstrating the property of light to exert pressure forces on the external surfaces of the device. Figure 1.1 below shows the plan and photo of the device used by Nichols and Hull to demonstrate the pressure force of light.

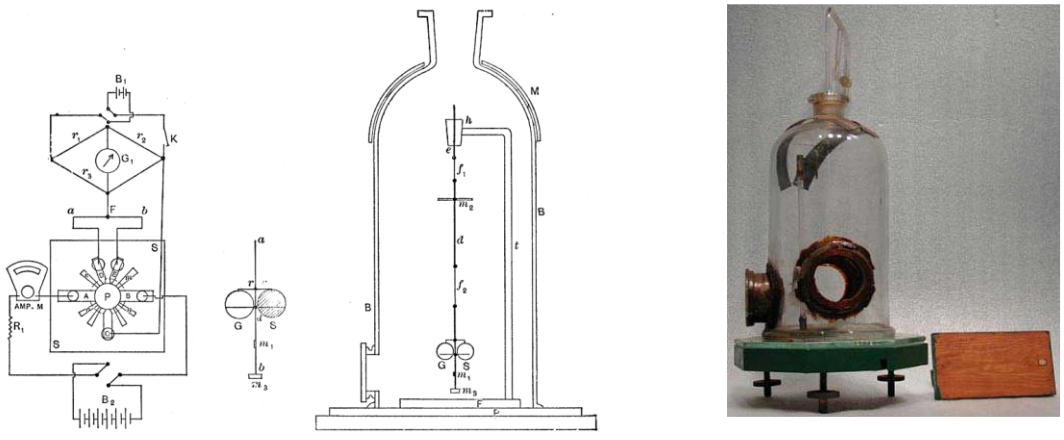

(a) (b)

Figure 1.1: (a) The design of the torsion balance suspension, used to measure the light radiation pressure (b) the image of the torsion balance [4].

In 1909, Einstein was able to theorize the radiation pressure force of the optical wave. For this he introduced a statistic of the photon fluctuations that are exerted on a moving mirror [5]. In his study he included the effects of friction of radiation that allowed him to discover the wave-particle nature of light. The mechanical interaction of photons on atoms or macroscopic objects were first demonstrated by Frisch in 1933 [6] and by Beth in 1936 [7]. In his experiment, Beth realized a rotating cavity which is activated by the light effect. Figure 1.2 shows the schematic and the photo of the device of Beth to prove the mechanical character of light.

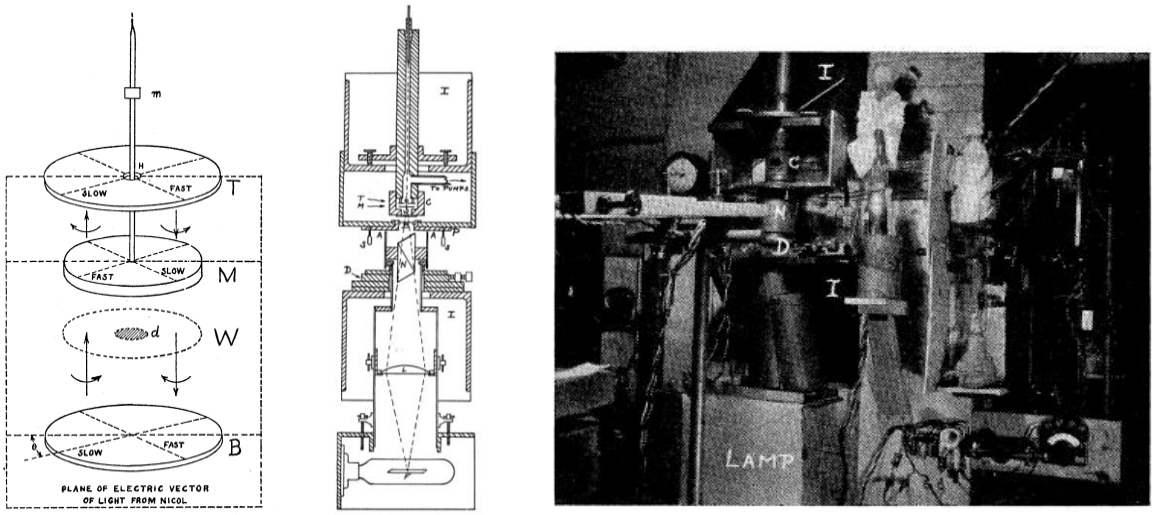

(a) (b)

Figure 1.2: (a) The design of the angular rotation device, used to prove the mechanical character of light (b) Photograph of the angular rotation device [7].

In the early 70's and 80's, the first experiments on opto-mechanical cavities were performed. In 1978, Dykman [8] explored the vibrations that light causes on solid systems. In 1983, Dorsel realized the first optomechanical cavities where he studied the force of radiation pressure acting on a macroscopic cavity mirror [9]. In 1994, Fabre [10], Mancini and Tombesi [11], Jacobs [12], began to develop the theory and understand the optical and mechanical properties of opto-mechanical systems.

At the beginning of the 2000's, different types of opto-mechanical systems started to be explored in order to develop them for specific applications. This is when the miniaturization of devices started to be seriously considered. In 2005, T. Carloman successfully designed micro-toroid optomechanical resonators having both optical and mechanical properties with a high optomechanical coupling.

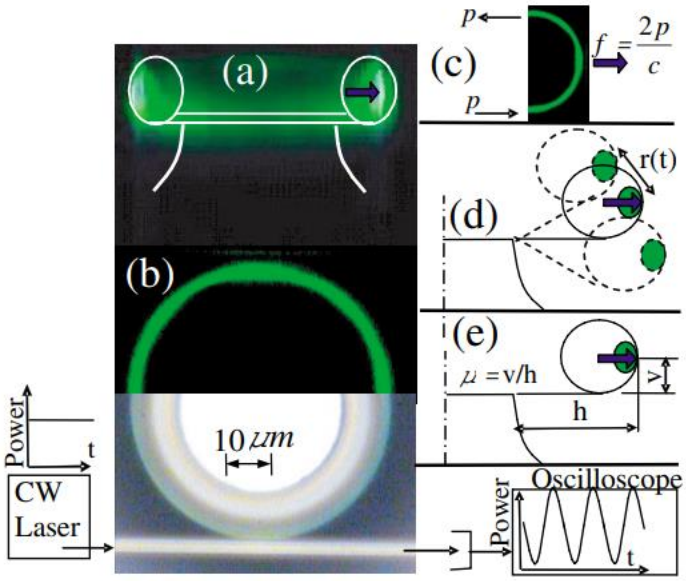

Figure 1.3: Experimental setup (a) Micro-toroid cavity (b) light propagation inside de cavity (c) circulating power (d) and (e) radial micro-toroid deformation [13]

Figure 1.3 shows the Carloman resonator. When a continuous optical power is injected, the resonator starts to resonate radially see Figure 1.3.d. This modulates the optical power to the mechanical resonance frequency of the resonator. After that, many major improvements followed and new optomechanical systems appeared. Among them, they are membranes [14], whispering gallery micro-disks [15]-[16], microspheres [17]-[19], photonic crystals [20].Thanks to all these theoretical and technological advances, optomechanical systems appear today as mature technologies.

1.1.2 Optomechanical cavity description

Optomechanics is a field of study in which light (optical) and mechanical motion (mechanical resonance) interact. Optomechanical devices are devices where these two characteristics coexist. Within an optomechanical cavity, the two physical domains (optical and mechanical) are linked together in a so-called “optomechanical coupling”.

Figure 1.4 presents a classical optomechanical system (OM). It is composed of an optical cavity of Fabry-Perot type delimited by two mirrors. A fixed mirror on the left (partially transparent) to let the light enter in the cavity. A moveable mirror which is connected to a spring held by a fixed support. When an optical power is injected through the left mirror, the photons start to bounce on the two mirrors and exert a pressure force that moves the moveable mirror. With a displacement $x(t)$, the moveable mirror behaves like a mechanical resonator. From an optical point of view, the cavity starts to resonate when photons are reflected between the mirrors as shown in Figure 1.4. Analytically, this condition is written:

$$2L = m\lambda_0 \tag{1.1}$$

where L is the Fabry-Perot cavity length, $\lambda_0 = 2\pi c/w_0$ is the optical resonance wavelength with c the speed of light and m an integer. The link between the optical resonance w_0 and the displacement $x(t)$ of the movable mirror is given by the optomechanical coupling. In general, this coupling is noted $g_{om}$and is defined as the derivative of the optical resonance frequency w_0 in relation to the elementary displacement ∂x. The expression is:

$$g_{om} = -\frac{\partial w_0}{\partial x} \tag{1.2}$$

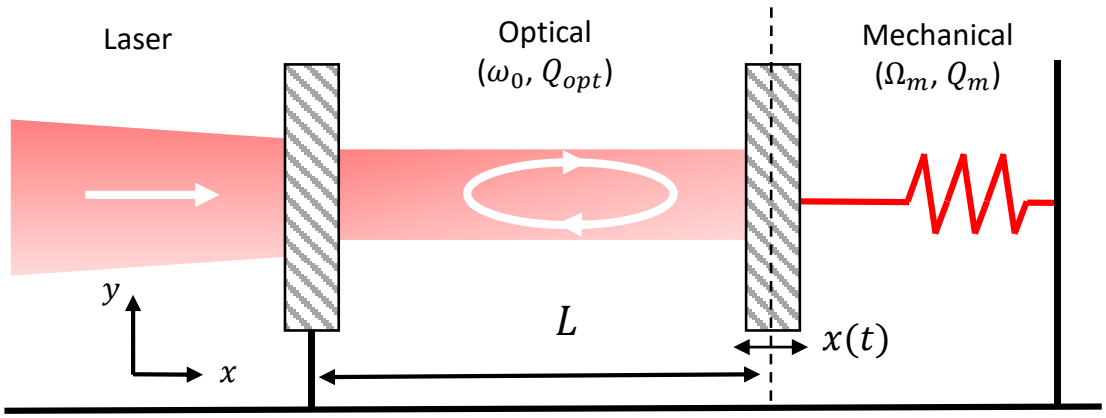

Figure 1.4: A classical optomechanical system (OM) with a fixed mirror and a moving mirror.

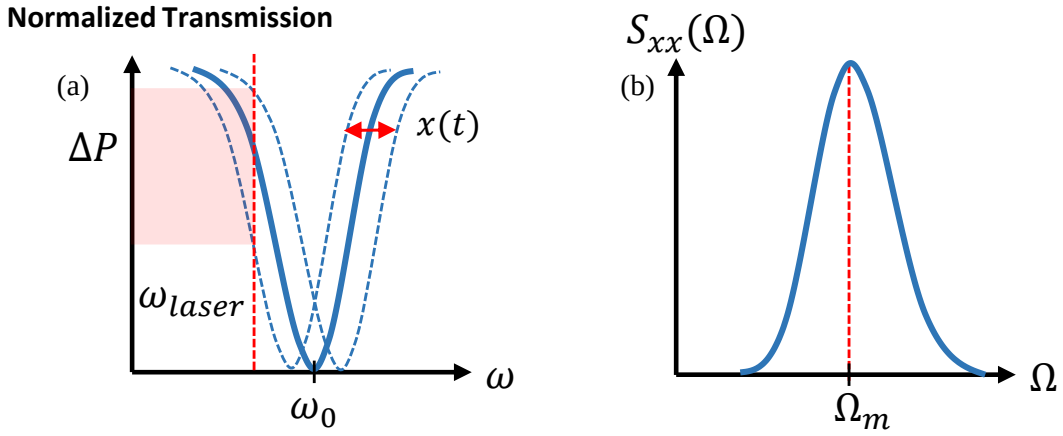

Figure 1.5: Optical reading of a mechanical movement (a) Modulation of the optical resonance (b) Spectral power density of the mechanical movement.

The optomechanical system illustrated in Figure 1.4 also behaves like a mechanical resonator. Indeed, when a continuous optical power is injected, the photons exert a pressure on the surface of the movable mirror. The latter vibrates by moving along the x axis. In this way, the light causes a mechanical movement. Also at the same time, the mechanics changes the optical resonance.

As shown in Figure 1.5.a, the displacement $x(t)$ changes the length L of the cavity and consequently modulates the optical resonance frequency w_0. This variation of the optical resonance frequency is only visible when the frequency of the laser $w_{laser}$is close to that of the resonator w_0. Equation (1.2) well describes the change of optical resonance. Figure 1.5.b shows the power spectral density of the mechanical motion generated by the optical power. The mechanical resonance frequency is noted Ω_m.

There are several types of optical forces that cause mechanical displacement. According to [21]-[22] the most important are:

- Radiation Pressure Force:

Electromagnetic waves in contact with any solid surface exert a force. This force is known as the radiation pressure force. For optomechanical devices, it is the force that primarily generates the mechanical motion. In physics, this can be explained simply by the fact that photons bounce off the edges of a cavity. Therefore, this force is proportional to the number of photons and therefore to the amount of optical power $P(t)$. The radiation pressure force is defined as follows:

$$F_{rp}(t) = \frac{2P(t)}{c} \tag{1.3}$$

- Photo-thermal Force :

The photo-thermal force or Langevin force is a force characteristic of optomechanical systems [23]. When photons impact on the cavity, some of them bounce back to give the pressure force F_{rp} seen previously. Other photons are absorbed by the material. This produces a heating of the wall which leads to an elastic distortion of the mechanical device.

- Electrostriction Force:

Within a dielectric material, the electrostriction force is a force that moves the ions contained in the crystal lattice [24]. Under the effect of an external electric field, positive ions move in the direction of the field and negative ions in the opposite direction. The displacement of these ions leads to a deformation of the cavity walls. The deformation induced by this force is proportional to the square of the polarization.

1.1.3 State of the art of optomechanical resonators

In the last few years, optomechanical systems have been developed very strongly. From a fabrication point of view, we have been able to realize smaller and smaller devices. Today in the state of the art, there are a variety of optomechanical devices: mirror cavities, Nano-rams, cantilevers, whispering gallery mode (WGM) micro-cavities and photonic crystals.

We propose here, to limit ourselves to optomechanical devices with a very strong interest for high resolution applications. With the help of [25], we will realize a state of the art of the micro-cavity devices and photonic crystals. These two optomechanical systems present a very strong optomechanical coupling, and very interesting optical and mechanical quality factors for sensing applications.

- State of the art of photonic crystals :

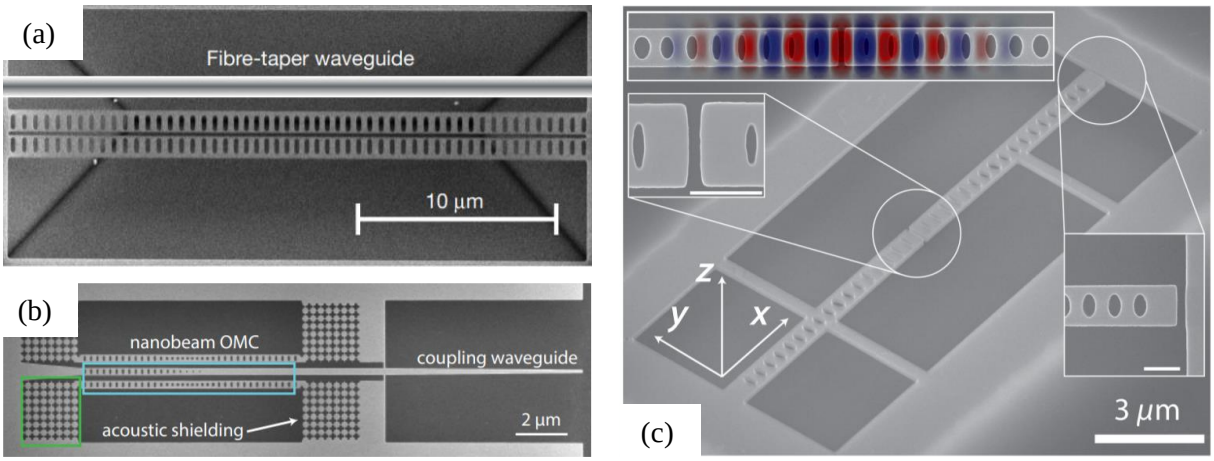

Figure 1.6: Optomechanical crystal photonic (a) SEM image of two coupled photonic crystal [26] (b) SEM of a single photonic crystal [27] (c) SEM of split coupled photonic crystal [28].

Photonic crystals are types of materials presenting a variation of the dielectric constant at the surface. They are ultra-sensitive to light and have a very strong optomechanical coupling. This means that when optical power is injected into photonic crystals, they begin to resonate mechanically with a very high mechanical quality factor of the order of 10^9. They constitute today a very promising field of research for applications of magnetic, mass, force detection...etc. The first optomechanical structure based on photonic crystals was realized by Painter's team in 2009 (see Figure 1.6.a). Today, there are many different optomechanical structures made of crystal nano-beams (see Figure 1.6.b) or coupled crystal structures (see Figure 1.6.c) with high quality factors up to 5×10^{10}.

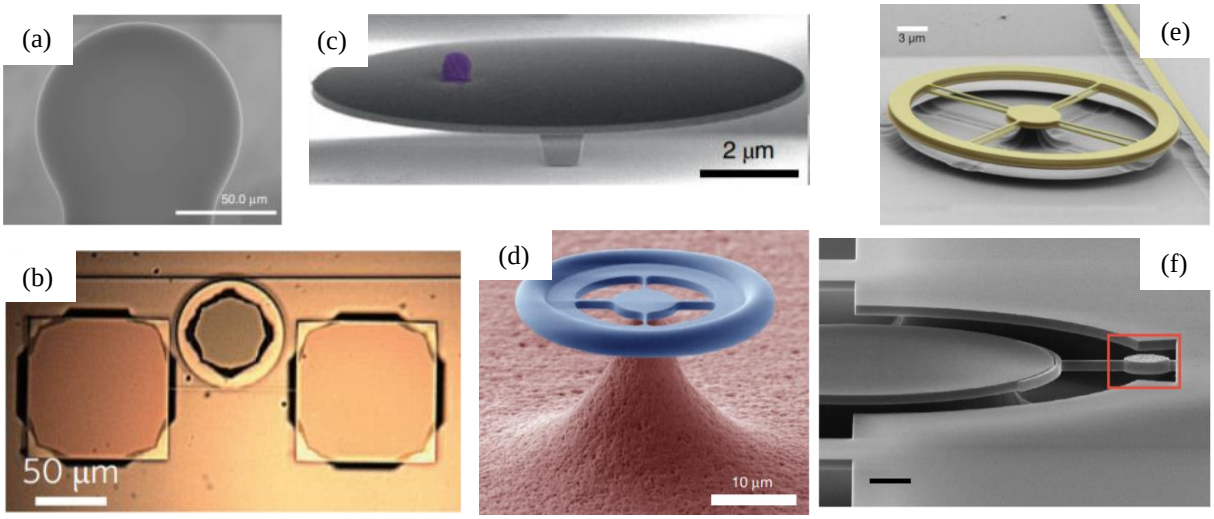

Figure 1.7: Whispering gallery mode (WGM) optomechanical resonators. (a) spherical resonator [29] (b), (c) and (f) micro-disk resonators [30]-[32] (d) and (e) micro-toroidal resonator [33]-[34].

- State of the art of whispering gallery mode (WGM) micro-cavities:

In the state of the art of optomechanical systems, there are also whispering gallery mode (WGM) devices. It is a type of device which presents a circular optical cavity in which the propagation of the light expands the walls in a mechanical way. There are several types of WGM resonators:

As illustrated in Figure 1.7.a, the spherical micro-resonator is a type of optomechanical resonator with WGM optical resonance. The first demonstration of this type was realized in silica by the team of Tao Liu [29] for mass detection. The realized microsphere had a diameter of 100 µm and exhibited optical and mechanical quality factor $Q_{opt} \sim 5 \cdot 10^6$ and $Q_{mec} \sim 3 \cdot 10^6$ respectively. Thanks to its performance, the microsphere is able to detect a BSA molecule of mass 66 KDa.

There are also micro-disk devices. They have a strong coupling between the WGM optical resonance mode and the mechanical resonance mode. This type of device is used for different types of applications, e.g. for the detection of biological particles [31], as shown in Figure 1.7.c. In this configuration the surface of the micro-disk is smoothed to receive receptors to fix bacteria, viruses, and proteins. They can help to detect a mechanical torsional motion [32] using the configuration of Figure 1.7.f. This kind of device has a coupling of 3.4 GHz/mrad. Or to detect a force [30] as presented in Figure 1.7.b with a sensitivity of about 74 $aN/\sqrt{Hz}$.

And finally, the micro-toroidal devices that have a greater degree of mechanical freedom. They are able to resonate mechanically both radially and azimuthally. As explained in section 1.1.1, the first optomechanical micro-toroidal device was realized by T. Carloman in 2005 [13]. Today this type of resonator is used to detect forces [33]-[16], as shown in Figures 1.7.d and 1.7.e.

1.2. Optomechanics for sensors applications

In the previous section we have presented, the different types of optomechanical resonators, such as photonic crystals and WGM resonators with circular cavities (micro-disks, spherical or micro-toroidal). Today these devices are used in several types of applications. As shown in Figure 1.8, optomechanical devices can be used to sense: a mass, a force, an acceleration, a magnetic field or an acoustic wave. We propose in this section to see each type of application and the associated optomechanical resonator.

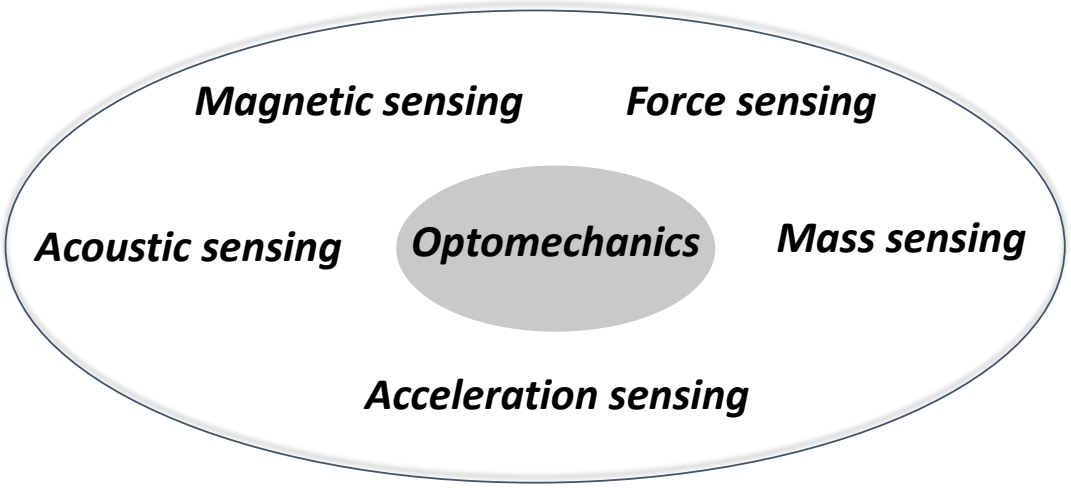

Figure 1.8: Types of applications of optomechanical resonators.

1.2.1 Force sensing

Optomechanical resonators are able to detect an external force with a very high accuracy. In general, the force is applied to the mechanical resonator in order to modify the mechanical behavior (frequency and displacement). Thanks to this change of mechanics, we are able to estimate the amplitude of the force that is exerted. To detect a force it is necessary to use resonators that have a very high mechanical sensitivity such as a photonic crystal or a micro-disk. A spherical resonator is not very suitable for this type of application.

In the state of the art, the first realization of a force sensor with an optomechanical resonator was published by T. J .Kinppenberg's team in 2012 [30]. They have successfully combined a silica optomechanical micro-disk with a Si_3N_4 nano-beam as illustrated on Figure 1.9.a. When an external force is applied, the nano-beam deforms. This affects the coupling between the micro-disk and the nano-beam and the optical power observed at the output. The variation of this power indicates the value of the applied force. The force sensitivity for this type of device is 74 $aN/\sqrt{Hz}$.

In 2017, Zhou's team [34] demonstrated that a classical optomechanical system could also be used to detect the magnitude of a force. Figure 1.9 b shows the experimental setup performed by Zhou. The optomechanical system is composed of a Fabry-Perot cavity bounded by two mirrors. A fixed mirror and a movable mirror placed above. The movable mirror is attached to

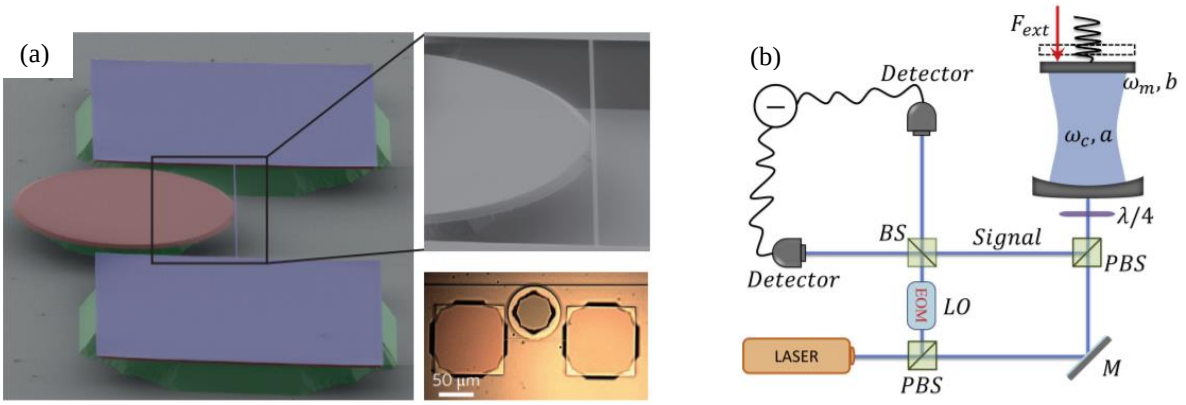

Figure 1.9: Optomechanical devices for force sensing applications (a) silica micro-disk resonator coupled to a Si_3N_4 nano-beam [30] (b) Fabry-Perot optomechanical cavity [34].

a spring and moves according to the external force applied. When a force is applied, the mirror moves and changes the length of the optical cavity. This results in reducing the distance that photons travel and therefore change the optical resonance. By following this shift of the resonance we are able to estimate the force.

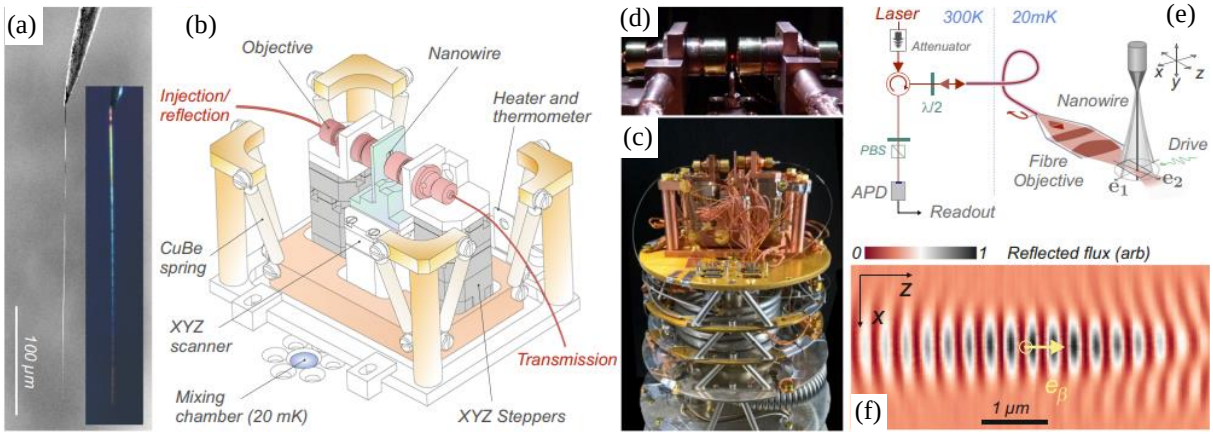

Figure 1.10: Experimental Setup (a) SEM of the silicon carbide nanowires (b) and (c) Cryogenic experimental platform (d) Optical apparatus showing a fraction of focused light (e) Schematics of the interferometric reading (f) Displacement of the nanowire [35].

In 2020, Arcizet's team have developed an ultra-sensitive nano-optomechanical sensor [35]. Specifically they have implemented optomechanical readout techniques where the idea is to evaluate photons to determine the dynamics of a silicon carbide nanowire suspended in a refrigerator. The vibrations or forces of this nanowire are measured using optical power. The force sensitivity of the sensor is about $40\ zN/\sqrt{Hz}$. Figure 1.10 above shows the complete experimental setup.

1.2.2 Acceleration sensing

An accelerometer is an inertial sensor that measures a linear non-gravitational acceleration. This measurement can be done on the three orthogonal axes (X, Y, and Z). The accelerometer

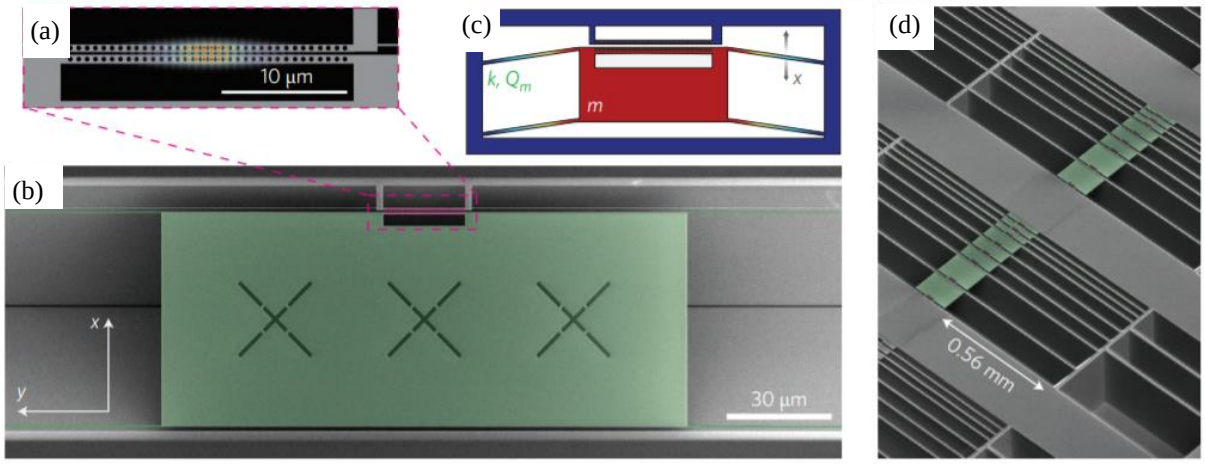

Figure 1.11: Presentation of an optomechanical accelerometer (a) Optical coupling between the two photonic crystals (b) SEM image of the optomechanical accelerometer (c) FEM simulation of the accelerometer (d) SEM image of an array of accelerometer devices [36].

applications, are used today in many fields (automotive, consumer electronics ...). The detection of acceleration is done by measuring the displacement of a mechanical mass compared to its state at rest. This reading can be done optically with optomechanical resonators with an excellent sensitivity. Among the optomechanical resonators used for the detection of acceleration, there are photonic crystals which have a very high sensitivity to displacement and the WGM circular cavity resonators.

Photonic crystal resonators have a very high displacement resolution of the order of a pico-meter. This makes them very interesting for the design of acceleration sensors. Alexander G. Krause [36] has realized for the first time an accelerometer based on photonic crystals. Figure 1.11.b depicts the optomechanical device for the detection of acceleration. It consists of an optical waveguide attached to a SiN nano-beam. A few nanometers from the waveguide is placed a moving mass. When the mass moves along the x axis, it disturbs the mass-waveguide optical coupling as shown in Figure 1.11.c. From this interference, we can determine the value of the acceleration. With an optical power less than a milliwatt, the resolution is $10\ ng/\sqrt{Hz}$ with a bandwidth of $20\ kHz$.

Optomechanical resonators with circular cavities can also detect acceleration. In Figure 1.12.a we present an accelerometer sensor with an optical ring [37]. The device is composed of a silicon optical ring, a waveguide and a moving suspended mass. When an optical power is injected on the waveguide, the light enters into the ring by evanescent coupling. As the mass moves it disturbs the propagation of photons inside the ring. This results in a modification of the optical resonance with a sensitivity of about $3.279\ pm/g$. The bandwidth of the resonator is about $30\ kHz$.

There are also spherical resonators for sensing acceleration [38]. Figure 1.12.b shows an optomechanical accelerometer based on a WGM microsphere. The device consists of an optical waveguide and a microsphere resonator placed at a few nanometers. The microsphere is positioned on a piezoelectric actuator. When the piezo vibrates it moves the microsphere vertically. This changes the waveguide-microsphere gap and the optical coupling. Therefore the contrast of the optical resonance is modulated as the microsphere moves. The resolution achieved by this device is $40\ \mu g/\sqrt{Hz}$.

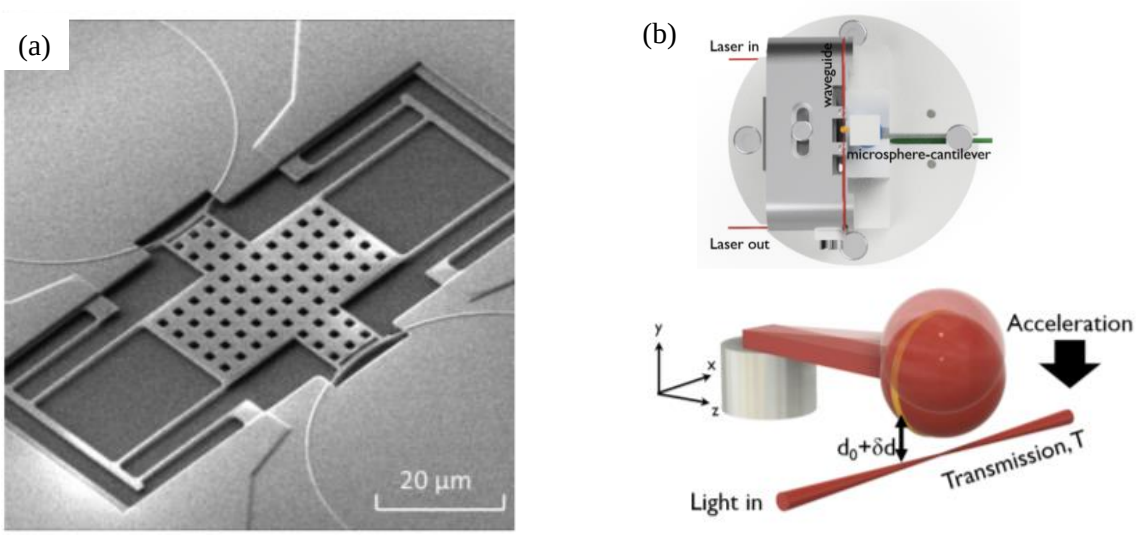

Figure 1.12: WGM optomechanical accelerometer (a) SEM image of an optical ring accelerometer [37] (b) SEM image of a micro-sphere accelerometer [38].

1.2.3 Magnetic field sensing

A magnetometer or magnetic sensor is an equipment able to measure the intensity and direction of a magnetic field. On Earth, due to the nature of the landscape, the magnetic field is not the same in all places. It is therefore interesting to design field sensors that can accurately measure the intensity of the magnetic field. Nowadays, the magnetometer is used in many fields (industry, automotive, aeronautics ...). Among the diversity of magnetometers existing in the state of the art, the optomechanical resonators are particularly distinguished. Thanks to the optical detection, they have an excellent sensitivity to magnetic fields. There are different types of optomechanical resonators (micro-toroidal, cylindrical cavity, micro-spherical ...) to detect the magnetic field.

The micro-toroidal optomechanical resonators can detect a magnetic field [39]-[40]. Figures 1.13.a and 1.13.b show the SEM image of optomechanical micro-toroidal devices. To be able to detect the magnetic field, the micro-toroidal devices use a ferromagnetic material (Terfenol-D) placed in the center as shown in Figures 1.13.a and 1.13.b. The whole structure is elevated to facilitate mechanical resonance. By applying a magnetic field, the micro-toroidal deforms and thanks to this mechanical deformation the field intensity can be estimated. There are also

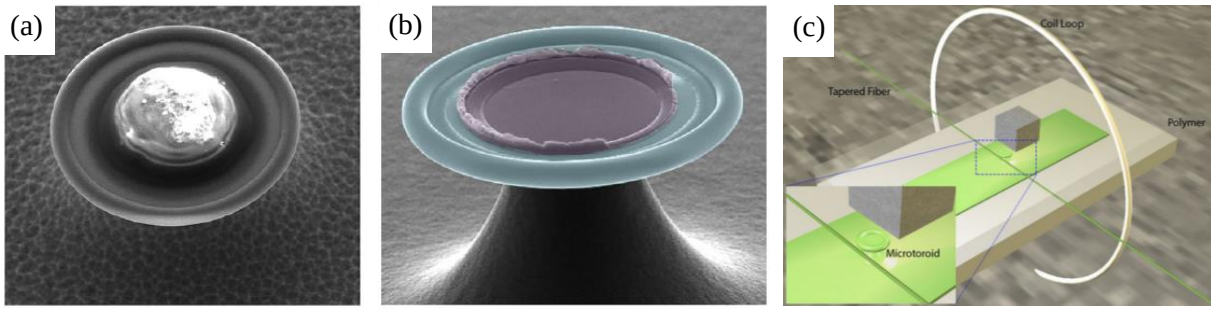

Figure 1.13: Optomechanical magnetometers (a) and (b) SEM image of a micro-toroid with Terfenol-D [39]-[40] (c) Microtoroid magnetometer using polydimethylsiloxane (PDMS) [41].

micro-toroidal using other ferromagnetic materials such as polydimethylsiloxane (PDMS) as illustrated in Figure 1.13.c.

Optomechanical cylinder resonators can be used to detect a magnetic field [42]. Figure 1.14.a shows the SEM image of the optomechanical cylinder resonator. The device is machined from a block of crystal CaF_2 attached to a ceramic base. First, the diameter of the block is reduced by machining to reach a diameter of 12 mm and a thickness of 4 mm respectively. Then the cylinder is covered with a ferromagnetic material (Terfenol-D). When a field is applied to the device, it mechanically deforms along the direction of the field. For an optical power of 100 µW, this magnetometer has a sensitivity up to 131 $pT/\sqrt{Hz}$.

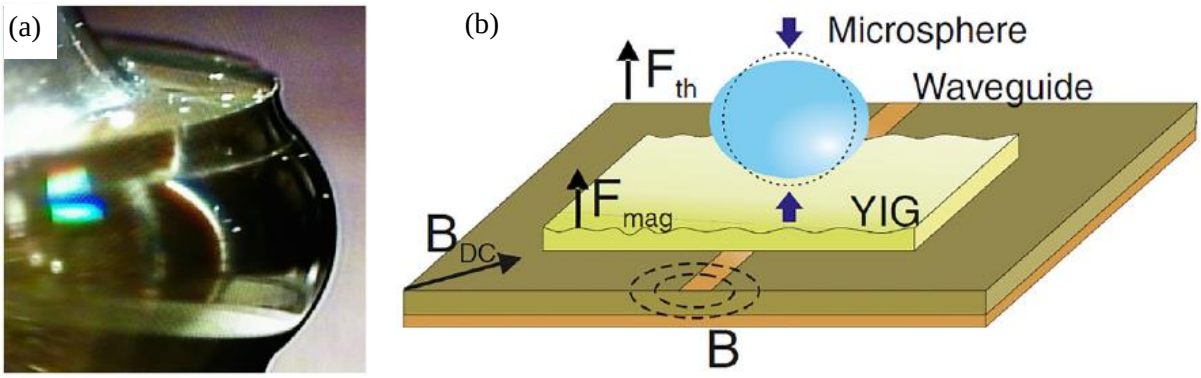

Figure 1.14: Optomechanical magnetometers (a) SEM image of a cylinder cavity [42] (b) Microsphere magnetometer working at hundreds of MHz to a few GHz [43].

As shown in Figure 1.14.b, microsphere optomechanical resonators can also detect a magnetic field. The device is composed of a barium-titanium-silicate microsphere and a thin magnetic film of yttrium iron garnet (YIG). The concept here is to couple the optical-mechanical interaction of the microsphere to the ferromagnetic resonance of the YIG thin film. As depicted in figure 1.14.b, when a field is applied the YIG layer deforms. This distorts the microsphere and changes its optical and mechanical resonance. This magnetometer has a sensitivity of 850 $pT/\sqrt{Hz}$.

1.2.4 Mass sensing

Mass detection is the reference application for nano/micro-mechanical resonators. In the state of the art there exists a great variety of devices allowing to detect a mass quantity. The most famous are the cantilevers or the nano-beam. Optomechanical resonators, according to their configuration, show very high sensitivity for mass sensing and this whatever the environment (vacuum, air or liquid).

This offers a significant benefit compared to cantilever or nano-beam. Indeed, due to the viscosity of the liquid, cantilever or nano-beam resonators can break down and do not resonate. Moreover, optomechanical WGM cavities (micro-disk, sphere or micro-toroidal) are much more resistant. They also present a moderate mechanical energy loss in liquid. In this section we will present the different types of optomechanical resonators (circular cavity, nano-ram…) dedicated to mass detection.

The detection principle of masses is very simple. The optomechanical resonator behaves like a mechanical resonator which resonance frequency is written as follows:

$$f_m = \frac{1}{2\pi}\sqrt{\frac{k_{eff}}{M}} \tag{1.4}$$

where $M = m_{eff} + m_p$ with m_{eff} the effective mass of the resonator and m_p the mass of the particle, k_{eff} is the effective stiffness of the resonator. From equation (1.4) and the sensitivity $S_m = \delta f_m / \delta M$, we can estimate the mass resolution M_{min} of the optomechanical resonator as follows :

$$M_{min} = -\frac{2M}{f_m}\delta f_m \tag{1.5}$$

- Microsphere for mass sensing :

An optomechanical microsphere presents interesting characteristics for mass detection. It presents both an optical WGM resonance with a very high-quality factor of the order of $10^6$and a mechanical resonance. A strong coupling allows the interaction between the optical and the mechanical. As the mass lands on the mechanical resonator (microsphere), the mechanical frequency changes according to equation (1.4). And this change is optically detectable.

The first realization of a microsphere for the detection of molecule was realized by the team of Tao Lu [29]. Figure 1.15.b illustrates the SEM image of a 100 µm diameter microsphere made in silica. When a mass (BSA protein) impacts the microsphere, the resonator becomes heavier and its resonance frequency changes as shown in figure 1.15.c. Also, the optical resonance wavelength is changed as depicted in Figure 1.15.a. In terms of resolution, the optomechanical microsphere can detect up to 66 kDa (1 Da = $1{,}66 \cdot 10^{-27} Kg$).

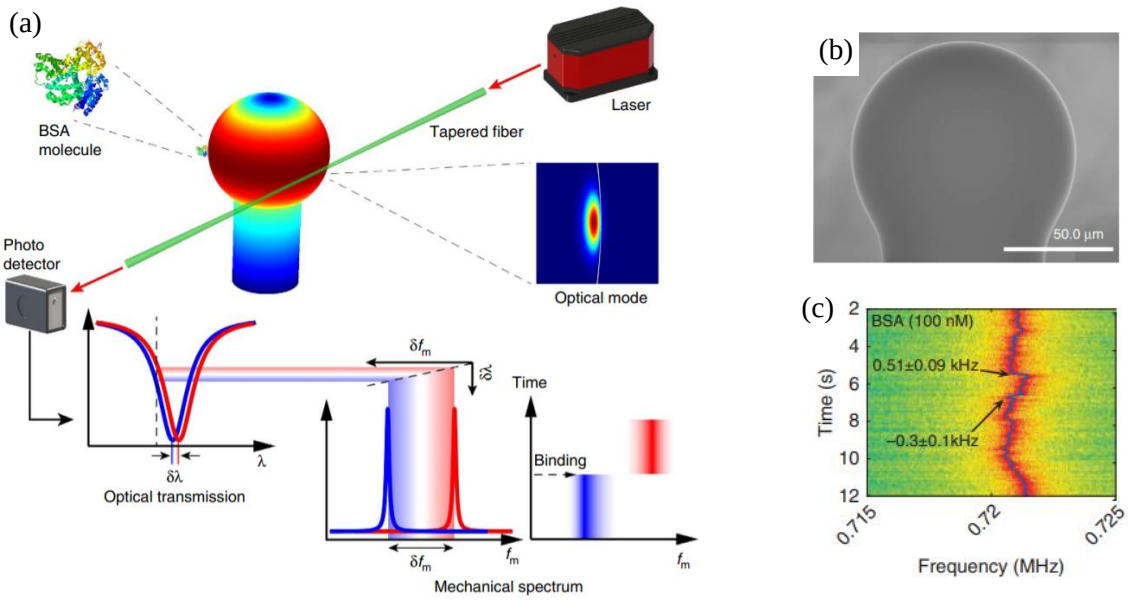

Figure 1.15: Optomechanical microsphere (a) Schematic illustrating the BSA mass detection (b) SEM image of the microsphere (c) Spectrogram of the mechanical resonance frequency [29].

- Nano-ram for mass sensing :

Optomechanical nano-ram resonators can be used as mass detectors. The optical resonator is completely dissociated from the mechanical resonator. Here the nano-ram is the mechanical resonator and an optical cavity the optical resonator. On this type of device, the idea is to make the mass deposit above the ram. The latter changes resonance frequency and this is visible in an optical way.

Figure 1.16 below shows an optomechanical nano-ram device [44]. The device is composed of an electrostatically excited nano-ram and an optical ring. The nano-ram is the mechanical resonator and the ring the optical resonator. When a mass is deposited on the nano-ram, its resonance frequency and its displacement are modified. This affects the light which propagates in the ring and thus the optical resonance. Figure 1.16.c shows the results of mass deposition.

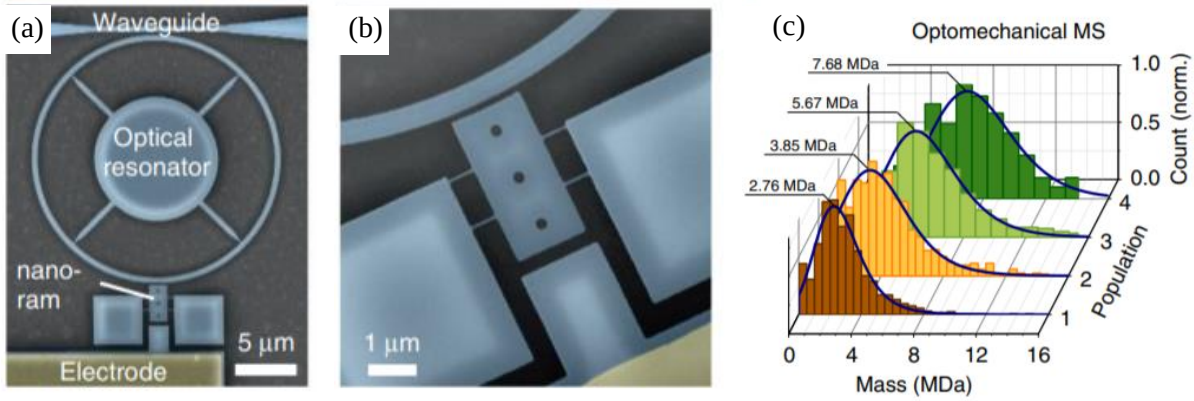

Figure 1.16: Optomechanical nano-ram (a) and (b) SEM image of an optomechanical nano-ram with an optical ring cavity (c) Mass sensing process [44].

- Microtoroid for mass sensing :

There are also other optomechanical resonators dedicated to mass detection. It is the case of the microtoroid [45] or the micro-disk resonator. Compared to the microsphere or nano-ram, the microtoroid resonator has a larger detection surface. Figure 1.17.a shows the SEM image of a 40 µm diameter silica microtoroid resonator. The particle deposition is done on the top of the microtoroid as depicted in figure 1.17.b. As more mass is deposited the mechanical resonance frequency is changed. In figure 1.17.c, we observe the resonance frequency associated with each quantity of mass.

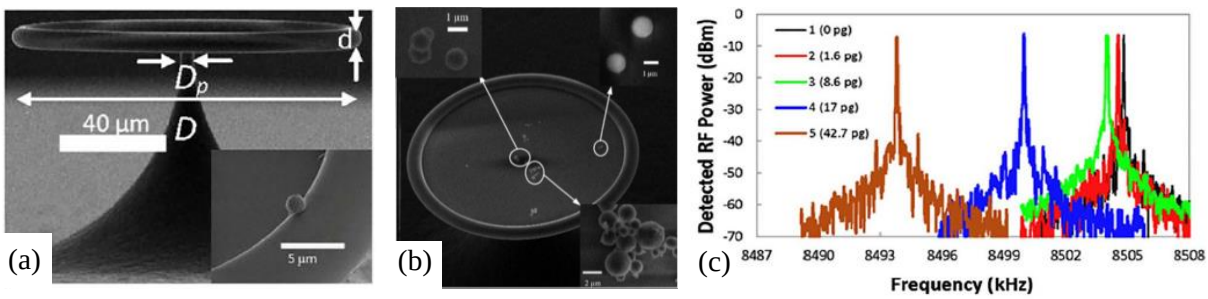

Figure 1.17: Optomechanical microtoroid (a) and (b) SEM image of the optomechanical microtoroid made in silica (c) Variation of the mechanical frequency as a function of the deposited mass [45].

1.2.5 Acoustic sensing

Thanks to its high optical sensitivity, optomechanical resonators can be used to detect an acoustic wave. In terms of application, acoustic sensors can be used in many fields such as avionics systems, or in the biomedical field. Today, the resonators used to detect acoustic waves are based on capacitive MEMS. However, they have some limitations such as low sensitivity and displacement. For this reason, optomechanical resonators are being considered as an alternative for acoustic wave detection.

- Microsphere for acoustic sensing :

Microsphere resonators can be used to detect acoustic waves [46]-[47]. Figure 1.18.a and 1.18.b show some examples of different microspheres used for ultrasonic wave detection. The idea is to place a sound wave just next to the microsphere. This wave will locally deform the resonator and change its mechanical frequency. This frequency variation is optically visible because the distance covered by the photons (optical resonance) is also disturbed.

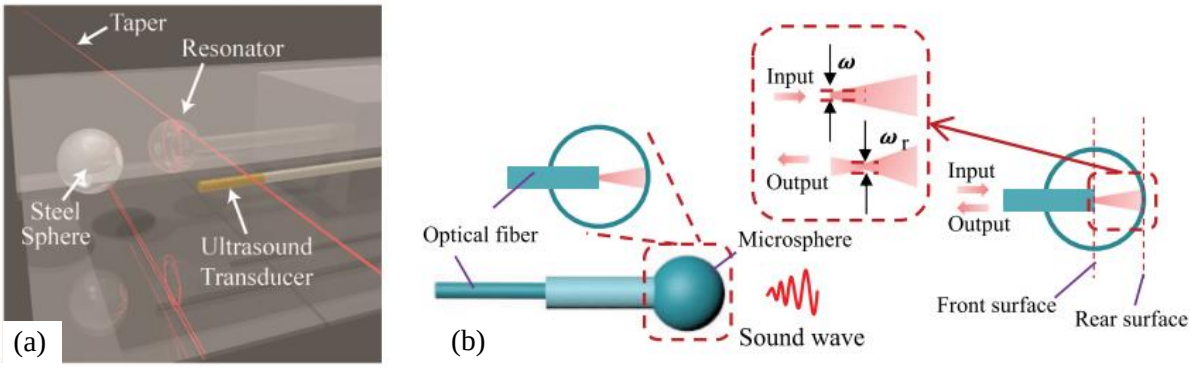

Figure 1.18: Optomechanical acoustic sensor (a) SEM image of a microsphere resonator [46] (b) Schematic of a microsphere-based sound detector [47].

- Micro-ring for acoustic sensing :

Optical rings can also detect an acoustic wave [48]. Figure 1.19.a shows an SEM image of the optical ring resonator. The operating principle is the same as for the microsphere. When an acoustic wave is applied the membrane is deformed on the optical ring. This changes the coupling between the membrane and the optical ring and consequently the optical resonance.

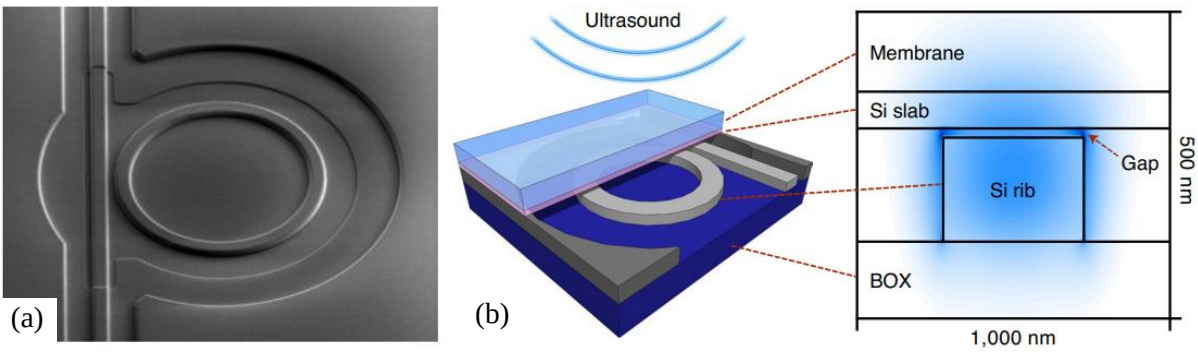

Figure 1.19: Optomechanical acoustic sensor (a) SEM image of an optomechanical ultrasound sensor (OMUS) (b) 3D schematic of the OMUS [48].

1.3. Mass detection context and available resonators

When we talk about mass detection, we are talking about detection in an unconstrained environment (air and vacuum) and in a constrained environment such as detection in a liquid medium. Concretely, it can be the detection of gas molecules, chemical or biological particles, ... In the state of the art, we can find a wide variety of resonators that can detect tiny masses.

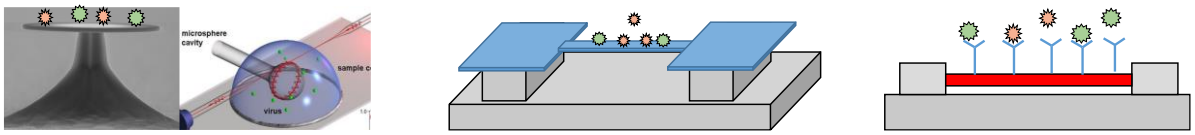

(a) (b) (c)

Figure 1.20: The main resonators that can detect particles (a) Optical resonators (b) Mechanical resonator (cantilevers or beam) (c) Nanowire sensor inspired from [49].

Figure 1.20 illustrates the main resonators able to detect a particle. There are optical resonators like the micro-disk, or microsphere (see Figure 1.20.a). This kind of resonator behaves like a very sensitive optical cavity and can detect extremely small masses. Mechanical resonators with cantilevers or beam (see Figure 1.20.b) are also known for their mechanical sensitivity especially in vacuum. And finally, the nanowire sensors (see Figure 1.20.c) in which the capacitance changes as a mass are applied to the wire.

	Optical Resonator (OR)	Mechanical resonator (MR)	Nanowire sensor (NS)
Transduction principle	Optical and Mechanical frequency variation	Mechanical frequency variation	Conductance change
Operability in a liquid environment	Resonates in liquid environment with Q_m~$10-30$ [50]	MR does not resonate in liquid environment due to viscosity	Resonates in a liquid environment [54]
Ability to detect a molecule	Yes [51]	Yes in vacuum [52]	Possible [55]
Microfluidic Integration	Fit to a continuous flow of particles	Fit to a continuous flow of particles	Fit to a continuous flow of particles
Matrix or multiplexing integration	Possible thanks to the dimensions of OR	Already demonstrated [53]	Possible thanks to the dimensions of NR

Table 1.1 : Comparison table of the main resonators capable to detect a molecule inspired from [49].

In this table, the resonators are evaluated on four criteria: operability in a liquid medium, ability to detect a molecule or a flow of molecules with a microfluidic channel and integration in a matrix form. If we refer to Table 1.1, the three resonators OR, MR and MS present the ability to detect a single molecule. In liquid medium, the OR and MS resonators have proven their capability to resonate. In contrast, the mechanical beam resonator breaks because of the high viscosity of the liquid environment. Only the optical resonators and the nanowire sensor can detect particles in this medium.

1.4. Optomechanical microdisk resonator

Among the available optical resonators, optomechanical micro-disks stand out. They can resonate in an unconstrained environment (vacuum, air) with excellent quality factor, and they are robust enough to not break in a liquid environment. Figures 1.21.a and 1.21.b show a graphical illustration of an optomechanical micro-disk embedded in liquid environment. The large area provides the opportunity to attach receptors so that the particles attach to the disk as shown in Figure 1.21.b. Otherwise, due to the inertia of the liquid, the particles will float and take a long time to attach to the disk.

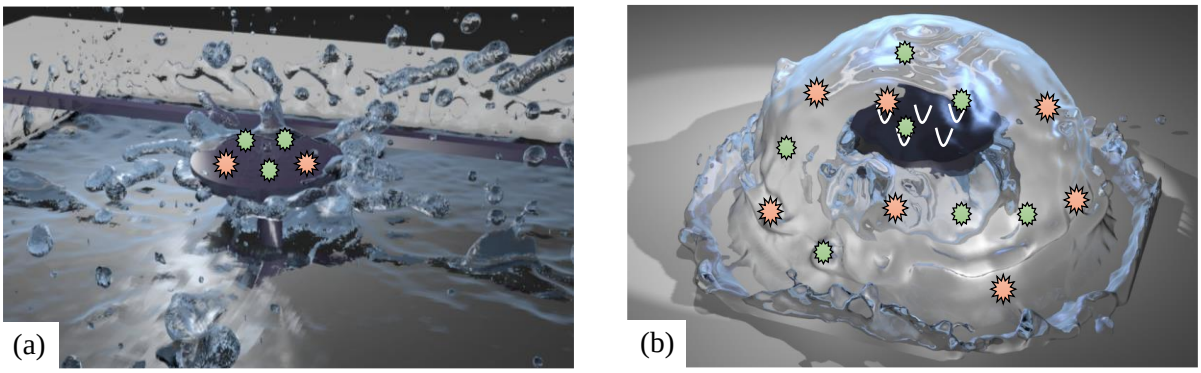

Figure 1.21: (a) and (b) Graphic illustration of an optomechanical micro-disk resonator in liquid with particle deposition inspired from [56].

The CEA has developed silicon optomechanical micro-disk resonators for mass applications. In terms of fabrication process, the resonators are made from a 200 mm SOI wafer. From the top to the bottom of the wafer, we have a thin layer (220 nm) of Si to realize the optomechanical micro-disk, then a layer of SiO_2 insulator (1 µm) to realize the pedestal and a thick layer of Si bulk. Today for the detection of particles, we have two types of resonators: optically actuated resonators and electrostatically actuated resonators.

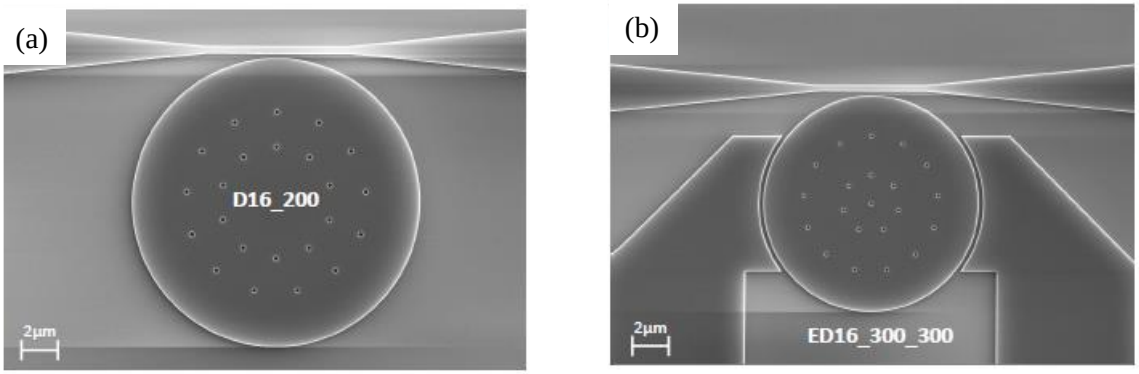

Figure 1.22: Optomechanical silicon micro-disk resonator (a) with optical actuation (Brownian) (b) with electrostatic actuation.

Optically actuated optomechanical resonators are devices in which the mechanics is optically stimulated. Figure 1.22.a shows the SEM image of our optomechanical micro-disk with optical actuation. The principle is the following, when an optical power is injected, the photons propagate in the waveguide and enter by evanescent coupling in the resonator disk. Then inside

the disk the photons propagate by successive reflection in WGM mode and exerts a radial pressure force on the walls of the cavity. This results in a radial mechanical movement of the disk. As seen in equation (1.3), the radial pressure force depends on the injected optical power. The higher this force is, the more the disk is mechanically stimulated. We will see this resonator in more detail in chapter 2.

Electrostatically actuated optomechanical resonators are devices in which the mechanics is electrically stimulated with electrodes. Figure 1.22.b shows the SEM image of the optomechanical micro-disk with electrostatic actuation. In this case we have both the optical excitation due to the photons that exert a radial pressure force and the external excitation with the electrodes. The electrostatically actuated resonator has a better mechanical quality factor, better SNR, better mass resolution than the optically actuated resonator. We prefer to work with this device to detect very small masses. We will see in the chapter 2 the operating principle of this resonator.

1.5 Conclusion

The objective of this chapter is to introduce optomechanical cavities. In the first part of the chapter, we have first presented the history of optomechanical cavities. From the very first experiments that highlighted the optical pressure forces to the present day with smaller and smaller cavities for more and more efficient sensor applications. In this section, we have presented the operating principle of an optomechanical system (OM) by explaining optical and mechanical resonance modes. The link between these two resonance modes is called “optomechanical coupling”. For sensing applications, we found two main families of optomechanical resonators: photonic crystal and WGM circular cavity.

In the second part of the chapter, we have reviewed the state of the art of optomechanical resonators and their applications. Today optomechanical devices are used in several fields of application. For example, to detect a force with a disk resonator [30] or a Fabry-Perot cavity [35], to measure an acceleration with photonic crystals [35] or a magnetic field with a microtoroid [40]-[42] or a microsphere [44]. The resonators are also able to measure with a very high accuracy a mass with a microsphere [29], a nano-ram [45] or a microtoroid [46]. Thanks to its high optical sensitivity, optomechanical resonators can also be used to detect an acoustic wave [47]-[48].

In the last part of the chapter, we explained the context of the thesis project. Among the resonators available for the mass sensing optomechanical micro-disks stand out. There are two types of optomechanical resonators : optically actuated and electrostatically actuated resonators which are both developed at CEA-Leti. During this thesis, we will work on the electrostatically actuated configuration to realize the compact modeling and the design of the readout circuit. We will see why in the next chapiter.

References

[1] M. Aspelmeyer, T. J. Kippenberg, et F. Marquardt, « Cavity optomechanics », Rev. Mod. Phys., vol. 86, no 4, p. 1391-1452, déc. 2014, doi: 10.1103/RevModPhys.86.1391.

[2] J. Kepler, De cometis libelli tres. Vindelicorvm: A. Apergeri, 1619.

[3] P. N. Lebedev, « EXPERIMENTAL EXAMINATION OF LIGHT PRESSURE », p. 26.

[4] E. F. Nichols et G. F. Hull, « A Preliminary Communication on the Pressure of Heat and Light Radiation », Phys. Rev. (Series I), vol. 13, no 5, p. 307-320, nov. 1901, doi: 10.1103/PhysRevSeriesI.13.307.

[5] The Collected Papers of Albert Einstein, Volume 2 (English). 1989.

[6] R. Frisch, « Experimenteller Nachweis des Einsteinschen Strahlungsrückstoßes », Z. Physik, vol. 86, no 1, p. 42-48, janv. 1933, doi: 10.1007/BF01340182.

[7] R. A. Beth, « Mechanical Detection and Measurement of the Angular Momentum of Light », Phys. Rev., vol. 50, no 2, p. 115-125, juill. 1936, doi: 10.1103/PhysRev.50.115.

[8] https://web.pa.msu.edu/people/dykman/pub06/Sov.Phys.Sol.St._78.pdf

[9] A. Dorsel, J. D. McCullen, P. Meystre, E. Vignes, et H. Walther, « Optical Bistability and Mirror Confinement Induced by Radiation Pressure », Phys. Rev. Lett., vol. 51, no 17, p. 1550-1553, oct. 1983, doi: 10.1103/PhysRevLett.51.1550.

[10] C. Fabre, M. Pinard, S. Bourzeix, A. Heidmann, E. Giacobino, et S. Reynaud, « Quantum-noise reduction using a cavity with a movable mirror », Phys. Rev. A, vol. 49, no 2, p. 1337-1343, févr. 1994, doi: 10.1103/PhysRevA.49.1337.

[11] S. Mancini et P. Tombesi, « Quantum noise reduction by radiation pressure », Phys. Rev. A, vol. 49, no 5, p. 4055-4065, mai 1994, doi: 10.1103/PhysRevA.49.4055.

[12] K. Jacobs, P. Tombesi, M. J. Collett, et D. F. Walls, « Quantum-nondemolition measurement of photon number using radiation pressure », Phys. Rev. A, vol. 49, no 3, p. 1961-1966, mars 1994, doi: 10.1103/PhysRevA.49.1961.

[13] T. Carmon, H. Rokhsari, L. Yang, T. J. Kippenberg, et K. J. Vahala, « Temporal Behavior of Radiation-Pressure-Induced Vibrations of an Optical Microcavity Phonon Mode », Phys. Rev. Lett., vol. 94, no 22, p. 223902, juin 2005, doi: 10.1103/PhysRevLett.94.223902.

[14] J. D. Thompson, B. M. Zwickl, A. M. Jayich, F. Marquardt, S. M. Girvin, et J. G. E. Harris, « Strong dispersive coupling of a high-finesse cavity to a micromechanical membrane », Nature, vol. 452, no 7183, Art. no 7183, mars 2008, doi: 10.1038/nature06715.

[15] X. Jiang, Q. Lin, J. Rosenberg, K. Vahala, et O. Painter, « High-Q double-disk microcavities for cavity optomechanics », Opt. Express, OE, vol. 17, no 23, p. 20911-20919, nov. 2009, doi: 10.1364/OE.17.020911.

[16] G. S. Wiederhecker, L. Chen, A. Gondarenko, et M. Lipson, « Controlling photonic structures using optical forces », Nature, vol. 462, no 7273, Art. no 7273, déc. 2009, doi: 10.1038/nature08584.

[17] R. Ma, A. Schliesser, P. Del'Haye, A. Dabirian, G. Anetsberger, et T. J. Kippenberg, « Radiation-pressure-driven vibrational modes in ultrahigh-Q silica microspheres », Opt. Lett., OL, vol. 32, no 15, p. 2200-2202, août 2007, doi: 10.1364/OL.32.002200.

[18] Y.-S. Park et H. Wang, « Resolved-sideband and cryogenic cooling of an optomechanical resonator », Nature Phys, vol. 5, no 7, Art. no 7, juill. 2009, doi: 10.1038/nphys1303.

[19] M. Tomes et T. Carmon, « Photonic Micro-Electromechanical Systems Vibrating at X-band (11-GHz) Rates », Phys. Rev. Lett., vol. 102, no 11, p. 113601, mars 2009, doi: 10.1103/PhysRevLett.102.113601.

[20] M. Eichenfield, J. Chan, R. M. Camacho, K. J. Vahala, et O. Painter, « Optomechanical crystals », Nature, vol. 462, no 7269, Art. no 7269, nov. 2009, doi: 10.1038/nature08524.

[21] P. W. Hease, « Gallium Arsenide optomechanical disks approaching the quantum regime », p. 148.

[22] B. Guha, « Surface-enhanced optomechanical disk resonators and force sensing », These de doctorat, Sorbonne Paris Cité, 2017. Consulté le: 28 février 2022. [En ligne]. Disponible sur: http://www.theses.fr/2017USPCC154

[23] C. Metzger, I. Favero, A. Ortlieb, et K. Karrai, « Optical self cooling of a deformable Fabry-Perot cavity in the classical limit », Phys. Rev. B, vol. 78, no 3, p. 035309, juill. 2008, doi: 10.1103/PhysRevB.78.035309.

[24] R. W. Boyd, « Chapter 2 - Wave-Equation Description of Nonlinear Optical Interactions », in Nonlinear Optics (Second Edition), R. W. Boyd, Éd. San Diego: Academic Press, 2003, p. 67-127. doi: 10.1016/B978-012121682-5/50003-1.

[25] B.-B. Li, L. Ou, Y. Lei, et Y.-C. Liu, « Cavity optomechanical sensing », Nanophotonics, vol. 10, no 11, p. 2799-2832, sept. 2021, doi: 10.1515/nanoph-2021-0256.

[26] M. Eichenfield, R. Camacho, J. Chan, K. J. Vahala, et O. Painter, « A picogram- and nanometre-scale photonic-crystal optomechanical cavity », Nature, vol. 459, no 7246, Art. no 7246, mai 2009, doi: 10.1038/nature08061.

[27] G. S. MacCabe et al., « Nano-acoustic resonator with ultralong phonon lifetime », Science, vol. 370, no 6518, p. 840-843, nov. 2020, doi: 10.1126/science.abc7312.

[28] M. Wu et al., « Dissipative and Dispersive Optomechanics in a Nanocavity Torque Sensor », Phys. Rev. X, vol. 4, no 2, p. 021052, juin 2014, doi: 10.1103/PhysRevX.4.021052.

[29] W. Yu, W. C. Jiang, Q. Lin, et T. Lu, « Cavity optomechanical spring sensing of single molecules », Nat Commun, vol. 7, no 1, Art. no 1, juill. 2016, doi: 10.1038/ncomms12311.

[30] E. Gavartin, P. Verlot, et T. J. Kippenberg, « A hybrid on-chip optomechanical transducer for ultrasensitive force measurements », Nature Nanotech, vol. 7, no 8, Art. no 8, août 2012, doi: 10.1038/nnano.2012.97.

[31] E. Gil-Santos et al., « Optomechanical detection of vibration modes of a single bacterium », Nat. Nanotechnol., vol. 15, no 6, p. 469-474, juin 2020, doi: 10.1038/s41565-020-0672-y.

[32] P. H. Kim, B. D. Hauer, C. Doolin, F. Souris, et J. P. Davis, « Approaching the standard quantum limit of mechanical torque sensing », Nat Commun, vol. 7, no 1, Art. no 1, oct. 2016, doi: 10.1038/ncomms13165.

[33] E. Verhagen, S. Deléglise, S. Weis, A. Schliesser, et T. J. Kippenberg, « Quantum-coherent coupling of a mechanical oscillator to an optical cavity mode », Nature, vol. 482, no 7383, Art. no 7383, févr. 2012, doi: 10.1038/nature10787.

[34] W.-Z. Zhang, Y. Han, B. Xiong, et L. Zhou, « Optomechanical force sensor in a non-Markovian regime », New J. Phys., vol. 19, no 8, p. 083022, août 2017, doi: 10.1088/1367-2630/aa68d9.

[35] F. Fogliano et al., « Ultrasensitive nano-optomechanical force sensor operated at dilution temperatures », Nat Commun, vol. 12, no 1, Art. no 1, juill. 2021, doi: 10.1038/s41467-021-24318-y.

[36] A. G. Krause, M. Winger, T. D. Blasius, Q. Lin, et O. Painter, « A high-resolution microchip optomechanical accelerometer », Nature Photon, vol. 6, no 11, Art. no 11, nov. 2012, doi: 10.1038/nphoton.2012.245.

[37] B. Dong, H. Cai, J. M. Tsai, D. L. Kwong, et A. Q. Liu, « An on-chip opto-mechanical accelerometer », in 2013 IEEE 26th International Conference on Micro Electro Mechanical Systems (MEMS), janv. 2013, p. 641-644. doi: 10.1109/MEMSYS.2013.6474323.

[38] Y. L. Li et P. F. Barker, « Field Evaluation of a Portable Whispering Gallery Mode Accelerometer », Sensors, vol. 18, no 12, Art. no 12, déc. 2018, doi: 10.3390/s18124184.

[39] B.-B. Li et al., « Ultrabroadband and sensitive cavity optomechanical magnetometry », Photon. Res., PRJ, vol. 8, no 7, p. 1064-1071, juill. 2020, doi: 10.1364/PRJ.390261.

[40] B.-B. Li et al., « Invited Article: Scalable high-sensitivity optomechanical magnetometers on a chip », APL Photonics, vol. 3, no 12, p. 120806, déc. 2018, doi: 10.1063/1.5055029.

[41] J. Zhu, G. Zhao, I. Savukov, et L. Yang, « Polymer encapsulated microcavity optomechanical magnetometer », Sci Rep, vol. 7, no 1, Art. no 1, août 2017, doi: 10.1038/s41598-017-08875-1.

[42] C. Yu et al., « Optomechanical Magnetometry with a Macroscopic Resonator », Phys. Rev. Applied, vol. 5, no 4, p. 044007, avr. 2016, doi: 10.1103/PhysRevApplied.5.044007.

[43] M. F. Colombano et al., « Ferromagnetic Resonance Assisted Optomechanical Magnetometer », Phys. Rev. Lett., vol. 125, no 14, p. 147201, oct. 2020, doi: 10.1103/PhysRevLett.125.147201.

[44] M. Sansa et al., « Optomechanical mass spectrometry », Nat Commun, vol. 11, no 1, p. 3781, déc. 2020, doi: 10.1038/s41467-020-17592-9.

[45] F. Liu, S. Alaie, Z. C. Leseman, et M. Hossein-Zadeh, « Sub-pg mass sensing and measurement with an optomechanical oscillator », Opt. Express, OE, vol. 21, no 17, p. 19555-19567, août 2013, doi: 10.1364/OE.21.019555.

[46] M. V. Chistiakova et A. M. Armani, « Photoelastic ultrasound detection using ultra-high-Q silica optical resonators », Opt. Express, OE, vol. 22, no 23, p. 28169-28179, nov. 2014, doi: 10.1364/OE.22.028169.

[47] C. Han, C. Zhao, H. Ding, et C. Chen, « Spherical microcavity-based membrane-free Fizeau interferometric acoustic sensor », Opt. Lett., OL, vol. 44, no 15, p. 3677-3680, août 2019, doi: 10.1364/OL.44.003677.

[48] W. J. Westerveld et al., « Sensitive, small, broadband and scalable optomechanical ultrasound sensor in silicon photonics », Nat. Photonics, vol. 15, no 5, Art. no 5, mai 2021, doi: 10.1038/s41566-021-00776-0.

[49] F. Vollmer and L. Yang, "Review Label-free detection with high-Q microcavities: a review of biosensing mechanisms for integrated devices," Nanophotonics, vol. 1, no. 3–4, pp. 267–291, Dec. 2012, doi: 10.1515/nanoph-2012-0021.

[50] "High-frequency nano-optomechanical disk resonators in liquids | Nature Nanotechnology." https://www.nature.com/articles/nnano.2015.160.

[51] E. Gil-Santos et al., "Optomechanical detection of vibration modes of a single bacterium," Nat. Nanotechnol., vol. 15, no. 6, Art. no. 6, Jun. 2020, doi: 10.1038/s41565-020-0672-y.

[52] "Towards single-molecule nanomechanical mass spectrometry | Nature Nanotechnology." https://www.nature.com/articles/nnano.2009.152

[53] "Very Large Scale Integration Optomechanics: a cure for loneliness of NEMS resonators? | IEEE Conference Publication | IEEE Xplore." https://ieeexplore.ieee.org/document/8614532.

[54] M. Curreli et al., "Real-Time, Label-Free Detection of Biological Entities Using Nanowire-Based FETs," IEEE Transactions on Nanotechnology, 2008, doi: 10.1109/TNANO.2008.2006165.

[55] F. Patolsky, G. Zheng, and C. M. Lieber, "Nanowire sensors for medicine and the life sciences," Nanomedicine (Lond), vol. 1, no. 1, pp. 51–65, Jun. 2006, doi: 10.2217/17435889.1.1.51.

[56] « Christopher G. Baker », Christopher G. Baker. https://christophergbaker.com/

Chapter 2

Optomechanical Sensor: Theory & Modeling

Contents

In this chapter we will analyze the behavior of a silicon micro-disk. In the first section, we will present the optical and mechanical resonator of the disk. An optomechanical coupling allows to link these two resonance modes. In this thesis we have at our disposal two kinds of optomechanical sensors: optically actuated and electrostatic. In the case of an optically driven resonator, the disk is mechanically stimulated by the optical power injected through the gratings. We will see in the second section how it works and the equations that describe it. In the case of an electrostatically actuated resonator, the disk is mechanically stimulated by electrodes. In this thesis, we will mostly work on this type of device because the resonator has better mechanical signal . In the perspective of the design of a readout electronics, we propose the development of a compact Verilog-A model.

2.1. Theory of a silicon optomechanical micro-disk

In this section, we present the physics of an optomechanical micro-disk. Fabricated in silicon, the micro-disk constitutes the basic element for the design of ultra-sensitive opto-mechanical sensors for the mass detection. In terms of dimensions, its diameter is in the micrometer order (from 5 µm and 20 µm) and has a thickness of several hundred nanometers (~220 nm). Thanks to its small size, the silicon micro-disk supports two resonance modes. An optical resonance mode and a mechanical resonance mode. The optical resonance mode is supported by the optical cavity that constitutes the micro-disk. In this mode, due to the difference of the refractive index, the light propagates by reflection, it is the Whispering Gallery Mode (WGM). The mechanical resonance mode is supported by the mechanical cavity. The micro-disk is able to resonate radially, it is the Radial Breathing Mode (RBM). This resonance mode appears only at high mechanical frequencies. Figure 2.1.a below illustrates the two resonance modes of the micro-disk. A coupling called "optomechanical coupling" allows linking its two resonance modes. In order to optimize this coupling, a SiO_2 pedestal as shown in Figure 2.1.b supports the micro-disk.

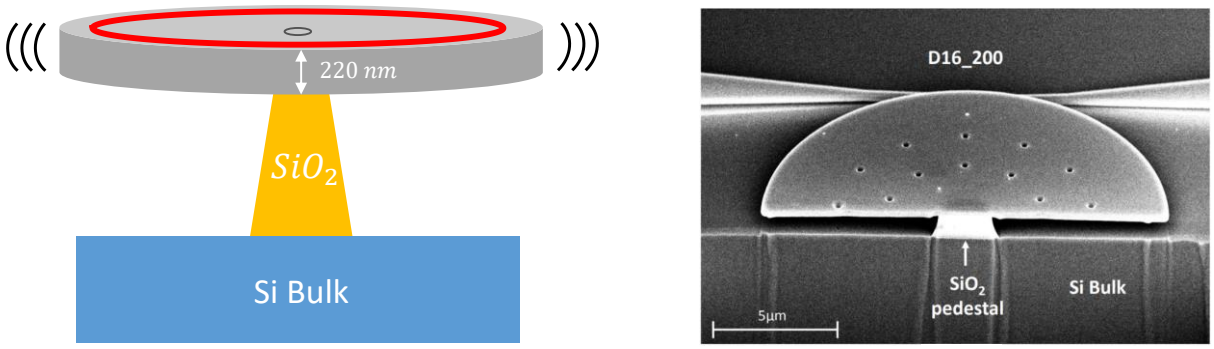

(a) (b)

Figure 2.1: (a) Graphical view of a silicon optomechanical micro-disk with the two resonance modes (optical and mechanical). (b) SEM image of a disk cross section, a SiO_2 pedestal supports the whole structure.

In the following sub-sections, we will first present the theory of the micro-disk optical cavity. Then we will see the theory of the micro-disk mechanical cavity. Finally, we will introduce the equations that describe the opto-mechanical coupling.

2.1.1 Optical micro-disk cavity

The silicon micro-disk hosts the WGM optical resonance mode. It behaves like an optical resonator and has a resonance wavelength λ_{res} and an optical quality factor Q_{opt}.

2.1.1.1 Whispering Gallery Mode

The Whispering Gallery Mode [1]-[3] is a concept introduced in the 19th century by Lord Rayleigh to explain the propagation of the sound inside the Saint-Paul Cathedral in London (see Figure 2.2.a). Indeed, he observed that inside the dome (30 m diameter) the whispering of a person located near the wall could be heard at any point of the gallery (see Figure 2.2. b).

(a) (b)

Figure 2.2: (a) The Saint-Paul Cathedral in London (b) The Cathedral dome in which Lord Rayleigh introduced the WGM resonance mode.

He assumed that the sound wave propagates along the dome by successive reflection. By sticking to the wall, the intensity of the sound only decreases as a function of the inverse of the distance. This explains why whispers are audible at any point in the dome. To support his thesis, he developed the acoustic theory of whispering waves [4]-[5].

The same behavior can be observed in the propagation of optical waves. In a circular optical cavity, because of the difference in refractive index, the light also propagates by successive reflections. For a silicon micro-disk resonator this property has been demonstrated [6], by analogy we speak of optical WGM mode.

- Micro-disk geometrical approach :

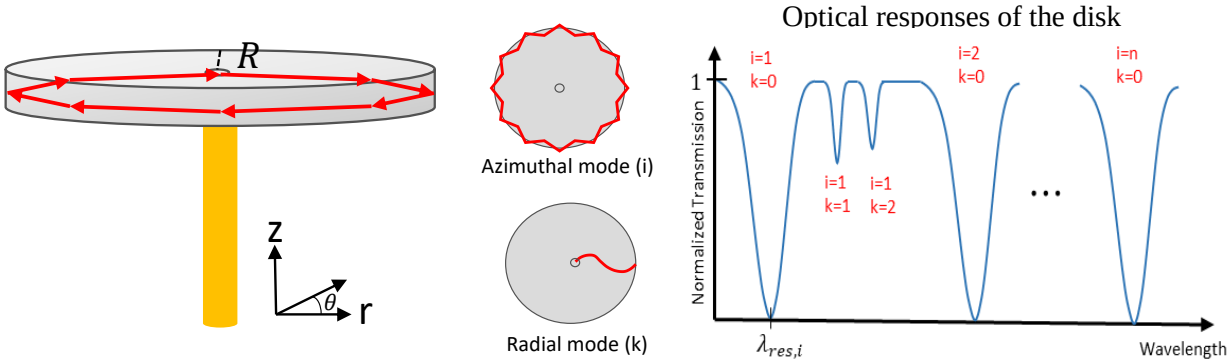

(a) (b) (c)

Figure 2.3: (a) Schematic of a micro-disk where the optical wave propagates in a WGM in red (b) The azimuthal (i) and radial propagation mode (k) (c) The multiple optical resonance of the micro-disk.

Within the micro-disk, the light propagates in two possible ways. In one case, it propagates by sticking to the wall and following the angle θ, this is the Azimuthal mode. In the other case, it propagates from the wall to the center of the disk along the r axis, this is the Radial mode. Figure 2.3.b above illustrates the two propagation modes.

Optically, a micro-disk resonates when the light makes a complete loop as illustrated in Figure 2.3.a. The photons, at the end of their turn loop on themselves in phase. This creates constructive interferences, which are at the origin of the several optical resonances of the disk as shown in Figure 2.3.c.

The optical resonance condition of the micro-disk is written as follows:

$$2\pi R n_{eff} = m\lambda_{res} \tag{2.1}$$

where R is the radius of the disk, n_{eff} is the effective index of the disk and m an integer such as $m = 1,2,3,...$ Equation (2.1) gives the optical multiple resonances of a micro-disk. The resonance wavelengths are spaced by $\Delta\lambda_{FSR}$ the Free Spectral Range (FSR) which is expressed as below :

$$\Delta\lambda_{FSR} = (m+1)\lambda_{res} - m\lambda_{res} \tag{2.2}$$

- FEM simulations of a micro-disk :

In an optical cavity of given geometry, the propagation of the WGM mode can be described analytically by Maxwell's equations. The propagation equation of the electromagnetic wave (electric field $\vec{E}$ and magnetic field $\vec{H}$) is given by Helmholtz's equations :

$$\begin{cases} \nabla^2\vec{E} + \left(\frac{\omega}{c}\right)^2 \vec{E} = \vec{0} \\ \nabla^2\vec{H} + \left(\frac{\omega}{c}\right)^2 \vec{H} = \vec{0} \end{cases} \tag{2.3}$$

where c is the speed of light in vacuum, and ω the angular frequency. The micro-disk can support two modes of field propagation: Transverse Electric (TE) and Transverse Magnetic (TM) modes. The TE mode corresponds to a type of field propagation where the E_r, E_θ, H_z components are non-zero. The TM mode corresponds to the field propagation where the H_r, H_θ, E_z components are non-zero. To implement and solve the propagation equations in a micro-disk we use the Finite Element Method (FEM).

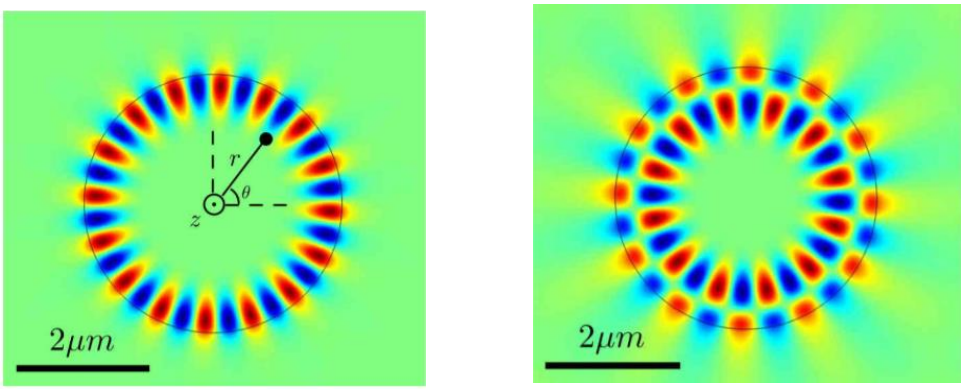

(a) (b)

Figure 2.4: 2D numerical simulations of WGMs for a 2 µm-radius disk (a) The FEM simulation of the azimuthal propagation mode (b) FEM simulation of the azimuthal and radial propagation mode [7].

Figure 2.4 depicts the FEM simulations made on a micro-disk. The red and blue colors correspond to the intensity of the electric field. In these simulations we can see in Figure 2.4.a that the optical wave propagates along the wall along the axis θ, it is the azimuthal mode. The radial mode corresponds to the propagation along the r axis. The optical wave can also propagate with a combined azimuthal and radial mode as illustrated in Figure 2.4.b.

2.1.1.2 Optical quality factor

Optically the micro-disk is a resonator and has a quality factor Q_{opt}. This factor is defined as the ratio between the maximum energy stored and the energy dissipated per cycle. Experimentally, Q_{opt} is calculated from the resonance spectrum by using the expression:

$$Q_{opt} = \frac{energy\ stored}{dissipated\ per\ cycle} = \frac{\lambda_{res}}{\Delta\lambda} \tag{2.4}$$

where $\lambda_{res}$is the resonance wavelength extracted when the gain is maximum and $\Delta\lambda$ is the resonance bandwidth. The quality factor indicates the damping of the optical resonator. The higher this factor is, the longer the resonator will oscillate. The micro-disk resonator has a very high optical quality factor in general of the order $Q_{opt}\sim10^5$. This is explained by the fact that the resonator is subject to low losses. As discussed in [7]-[8], the different sources of energy loss of a micro-disk are:

- Bending losses :

Bending losses are a very common type of loss for waveguide devices with curved geometry. Indeed, the wave is not totally reflected near the curvature between the junction of the two mediums. This induces internal and external losses to the surrounding environment. In the case of the micro-disk, these losses are not negligible because of its circular structure. Every time the optical wave is reflected on the wall of the disk, there exists an inflection loss. The bending losses of a disk depend strongly on its radius and its effective index. The larger the radius and the effective index, the lower the bending losses.

- Absorption losses :

The loss of absorption is related to the properties of the materials and chemicals used in the fabrication process of the micro-disk. There are two types of absorption losses, internal and external. The internal losses depend on the micro-disk composition. Here the device is made of silicon (Si), which has an energy gap of $1{,}14\ eV$ at $273\ K$. To avoid the linear absorption zone, it is necessary that the photons propagate by respecting this condition $\hbar\omega < 1{,}14\ eV$. This corresponds to a minimum wavelength of 1087 nm. In our experiments, we generally work between 1500 nm and 1600 nm, which guarantees the non-absorption condition. External losses are generated by other materials and chemical elements used in the fabrication process.

- Scattering losses :

Scattering losses are caused by the interaction between light and wall imperfections. At the end of the fabrication process, the wall of the disk is not smooth. At the nano-metric level, roughness and structural imperfections are observed due to the different manufacturing processes (etching step ...). In contact with these imperfections, the light diffuses in a radiative way in all directions.

- External evanescent losses :

These losses are visible when two optical devices are very close. A part of the wave that propagated in the first cavity is transmitted by evanescence to the other cavity.

2.1.2 Mechanical micro-disk cavity

In the section above, we have presented the optical properties of the micro-disk. We will see in this section its mechanical properties. When an optomechanical micro-disk is placed on a pedestal, it behaves like a mechanical resonator. This means that for a certain range of frequencies, it enters in resonance and deforms mechanically. This frequency range depends on the disk radius. The smaller the radius, the higher the mechanical resonance frequency. The main resonance mode of the disk is the Radial Breathing Mode (RBM). As a mechanical resonator, the micro-disk has a resonance frequency f_m and a quality factor Q_m.

2.1.2.1 Radial Breathing Mode (RBM)

The radial breathing mode [9]-[11] is a mechanical resonance mode based on the phonon. Phonons are the ability of a crystalline solid to vibrate mechanically when an energy is brought to it. In our case, the micro-disk is considered as a crystalline structure composed of silicon atoms. When a quantity of energy is supplied, the atoms start to vibrate mechanically from near to near in a radial way, this is called radial breathing. There are several ways to provide energy to the structure. Optically through the wave that propagates in the cavity or by external stimulation. In the next sections, we will see these two types of excitation.

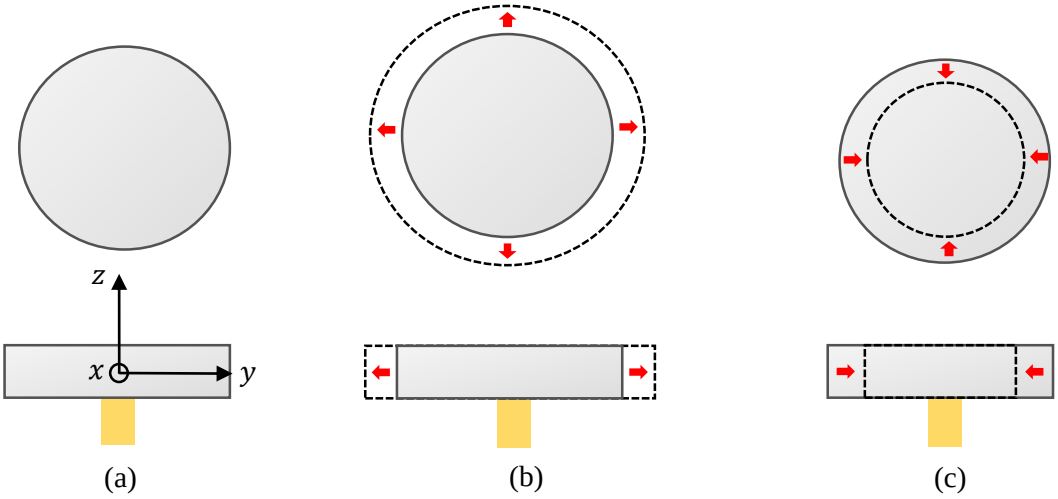

Figure 2.5: Graph explaining the disk RBM resonance mode (a) initial disk configuration (b) configuration where the disk expands (c) configuration where the disk contracts.

Figure 2.5 is a schematic diagram explaining the different steps of the RBM mechanical mode. Figure 2.5.a shows the initial state of the disk without deformation. When a quantity of energy is supplied, it expands (Figure 2.5.b) and then contracts (Figure 2.5.c), this is the breathing mode.

- FEM simulations of a micro-disk :

To determine the resonance frequency f_m and the micro-disk radial displacement, COMSOL numerical simulations were performed. We considered, as shown in Figure 2.1.a, a silicon disk of radius 5 µm, fixed at the center by a SiO_2 pedestal. Figure 2.6 below shows the results of FEM simulations. At the mechanical resonance here at 509 MHz, the disk expands to up to 5.5 µm radius as illustrated in Figure 2.6.b. It then re-contracts down to 4.1 µm in radius.

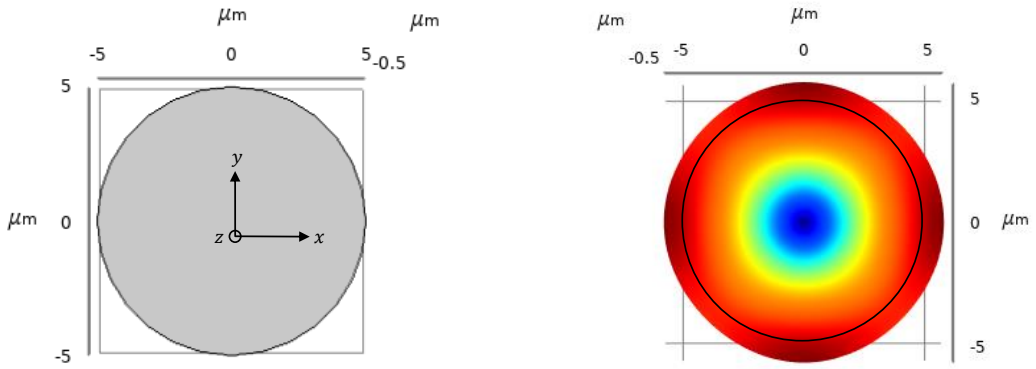

Figure 2.6: COMSOL numerical simulations of RBM resonance mode for a 5 µm-radius disk (a) initial disk configuration (b) Configuration where the radius of the disk expands.

2.1.2.2 Mechanical quality factor

As a mechanical resonator, the micro-disk has a mechanical quality factor Q_{mec}. This factor is defined as the ratio between the maximum energy stored and the energy dissipated per cycle. Experimentally, Q_{mec} is calculated from the resonance spectrum by using the following expression:

$$Q_m = \frac{energy\ stored}{dissipated\ per\ cycle} = \frac{f_m}{\Delta f} \tag{2.5}$$

where f_m is the mechanical resonance frequency extracted when the gain is maximum and Δf is the bandwidth of the resonator. The mechanical quality factor is an important feature to evaluate the performance of our mass sensor. A high-quality factor allows us to have a very high signal-to-noise-ratio and therefore a better mass resolution. To estimate the quality factor, it is necessary to know the different sources of mechanical losses. The main sources are [7]-[8]:

- Viscosity damping :

The surrounding environment is an important source of energy loss for the mechanical resonator. Indeed, depending on the environment viscosity, the resonator has not the same mechanical quality factor. In liquid, for example, because of the high viscosity, the micro-disk resonator has a moderate mechanical quality factor $Q_m \sim 10 - 50$. While in vacuum or air, this mechanical quality factor is very high up to 1000. To evaluate the losses caused by the damping from the environment to the mechanical quality factor, a simplified analytical expression has been proposed by [12]:

$$Q_{viscosity} = \frac{3.34 \cdot 10^5}{3.18/\sqrt{R} + \sqrt{R}/H} \frac{1}{\sqrt{\rho\mu}} \tag{2.6}$$

where R and H are the radius and thickness of the disk respectively, ρ and μ are the density and the fluid viscosity respectively of the surrounding environment. If we consider air ($\rho = 1200\ kg/m^3$, $\mu = 1.8 \cdot 10^{-5} Pa/s$) and liquid water ($\rho = 1000\ kg/m^3$, $\mu = 1 \cdot 10^{-3} Pa/s$) as the

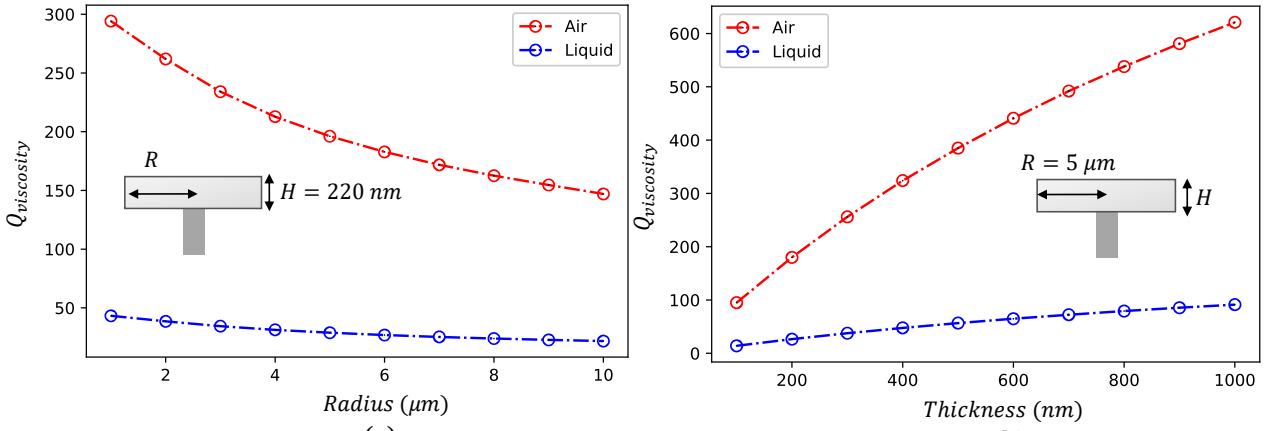

Figure 2.7: Analytical variation of viscosity losses in air and liquid (water) as a function of (a) disk radius variation (b) and thickness variation.

medium, we can plot an analytical estimation of the viscosity based on Equation (2.6). Figure 2.7 shows the variation of viscosity as a function of disk radius and thickness for different environment (air and liquid). Viscosity losses are very important in the liquid and this strongly limits the mechanical quality factor Q_m. In order to have negligible viscosity losses, it is necessary to adjust the dimensions of the disk. For a given thickness, reducing the disk radius will reduce the viscosity losses as shown in Figure 2.7.a. Similarly, for a given radius, increasing the thickness helps to reduce the losses as represented in Figure 2.7.b.

- Clamping losses :

The clamping losses correspond to the dissipation of the mechanical energy caused by the disk-pedestal clamping area. The more the clamping area is important and the more the mechanical energy losses by clamping is high. According to [13], to get a very low clamping loss, the ratio $(R - R_{pd})/\ R$ between the disk radius R and the pedestal radius R_{pd}must be between 0.822 and 0.835.

- Thermo-elastic damping :

When an elastic solid is set in motion, it becomes unstable and has an excess of kinetic and potential energy. This excess energy is dissipated thanks to the coupling between the mechanical deformation and the temperature, which allows the system to return to equilibrium. This energy dissipation process is called thermo-elastic damping. Based on [14], for a circular silicon resonator with a radius between 3 and 20 µm, the thermo-elastic losses are estimated at 10^6. These losses are not the main losses limiting the mechanical quality factor.

2.1.3 Optomechanical coupling coefficient

In the previous sections 2.1.1 and 2.1.2, we have seen that the micro-disk behaves both as an optical resonator and as a mechanical resonator. Optically the disk resonates in WGM mode and mechanically in RBM mode. These two modes of resonance are superimposed by a coupling called the optomechanical coupling (see Figure 2.8.a). We describe here this optomechanical coupling to understand the physical interaction between the optical and mechanical resonance modes.

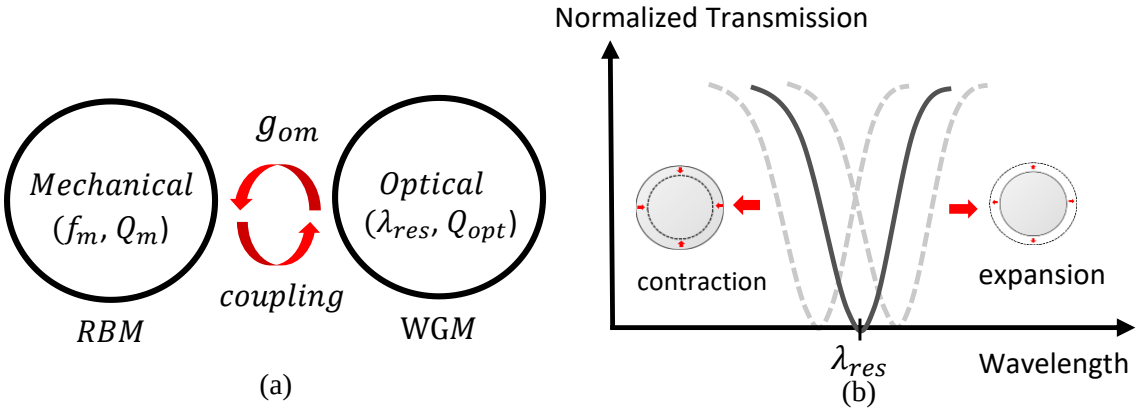

Figure 2.8: Principle of the optomechanical coupling (a) interaction between the mechanical and optical resonators (b) Displacement of the optical resonance as a function of the mechanical deformation.

Physically, the optomechanical coupling can be explained as follows. When photons propagate in WGM (successive reflection) mode, they exert a radial pressure force on the disk wall. Depending on the magnitude of this force, the disk expands or contracts (RBM). Conversely this contraction and dilation changes the distance that the optical wave travels and therefore the optical resonance wavelength (see Figure 2.8.b). The shift of the optical resonance wavelength is written as follows:

$$\lambda'_{res}(t) = \lambda_{res} - \frac{c \cdot g_{om}}{\upsilon_{res}^2} r(t) \tag{2.7}$$

where λ_{res} is the initial resonance wavelength, c is the speed of light, υ_{res} is the initial resonance frequency, $r(t)$ is the disk radius variation and g_{om} the optomechanical coupling coefficient described as follow :

$$g_{om} = -\frac{d\,\upsilon_{res}}{dr} \tag{2.8}$$

As defined by Equation (2.8), for a micro-disk, the optomechanical coupling is the variation of the optical resonance frequency υ_{res} with respect to the disk radial displacement r. Here, g_{om} is estimated by a 2-D axisymmetric FEM model. In this model, the silicon disk is represented by a rectangle whose length and width are respectively equal to the radius and the thickness of the disk. The rectangle is placed in a first medium (air or liquid) delimited by a semicircle and then a perfectly matched layer (PML) with the same properties is added to simulate the infinite space around it. The optomechanical coupling coefficient is estimated at 15 GHz/nm, for a disk with a 10 µm radius.

2.2. Analytical Modeling of an Optomechanical Sensor with Optical Actuation

The optomechanical micro-disk resonator alone cannot be a sensor for mass detection. To have a complete sensor, we need a device that can introduce light from an external laser source, for example a grating coupler and an optical waveguide to direct the light into the optomechanical resonator disk by evanescent coupling. Among the optomechanical devices compatible with mass detection, we can distinguish two types: electrostatically actuated devices and optically actuated devices. In this section, we will present the analytical modeling of the optomechanical sensor with optical actuation. The electrostatically actuated opto-mechanical sensor will be described in the next section.

2.2.1 Operating Principle

The optomechanical sensor with optical actuation is a sensor in which the mechanical movement is stimulated by the injected optical power [15]. In fact, when the power is injected into the disk, the photons propagate by successive reflection on the wall of the cavity in WGM mode. They exert a radial pressure force (introduced in the Chapiter 1) which generates a radial displacement of the micro-disk resonator. The greater this pressure force, the greater the induced mechanical movement.

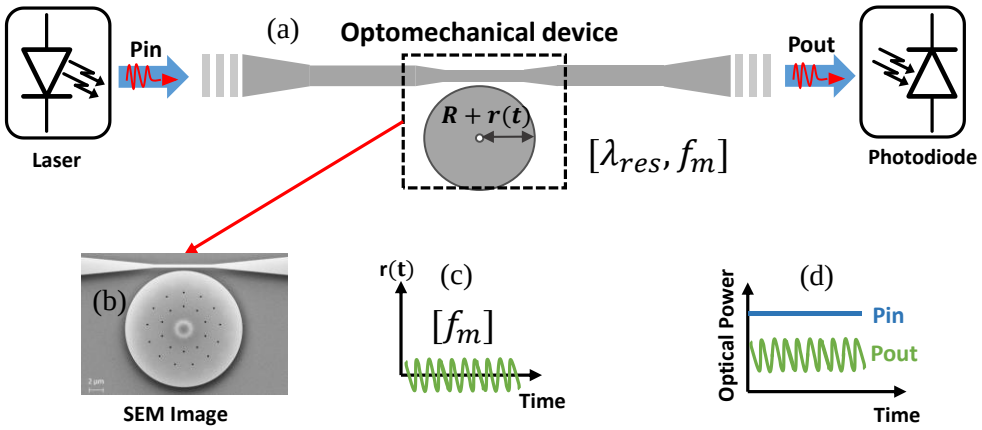

Figure 2.9: Operating principle [15] (a) schematic view of the optomechanical sensor with optical actuation (b) SEM Image (c) the disk radius variation (d) Input and output optical power.

Figure 2.9 shows the operating principle of a silicon optomechanical device with optical actuation. As illustrated in Figure 2.9.a, the device is composed of a waveguide with two gratings couplers at its ends. A micro-disk optomechanical resonator is placed at a few hundred nm from the waveguide. In order to optimize the disk radial displacement and waveguide-disk optical coupling the entire structure is suspended on a pedestal (see Figure 2.1.b).

When an optical power Pin (DC component) is injected into the input grating, the light propagates in the waveguide and couples to the disk by evanescent coupling at some resonance

frequencies. The injected photons exert a radial pressure force and induce a dilatation then a contraction of the disk radius. Figure 2.9.c, shows the radial displacement $r(t)$ of the disk. As described in Equation (2.1), the radius variation changes the distance covered by the optical wave and therefore the optical resonance wavelength λ_{res}. If we consider λ_{res} close to the laser wavelength, the output optical power Pout is modulated at the disk mechanical frequency f_m (see Figure 2.9.d).

2.2.2 Analytical Modeling

The modeling of the optomechanical sensor with optical actuation involves several fields of physics (optical, mechanical, thermal ...). Optical because the sensor is composed of several optical devices like the grating, the waveguide and the micro-disk (considered as an optical cavity). Mechanical, because the disk behaves like a mechanical resonator and resonates radially in RBM mode. An opto-mechanical coupling gain allows to easily switch from the optical cavity to the mechanical cavity. In addition, thermally, because the sensor self-heats due to the injected power. In the following, we will describe analytically all these behaviors.

2.2.2.1 Optomechanical Sensor: Optical Description

To describe analytically the optical behavior of the sensor, it is necessary to know the mathematical expression of the optical responses of the gratings, the waveguide and the micro-disk resonator. Figure 2.10.a below represents the global optical response of the optical sensor. We can see the multiple resonances introduced by the micro-disk, then the optical response of the grating (the bell) and the waveguide (attenuation of the amplitude level).

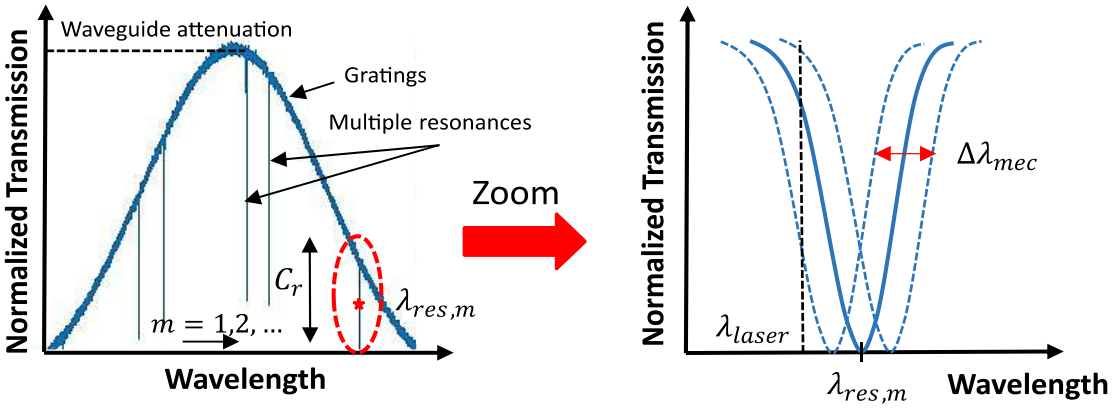

(a) (b)

Figure 2.10: Optical description (a) Optical responses of the optomechanical sensor (waveguide, gratings and multiple resonances of the disk) (b) Optical response of the micro-disk resonator.

- Micro-disk optical response :

The microdisk resonates each time the photons make a complete loop. At the end of their turn, the photons loop back on themselves in phase and create constructive interference, which is at the origin of a second optical resonance. This process is repeated as many times as the photons are in phase with each other, resulting in several optical resonances. We can discriminate the resonance wavelengths, with the index $m = 1,2,3, \ldots$ as illustrated in Figure 2.10.b. Each resonance condition $\lambda_{res,m}$ was introduced in Section 2.1.1.1 with Equation (2.1).

For a given resonance $\lambda_{res,m}$, the disk optical response can be mathematically expressed as a Lorentzian function (see Figure 2.10.b). The disk optical response expression is defined as follows [16]:

$$T_{disk,m}(\lambda) = 1 - C_{r,m}\frac{\frac{\lambda_{res,m}^2}{Q_{opt,m}^2}}{4(\lambda_{res,m}-\lambda)^2 - \frac{\lambda_{res,m}^2}{Q_{opt,m}^2}} \tag{2.9}$$

where $C_{r,m}$ is the intrinsic contrast and $Q_{opt,m}$ is the optical quality factor for each disk resonance labelled m. The contrast is a normalized parameter. It characterizes the absorption rate of the resonator (see Figure 2.10.a). Analytically, it is expressed as follows:

$$C_{r,m} = \frac{k_{in}k_{ext}\lambda_{res,m}^2}{(\pi c)^2}Q_{opt,m}^2 \tag{2.10}$$

where $Q_{opt,m} = 2\pi c/\lambda_{res,m}(k_{in}+k_{ext})$, k_{in} is the total intrinsic losses of the disk, k_{ext}represents the evanescent coupling losses between the waveguide and the disk and c is the light speed. The k_{ext} parameter depends on disk-waveguide gap and the k_{in} parameter is obtained by FEM. In the optical resonator, several absorption regimes can be distinguished:

- When $C_{r,m} = 1$, this means that the entire optical power transmitted by the waveguide is absorbed by the disk. In this condition, $k_{in} = k_{ext}$ it is the critical coupling regime. In practice for mass detection, we prefer to work on a resonance wavelength where the disk is in critical coupling.

- When $C_{r,m} < 1$, we are either in an over-coupling regime or an under-coupling regime. The over-coupling regime ($k_{ext} > k_{in}$) is a regime where the power injected is greater than the power required by the disk. There is an excess of energy, which is dissipated by thermal or radiation losses. The under-coupling regime ($k_{ext} < k_{in}$), is a regime where the power injected is lower than the power required by the disk. In this configuration, the quantity of photons introduced is insufficient and this can limit the mechanical movement of the disk.

- Grating coupler optical response :

As seen in Figure 2.9, two gratings couplers are used to introduce the optical wave in the waveguide. The gratings are designed to work between 1500 nm and 1600 nm with a transmission peak placed at 1550nm. Mathematically, the optical response of the gratings can be seen as a Gaussian function. The optical response is:

$$T_{gratings}(\lambda) = \frac{1}{\sigma\sqrt{2\pi}}e^{-\frac{1}{2}\left(\frac{\lambda-\lambda_c}{\sigma}\right)^2} \tag{2.11}$$

where λ_c is the wavelength for which the transmission is maximum and σ is the standard deviation. λ_c and σ depend on the fiber angle of attack and also on the effective index of the grating. For simplicity, these parameters are determined from experimental data.

- Waveguide optical response :

When the optical wave propagates in the waveguide, it is attenuated due to propagation losses. Portions of the losses are due the absorption of the material and the rest due to roughness or fabrication defects. In general, for a silicon waveguide with a thickness of 5 µm and a length 1-5 mm, the insertion losses are about 1-3dB at 1500 nm [17].

- Global optical responses :

The total optical response $T_{opt,m}$of the optomechanical sensor around the wavelength $\lambda_{res,m}$ is a combination of the optical responses of the disk, grating coupler, and waveguide. $T_{opt,m}$ is calculated from Equation (2.9) and (2.11) as follow:

$$T_{opt,m}(\lambda) = T_{gratings}(\lambda) \cdot T_{disk,m}(\lambda) \cdot 10^{-\frac{\alpha}{10}} \cdot \eta \tag{2.12}$$

where α is the insertion loss of the waveguide and η is the background optical noise term (white noise). The complete expression of the global optical responses is:

$$T_{opt,m}(\lambda) = \frac{10^{-\frac{\alpha}{10}}}{\sigma\sqrt{2\pi}} e^{-\frac{1}{2}\left(\frac{\lambda-\lambda_c}{\sigma}\right)^2} \left(1 - C_{r,m} \frac{\frac{\lambda_{res,m}^2}{Q_{opt}^2}}{4(\lambda_{res,m} - \lambda)^2 - \frac{\lambda_{res,m}^2}{Q_{opt,m}^2}} \right) \tag{2.13}$$

$T_{opt,m}$ represents the optical response of the sensor for a given resonance peak. To consider the multiple resonances of the disk (see Figure 2.10.a), it is necessary that $T_{disk} = \prod_m T_{disk,m}$. Equation (2.12) becomes:

$$T_{opt}(\lambda) = T_{gratings}(\lambda) \cdot 10^{-\frac{\alpha}{10}} \cdot \eta \cdot \prod\nolimits_m T_{disk,m}(\lambda) \tag{2.14}$$

2.2.2.2 Optomechanical Sensor: Mechanical Description

To describe the mechanical response of the sensor, we need to know the resonance of the disk. As shown in Figure 2.11, to resonate radially, the disk is subjected to two forces: the radial pressure force [18] and the thermal force [19]. The radial pressure force F_{rp} is exerted by the photons, which by successive reflection expand the micro-disk. The thermal force F_{th} is the force that characterizes the thermal fluctuation of the disk. More this force is important and more the disk is easily deformed. This force is not constant and has a stochastic character. As shown in figure 2.11.b, the radial movement of the disk is assimilated to a double mass-spring-damper system. In the center, the systems are fixed around the pedestal, which is itself embedded on the bulk substrate. The disk mechanics is defined by the following differential equations:

$$\begin{cases} \frac{m}{2}\ddot{r}(t) + \frac{m\Gamma_m}{2}\dot{r}(t) + \frac{K_m}{2}r(t) = \frac{F_{rp}(t) + F_{th}(t)}{2} \\ \frac{m}{2}\ddot{r}(t) + \frac{m\Gamma_m}{2}\dot{r}(t) + \frac{K_m}{2}r(t) = \frac{F_{rp}(t) + F_{th}(t)}{2} \end{cases} \tag{2.15}$$

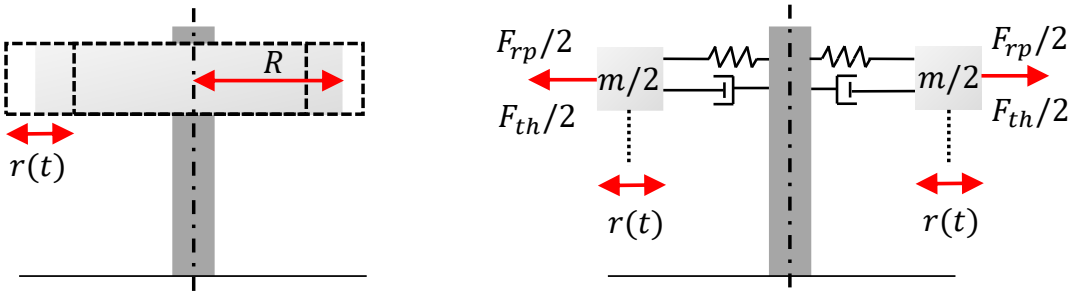

Figure 2.11: Mechanical description of the micro-disk (a) Schematic explaining the disk RBM resonance mode (expansion and contraction) (b) Mechanical model: double mass-spring-damper system.

The disk is homogeneous, so the differential equations add up, Equation (2.15) becomes:

$$m\ddot{r}(t) + \Gamma_m \dot{r}(t) + K_m r(t) = F_{rp}(t) + F_{th}(t) \tag{2.16}$$

where $r(t)$ is the disk radial displacement, $m = M + m_p$ is the mass of the disk M plus the mass of particles m_p , Γ_m is the damping and K_m is the stiffness of the disk. $F_{rp}(t) = \hbar \cdot g_{om} \cdot P(t)$ is the expression of the radial pressure force with $\hbar$ the reduced Planck constant, g_{om} is the optomechanical coupling coefficient and $P(t) = C_{r,m} \cdot P_{in}(t)$ the optical power inside the disk which depends on the contrast and the input power.

$F_{th}(t)$ is the thermal Langevin force, it describes the random thermal fluctuation of the disk. This force is estimated analytically as a Gaussian distribution. For our case, compared to its initial state, the thermal fluctuation of the disk is low, so we assume $\langle F_{th}(t) \rangle = 0$ (constant over time). If we take into account this hypothesis in the frequency domain, the transfer function from Equation (2.16) is written:

$$H_{mec}(s) = \frac{\frac{\hbar \cdot g_{om} \cdot C_{r,m} \cdot P_{in}}{m}}{s^2 + \Gamma_m s + \frac{k_m}{m}} \tag{2.17}$$

$H_{mec}(s)$ is the transfer function that characterizes the mechanics of the disk . The system receives at its input an optical power and generates at its output a radius deformation. The resonance frequency is $\Omega_m = \sqrt{k_m/m}$ and the mechanical quality factor $Q_m = \Omega_m/\Gamma_m$.

2.2.2.3 Optomechanical coupling

We have presented in section 2.1.3, the opto-mechanical coupling. As a reminder, this coupling allows to link the mechanical resonator to the optical resonator. As seen in Figure 2.8, the variation of the radius modulates the optical resonance wavelength λ_{res}. The expression of this wavelength modulation is given in Equation (2.7). If we inject this variation of resonance in the expression of the optical response of the disk, the Equation (2.9) becomes:

$$T_{disk,m}(\lambda) = 1 - C_{r,m} \frac{\frac{(\lambda'_{res}(t))^2}{Q_{opt}^2}}{4(\lambda'_{res}(t) - \lambda)^2 - \frac{(\lambda'_{res}(t))^2}{Q_{opt}^2}} \tag{2.18}$$

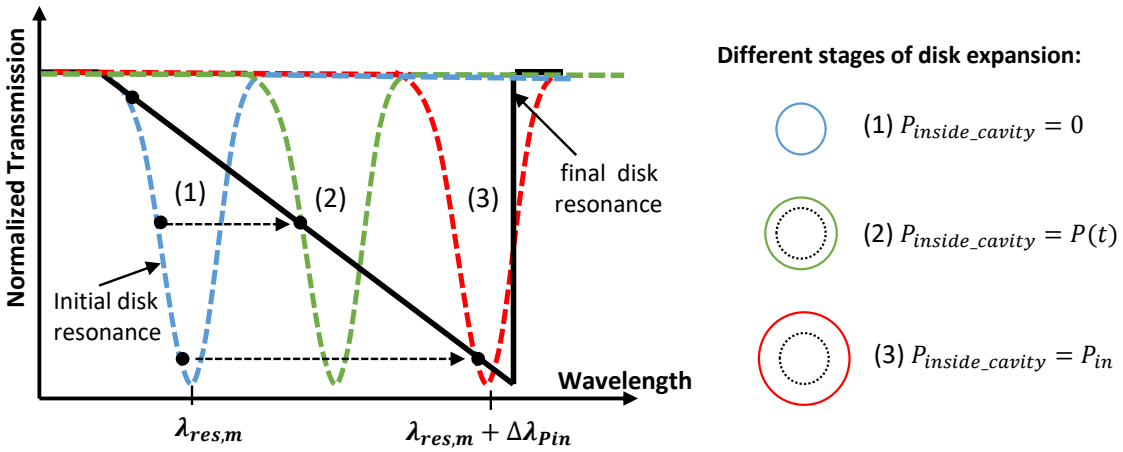

Figure 2.12: Illustration of the thermo-optical effect. When the power dissipated inside increases, we observe a non-linear shift of the disk resonance, which gives the triangular shape.

where $\lambda'_{res}(t)$ is defined in Equation (2.7) and modulates optical resonance wavelength. Equation (2.18) represents the modulated optical response of the disk. The optical response of the gratings and the waveguide remain unchanged. The optical response of the sensor is determined by injecting Equation (2.18) into Equation (2.14).

2.2.3 Thermo-optical effect

The thermo-optical effect is a physical effect observed consistently. It reflects the self-heating of the micro-disk. Figure 2.12 shows an illustration of the thermo-optical effect. The disk optical resonance is obtained by sweeping the wavelength of the laser (see the black point in the Figure 2.12). At the beginning, a small quantity of power is dissipated inside the disk, the optical resonance corresponds to the blue curve with the first black point.

When the optical power inside the disk becomes important, the optical resonance shifts (green and red curves). Equation (2.1) shows it clearly, the increase of the temperature modifies the effective index and thus the optical resonance of the disk. Within the disk, there is a moment where the maximum power is reached (red curve) and increasing the wavelength decreases the dissipated power. The disk abruptly returns to its initial state, which gives the triangle shape.

As shown in Figure 2.12, the thermo-optical effect can be seen mathematically as a shift of the resonance wavelength. This shift is introduced by $\Delta\lambda_{Pin}$the thermo-optical term. The works [20] and [21], propose the following expression:

$$\Delta\lambda_{Pin} = \frac{\lambda_{res,m}}{n_g}\frac{dn_{eff}}{dT}\Delta T \tag{2.19}$$

where n_g is the group index, n_{eff} is the effective index, T and ΔT are the temperature and temperature variation respectively. It is more convenient to express $\Delta\lambda_{Pin}$ as a function of the input optical power. Equation (2.19) becomes:

$$\Delta\lambda_{Pin} = \frac{\lambda_{res,m}}{n_g}R_{th}P_{abs} \tag{2.20}$$

where $P_{abs} = \alpha_{abs} \cdot C_{r,m} \cdot P_{in}$ is the absorbed power, $n_g = \frac{\lambda_{res,m}^2}{2\pi R \Delta\lambda_{FSR}}$ is the group index, R_{th} is the thermal resistance of the disk calculated form the geometric parameters (radius, thickness) and the thermal conductivity of silicon. For example, a 16 µm disk-radius and 220 nm of thickness has an $R_{th} = 2.84 \cdot 10^{-4}\ K/mW$.

Equation (2.19) describes the resonance shift introduced by the thermo-optical effect independently of the disk mechanics. The complete optical response of the disk is therefore written :

$$T_{disk,m}(\lambda) = 1 - C_{r,m} \frac{\frac{\lambda_{res,f}^2}{Q_{opt,m}^2}}{4(\lambda_{res,f} - \lambda)^2 - \frac{\lambda_{res,f}^2}{Q_{opt,m}^2}} \tag{2.21}$$

where,

$$\lambda_{res,f}(t) = \lambda_{res,m} - \frac{c \cdot g_{om}}{v_{res}^2} r(t) + \Delta\lambda_{Pin} \tag{2.22}$$

$\lambda_{res,f}$ is the final optical resonance wavelength which depends on the initial wavelength $\lambda_{res,m}$, the disk radius modulation term $\frac{c \cdot g_{om}}{v_{res}^2} r(t)$ and the thermo-optical coefficient $\Delta\lambda_{Pin}$. The optical response of the gratings and the waveguide remain unchanged. The optical response of the sensor is determined by injecting Equation (2.21) into Equation (2.14).

2.2.4 Experimental Validation and discussion

In the previous sections 2.2.2 and 2.2.3, we presented the equations describing the analytical behavior of the optomechanical sensor with optical actuation. Its optical response is the combination of the responses of the gratings, waveguide, and disk resonator. Mechanically the sensor is modeled by a double mass-spring-damper system. The analytical equations describing the optomechanical coupling and the thermo-optical effect have been implemented.

In this section, we propose an experimental validation of these analytical equations. At our disposal, we have several optomechanical devices with different radius. The aim is to evaluate the relevance of our optical, mechanical and optomechanical coupling descriptions. We will also evaluate the accuracy of our thermo-optical model.

- Optical description of the sensor :

The optical response of the sensor is given analytically by Equation (2.14) with the disk response, which includes the multiple resonances. The response of the gratings is a Gaussian function whose parameters λ_c and σ have been adjusted to match the model to the experiment. For the disk, the first resonance wavelength is fitted. When this wavelength is fixed, we can predict with Equation (2.1) the successive resonances of the disk. The contrast and quality factor are calculated from the coupling coefficients $k_{in}$and k_{ext} see Equation (2.10). The k_{ext} parameter depends on the disk-waveguide gap ($\sim 75 - 120\ nm$) and the k_{in} parameter is obtained by FEM.

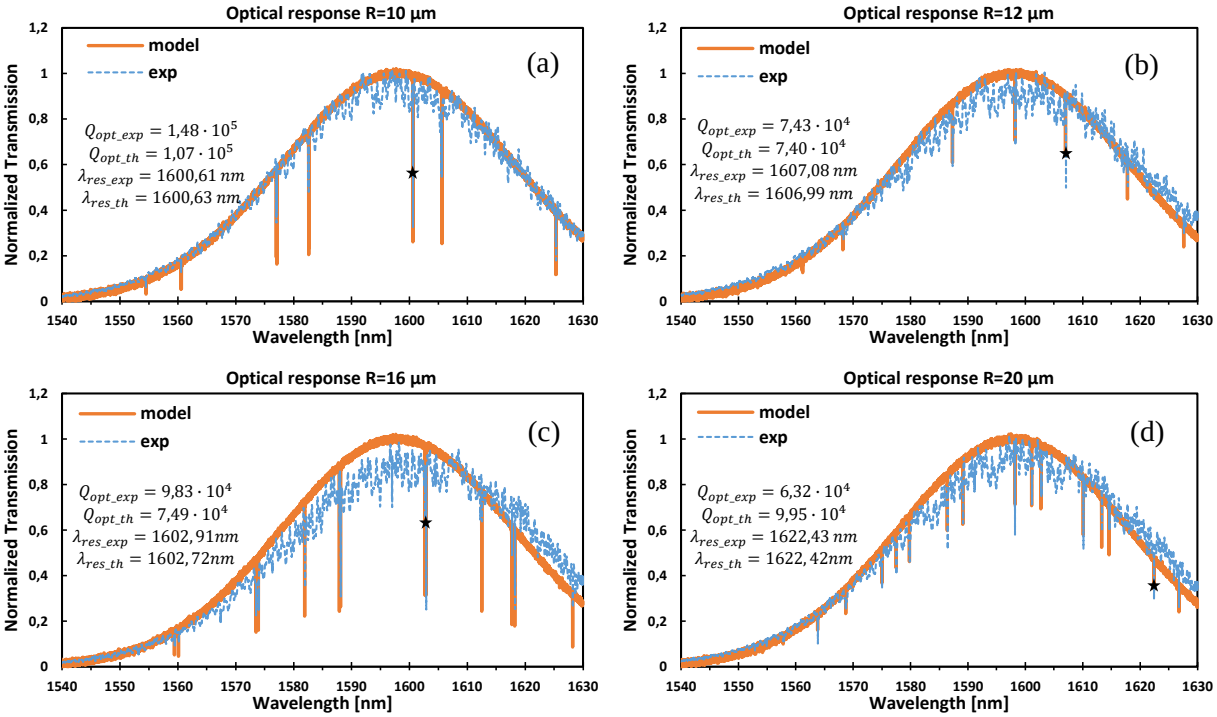

Figure 2.13: Experimental/theoretical comparison of the sensor optical response for a disk of (a) 10 µm radius (b) 12 µm radius (c) 16 µm radius (d) 20 µm radius.

As shown in Figure 2.13, the optical response of the gratings (the bell) is well estimated. However, a very slight shift is observed for the configuration where R=20um, probably due to the perturbation of the fiber angle of attack. Once the first resonance wavelength is fitted, Equation 2.19 predicts with a low error rate the successive resonances of the disk. The theory/experimental comparison of contrast and quality factor shows a slight mismatch due to the incertitude on the coupling coefficients $k_{in}$and k_{ext}.

- Mechanical description of the sensor :

It is commonly assumed that disk mechanics is a double mass-spring-damper system, so it is not necessary to validate experimentally these equations. To predict the resonance frequency and the quality factor, it is necessary to know the stiffness of the silicon disk and the damping coefficient. The amplitude of the mechanical movement depends on the nature of the environment (viscosity, permittivity,…) .

- Thermo-optical effect :

We will verify by experiment the validity of our thermo-optical model. Indeed as presented in the Equation (2.20), we consider the thermo-optical effect as a linear shift of the optical resonance. For experimental validation, we consider a disk of radius R = 16 µm. We change the optical input power in order to observe, for a given resonance, the shift introduced by the thermo-optical effect. In this experiment, we will limit the power to 2.5mW, because above that, the optical resonance becomes too unstable, with the appearance of non-linearity [22].

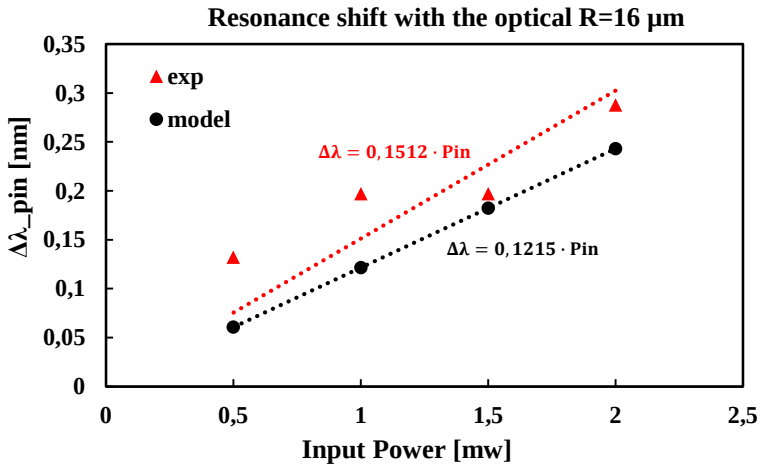

Figure 2.14: Experimental/theoretical comparison of the wavelength shift introduced by the thermo-optical effect as a function of the input optical power.

Figure 2.14 below illustrates the model/experimental comparison. We observe that as the injected power increases, the optical resonance shifts almost linearly. For an input power between 1.5 to 2 mW, the measured shifts correspond to the shifts determined by the linear model. For higher optical powers, this linear model must be readjusted.

2.3. Compact Modeling of an Optomechanical Sensor with Electrostatic Actuation

In the previous section we presented and validated the equations that describe the optomechanical devices with optical actuation. We introduce here the electrostatically actuated devices. Electrostatically actuated devices have better SNR and a higher mechanical quality factor than optically actuated devices. With such performance, the electrostatically actuated devices have better mass resolution. Based on a part of the equations developed in the previous section, we propose the compact modeling of the optomechanical sensor with electrostatic actuation. This model is described in Verilog A language and is compatible with all SPICE electrical simulators. When designing the readout circuit, this model will allow us to perform electrical simulations (sensor + readout circuit) of AC, DC and transient type.

2.3.1 Operating Principle

The electrostatically actuated optomechanical sensor is a kind of sensor in which mechanical motion is stimulated by electrostatic excitation. This stimulation is usually performed by an external source. The radial displacement caused by the external stimulation is much greater than in the case where the device is optically actuated. The radial motion due to photons during their successive reflection displacement (WGM) exists, but its amplitude remains marginal.

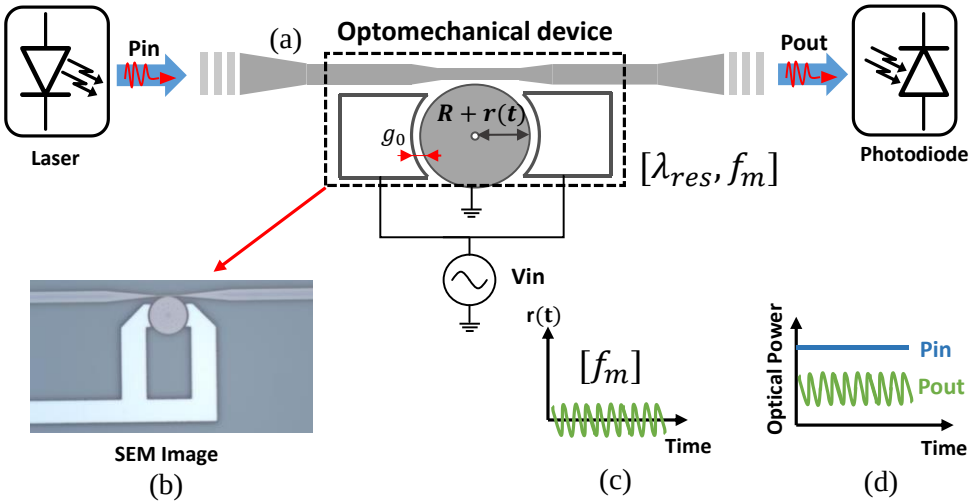

Figure 2.15: Operating principle (a) schematic view of the optomechanical sensor with electrostatic actuation (b) SEM Image (c) Disk radius variation (d) Input and output optical power.

Figure 2.15 depicts the operating principle of a silicon optomechanical device with electrostatic actuation. As illustrated in Figure 2.15.a, the device is composed of a waveguide with two gratings couplers at its ends. A micro-disk optomechanical resonator is placed at a few hundred nm from the waveguide. Two metal armatures are set g_o apart from the disk to apply electrostatic actuation. These two electrodes are connected to an external excitation source. The whole structure is maintained on a pedestal in order to optimize the mechanical displacement of the disk and the waveguide-disk coupling coefficient.

When an optical power Pin (DC component) is injected into the input grating, the light propagates in the waveguide and couples to the disk by evanescent coupling at some resonance wavelength. A voltage V_{in} (DC and AC components) is applied to the armatures. The disk is subjected to an electrostatic force which modifies its radius R by introducing a variation of radius $r(t)$. This variation modifies the distance traveled by the optical wave and modulates the optical resonance λ_{res} of the disk. If we consider λ_{res} close to the laser wavelength, the output optical power Pout is modulated at the disk mechanical frequency f_m (see Figure 2.15.d).

2.3.2 Analytical Modeling

The optomechanical sensor with electrostatic actuation also involves several fields of physics (optical, mechanical, thermal …). Optical because the sensor is based on optical components such as grating, waveguide and a micro-disk resonator. Mechanical, because the disk is a mechanical resonator and resonates radially in RBM mode. These two physical domains are linked by the opto-mechanical coupling seen previously. Finally, thermal because the sensor self-heats due to the injected power.

- Optical description of the sensor :

The optical description of the electrostatically actuated sensor is exactly the same as for the optically actuated sensor. The gratings couplers have an optical response that can be assimilated to a Gaussian function. The multiple responses of the disk can be seen as a Lorentzian function. Since it is the same silicon waveguide, the insertion losses are about 1-3dB at 1500 nm [17]. The overall optical response is therefore expressed as follows:

$$T_{opt}(\lambda) = T_{gratings}(\lambda) \cdot 10^{-\frac{\alpha}{10}} \cdot \eta \cdot \prod_m T_{disk,m}(\lambda) \tag{2.23}$$

where $T_{gratings}$ is the optical response of the gratings defined in the Equation (2.11), $T_{disk,m}$ is the optical expression of the disk resonance defined in the Equation (2.21) which includes the optomechanical coupling and thermo-optical effect. α is the insertion loss coefficient of the waveguide and η the optical background noise.

- Mechanical description of the sensor :

As seen in Figure 2.16, mechanically the micro-disk is subjected to a force F. This force F is composed of electrostatic, thermal and radial pressure forces.

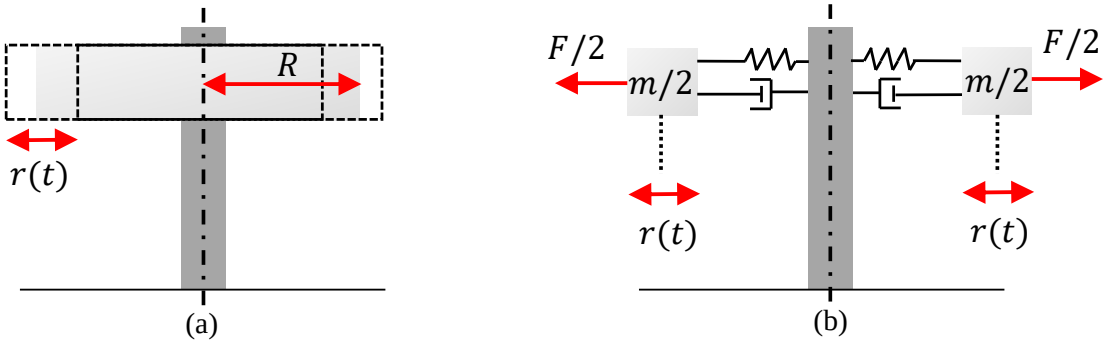

Figure 2.16: Mechanical description of the micro-disk (a) Schematic explaining the disk RBM resonance mode (expansion and contraction) (b) Mechanical model: double mass-spring-damper system.

As a reminder, the radial pressure force F_{rp} is the force exerted by photons during propagation inside the disk. The thermal force F_{th} is the force that characterizes the thermal fluctuation of the disk. The electrostatic force F_{elec} is the force applied to the disk by the two metal armatures. This force is expressed as follows [23]:

$$F_{elec}(t) = \frac{\epsilon_0 S}{2\big(g_0 - r(t)\big)^2} V_{in}^2(t) \tag{2.24}$$

where $V_{in}(t) = V_{dc} + V_{ac}\sin(wt + \varphi)$ is the voltage applied to the disk, ϵ_0 is the permittivity of the vacuum, S is the contact surface of the electrode, g_0 is the distance between the disk and the electrodes, and $r(t)$ is the variation of the disk radius. As the displacement $r(t) \ll g_0$, Equation (2.24) can be approximated by a first-order Taylor's series as follows:

$$F_{elec}(t) = \frac{\epsilon_0 S}{2g_0^2}\left(1 + 2\frac{r(t)}{g_0}\right) V_{in}^2(t) \tag{2.25}$$

As illustrated in Figure 2.16.b, the mechanical movement can be modeled as a double mass-spring-damper system. The disk is homogeneous, so the general differential equation is expressed as follows:

$$m\ddot{r}(t) + \Gamma_m \dot{r}(t) + K_m r(t) = F_{elec}(t) + F_{rp}(t) + F_{th}(t) \tag{2.26}$$

where $m = M + m_p$ is the mass of the disk M plus particles m_p , Γ_m is the damping and K_m is the stiffness of the disk. The radial displacement generated by radial pressure and thermal forces is negligible compared to the electrostatic force $F_{elec}(t) \gg F_{rp}(t) + F_{th}(t)$. If we inject equation (2.25) into equation (2.26), we obtain a simplified form of the differential equation:

$$m\ddot{r}(t) + \Gamma_m \dot{r}(t) + \left(K_m - \frac{\epsilon_0 S}{g_0^3} V_{in}^2(t)\right) r(t) = \frac{\epsilon_0 S}{2g_0^2} V_{in}^2(t) \tag{2.27}$$

2.3.3 Verilog A description model

Based on the equations developed previously, we propose here to realize a compact Verilog-A model of the optomechanical sensor with electrostatic actuation [24]. The goal is to realize a complete dynamic model allowing us to make transient, AC, DC and mass deposition simulations. To have a complete simulation setup, we decided to also implement simplified models of a laser source and a photodiode. Figure 2.17.b, shows our simulation setup in the Cadence Virtuoso environment. Each module (laser, sensor and photodiode) is based on equations whose parameters are given by Table 2.1. In this section, we will explain how to implement in Verilog A the equations of each module.

- Laser Module :

The laser block generates optical power from an electrical source. It involves two physical domains that must be defined before implementing the equations. With the *discipline* function of Verilog A, we define the input of the module as electrical and the output as optical. As shown in Table 2.1, the voltage $V_{in}$is used to adjust the DC level of the optical power. The wavelength

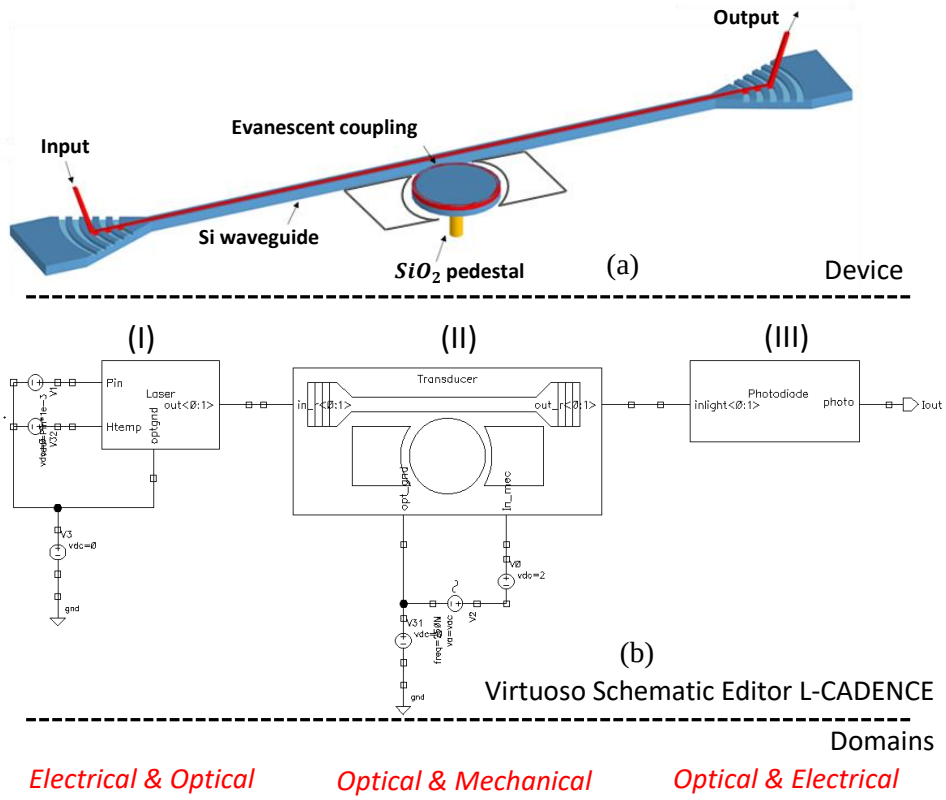

Figure 2.17: (a) Schematic of an opto-mechanical device with electrostatic actuation. (b) Screenshot of the simulation test bench (laser, sensor and photodiode) in the Cadence Virtuoso environment.

Module	Symbol	Parameters	Value	Unit
(I) Laser	V_{in}	input voltage	1	mV
	$Stab$	laser stability	0	nm/min
	$offset\_wav$	wavelength offset	0	nm
	$gain$	gain	100	W/V
	λ_{laser}	laser wavelength	1600,60	nm
(II) Transducer	Q_{opt}	optical quality factor	$1 \cdot 10^4$	$-$
	λ_{res}	optical resonance	1600,61	nm
	C_r	contrast	1	$-$
	m	optimal gratings wavelength	1589	nm
	ν	gratings bandwidth	20	nm
	g_{om}	optomechanical coupling	15	GHz/nm
	$thermo$	thermo-optical coefficient	0,1312	nm/mW
	k_m	disk stiffness constant	$3{,}029 \cdot 10^8$	N/m
	α_v	damping coefficient	$3{,}5 \cdot 10^{-5}$	$N/m.s^{-1}$
	g_0	armature-disk gap	300	nm
	ϵ_0	vacuum permittivity	$8{,}845 \cdot 10^{-12}$	$F.m^{-1}$
	S	contact surface	$1{,}4 \cdot 10^{-12}$	m^2
	M	disk mass	121,88	pg
	m_p	mass placed on the disk	0	pg
	$\hbar$	reduced Planck's constant	$1{,}054 \cdot 10^{-34}$	$J.s$
	c	speed of light	$3 \cdot 10^8$	$m.s^{-1}$
(III) Photodiode	τ	response time	400	ps
	Res	responsivity	0,95	A/W
	B	Bandwidth	100	MHz
	R_{sh}	Shunt resistance	30	$M\Omega$

Table 2.1: Design parameters of the Verilog A models of the laser, sensor and photodiode blocks.

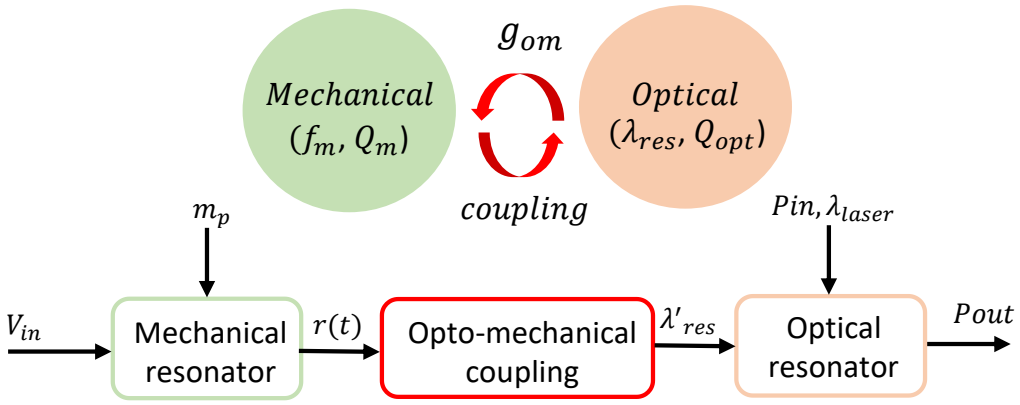

Figure 2.18: Schematic block diagram of the Optomechanical module which consists of three sub-modules: mechanical, optomechanical and optical.

is given by the fixed parameter λ_{laser}. In the model, it is possible to introduce an offset by using the *offset_wav* parameter. The *stab* parameter allows to characterize the stability of the resonance wavelength in time. The relative intensity noise (RIN) of the laser is modeled in Verilog A with the *flicker* and *white_noise* functions added to the laser output.

- Optomechanical Sensor Module :

The optomechanical sensor integrates the different physical domains : optical, mechanical, and thermal. It is necessary to define these domains with the *discipline* function. As shown in the Figure 2.18, the optomechanical module is composed of three sub-modules:

A mechanical module reproduces the mechanical behavior of the micro-disk. In this module, the differential equation (2.27) is implemented using the *laplace_nd* function. Depending on the mass, the resonance frequency is different. We consider here the mass of the disk as a fixed parameter and the mass of the particle as a variable input that we can adjust in simulation.

An optomechanical coupling gain allows to transcribe the mechanical resonance into the optical resonance. The optomechanical module integrates equation (2.7), which transforms the radial variation $r(t)$ of the disk into a modulation of the optical resonance λ'_{res}.

Finally, an optical module reproduces the behavior of the optical resonator. In this module, equation (2.21), equation (2.22) and (2.23) are implemented. This module integrates the thermo-optical effect and generates a modulated optical power $P_{out} = T_{opt}(\lambda_{laser})P_{in}$.

- Photodiode Module :

The photodiode module converts an optical power into an electrical current. This current can be used by the readout circuit using a transimpedance amplifier (TIA). The light-current transfer function of the photodiode corresponds to a first-order response with gain $R_{resp} = 0.95\ A/W$(called the diode's responsivity) and time constant τ = 400 ps (standard value). The amplitude noise of the photodiode can be modeled with the *flicker* and *white_noise* functions of Verilog A.

2.3.4 Compact model results

In this section, we propose to evaluate by measurements the coherence of the compact model developed in Verilog A. For this purpose, different types of electrical simulation are performed in Cadence environment thanks to the optomechanical setup shown in Figure 2.17.b.The same conditions are used in the simulation and in the experiment. We consider the same micro-disk and the optical power of the laser is fixed at $1\ mW$ and its wavelength at $1550\ nm$. First, we propose to study the behavior of the mechanical resonance as a function of the DC and AC voltages applied to the disk. Then, we present the results of transient and parametric simulations to simulate the deposition of particles.

- Variation of the DC voltages applied to the disk :

The idea here is to vary the DC voltage applied to our disk in order to see if our mechanical model is consistent with the experimental results. For an AC voltage fixed at 100 mV, Figure 2.19 shows the evolution of the resonance frequency as a function of the DC voltage. As the DC voltage increases, the mechanical frequency decreases. Indeed, according to equation (2.27), as the DC voltage increases, a linear electrical spring constant reduces the stiffness of the mechanical resonator and thus the mechanical frequency. This variation Δf is perfectly consistent with the result expected in theory. It is also consistent with the measurement with an error of less than 10%.

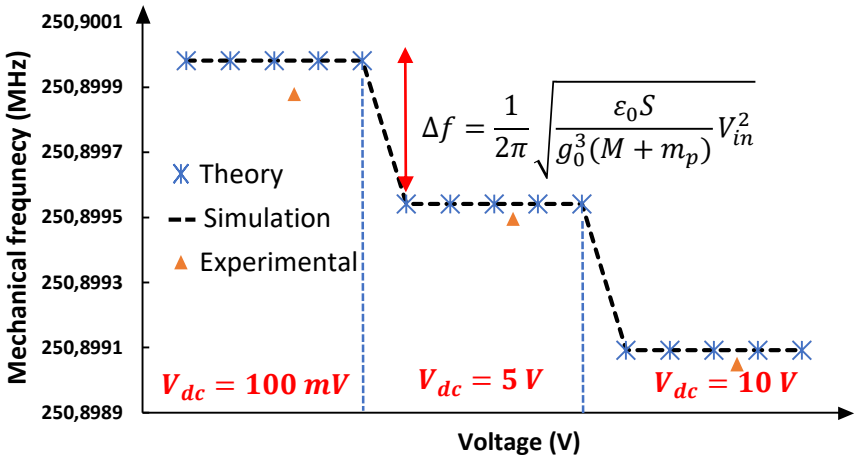

Figure 2.19: Variation of the mechanical frequency as a function of the DC voltage applied to the optomechanical micro-disk

- Variation of the AC voltages applied to the disk :

In simulation, we change the AC voltage applied to our optomechanical micro-disk. Figure 2.20 shows the results of this simulation. For a DC voltage fixed at $2\ V$, when the AC voltage increases, the modulated optical power also increases. This can be explained by the fact that when the electrostatic excitation increases, the amplitude of the mechanical movement of the disk becomes important and that translates into more optical power modulation. For a V_{ac} at $100\ mV$ the power amplitude is $50\ \mu W$ and for a V_{ac} of $900\ mV$ the amplitude can reach up to $450\ \mu W$. For this part of the model, we did not have time to compare it with the measurements. This is a necessary experiment to do in the perspective of this thesis.

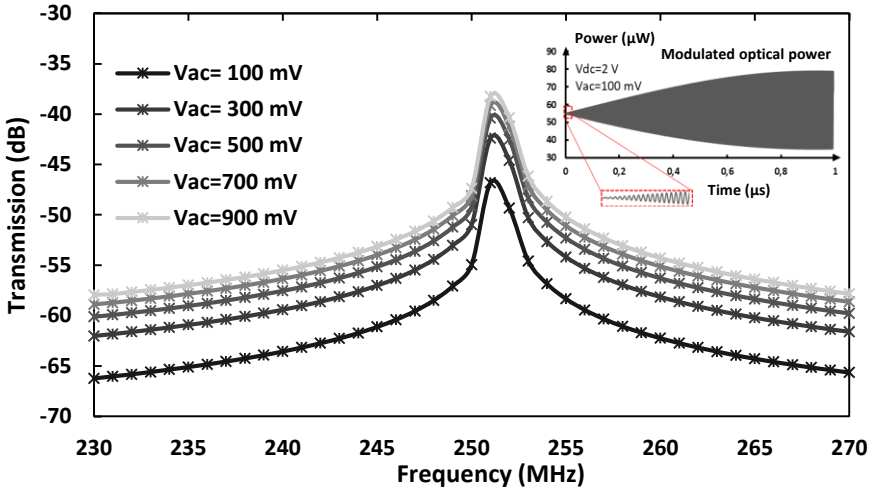

Figure 2.20: Variation of the output power as a function of the AC voltage applied to the optomechanical micro-disk.

- Mass Deposition Simulation:

The mechanical model developed in the previous sections in Verilog A can simulate a mass deposition. Indeed, in the differential equation (2.26), the system mass is considered to be the sum of the intrinsic disk mass M and the mass of the particles m_p. Here, we present the results of the mass deposition simulations. The electrostatic actuating voltages V_{ac} and V_{dc} are, respectively, fixed at 100 mV and 2 V.

The first simulation is a parametric simulation where a mass deposition is done in a static way. Figure 2.20 shows the variation of the mechanical frequency as a function of the deposited mass. As more particles are added, the mechanical resonator becomes heavier, and the resonant frequency decreases. The sensitivity of the optomechanical sensor in simulation is about $-1\ Hz/ag$. This simulated sensitivity corresponds to the measured sensitivity.

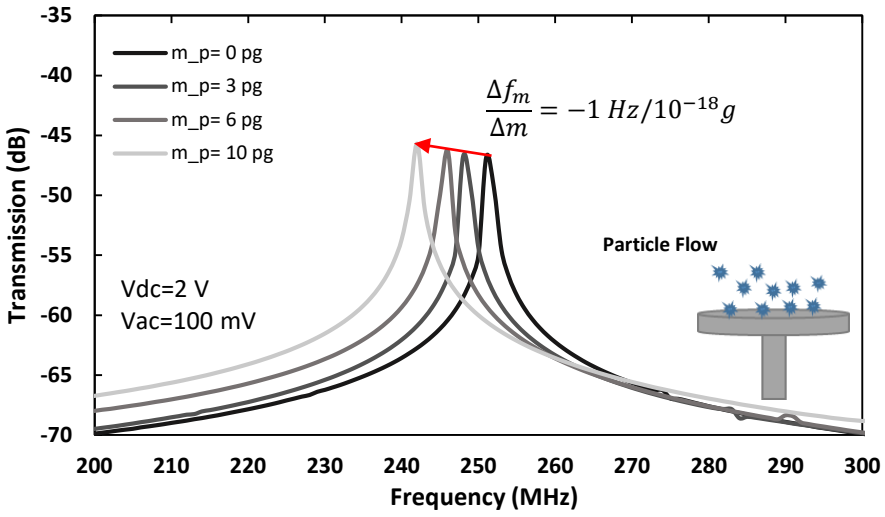

Figure 2.21: Mass deposition simulation: mechanical frequency variation as a function of the particle mass deposited on the top of the micro-disk.

The second simulation is a transient simulation. It reproduces the real time behavior of mass deposition. This type of simulation is very useful when designing a real-time readout electronics. Figure 2.22 illustrates the real time simulation of particle deposition. Every 100 µs, a certain amount of mass is continuously deposited. The mechanical resonance frequency of the disk decreases. At 400 µs, we simulate the case where a certain amount of particle leaves the disk. In this case, the mechanical resonance frequency increases. The sensitivity in simulation is the same as that measured at $-1\ Hz/ag$.

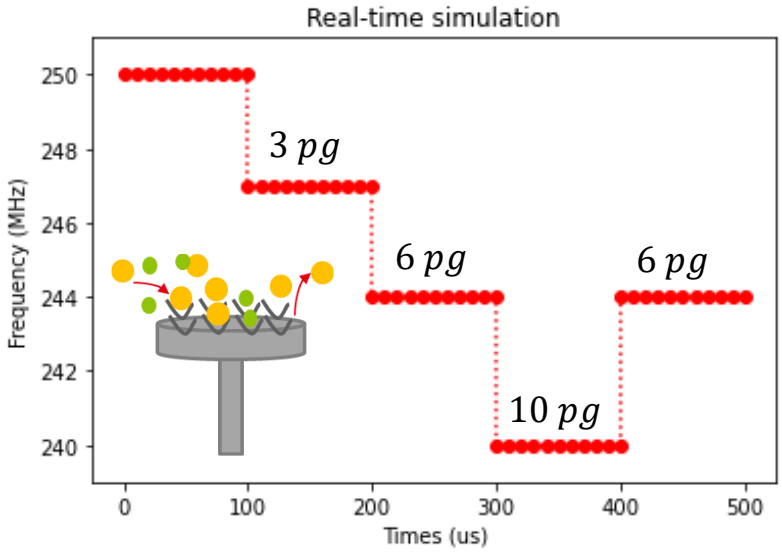

Figure 2.22: Real-time simulation of the mass deposition: mechanical frequency variation as a function of the particle mass deposited on the top of the micro-disk.

2.4 Conclusion

In the first part of the chapter, we explained that the optomechanical micro-disk behaves like an optical resonator. Indeed, within the optical cavity, the light travels by successive reflection, it is the WGM mode. The optical quality factor of the micro-disk is very high, of the order of 10^5. The opto-mechanical resonator also behaves like a mechanical resonator. It resonates by dilating in a radial way, it is the RBM mode. An opto-mechanical coupling connects the mechanical cavity to the optical cavity.

In the second part, we have presented the optomechanical sensor with optical actuation. This type of sensor is used for the mass detection. It consists of an optomechanical micro-disk resonator, an optical waveguide, gratings coupler. In this section, we have developed the analytical equations describing the optical, mechanical and thermal behavior of the sensor. The analytical equations were then validated by experiment.

In the third part, we have presented the electrostatically actuated optomechanical sensor. This kind of sensor has a better SNR and resolution than the optically actuated sensor. In this thesis, we will mainly work on this type of device. In the perspective of the design of a readout electronics, we propose here the development of a compact model in Verilog A. The presented model includes the mechanical, optical, optomechanical coupling and thermal equations of the sensor.

References

[1] F. Vollmer et S. Arnold, « Whispering-gallery-mode biosensing: label-free detection down to single molecules », *Nat Methods*, vol. 5, nº 7, p. 591-596, juill. 2008, doi: 10.1038/nmeth.1221.

[2] Y. Zheng *et al.*, « Sensing and lasing applications of whispering gallery mode microresonators », *Opto-Electronic Advances*, vol. 1, nº 9, p. 18001501-18001510, 2018, doi: 10.29026/oea.2018.180015.

[3] M. Wang, X. Jin, F. Li, B. Cai, et K. Wang, « Whispering-gallery modes in a triple-layer-coated microsphere resonator for refractive index sensors », *Optics Communications*, vol. 427, p. 70-78, nov. 2018, doi: 10.1016/j.optcom.2018.06.017.

[4] Lord Rayleigh, « IX. Further applications of Bessel's functions of high order to the Whispering Gallery and allied problems », *The London, Edinburgh, and Dublin Philosophical Magazine and Journal of Science*, vol. 27, nº 157, p. 100-109, janv. 1914, doi: 10.1080/14786440108635067.

[5] Lord Rayleigh, « CXII. The problem of the whispering gallery », *The London, Edinburgh, and Dublin Philosophical Magazine and Journal of Science*, vol. 20, nº 120, p. 1001-1004, déc. 1910, doi: 10.1080/14786441008636993.

[6] Y. Chen, Y. Yin, L. Ma, et O. G. Schmidt, « Recent Progress on Optoplasmonic Whispering-Gallery-Mode Microcavities », *Advanced Optical Materials*, vol. 9, nº 12, p. 2100143, 2021, doi: 10.1002/adom.202100143.

[7] P. W. Hease, « Gallium Arsenide optomechanical disks approaching the quantum regime », p. 148.

[8] M. Hermouet, « Microdisques optomécaniques résonants en silicium pour la détection biologique en milieu liquide », These de doctorat, Université Grenoble Alpes (ComUE), 2019. Consulté le: 4 février 2022. [En ligne]. Disponible sur: https://www.theses.fr/2019GREAT013

[9] J. Maultzsch, H. Telg, S. Reich, et C. Thomsen, « Radial breathing mode of single-walled carbon nanotubes: Optical transition energies and chiral-index assignment », *Phys. Rev. B*, vol. 72, nº 20, p. 205438, nov. 2005, doi: 10.1103/PhysRevB.72.205438.

[10] M. Mitchell, D. P. Lake, et P. E. Barclay, « Optomechanically amplified wavelength conversion in diamond microcavities », *Optica, OPTICA*, vol. 6, nº 7, p. 832-838, juill. 2019, doi: 10.1364/OPTICA.6.000832.

[11] X. Lu, J. Y. Lee, et Q. Lin, « High-frequency and high-quality silicon carbide optomechanical microresonators », *Sci Rep*, vol. 5, nº 1, Art. nº 1, nov. 2015, doi: 10.1038/srep17005.

[12] E. Gil-Santos *et al.*, « High-frequency nano-optomechanical disk resonators in liquids », *Nature Nanotech*, vol. 10, nº 9, p. 810-816, sept. 2015, doi: 10.1038/nnano.2015.160.

[13] X. Sun, X. Zhang, et H. X. Tang, « High-Q silicon optomechanical microdisk resonators at gigahertz frequencies », *Appl. Phys. Lett.*, vol. 100, nº 17, p. 173116, avr. 2012, doi: 10.1063/1.4709416.

[14] SunYuxin, JiangYan, et YangJialing, « Thermoelastic damping of the axisymmetric vibration of laminated trilayered circular plate resonators », *Canadian Journal of Physics*, janv. 2014, doi: 10.1139/cjp-2013-0374.

[15] H. E. Dawale, G. Jourdan, L. Sibeud, F. Lamberti, S. Hentz, et F. Badets, « Analytical Compact Model for Opto-Mechanical Sensor », in *2020 IEEE 33rd International Conference on Micro Electro Mechanical Systems (MEMS)*, janv. 2020, p. 869-872. doi: 10.1109/MEMS46641.2020.9056258.

[16] J. F. Buckwalter, X. Zheng, G. Li, K. Raj, et A. V. Krishnamoorthy, « A Monolithic 25-Gb/s Transceiver With Photonic Ring Modulators and Ge Detectors in a 130-nm CMOS SOI Process », *IEEE Journal of Solid-State Circuits*, vol. 47, nº 6, p. 1309-1322, juin 2012, doi: 10.1109/JSSC.2012.2189835.

[17] Y. A. Vlasov et S. J. McNab, « Losses in single-mode silicon-on-insulator strip waveguides and bends », *Opt. Express, OE*, vol. 12, nº 8, p. 1622-1631, avr. 2004, doi: 10.1364/OPEX.12.001622.

[18] C. Metzger, I. Favero, A. Ortlieb, et K. Karrai, « Optical self cooling of a deformable Fabry-Perot cavity in the classical limit », *Phys. Rev. B*, vol. 78, nº 3, p. 035309, juill. 2008, doi: 10.1103/PhysRevB.78.035309.

[19] « Thermal fluctuations: A generalization of the Langevin equation: American Journal of Physics: Vol 52, No 4 ». https://aapt.scitation.org/doi/10.1119/1.13885 (consulté le 4 février 2022).

[20] M. J. Shin, Y. Ban, B.-M. Yu, J. Rhim, L. Zimmermann, et W.-Y. Choi, « Parametric Characterization of Self-Heating in Depletion-Type Si Micro-Ring Modulators », *IEEE Journal of Selected Topics in Quantum Electronics*, vol. 22, nº 6, p. 116-122, nov. 2016, doi: 10.1109/JSTQE.2016.2560149.

[21] M.-J. Shin, B.-M. Yu, L. Zimmermann, et W.-Y. Choi, « Parametric characterization of self-heating in Si micro-ring modulators », in *2016 IEEE 13th International Conference on Group IV Photonics (GFP)*, août 2016, p. 66-67. doi: 10.1109/GROUP4.2016.7739112.

[22] B. Sarma et A. K. Sarma, « Optical bistability and cooling of a mechanical oscillator induced by radiation pressure in a hybrid optomechanical system », *arXiv:1503.03813 [physics, physics:quant-ph]*, mars 2015, Consulté le: 4 février 2022. [En ligne]. Disponible sur: http://arxiv.org/abs/1503.03813

[23] T. Konishi, K. Machida, S. Maruyama, M. Mita, K. Masu, et H. Toshiyoshi, « A Single-Platform Simulation and Design Technique for CMOS-MEMS Based on a Circuit Simulator With Hardware Description Language », *Journal of Microelectromechanical Systems*, vol. 22, nº 3, p. 755-767, juin 2013, doi: 10.1109/JMEMS.2013.2243111.

[24] H. E. Dawale, L. Sibeud, S. Regord, G. Jourdan, S. Hentz, et F. Badets, « Compact Modeling and Behavioral Simulation of an Optomechanical Sensor in Verilog A », *IEEE Transactions on Electron Devices*, vol. 67, nº 11, p. 4677-4681, nov. 2020, doi: 10.1109/TED.2020.3024477.

Chapter 3

Towards a matrix integration of optomechanical resonators

Contents

In this chapter, we present for the first time an optomechanical matrix topology designed for mass detection. First, we will explain the importance of such a matrix. Then we will specify it (reading principle, matrix organization, type of actuation, ...) and compare it to existing matrix devices. From this specification, we suggest the concerned matrix topology.

3.1. Optomechanical Matrix : constraints & interests

Due to the small radius of a single micro-disk resonator (some µm radius), the detection area of the optomechanical sensor is too small to consider the use of a single device in mass detection systems. The optomechanical sensor array should be designed to significantly increase the effective area, which will reduce the readout time. In this section, we will concretely see the interest of such an array and the different constraints under which the array will be used.

3.1.1 Optomechanical Matrix : constraints

The matrix of the optomechanical resonator must be designed in such a way as to be able to operate in a non-constraining medium (air, vacuum) as well as in a constraining medium (liquid environment). Let's start with the constraints to which such a matrix will be subjected. In air or in vacuum there is not much constraint. Conversely, in a liquid medium, for a disk resonator of a few micrometers radius, the particles take some time to settle [1], [2].

Indeed, this long deposition time is due to the viscosity and inertia of the medium that makes the particle difficult to deposit. Usually, in a liquid environment, receptors are placed on top of the disk to easily catch the particles [3]. Before measurement, a functionalization time is required to place the receptors. Figure 3.1.a and 3.1.b below shows the process of detecting a particle. The receptors in white in the figure are attached to the top of the disk during the functionalization step.

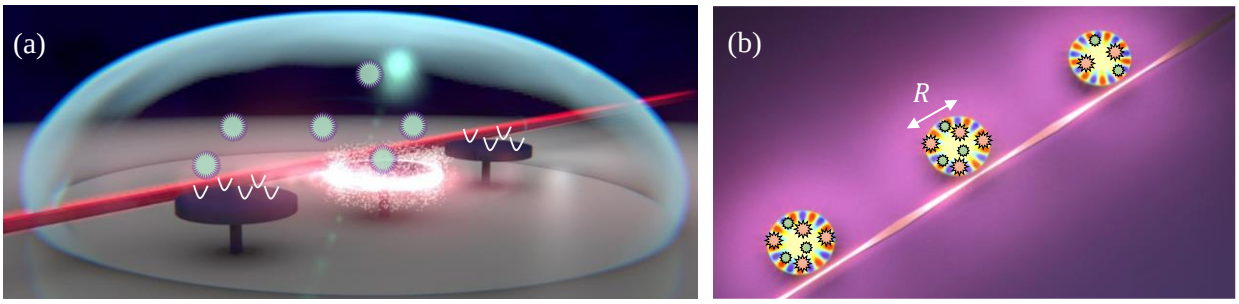

Figure 3.1: (a) Illustration of a device with several optomechanical disks sharing the same optical waveguide in a liquid medium inspired by [4] (b) Mass deposition on top of several optomechanical micro-disks sharing an optical waveguide inspired by [5].

3.1.2 Optomechanical Matrix : Interests

Optomechanical resonators are suitable for mass flow detection applications. This means that the sensor detects a continuous flow of particles. However, today a single resonator can only detect a limited number of particles. This is due to its small detection surface and its mass which cannot accumulate a large quantity of mass. If we want to increase the number of particles detected while maintaining the performance, it is necessary to think of a new configuration.

A simple idea is to increase the detection area by increasing the radius of the optomechanical micro-disk while keeping the same thickness (~220 nm). This way is complex to implement. Indeed, if we increase the radius of the disk, the resonator becomes heavier, its resonance frequency and mechanical quality factor degrades (see Figure 2.7a). The coupling between the optical and mechanical cavity and the sensitivity deteriorates. To keep both the performance (sensitivity, noise ...) and to have a large detection area, a solution would be to put the optomechanical resonators in matrix form.

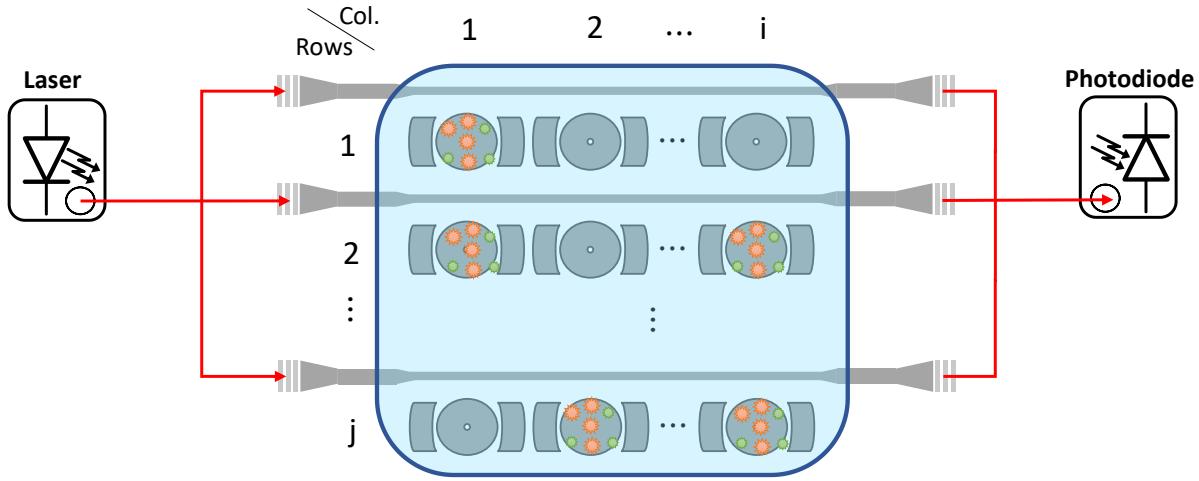

Figure 3.2: Very large-scale example of an optomechanical resonator matrix with particle deposition.

Figure 3.2 shows an example of the optomechanical matrix. Optomechanical micro-disks will share the same optical waveguide. It is organized in rows and columns and presents $i * j$ optomechanical sensors. On this matrix, all the resonators will have the same dimensions (radius, thickness ...) to have the same mechanical resonance frequency and a similar optical resonance wavelength. Thus, the optomechanical matrix exhibits the same performance as a single resonator with a larger detection area. For a configuration like the one shown in Figure 3.2, all disks should be electrostatically stimulated to achieve better SNR and thus better resolution.

3.2. Reflections on the “ideal” matrix configuration

Previously we saw in Figure 3.2, a typical example of what the future optomechanical matrix may look like. To read such a matrix, there are two possible techniques. A sequential reading in which the disks of each row are read one by one. Simultaneous reading, in which all the disks in the row are read at the same time. In this section, we will review these two techniques and then discuss the appropriate technique for mass detection. Once the reading principle has been chosen, we will define the specifications and expose all the constraints to which the future matrix must conform.

3.2.1 Sequential reading

Sequential reading is a reading principle widely used to read a pixel matrix or a position sensor matrix. If we take the example of a Touch Sensor matrix [6], the reading is done as follows. The position of the finger on the matrix varies the value of a capacitance. All capacitors have the same value by default. To read the position of the finger, an electrical signal is sent sequentially row by row, to determine the capacitor whose value has changed. There are also other configurations where this type of reading is used [7]-[9].

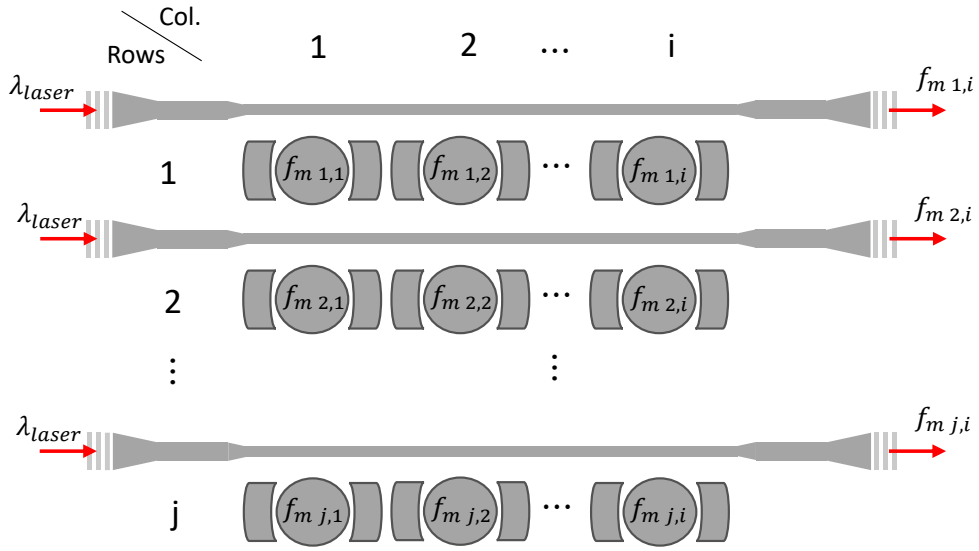

Figure 3.3: Sequential reading principle of an optomechanical resonator matrix.

We can apply this reading principle to our optomechanical sensor matrix, the idea is that this time the reading is done column by column. Thus, we can place the electronics at the output of each row and read the matrix column by column. Unlike the multiplexed configuration seen previously, this kind of reading requires only one laser wavelength to excite all the disks. It supposes obviously that all disks are of the same dimensions with a precision of the order of the nm. When reading the disks column by column, it is necessary to think of making invisible the other disks of the matrix. Indeed, the disks placed on the same row share the same optical waveguide. The optical power is modulated as many times as there are disks on the row.

To keep only one mechanical resonance frequency at the output of each waveguide (see Figure 3.3), the mechanical resonance of the other disks must be either masked or stopped. We will see in detail these different techniques in section 3.4.

3.2.2 Simultaneous reading

Simultaneous reading is a reading principle in which all the resonators are read at the same time. It is a reading technique that is frequently used, especially when we have a very large matrix. For example, it is the technique used to read a micro cantilever array for gas detection [10]. In this application, the output signals of the sensors are multiplexed and then converted to digital. With a very accurate ADC we can extract the resonance frequencies of each micro cantilever. There are also other configurations where this type of reading is used [11] and [12].

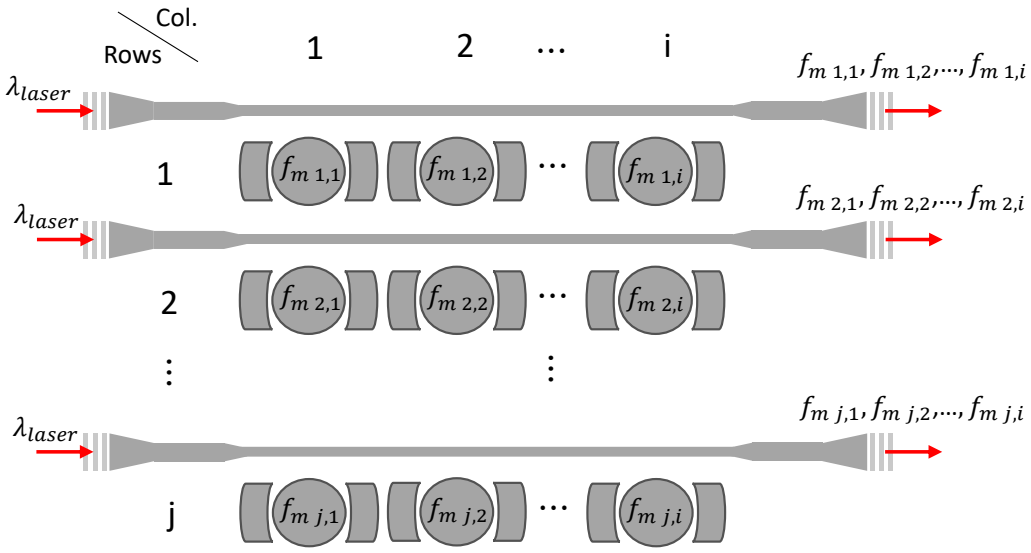

Figure 3.4: Simultaneous reading principle of an optomechanical resonator matrix

We have the possibility to apply this reading principle to our optomechanical sensor array (see Figure 3.4), the idea is that this time we read all the resonators of the array at the same time. This method has the advantage of being very fast. Nevertheless, the simultaneous reading principle is not adapted to our optomechanical sensor array. Indeed, it is very difficult to read at the same time all the disks of a single line. As the optomechanical disks are placed on the line, the signal is attenuated until it is no longer visible at the output.

3.2.3 Discussion on the appropriate reading configuration

The mass deposition time, especially in liquid context, is very slow. This is due to the viscosity and inertia of the environment. Maxime Hermouet demonstrated in his thesis that this time could be up to 1 hour for a complete deposition of particles [13].Therefore, for the optomechanical resonator array in liquid, the reading time is not really a fundamental criterion to choose a reading configuration.

Sequential reading is suitable for small size arrays. Its reading electronics is relatively simple since it consists in reading a single frequency at the output of each optical waveguide. Closed loop architectures (self-oscillating loop or phase-locked loop) can be adapted to this type of reading configuration. For greater accuracy, a lock-in-amplifier architecture can be applied. Also, with this technique we can identify both the position and the mass of the particle.

Simultaneous reading is more suitable for larger arrays. Its reading electronics is a little more complicated since it consists in extracting a single frequency embedded in a signal where the resonance frequencies are multiplexed. In general architectures for this configuration are more digital. With a very precise ADC (Analog to Digital Converter) we convert the analog multiplexed signal into digital. And then with a digital band-pass filter, we extract one by one the mechanical resonance frequencies.

To read our optomechanical sensor array, we finally choose a sequential reading. The reading time is certainly slower than the simultaneous reading. The convergence time of a phase-locked loop is of the order of micro-seconds. This is enough to read sequentially a very large matrix. Also, unlike simultaneous reading, we will be able to determine the position of the particle in the matrix.

3.2.4 Specifications and Features of the “ideal” matrix

In this section, we propose to define the outlines of the "ideal" optomechanical matrix. For mass detection, the matrix should have the following characteristics:

- The matrix must be organized in rows and columns. The idea is to optimize the dimension of the matrix by placing on each row a waveguide as shown in Figure 3.2. it will optically excite a multitude of optomechanical resonators placed along the optical waveguide.

- The optomechanical disks must have the same dimensions (radius, thickness,...). This will allow to unify the resonance frequency of the disks and to read more easily the matrix. A slight dispersion due to the manufacturing process is possible, that's why we add a condition on the dispersion which must be of the order of nm.

- Each disk must be electrostatically stimulated. At the output, the signal will be amplified, and we will have a better SNR and a high mass resolution.

- The mechanical excitation can be individual or common to the matrix. Depending on the chosen reading configuration (simultaneous or sequential reading), the electrostatic excitation can be individual or common.

- The matrix must be able to read sequentially disk by disk. During the reading, it is necessary to be able to activate the disk to be read and to deactivate other disks. To do this, two methods exist. The optical method which consists in optically masking the mechanical resonance. The mechanical method where the idea is to interrupt the mechanical displacement of the optomechanical disk. We will see in detail these methods in section 3.4.

3.3. Available optomechanical matrix topologies

For its exploratory research, CEA-Leti has developed and characterized different matrix topologies with optomechanical resonators. A first topology called "multiplexed configuration". This topology is close to the configurations [4], [5], where resonator disks of different radius are placed on the same optical waveguide. In this case, the disk hosts both the optical and mechanical cavity. The second is a configuration where the optomechanical disk is used as an optical cavity. This cavity is mechanically stimulated by nano-rams placed around it. The principle is that the nano-rams disturb the light propagating in the optical cavity. This results in modulated optical power at the mechanical resonance frequency of the nano-rams. We will see in this section two topology.

3.3.1 Multiplexed Configuration

The multiplexed configuration of optomechanical resonators is a matrix configuration, in which several disks are placed around the same optical waveguide. These disks have different radius to avoid the interference of optical and mechanical resonances. Figure 3.5 below, shows a SEM picture of our multiplexed optomechanical resonators in silicon. For the moment we have considered only three micro-disks to validate the multiplexing principle. The disks have respective radius $R_1 = 20\mu m$, $R_2 = R_1 + 32\,nm$, $R_2 = R_1 + 64\,nm$. All disks are electrostatically stimulated by electrodes.

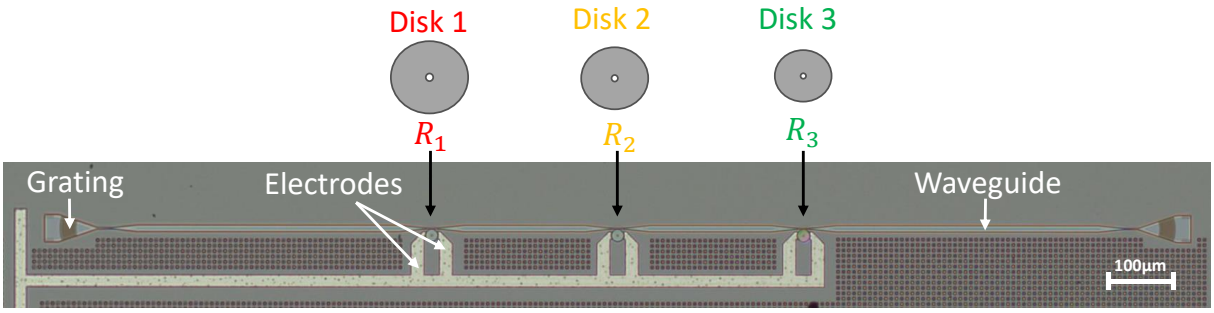

Figure 3.5: SEM image of multiplexed optomechanical resonators

Concerning the reading principle, the idea is to inject at the input of the gratings several wavelengths corresponding to the resonance wavelength of the disks. At the output at the photodiode, this will make visible all the mechanical resonances of the disks. Thus, we can then determine the masses deposited on each disk. The advantage of this type of matrix configuration is that we can read simultaneously all the disks of the same waveguide. The main disadvantage comes from the difference in mechanical frequency of the disks. As the optomechanical resonators are excited, it is necessary to provide different oscillators to drive them separately.

Figure 3.6 represents the optical response of the multiplexed optomechanical system presented in Figure 3.5. This figure is obtained by sweeping the wavelength of the laser between 1500 and 1620 nm. If we analyze this optical response, we find the "bell shape" that corresponds to the optical response of the gratings coupler and the multiple resonances of the optomechanical disks. As the disks have different radius, the optical resonances do not overlap. We can easily identify the optical resonances and associate them with the corresponding disks with colored crosses as illustrated in Figure 3.6.

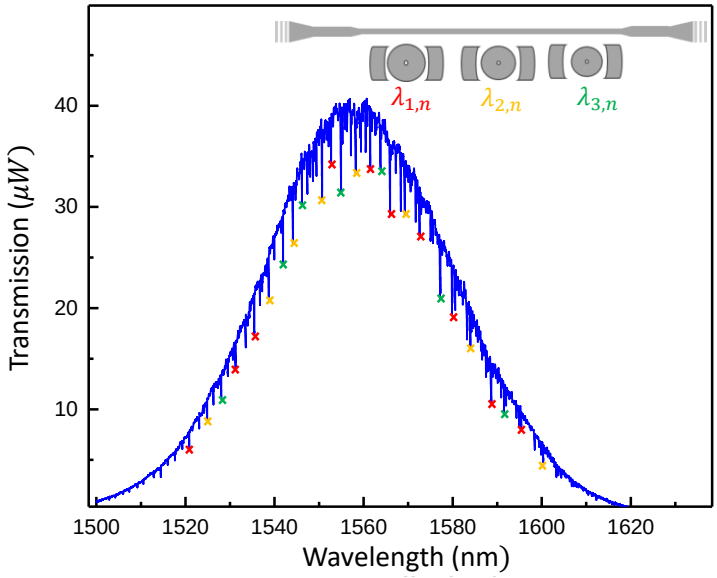

Figure 3.6: Measurement of the optical response of the optomechanical multiplexed system with the optical resonances of each disk [14].

Figure 3.7 below represents the mechanical resonances of the multiplexed system as a function of the excitation voltage. At the output of the photodiode, we can see the three resonance frequencies ($f_{m,1}$, $f_{m,2}$ and $f_{m,3}$) corresponding to the three optomechanical disks (R_1, R_2 and R_3). We also note that increasing the electrostatically excitation of the disks improves the SNR and thus the resolution.

To discriminate mechanical frequencies, there are several techniques. In general, in the laboratory, three PLL are used to simultaneously track the mechanical resonance frequencies of the three disks. But for a large-scale matrix with a high number of disks, this becomes very complex electronically. The other technique is to use a digital band-pass filter that will select the desired resonant frequency.

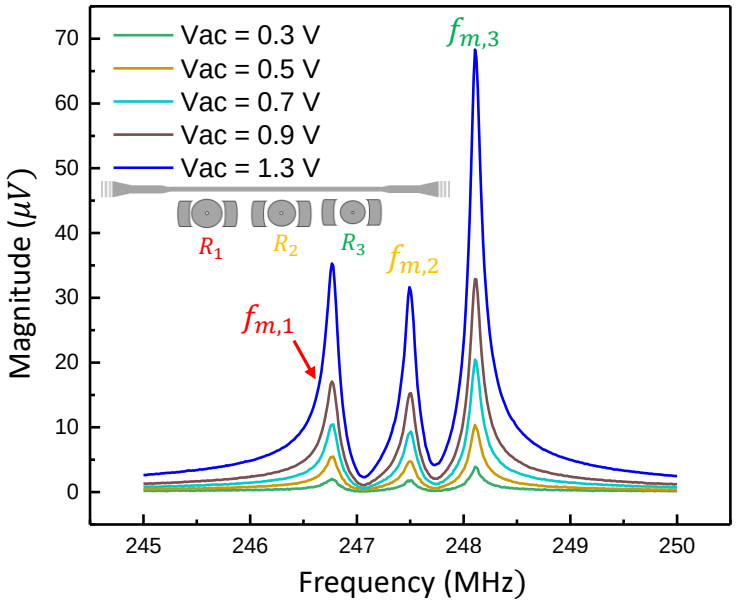

Figure 3.7: Measurement of the mechanical resonances of the optomechanical multiplexed system for different excitation voltage [14].

3.3.2 Nano-rams with an optical disk cavity

The matrix configuration presented in this section is a configuration in which several nano-rams are placed around an optomechanical disk. In this case, the disk is an optical cavity, and the mechanical cavity is represented by the nano-rams. The device works as follows. The light propagates in the optomechanical disk and is disturbed by the mechanical movement of the nano-rams. Consequently, the optical power is modulated at the mechanical resonance frequency of the nano-rams.

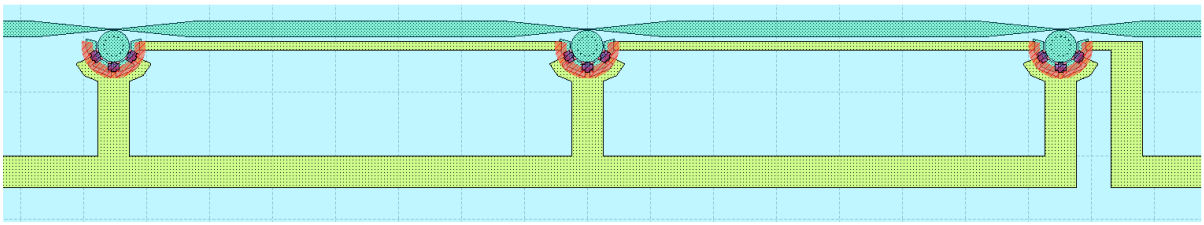

Figure 3.8: Illustration of our silicon optomechanical disk device with several nano-rams

Figure 3.8 shows our nano-rams silicon devices with several optical cavities. On this device are placed several optomechanical disks of radius 5 µm. Each disk is surrounded by three nano-rams spaced at an angle of 60°. But as the nano-ram surface is used for mass deposition it is necessary to plan a reflection on a matrix configuration. For the moment we consider only three nano-rams around the disk just to validate the concept.

The Figure 3.9 above corresponds to zoom made on the disk area. The distance between the nano-ram and the disk is in the order of a hundred nanometers. The rams are electrostatically excited by electrodes placed at a few hundred nanometers.

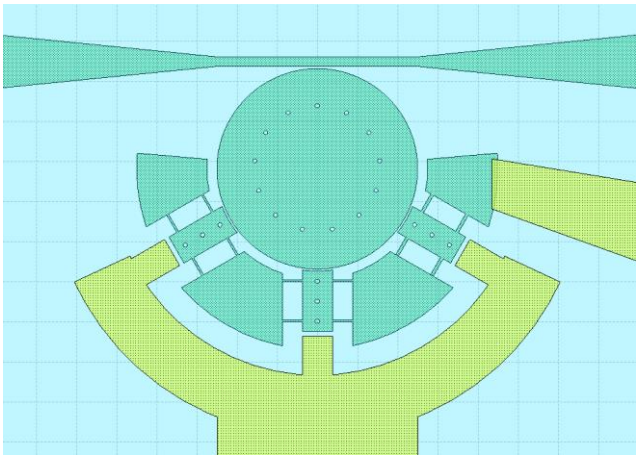

Figure 3.9: Zoom on our silicon optomechanical disk device with several nano-rams

The three nano-rams have different dimensions. Therefore, they have different mechanical resonance frequencies. The mass deposition is done on the top of the ram because they are the support of the mechanical resonance. Here the disk is only used as an optical cavity. In terms of detection area, a ram is less wide than a disk. They have lower resonant frequencies than disks (about 40-50MHz).

3.3.3 Discussion on existing matrix topologies

Both configurations presented above, are the result of the first thought carried out on the optomechanical matrix.

In the multiplexed configuration, the disks do not have the same dimensions. The reason is that it allowed the multiple optical resonances of the disks to not overlap. Moreover, the reading is done in a simultaneous way. At the output of the photodiode the three mechanical resonance frequencies are visible. Such a configuration, because of the multiple optical resonances, limits us on the number of disks to be placed on a single waveguide. This means that we cannot realize a very large matrix as we wish. For the nano-rams configuration, the problem is the small detection area of the rams compared to the optomechanical disks.

3.4. Activation or deactivation an optomechanical disk

According to the specifications made in section 3.2.4, the "ideal" matrix must be able to be read sequentially. The idea is to read the disks of the array one by one. The example of the "ideal" array configuration that we have presented in Figure 3.2, shows that several optomechanical disks share the same waveguide. When an optical power is injected, all the disks positioned along the waveguide modulates the optical power at their mechanical resonance frequencies. In our case, the disks have the same dimensions, it is therefore very difficult from an electronic point of view to extract all these frequencies.

To solve this problem, we need to find a way to turn the optomechanical disks on and off in order to read them only when we want to. Several solutions could be envisaged. We can do it in an optical way where the idea here is to make the mechanics of the disks invisible. Or mechanical where the idea is to stop the mechanics of the disk. We will see in this section these two techniques.

3.4.1 The optical method

An optomechanical disk can be optically activated and deactivated. The principle consists in making the mechanical resonance optically invisible. In other words, the optomechanical disk resonates mechanically but this resonance is invisible at the output of the waveguide. There are two different ways to do this. First, the optical resonance of the disk is shifted by using the thermo-optical effect seen before. Or we can act on the disk-waveguide evanescent coupling.

3.4.1.1 Shift of the optical resonance

The modulation of the optical power inside the optomechanical disk is made from the optical resonance λ_{res} and the laser wavelength λ_{laser}. The idea here is to shift the resonance λ_{res} in order that the modulation is done outside λ_{laser}. The offset required remains small because the

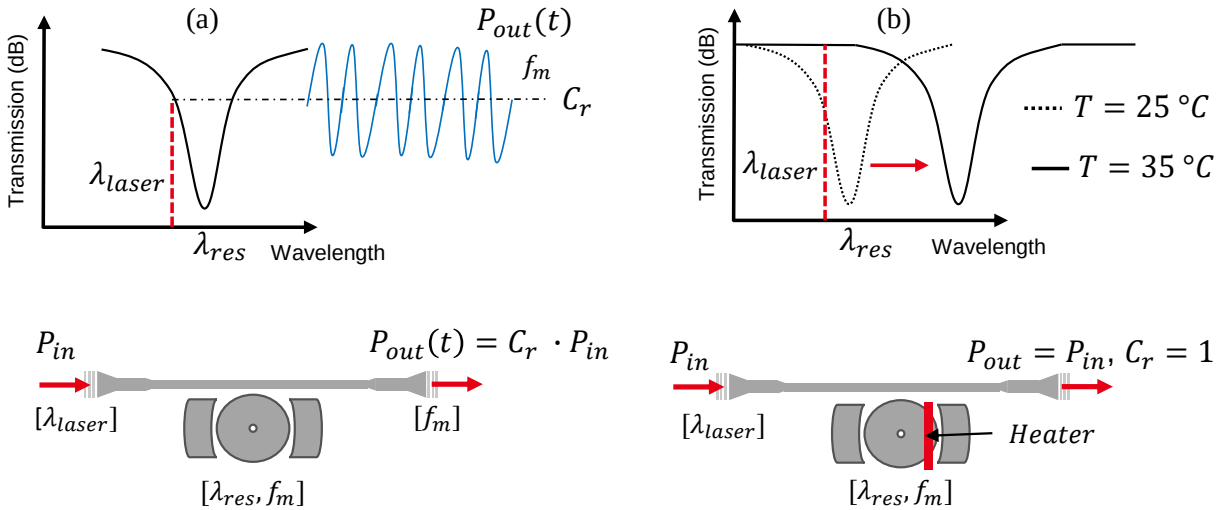

Figure 3.10: Operating Principle of (a) an optomechanical disk (b) an optomechanical disk with a heater

optical resonator has a very high-quality factor of the order Q_{opt}~10^5. One way to shift the disk optical resonance is to exploit the thermo-optical effect. To make this shift it is necessary to heat the disk.

Figure 3.10.a shows the normal operation of an optomechanical disk. The injected optical power is modulated at the mechanical frequency fm. Figure 3.10.b shows the operation of an optomechanical disk with a heater. When the disk is heated, its optical resonance shifts. It behaves like a unitary gain and its contrast $C_r = 1$. To be in this configuration it is necessary that the shift introduced by the thermo-optical effect is greater than the modulation of the resonance wavelength.

One way to realize this heater is to put a heating resistor. The paper [15], shows how to make a heater on a micro optical disk. A metal ring is placed over the resonator disk. This ring behaves like a thermal resistor and heats up with the help of a current.

- Calculation of the thermal sensitivity of a silicon disk :

Our optomechanical disks are made of silicon, so their thermal sensitivity can be calculated using the expression of the optical resonance:

$$\lambda_{res,m}(T) = \frac{n_{eff}(T)2\pi R}{m} \tag{3.1}$$

with $n_{eff}(T)$ the effective index of the medium which depends on the temperature, R the radius of the disk and m the resonance index. According to [16] and [17], the index of silicon at 250 K and 300 K is:

$$\frac{dn_{eff}}{dT}(250\ K) = 1{,}78 \cdot 10^{-4}\ and\ \ \frac{dn_{eff}}{dT}(300\ K) = 2 \cdot 10^{-4} \tag{3.2}$$

By injecting (2) into (1), we obtain:

$$\frac{\lambda_{res,m}(300\ K)}{\lambda_{res,m}(250\ K)} = \frac{n_{eff}(300\ K)}{n_{eff}(250\ K)} = 1{,}123 \tag{3.4}$$

If $\lambda_{res,m}(250\ K) = 1550\ nm$, $\lambda_{res,m}\ (300\ K) = 1{,}123 * 1550 = 1741{,}5\ nm$.The theoretical thermal sensitivity is therefore written as follows:

$$\frac{\Delta\lambda_{res,m}}{\Delta T} \approx 3{,}8\ nm/K \tag{3.5}$$

For a silicon resonator, equation (3.5) allows to estimate the wavelength shift as a function of temperature. As our optomechanical resonator has a very high-quality factor, a slight change of the temperature (a few ° K) can make the optical resonance invisible. To induce such temperature shift, it is necessary to calculate from the thermal resistance defined in chapter equation (2.20) the required current density.

3.4.1.2 Acting on the waveguide-disk optical coupling

The other way to make the optomechanical disk invisible is to act on the optical disk-waveguide coupling. This means that the optical wave does not enter the optomechanical disk. We saw in the previous chapter that the optical wave enters the disk by evanescent wave. This requires that the disk is very close to the waveguide (a few hundred nanometer). The idea is to vary this gap $g_{opt}$to activate or deactivate the mechanical resonance. To vary this gap g_{opt}, we place an electrode near the optomechanical disk. Figure 3.11 shows the configuration in which the gap is varied using an electrode. The principle is that with this electrode, we can move the disk away from the waveguide to prevent the optical wave from coupling to the disk. The displacement of the disk must be small in order not to break the pedestal (see Figure 3.11b). The gap control electrode is completely dissociated from the electrostatic actuation electrodes.

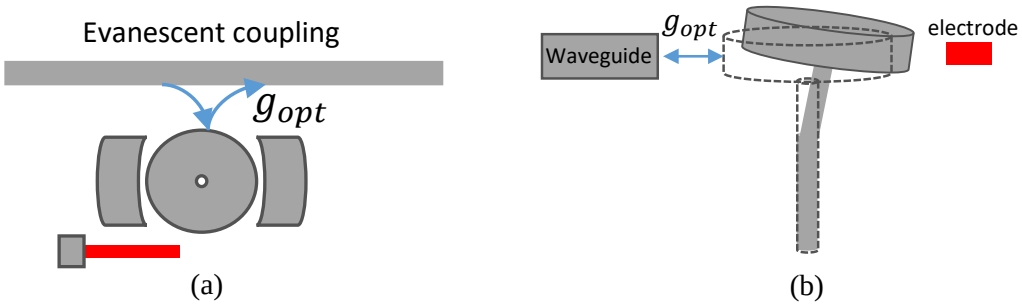

Figure 3.11: Illustration of the optomechanical disk with an electrode that controls the optical gap (a) top view (b) side view with the pedestal.

In the team, we have at our disposal different optomechanical devices with different optical gaps. Figure 3.12 illustrates the measurements of the optical responses performed on devices with a gap of 200, 300, 400 nm. When the gap is 200 nm (in green), we can see the multiple resonances of the disk. At 300 nm gap (in blue), the resonances are visible but with a low contrast. And at 400 nm gap (in yellow), the optical resonances are no longer visible. The disk is far enough from the waveguide to allow evanescent coupling.

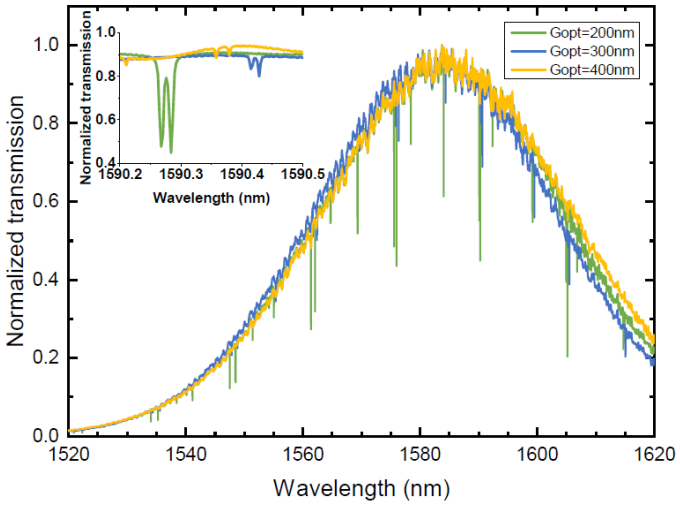

Figure 3.12: Measurement of the optical response for various optomechanical devices with an optical gap of 200, 300 and 400nm [13]

3.4.2 The mechanical method

The other method to activate and deactivate an optomechanical disk is a mechanical method. The idea here is to stop or to put in resonance the disk according to our request. To start the oscillation of the resonator it is only necessary to stimulate it with the electrostatic electrodes. The hardest thing is to stop the resonance. There are two ways to stop the resonance. One way is to stop the electrostatic stimulation and wait for the disk to dampen itself. And a brutal way where the idea is to stop the disk mechanics in a clear and fast way.

The first way is to stop the resonance in a slow way, by interrupting the electrostatic excitation. The disk dampens and takes some time to stop. This stopping time is problematic for our matrix configuration. Depending on the viscosity of the environment this stopping time can be more or less important. One way to do this technologically is to imagine mobile electrodes. We will approach these electrodes when we want to excite a disk. And in the contrary case one will move away the electrodes and let the disk dampen itself until the stop.

The second way is to stop the resonance abruptly and quickly. This approach is more suitable for the matrix configuration but is complicated to realize. Technologically it would be necessary to imagine putting flippers next to the disk. The flippers would be activated so that they force the disk to stop resonating. And in the contrary case the flippers would move away to let the disk resonate freely.

3.4.3 Discussion on the adequate way to activate and deactivate

To activate and deactivate an optomechanical disk, we have the optical method where the idea is to optically mask the mechanical resonance. We have also seen the mechanical method where the idea is to stop the mechanical resonance of the disk. These two methods will allow us to read our matrix sequentially.

An optomechanical disk can be optically activated and deactivated. There are two different ways to accomplish this. First, the optical resonance of the disk is shifted by using the thermo-optical effect seen in chapter 2. With the help of a heater, the disk is heated locally and that modifies the effective index and thus the optical resonance by introducing a shift. We can also act on the evanescent coupling of the disk and the waveguide. For this we can place an electrode near the disk to vary the gap g_{opt}. Normally an important displacement is not necessary, it is enough that this gap is 400 nm for the disk not to be visible optically.

Mechanically the optomechanical disk can also be activated and deactivated. The simplest way is to act on the electrostatic stimulation. When the stimulation is stopped, the disk is damped until it stops. The damping depends on the viscosity of the environment. For example, the disk will stop faster in liquid than in vacuum. But if we want to stop the mechanics faster, we must place flippers. The role of these flippers will be to clamp on the disk to force it to stop. From a technological point of view this is complicated to achieve.

For the upcoming optomechanical matrix, it is possible to use both techniques (optical and mechanical) to activate and deactivate the disks. In general, the optical technique by heating element is widely used in the state of the art, especially for optical modulators [15] and [18].

3.5. Optomechanical matrix: what will it look like ?

Previously, we have seen the features that the "ideal" optomechanical matrix for mass detection must exhibit. The matrix must be realized in columns and rows with disks of the same dimensions. To read sequentially the array we have chosen to activate and deactivate the disks in an optical way by exploiting the thermo-optical effect. Based on all the reflections carried out, we present in this section the final configuration adopted for the optomechanical matrix. This matrix topology is innovative for mass detection applications. A patent has been granted for it in the context of this thesis.

3.5.1 Matrix topology selection

To thermally displace the optical resonance, a simple approach is to implement a resistor. The resistor comes to heat locally the surface of the disk. This modifies the effective index of the material and thus the optical resonance. Moreover, with an adjustable current source, we can control the thermal dissipation of the resistor and thus the shift of the optical resonance. Using this technique on our optomechanical sensor array we obtain the configuration shown in Figure 3.13.a . The optomechanical disks are represented in top view by the dotted circles. Above the disks are placed metal grids where the resistive elements are placed.

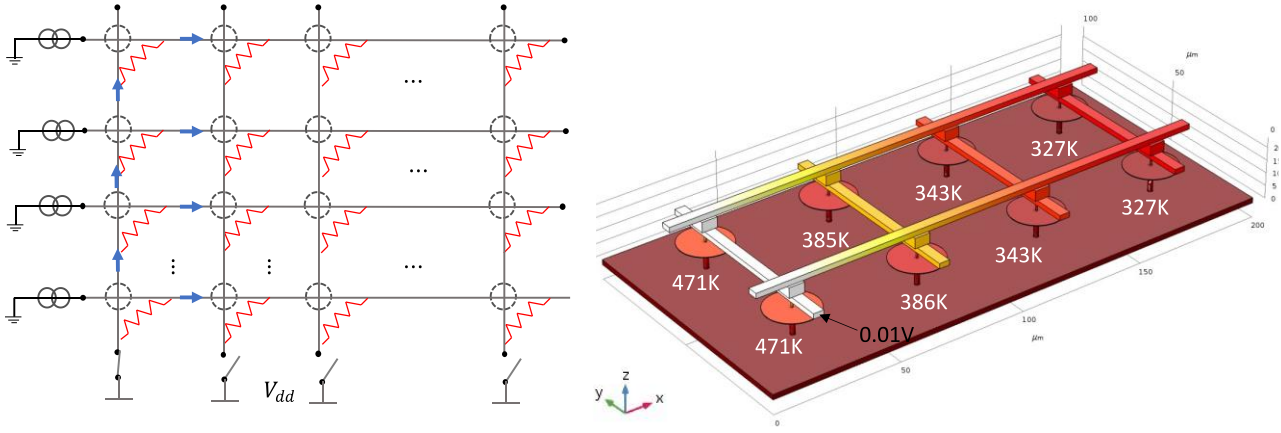

(a) (b)

Figure 3.13: Matrix topology with resistors (a) electrical view of the optomechanical matrix (b) thermal simulation of a 2x4 matrix in COMSOL

When we feed the disks placed on the 1st column, the current propagates and heats the disks of the 1st column and the disks of the other columns. To illustrate this, we have performed a COMSOL simulation on a 2x4 disk array. When we feed the disks of the 1st column only, we see that residual currents come to heat the other disks of the matrix as shown on Figure 3.13.b. The temperature shown in the Figure corresponds to the temperature on the disk surface. The further away from the current source the lower the temperature rise. These residual currents are not suited with our sequentially reading strategy. In fact, we only move the optical resonance of the disk we want to read.

To solve this problem, we decided to place p-n junctions instead of resistors. The new array is represented in Figure 3.14. This time, thanks to the P-N junctions, the residual currents which

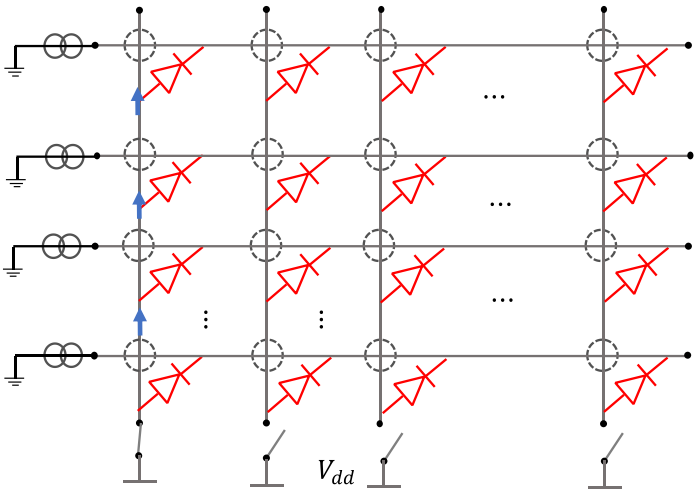

Figure 3.14: Electrical view of the optomechanical matrix with a P-N junctions

affected the other disks of the matrix are now blocked. Therefore, we can read such a matrix sequentially, one column at a time, without altering the state of the neighboring disks.

3.5.2 Overview and operating principle of the future matrix

Figure 3.15 below shows the general view of the future optomechanical array. This array will be designed to detect a large number of particles in liquid environment. For the moment, it is assumed that it is $i \times j$ in size. In total we will have $i \times j$ optomechanical disks arranged in rows and columns. The resonators placed on the same row share a common optical waveguide. As a reminder, we have chosen to work on the electrostatically actuated resonators for their excellent SNR. Therefore, it is necessary to provide around the disks the realization of metallic electrodes.

The electrodes can be connected to each other and to the same excitation source. Thus, mechanically all the disks are excited at the same time. During the sequential reading, to make visible or invisible the mechanical resonances of the disks, p-n junctions are placed. These junctions are placed underneath the disks through a metallic grid which allows the passage of the current. To heat in a uniform way, we place a metallic nail in the center of the disks directly in the SiO2 pedestal (see the brown circle in the center of the disks Figure 3.15.). We will see the fabrication process into details in the next section.

The principle of reading is as follows. We inject a wavelength λ_{laser} on the optical waveguides. Mechanically thanks to the electrodes all the resonators of the matrix are excited. As the disks have the same dimensions (except manufacturing defect) they have consequently the same optical resonance λ_{res}. By default, λ_{laser} and λ_{res}. are distant. This allows to have no visible signal at the output of the waveguides. To make visible the mechanical resonances, a current is injected on the first column. The disks of the first column heat up and their optical resonance moves towards λ_{laser}. Automatically at the output, the mechanical resonances of the disks of the first column become visible. We repeat this operation column by column, while taking care to deactivate the previous columns.

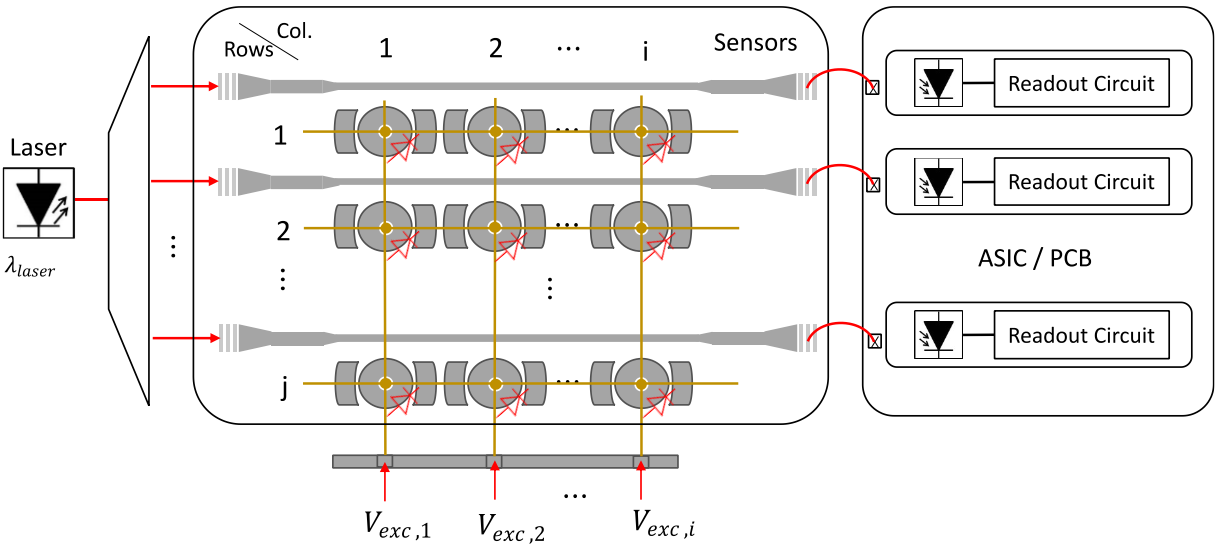

Figure 3.15: Overview of the future optomechanical array for mass sensing in chip form

Thanks to this principle, all the disks of the matrix are individually read and this in a very fast way. A reading electronic is placed at the output of each row. It is composed of a photodiode and a circuit which allows to track the resonance frequency. In the future we would like the laser, the optomechanical matrix and the reading electronics to be contained on the same chip as shown in Figure 3.15.

3.5.3 Fabrication process : Main steps

This new array configuration does not add much complexity compared to the conventional fabrication process of our resonators [13]. The idea is just to implement a p-n junction and a metal nail in the pedestal. Today, our optomechanical resonators are made on a 200 mm SOI wafer. An SOI wafer is composed of a thin Si layer (220 nm), a SiO2 layer of about 1 um and a larger layer of bulk Si (as illustrated in Figure 3.16. a) .

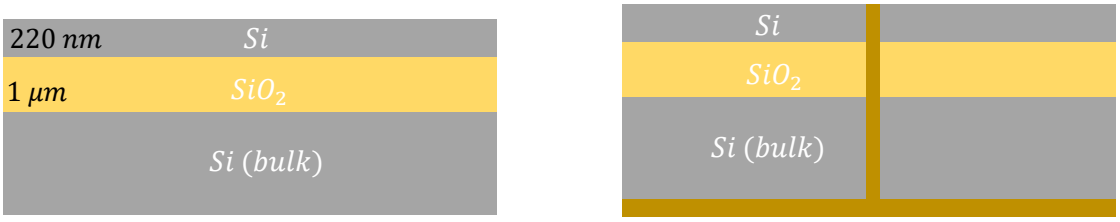

(a) (b)

Figure 3.16: (a) Initial 200 mm SOI (b) Base metallization of the bulk and creation of the metal nail.

The second step consists in the metallization of the structure as shown in Figure 3.16.b. A layer of metal is deposited on the base of the Si bulk. This layer will be connected to the ground to dissipate the injected current. Then the metal nail is formed on the SiO2 layer and the thin TOP layer. This metal will ensure the electrical connection between the TOP layer and the base of the bulk. It will also allow to heat uniformly the optomechanical disks.

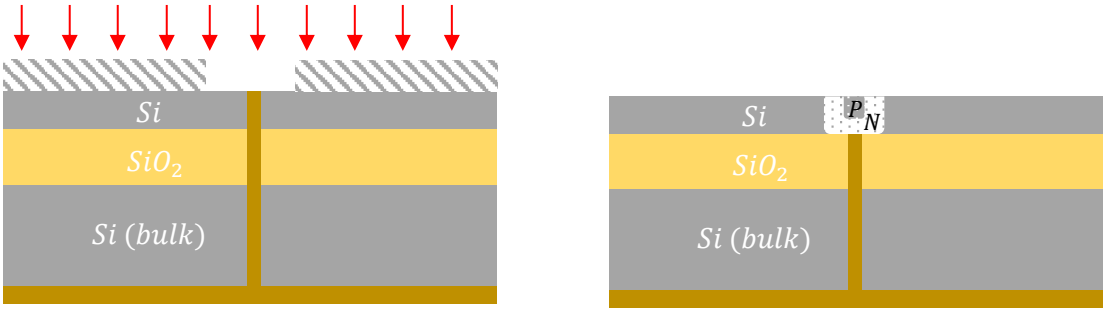

(a) (b)

Figure 3.17: (a) Ion implantation (Phosphorus and Boron) (b) Formation of N and P doped boxes

Figure 3.17.a presents the step where the p-n junction is formed. To achieve this, an oxide deposition is made on the thin TOP layer, followed by an implantation of phosphorus atoms to create the N-doped box. Then we repeat the operation with this time an implantation of Boron atoms to realize the P box. Thus, on Figure 3.17.b, we have formed the p-n junction. The current is passing in the direction of the TOP layer towards the bulk in the opposite direction it is blocked.

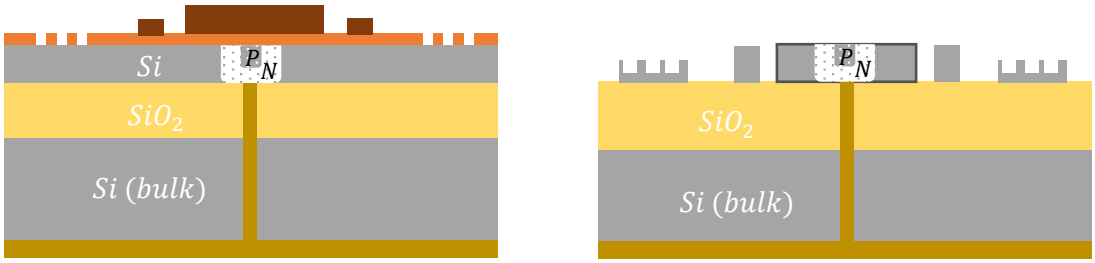

(a) (b)

Figure 3.18: (a) Thermal oxide layer deposition + SiH4 mask (b) Lithography + Etching

The next step in Figure 3.18.a consists of forming the coupler gratings, the optical waveguide, the resonator disk, and the supports for the actuation electrodes. A thermal oxide is deposited first and then a SiH4 mask which constitutes the photo-resistance. By Lithography and etching one comes to form the disk, the supports of the electrodes and the grating coupler. In Figure 3.18.b, we have the structure of the resonator almost formed.

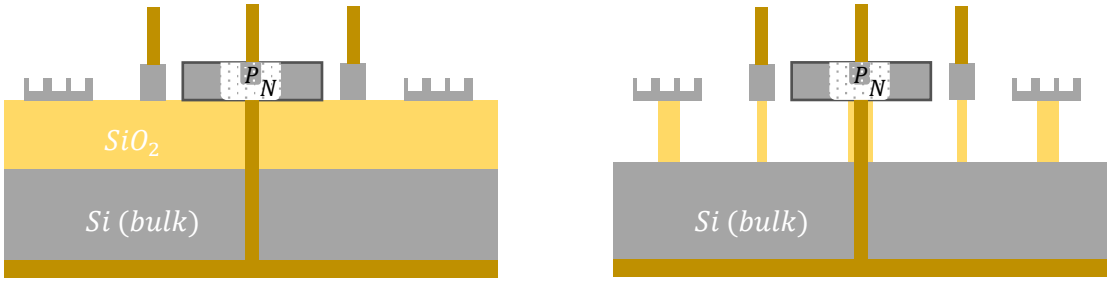

(a) (b)

Figure 3.19: (a) Metallization of the actuation electrodes and the disk (b) After etching all the structure is released.

The last step shown in Figure 3.19.a is the release of the structure. Before this, the metal structures are placed first on the actuating electrodes and then on the resonator disk. A pre-release step is necessary to etch the oxide layer with HF vapor and then etch it with the same HF vapor in an isotopic way to the bulk (see Figure.3.19.b).

3.6 Conclusion

The objective of this chapter is to study the possibilities of integrating optomechanical resonators in matrix form. In the first section, we presented the interest of this kind of matrix. Indeed, due to the small detection area of the optomechanical sensor, an array must be designed to significantly increase the effective area, which will reduce the reading time. We have also seen the different constraints that such a matrix will be subjected to.

In the second part, we looked at the reading principle of such a matrix. There are two possible reading principles. A sequential reading, where the idea is to read the matrix disk by disk. A simultaneous reading where the idea is to read all the resonators of the matrix at the same time. The reading principle chosen for the optomechanical matrix is the sequential reading. This type of reading is simple to read from an electronic point of view and allows to know in real time the position of the particle in the matrix. Then, based on a specification, we defined the contours of the "ideal" matrix for our mass detection application.

Following, we presented the optomechanical array systems at our disposal. Currently, we have two configurations of arrays. A configuration called "multiplexed" in which three optomechanical disks of different radius share the same waveguide. And a configuration with nano-rams placed around an optical disk.

Thus, in the next section, we continue our reflection on the " ideal " matrix by presenting the different techniques to activate or deactivate the optomechanical disks. Indeed, we have chosen a sequential reading for the optomechanical resonator array. As the disks share the same waveguide at each row of the array. It is necessary to read only one disk at a time while the other disks are disabled. This can be done optically (shift of the optical resonance, variation of the disk-waveguide gap) in order that the mechanical resonance becomes invisible. But also, mechanically where the idea would be to stop the mechanical movement of the disk.

In the last part, we finally present the matrix topology chosen for mass detection context. This configuration is innovative, a patent has been granted in the context of this work. Briefly, the future optomechanical matrix will be read sequentially column by column. To optically activate and deactivate the mechanical resonance we have opted for the introduction of a p-n junction. Thus, we will let the current pass in one direction without disturbing the state of the neighboring disks with the residual current. We also explained the different steps of the fabrication process of such a structure. This allows to see the complexity of the work needed to achieve one day such a matrix.

References

[1] « Cavity optomechanical spring sensing of single molecules | Nature Communications ». https://www.nature.com/articles/ncomms12311.

[2] M. Sansa *et al.*, « Optomechanical mass spectrometry », *Nat Commun*, vol. 11, n° 1, Art. n° 1, juill. 2020, doi: 10.1038/s41467-020-17592-9.

[3] D. Ramos *et al.*, « Arrays of dual nanomechanical resonators for selective biological detection », *Anal Chem*, vol. 81, n° 6, p. 2274-2279, mars 2009, doi: 10.1021/ac8024152.

[4] E. Gil-Santos *et al.*, « Scalable high-precision tuning of photonic resonators by resonant cavity-enhanced photoelectrochemical etching », *Nat Commun*, vol. 8, n° 1, Art. n° 1, janv. 2017, doi: 10.1038/ncomms14267.

[5] « Gallery », *Christopher G. Baker*, 7 février 2018. https://christophergbaker.com/gallery.

[6] O.-K. Kwon, J.-S. An, et S.-K. Hong, « Capacitive Touch Systems With Styli for Touch Sensors: A Review », *IEEE Sensors Journal*, vol. 18, n° 12, p. 4832-4846, juin 2018, doi: 10.1109/JSEN.2018.2830660.

[7] M. El-Desouki, M. J. Deen, Q. Fang, L. Liu, F. Tse, et D. Armstrong, « CMOS Image Sensors for High-Speed Applications », *Sensors (Basel)*, vol. 9, n° 1, p. 430-444, 2009, doi: 10.3390/s90100430.

[8] Ó. Oballe-Peinado, J. Castellanos-Ramos, J. A. Hidalgo-López, et F. Vidal-Verdú, *Direct Interfaces for Smart Skins Based on FPGAs*, vol. 7365. 2009. doi: 10.1117/12.821642.

[9] J. A. Hidalgo-López, J. Romero-Sánchez, R. Fernández-Ramos, J. F. Martín-Canales, et J. F. Ríos-Gómez, « A low-cost, high-accuracy temperature sensor array », *Measurement*, vol. 125, p. 425-431, sept. 2018, doi: 10.1016/j.measurement.2018.04.085.

[10] M. Possas *et al.*, « Frequency profile measurement system for microcantilever-array based gas sensor », in *2015 Symposium on Design, Test, Integration and Packaging of MEMS/MOEMS (DTIP)*, avr. 2015, p. 1-5. doi: 10.1109/DTIP.2015.7160999.

[11] N. Radha Shanmugam, S. Muthukumar, S. Chaudhry, J. Anguiano, et S. Prasad, « Ultrasensitive nanostructure sensor arrays on flexible substrates for multiplexed and simultaneous electrochemical detection of a panel of cardiac biomarkers », *Biosensors and Bioelectronics*, vol. 89, p. 764-772, mars 2017, doi: 10.1016/j.bios.2016.10.046.

[12] A. T. Güntner *et al.*, « Sniffing Entrapped Humans with Sensor Arrays », *Anal. Chem.*, vol. 90, n° 8, p. 4940-4945, avr. 2018, doi: 10.1021/acs.analchem.8b00237.

[13] M. Hermouet, « Microdisques optomécaniques résonants en silicium pour la détection biologique en milieu liquide », These de doctorat, Université Grenoble Alpes (ComUE), 2019.

[14] F.-R. Lamberti et al., “Real-Time Sensing with Multiplexed Optomechanical Resonators,” Nano Lett., vol. 22, no. 5, pp. 1866–1873, Mar. 2022, doi: 10.1021/acs.nanolett.1c04017.

[15] M.-H. Kim, L. Zimmermann, et W.-Y. Choi, « A Temperature Controller IC for Maximizing Si Micro-Ring Modulator Optical Modulation Amplitude », *Journal of Lightwave Technology*, vol. 37, nº 4, p. 1200-1206, févr. 2019, doi: 10.1109/JLT.2018.2889899.

[16] J. Komma, C. Schwarz, G. Hofmann, D. Heinert, et R. Nawrodt, « Thermo-optic coefficient of silicon at 1550 nm and cryogenic temperatures », *Appl. Phys. Lett.*, vol. 101, nº 4, p. 041905, juill. 2012, doi: 10.1063/1.4738989.

[17] F. G. Della Corte, M. Esposito Montefusco, L. Moretti, I. Rendina, et G. Cocorullo, « Temperature dependence analysis of the thermo-optic effect in silicon by single and double oscillator models », *Journal of Applied Physics*, vol. 88, nº 12, p. 7115-7119, déc. 2000, doi: 10.1063/1.1328062.

[18] K. Padmaraju et K. Bergman, « Resolving the thermal challenges for silicon microring resonator devices », *Nanophotonics*, vol. 3, nº 4-5, p. 269-281, août 2014, doi: 10.1515/nanoph-2013-0013.

Chapter 4

Frequency tracking readout architectures

Contents

In this chapter we will present the different readout architectures applicable to optomechanical resonators. We will see the closed-loop architectures such as the self-oscillating loop (SOL) and the frequency locked loop (FLL). We will also discuss open-loop architectures such as the lock-in-amplifier (LIA). For each of these architectures we propose a theoretical analysis of loop stability, phase noise and mass resolution. Then we compare the architectures on the basis of these criteria. For each architecture, the ability to read a resonator array is assessed. To read our optomechanical resonator, we have selected a FLL-based architecture, which is called AH-FLL for Adjustable Heterodyne Frequency Locked-Loop. We will see in the last part of the chapter the operating principle and the specification of this new architecture.

4.1. Closed-loop readout architecture

To minimize disturbances (long term drift of the sensor) and improve the dynamic range, we usually prefer to integrate resonant sensors in a closed loop. In the state of the art there are two types of closed-loop architectures: the self-oscillating loop (SOL) and frequency locked loop (FLL). The first technique consists in placing the resonator inside a feedback loop to allow self-oscillation. The second approach is to place the resonator in a loop which allows to exploit the phase shift between the oscillator and a voltage-controlled oscillator (VCO).

4.1.1 Self-oscillating loop (SOL)

The optomechanical resonator can be placed within a self-oscillating closed loop. In this configuration we use the term of self-oscillating architecture. The SOL architecture is a circuit that maintains the oscillation frequency of the resonator. This is achieved by fulfilling the gain and phase conditions of the Barkhausen criterion [1]-[2]. At the beginning the loop starts on noise, here the thermomechanical noise, then this signal is amplified by the loop to be reinjected into the resonator.

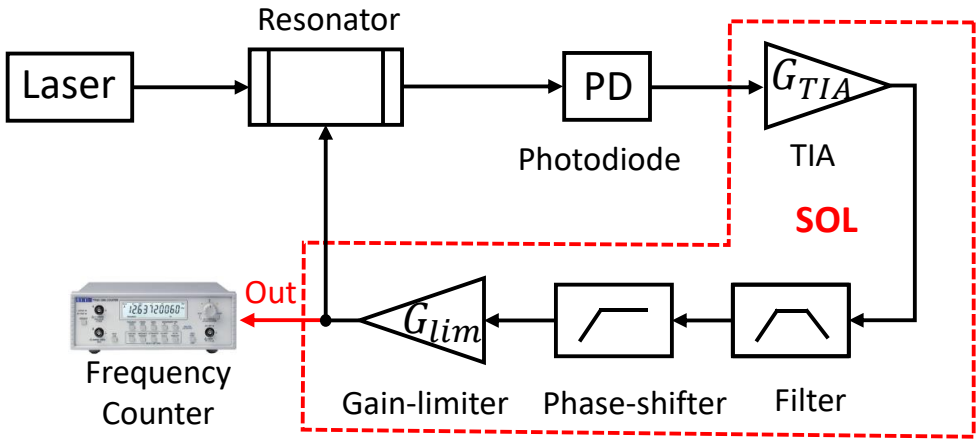

Figure 4.1: Architecture of an Optomechanical self-oscillating loop

Figure 4.1 shows the complete architecture of a self-oscillating loop with an optomechanical resonator. The architecture is composed of a Transimpedance Amplifier (TIA), a band-pass filter, a phase-shifter, and a gain limiter. The operating principle is as follows. The resonator modulates the optical power of the laser at its mechanical resonance frequency. The photodiode and the TIA transform the optically modulated signal into an electrical signal. After filtering and amplification this signal is injected into the resonator.

At the beginning, the oscillation starts on the noise of the electronics (mainly amplifiers) and the thermomechanical noise of the resonator. This noise is then injected into the resonator which filters around its resonance frequency. As the signal is amplified by the loop, it is also filtered around the resonator frequency. Once the oscillation is established (desired amplitude reached), the amplification is limited by a second amplifier used as a gain limiter. In this way, the amplitude condition of the Barkhausen criterion is respected. A second bandpass filter is generally used to enhance the filtering around the resonance frequency. To fulfill the phase condition of the Barkhausen criterion, a low-pass filter is implemented to adjust the phase shift along the oscillator loop.

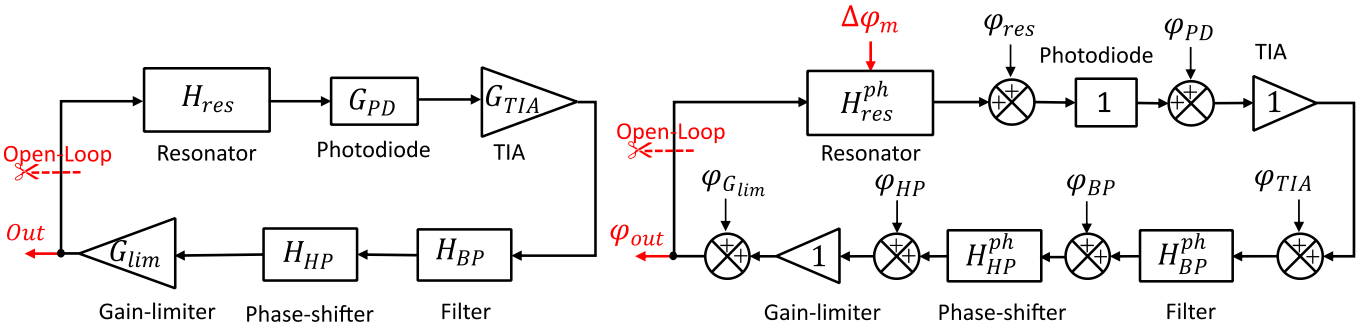

Figure 4.2: (a) Self-oscillating loop model in the analog domain (b) Self-oscillating loop model in the phase domain.

4.1.1.1 Open-Loop Analysis

The oscillation conditions of a self-oscillating loop are calculated from the open-loop transfer function. To do this, we open the loop just at the resonator input as illustrated in Figure 4.2.a. The architecture starts to oscillate, if:

$$\left|H_{SOL\_OL}(\omega_0)\right| > 1 \tag{4.1}$$

and

$$\arg\left(H_{SOL\_OL}(\omega_0)\right) = 0\ [2\pi] \tag{4.2}$$

where $H_{SOL\_OL} = H_{res}H_{BP}H_{HP}G_{TIA}G_{lim}G_{PD}$ with $H_{res},\ H_{BP}, H_{HP}, G_{TIA}, G_{lim}, G_{PD}$ respectively the transfer functions of the resonator, the band-pass filter, the phase shifter, the TIA, the gain limiter and the photodiode. Equation (4.1) is the gain condition and equation (4.2) the phase condition of the Barkhausen criterion. To respect condition (4.1) it is necessary that the loop has a gain greater than 1. Indeed, the oscillations start on the electronic and the resonator noise which are amplified by the loop. Once the desired amplitude is reached, equation 4.1 becomes:

$$\left|H_{SOL\_OL}(\omega_0)\right| = 1 \tag{4.3}$$

The Barkhausen criterion requires that the loop has a gain greater than 1 to start the oscillation and a unity gain to maintain the oscillation. To have a loop with variable gain, there are two methods:

- By implementing a real amplifier with a natural saturation of the large signal, as shown in Figure 4.2.a. This technique is very fast and does not significantly affect the stability of the frequency [3].

- Or by implementing an automatic gain amplifier (AGC). The idea is to use an adjustable amplifier to adjust the gain of the loop inversely proportional to the amplitude of the oscillation. This technique also has the advantage reducing the phase noise of the resonator by reducing the Leeson effect [4].

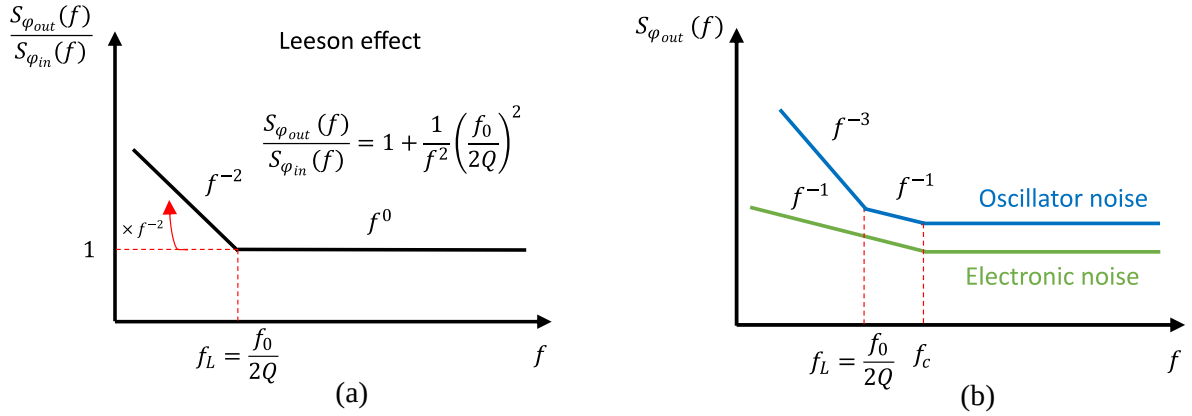

Figure 4.3: Log-Log scale (a) The transfer function of the Leeson effect (b) Phase noise of the electronics and the oscillator inspired from [5].

The Leeson effect was introduced in 1966 by D. B. Leeson during his research [6] to explain the shaping of phase noise in an oscillator. He developed a model with transfer functions to pass from input phase noise $S_{\varphi_{in}}$to output phase noise $S_{\varphi_{out}}$. The plot of the transfer function of Leeson's model as a function of frequency is depicted in Figure 4.3.a. At high frequencies, the transfer function is a unitary gain. At low frequencies, up to the Leeson frequency f_L it behaves as a second order integrator. This frequency f_L depends on the frequency f_0 and the quality factor Q of the resonator.

Figure 4.3.b illustrates the Leeson effect on the phase noise of the oscillator. The green curve corresponds to the noise of the electronics with a white noise component and a first order flicker at the corner frequency f_c. Obviously the global noise of the oscillator here in blue follows the electronic noise until f_L where the noise becomes a 3rd order flicker.

4.1.1.2 Phase Noise Analysis

In this section we will analyze the phase noise of the SOL architecture with the optomechanical resonator. Figure 4.2.b shows the complete phase model of the SOL architecture. The photodiode and the transimpedance amplifier correspond to a unitary gain in the phase domain. They do not modify the phase at their output.

However, each of them has a phase noise and contributes to the overall phase noise. The transfer function of the resonator in the phase domain corresponds to the transfer function of a 1st order low-pass filter [3]. The so called Rubiola approximation remains true even for the phase shifter and the bandpass filter. The phase transfer functions of these filters also correspond to 1st order loop filter. The output phase of the SOL architecture is written as follows (see Appendix A):

$$\varphi_{out} = \frac{1}{H_d}\left(\varphi_{G_{lim}} + \varphi_{HP}\right) + \frac{H_{HP}^{ph}}{H_d}\varphi_{BP} + \frac{H_{HP}^{ph}H_{BP}^{ph}}{H_d}\left(\varphi_{TIA} + \varphi_{PD} + \varphi_{res}\right) \tag{4.4}$$

where,

$$H_d = 1 - H_{HP}^{ph}H_{BP}^{ph}H_{res}^{ph} \tag{4.5}$$

$H_{res}^{ph}(s) = 1/\left(1 + 2\frac{Q_{res}}{w_{res}}s\right)$ is the phase transfer function of the resonator where Q_{res} and w_{res} are the quality factor and the resonance frequency respectively. H_{HP}^{ph} and H_{BP}^{ph} are the respective phase transfer functions of the phase-shifter and the band-pass filter.

- Power Spectral Density (PSD) of the output phase noise :

From the output phase φ_{out} of the SOL architecture defined in equation (4.4) we can calculate the power spectral density (PSD) of the phase noise. The spectral density is noted $S_{\varphi_{out}}$ and informs us about the phase contribution of each of the blocks which constitute the SOL architecture. The power density $S_{\varphi_{out}}$ is written as follows :

$$S_{\varphi_{out}} = \left|\frac{1}{H_d}\right|^2 (S_{\varphi_{G_{lim}}} + S_{\varphi_{HP}}) + \left|\frac{H_{HP}^{ph}}{H_d}\right|^2 S_{\varphi_{BP}} + \left|\frac{H_{HP}^{ph}H_{BP}^{ph}}{H_d}\right|^2 (S_{\varphi_{TIA}} + S_{\varphi_{PD}} + S_{\varphi_{res}}) \quad (4.6)$$

where, $S_{\varphi_{G_{lim}}}, S_{\varphi_{HP}}, S_{\varphi_{BP}}, S_{\varphi_{TIA}}, S_{\varphi_{PD}}, S_{\varphi_{res}}$ are respectively the phase noise spectral density of the gain limiter, high-pass filter, band-pass filter, transimpedance amplifier, photodiode and optomechanical resonator.

4.1.1.3 Allan Deviation and Mass resolution

For resonant sensors like the optomechanical resonator, we do not discuss in terms of phase noise. We use the Allan deviation (ADEV). The Allan deviation noted $\sigma(\tau)$ is calculated from the Allan variance (AVAR) noted $\sigma^2(\tau)$. The AVAR is a mathematical calculation that allows to characterize the frequency stability of resonators. The definition of the AVAR is written as follows [3]:

$$\sigma^2(\tau) = \int_0^\infty S_y(f)|H_A(jf)|^2 df \tag{4.7}$$

where, $S_y(f) = \left(\frac{f}{f_0}\right)^2 S_{\varphi_{out}}(f)$ is the power spectral density of a fractional frequency deviation and $|H_A(jf)|^2$ is the filter transfer function defined as :

$$|H_A(jf)|^2 = 2\frac{sin^4\pi\tau f}{(\pi\tau f)^2} \tag{4.8}$$

τ is the integration time where the AVAR is calculated. We can transform the phase noise density of the SOL equation (4.6) into an Allan variance expression. To do this, we simply inject equation (4.6) into the definition of equation (4.7). The AVAR of the SOL architecture can be written as follows:

$$\sigma_{SOL}^2(\tau) = \int_0^\infty \left(\frac{f}{f_0}\right)^2 \left[S_{\varphi_{elec}}(f) + \left|\frac{H_{HP}^{ph}H_{BP}^{ph}}{H_d}\right|^2 \left(S_{\varphi_{PD}}(f) + S_{\varphi_{res}}(f)\right)\right] |H_A(jf)|^2 df \tag{4.9}$$

where,

$$S_{\varphi_{elec}}(f) = \left|\frac{1}{H_d}\right|^2 \left(S_{\varphi_{G_{lim}}}(f) + S_{\varphi_{HP}}(f)\right) + \left|\frac{H_{HP}^{ph}}{H_d}\right|^2 S_{\varphi_{BP}}(f) + \left|\frac{H_{HP}^{ph}H_{BP}^{ph}}{H_d}\right|^2 S_{\varphi_{TIA}}(f) \tag{4.10}$$

To simplify (see Appendix A), equation (4.9) becomes:

$$\sigma_{SOL}^2(\tau) = \sigma_{elec}^2(\tau) + \sigma_{res}^2(\tau) + \sigma_{PD}^2(\tau) \tag{4.11}$$

where, $\sigma_{elec}^2(\tau)$, $\sigma_{res}^2(\tau)$, $\sigma_{PD}^2(\tau)$ are respectively the Allan variance of the SOL electronics (gain limiter, phase-shifter, transimpedance amplifier and band-pass filter), of the resonator and of the photodiode. To realize a SOL architecture with a high frequency resolution, it is necessary to minimize the variance given by equation (4.11). In general, the oscillator designer cannot optimize the stability of the resonator frequency that was set by the MEMs designer. It depends on many technological parameters that only the resonator designers can control. However, we can design an electronic system which has a stability equivalent or superior to the resonator. Therefore, we must respect the condition $\sigma_{elec}^2(\tau) + \sigma_{PD}^2(\tau) \leq \sigma_{res}^2(\tau)$.

The mass resolution of the SOL architecture depends on the minimum ADEV reached $\sigma_{SOL,min}$ and the mass of the resonator M_{res} [7]. The mass resolution is therefore written:

$$\sigma_m = 2M_{res}\sigma_{SOL,min}(\tau) \tag{4.12}$$

4.1.2 Frequency Locked-Loop (FLL)

The second closed-loop architecture that allows resonators to be read is the frequency locked loop (FLL) . The FLL architecture is a circuit in which the resonator is placed in a feedback loop. Figure 4.4 below shows the complete architecture. In this loop, we exploit the phase shift $\Delta\varphi$ between the resonator phase φ_{res} and the voltage-controlled oscillator (VCO) phase φ_{vco}. The idea is to lock the VCO frequency to the resonance frequency of the resonator. This architecture is simpler to implement than the SOL architecture for resonant sensors and is also more robust to disturbances.

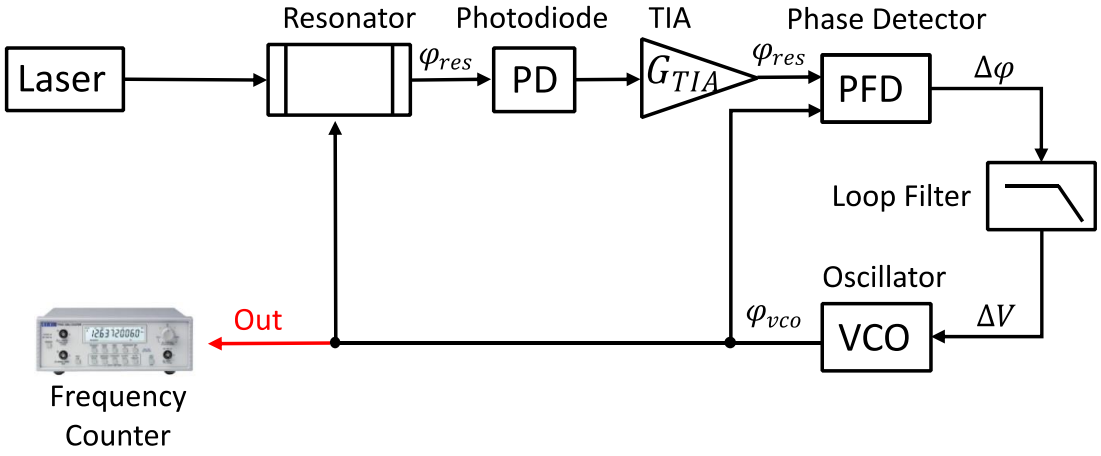

Figure 4.4: Overview of the FLL/PLL architecture with an Optomechanical resonator

The circuit contains a transimpedance amplifier (TIA) that converts the photodiode current into a voltage with some gain. The PLL block is composed of a phase and frequency detector (PFD), a loop filter and a VCO. In general, the PFD is designed with two D-type flip flops that drive two switches and a charge pump [8]. The loop filter is a low-pass filter, usually of the second or third order, whose design is crucial to ensure the stability of the loop. The operating principle is as follows. The PFD determines the phase or frequency difference between the reference (the resonator frequency) and the VCO signal. As long as the PFD output error is not null, the loop filter integrates the phase error and changes the VCO frequency until the phase error $\Delta\varphi$ is cancelled.

4.1.2.1 Open-Loop Analysis

Figure 4.5 presents in the phase domain the linear time invariant model of the FLL. This model includes the noise of each of the blocks forming the FLL. The transfer function of the resonator corresponds to a 1st order low-pass filter. The photodiode and the transimpedance amplifier have a unitary gain in the phase domain. The loop filter can be a 2nd or higher order low pass filter. The phase detector corresponds to a gain in terms of transfer function and the VCO to an integrator.

The FLL architecture is a closed-loop architecture. In order that the FLL converges, it is necessary to guarantee the loop stability in the phase domain. To do this, we must calculate the open loop transfer function.

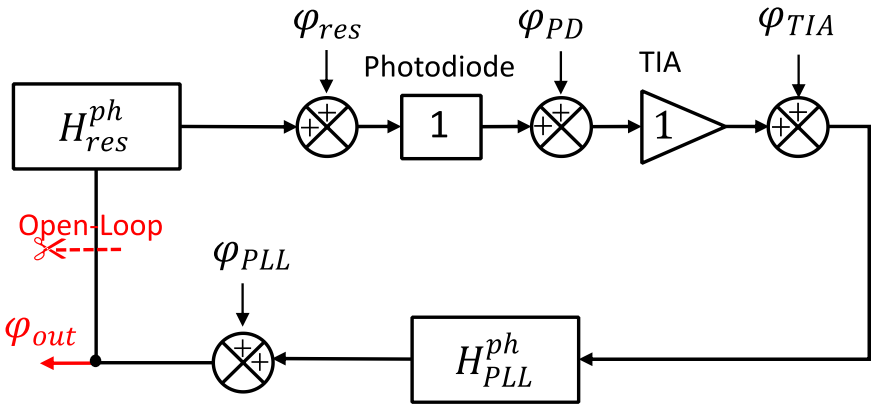

Figure 4.5: Phase noise model of the Frequency locked-loop architecture

As illustrated in Figure 4.5, we open the loop at the input of the resonator. We consider the resonator input as the input of the system and φ_{out} as the output. The open loop function is therefore written (see Appendix B):

$$H_{FLL\_OL}(s) = H_{res}^{ph}(s)H_{PLL}^{ph}(s) \tag{4.13}$$

where,

$$H_{res}^{ph}(s) = \frac{1}{1 + 2\frac{Q_{res}}{w_{res}}s} \quad \text{and} \quad H_{PLL}^{ph}(s) = \frac{H_{VCO}(s)H_{LF}(s)H_{PFD}(s)}{1 + H_{VCO}(s)H_{LF}(s)H_{PFD}(s)} \tag{4.14}$$

H_{res}^{ph} and H_{PLL}^{ph} the phase transfer function of the resonator and the PLL block respectively. $H_{VCO}(s) = \frac{K_{VCO}}{s}$ is the transfer function of the VCO with K_{VCO} the gain. $H_{PFD}(s) = \frac{I_{pump}}{2\pi}$ and $H_{LF}(s)$ are respectively the transfer function of the charge pump and the loop filter.

The FLL loop stability is evaluated from the transfer function defined in equation (4.13). The bode diagram corresponding to this transfer function is traced and then the graphical stability methods are used to determine the phase margin $M_\varphi$and the gain margin M_G. Figure 4.6 below shows the trace of the transfer function H_{FLL_OL}. M_φ and M_G are defined as follows :

$$M_\varphi = \arg\left(H_{FLL\_OL}(jw_{c\_FLL})\right) + \pi \tag{4.15}$$

and

$$M_G = -20\text{Log}_{10}\left|H_{FLL\_OL}(jw_{-\pi})\right| \tag{4.16}$$

where w_{c_FLL} is the cut-off frequency when the gain is at 0 dB and $w_{-\pi}$ is the frequency when the phase is at -π. To have a good stability, it is necessary that $M_\varphi \geq 45°$ and $M_G \geq 10\ dB$.

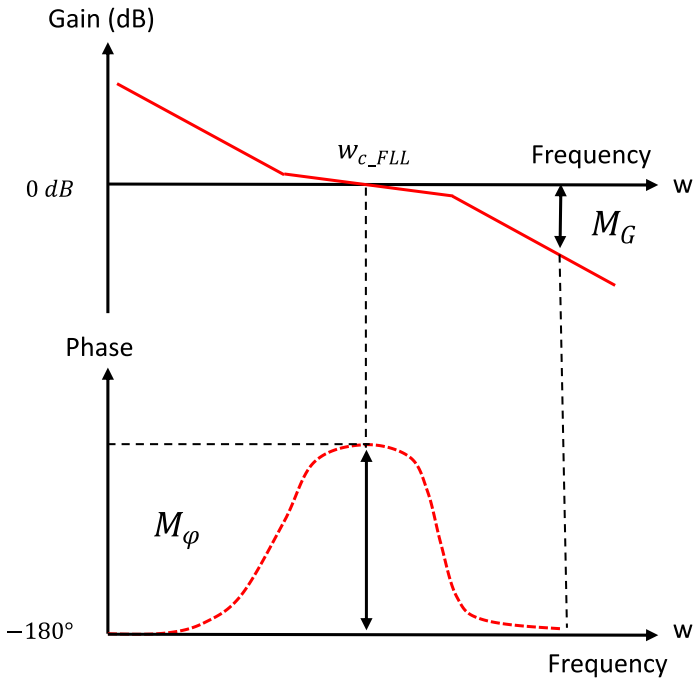

Figure 4.6: Loop stability analysis from the bode diagram of the open loop transfer function H_{FLL_OL}

4.1.2.2 Phase noise Analysis

In this section we will analyze the phase noise of the FLL architecture. Figure 4.5 below presents in the phase domain the linear time invariant model of the FLL. This model includes the noise of each of the blocks forming the FLL. The transfer function of the resonator corresponds to a 1st order low-pass filter. The photodiode and the transimpedance amplifier have a unitary gain in the phase domain. In PLL block, the loop filter can be a 2nd or higher order low pass filter. The phase detector corresponds to a gain in terms of transfer function and the VCO to an integrator. The output phase is described as (see Appendix B):

$$\varphi_{out} = \frac{1}{1 - H_{res}^{ph} H_{PLL}^{ph}} \varphi_{PLL} + \frac{H_{PLL}^{ph}}{1 - H_{res}^{ph} H_{PLL}^{ph}} (\varphi_{res} + \varphi_{TIA} + \varphi_{PD}) \qquad (4.17)$$

As expressed above in equation (4.14), H_{res}^{ph} is the phase transfer function of the resonator and H_{PLL}^{ph} is the phase transfer function of the PLL block.

- Power Spectral Density (PSD) of the output phase noise :

From the output phase φ_{out} of the FLL architecture defined in equation (4.17) we can calculate the power spectral density (PSD). The spectral density is noted $S_{\varphi_{out}}$ and informs us about the phase contribution of each of the blocks which constitute the FLL architecture. The power density $S_{\varphi_{out}}$ is written as follows:

$$S_{\varphi_{out}} = \left|\frac{1}{1 - H_{res}^{ph} H_{PLL}^{ph}}\right|^2 S_{\varphi_{PLL}} + \left|\frac{H_{PLL}^{ph}}{1 - H_{res}^{ph} H_{PLL}^{ph}}\right|^2 \left(S_{\varphi_{res}} + S_{\varphi_{TIA}} + S_{\varphi_{PD}}\right) \quad (4.18)$$

where, the output spectral density $S_{\varphi_{out}}$ depends on the spectral density of the noise introduced by the PLL block (phase-detector, loop filter and VCO) noted $S_{\varphi_{PLL}}$, the spectral density of the transimpedance amplifier noted $S_{\varphi_{TIA}}$, the spectral density of the photodiode and the resonator noted $S_{\varphi_{res}}$ and $S_{\varphi_{PD}}$ respectively. In general, it is assumed that the resonator noise $S_{\varphi_{res}}$is predominant. Indeed, the signal power at the output of the resonator is very low, so the contribution of the floor noise is important.

4.1.2.3 Allan Deviation and Mass resolution

To evaluate the phase noise of the FLL architecture in a relevant way we calculate the AVAR defined in section 4.1.1.3. We inject the spectral density equation (4.18) to the definition of the AVAR equation (4.7). The Allan variance of the FLL architecture is thus written as follows:

$$\sigma_{FLL}^2(\tau) = \int_0^\infty \left(\frac{f}{f_0}\right)^2 \left[S_{\varphi_{elec}}(f) + \left|\frac{H_{PLL}^{ph}}{1 - H_{res}^{ph} H_{PLL}^{ph}}\right|^2 \left(S_{\varphi_{PD}}(f) + S_{\varphi_{res}}(f)\right)\right] |H_A(jf)|^2 df \quad (4.19)$$

where,

$$S_{\varphi_{elec}}(f) = \left|\frac{1}{1 - H_{res}^{ph} H_{PLL}^{ph}}\right|^2 S_{\varphi_{PLL}}(f) + \left|\frac{H_{PLL}^{ph}}{1 - H_{res}^{ph} H_{PLL}^{ph}}\right|^2 S_{\varphi_{TIA}}(f) \quad (4.20)$$

To simplify (see Appendix B), equation (4.19) becomes:

$$\sigma_{FLL}^2(\tau) = \sigma_{elec}^2(\tau) + \sigma_{res}^2(\tau) + \sigma_{PD}^2(\tau) \quad (4.21)$$

where, $\sigma_{elec}^2(\tau)$, $\sigma_{res}^2(\tau)$, $\sigma_{PD}^2(\tau)$ are respectively the Allan variance of the FLL electronics (PLL block and TIA), of the resonator and the photodiode. To realize a FLL electronics with high frequency stability, it is necessary to minimize the AVAR given by equation (4.19). Properly designed FLL electronics should not degrade the measurement of the resonator frequency stability. Therefore, we must respect the condition : $\sigma_{elec}^2(\tau) + \sigma_{PD}^2(\tau) \leq \sigma_{res}^2(\tau)$.

The mass resolution of the FLL architecture depends on the minimum ADEV reached $\sigma_{FLL,min}$ and the mass of the resonator M_{res} . The mass resolution is expressed as follows:

$$\sigma_m = 2M_{res}\sigma_{FLL,min}(\tau) \quad (4.22)$$

4.2. Open loop readout architecture

To read resonant sensors there are also open loop architectures. In this case, the readout circuit is separated from the drive circuit of the sensor. The aim is only to read out the sensor, so an external excitation source is necessary. In the state of the art, the most known technique consists in making a frequency sweep with a Local Oscillator (LO) over the entire measurement range to track the resonance of the transducer, this is the principle of Lock-In-Amplifier (LIA).

There are also other open loop reading techniques such as the amplitude & phase reading. In this section we will only see the frequency sweep method. Appendix C describes the amplitude & phase readout architecture.

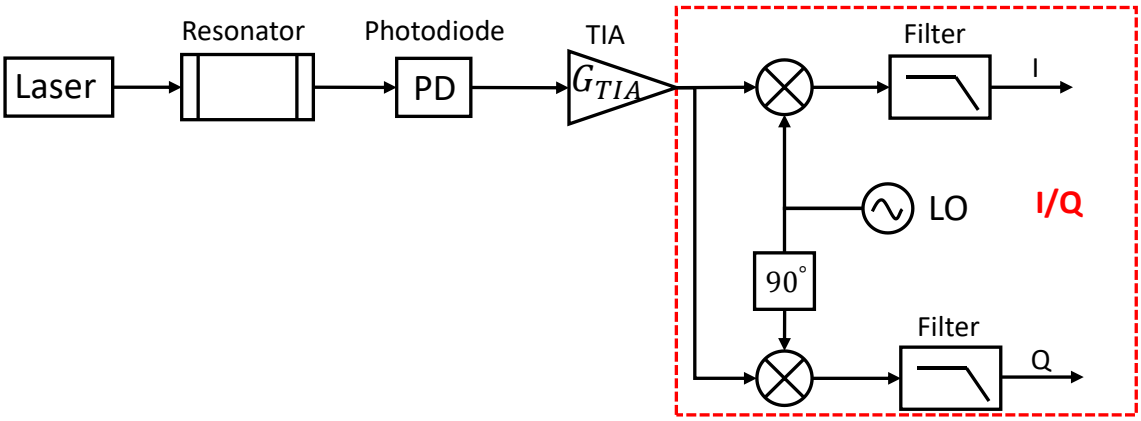

Figure 4.7: Overview of the LIA architecture with an Optomechanical resonator

The lock-in-amplifier or I/Q demodulation is an open loop architecture. It allows the extraction of narrow band signals with low amplitude (such as the resonator signal) embedded in wideband noise. This extraction is made possible by mixing with a signal having a close frequency. Figure 4.7 shows the complete LIA architecture with the optomechanical resonator. The operating principle is as follows. The signal at the output of the resonator is amplified by the transimpedance amplifier. Once amplified, the signal is mixed with an oscillator adjustable in frequency. When the oscillator frequency corresponds to the resonator frequency, we obtain two DC signals (I and Q).

4.2.1 Noise analysis

In this section we will analyze the phase noise of the LIA architecture. Figure 4.8 presents the noise model of the LIA. In this architecture the phase noise is transformed into amplitude noise at the output. For this reason, in Figure 4.8 one part is expressed in phase and the other part in amplitude. The photodiode and the transimpedance amplifier have a unitary gain in the phase domain. The phase φ_x correspond to the phase noise at mixers inputs and can be expressed as follows:

$$\varphi_x = \varphi_{TIA} + \varphi_{PD} + \varphi_{res} + H_{res}^{ph}\varphi_{in} \tag{4.23}$$

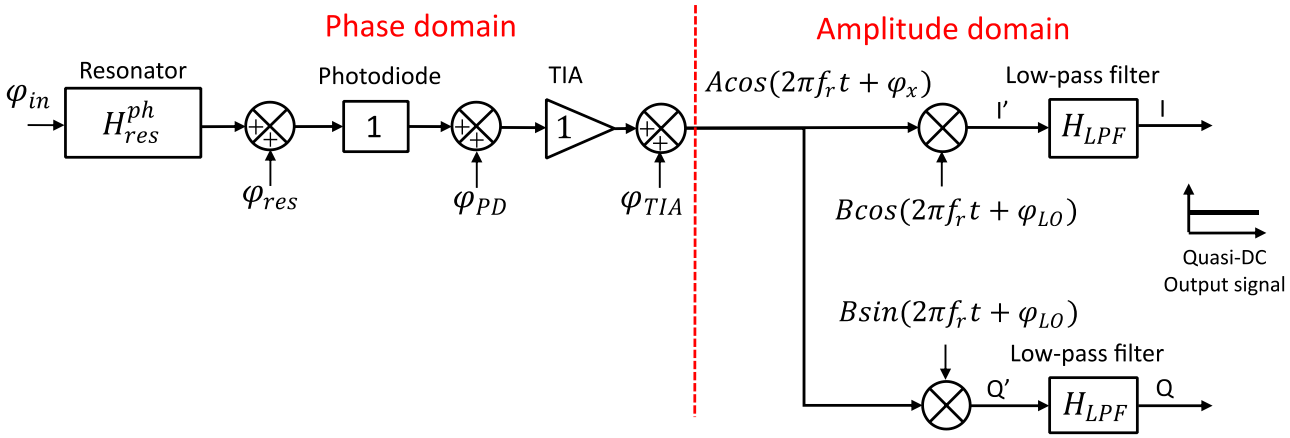

Figure 4.8: Noise model of the lock-in-amplifier (LIA) architecture

At the output of the mixer, the phase noise φ_x is transformed into the amplitude domain and becomes :

$$I' = \frac{AB}{2}(\cos(4\pi f_r t + \varphi_x + \varphi_{LO}) + \cos(\varphi_x - \varphi_{LO})) \tag{4.24}$$

and

$$Q' = \frac{AB}{2}(\sin(4\pi f_r t + \varphi_x + \varphi_{LO}) + \sin(\varphi_x - \varphi_{LO})) \tag{4.25}$$

The low-pass filter removes the high-frequency components. The I/Q outputs of the LIA architecture depend on the φ_x and can be written as:

$$I = \frac{AB}{2}\cos(\varphi_x - \varphi_{LO}) \tag{4.26}$$

and

$$Q = \frac{AB}{2}\sin(\varphi_x - \varphi_{LO}) \tag{4.27}$$

- Power Spectral Density (PSD) :

The spectral density noted $S_I(f)$ and $S_Q(f)$ informs us about the noise at the output of the LIA architecture. These spectral densities are expressed as :

$$S_I(f) = |H_{LPF}(f)|^2 S_{I'}(f) \tag{4.28}$$

with,

$$S_{I'}(f) = \left(\frac{AB}{2}\cos(\varphi_x - \varphi_{LO})\right)^2 \delta(f) + A^2B^2[\delta(f - 2f_r) + \delta(f + 2f_r)] \tag{4.29}$$

where, $S_{I'}(f)$ corresponds to the spectral density of the expression defined in the equation (4.24) and $\delta(f)$ the expression of a Dirac delta distribution. Similarly, the equation of the spectral density at the output Q is :

$$S_Q(f) = |H_{LPF}(f)|^2 S_{Q'}(f) \tag{4.30}$$

with,

$$S_{Q'}(f) = \left(\frac{AB}{2}\cos(\varphi_x - \varphi_{LO})\right)^2 \delta(f) + A^2B^2[\delta(f - 2f_r) + \delta(f + 2f_r)] \tag{4.31}$$

4.2.2 Allan Deviation and Mass resolution

Based on the spectral densities $S_I(f)$ and $S_Q(f)$, we calculate the Allan variance defined in section 4.1.1.3. For both I and Q outputs of the LIA architecture, AVAR is written as follows:

$$\sigma_I^2(\tau) = \int_0^\infty \left(\frac{f}{f_0}\right)^2 \left(|H_{LPF}(f)|^2 S_{I'}(f)\right)|H_A(jf)|^2 df \tag{4.32}$$

and

$$\sigma_Q^2(\tau) = \int_0^\infty \left(\frac{f}{f_0}\right)^2 \left(|H_{LPF}(f)|^2 S_{Q'}(f)\right)|H_A(jf)|^2 df \tag{4.33}$$

To achieve a LIA electronics with excellent frequency resolution it is necessary to minimize the AVAR given by equations (4.32) and (4.33). In order to optimize these variances, we usually choose a filter with a low cutoff frequency. It increases the resolution to the detriment of a longer integration time.

- Mass resolution of the lock-in-amplifier architecture :

The mass resolution is the detection limit reached by the lock-in-amplifier architecture. It is calculated from the minimum stability frequency of the electronics. The resolution is noted σ_m and is written:

$$\sigma_m = 2M_{res}\sigma_{LIA,min}(\tau) \tag{4.34}$$

where M_{res} is the mass of the resonator and $\sigma_{LIA,min}$ is the lock-in-amplifier frequency minimum stability, equal to $\sigma_{I,min}$ or $\sigma_{Q,min}$.

4.3. Readout Architecture comparison

To read the resonant sensors, we have presented the most known reading architectures such as SOL, FLL and LIA. Other architectures not mentioned here exist, especially amplitude and phase tracking (see Appendix C) or IQ-FLL (see Appendix D).We have seen in the previous sections for each presented architecture, the operating principle, and the theoretical analysis in terms of phase noise, Allan deviation or frequency resolution. Table 4.1 below lists the essential information (operating principle, phase noise, frequency resolution, and complexity) of each readout architecture.

To put an optomechanical resonator in self-oscillation (SOL), it is necessary to design amplifiers (transimpedance and gain limit) and filters (phase-shifter and band-pass) in order to respect the Barkhausen criteria defined in equation (4.1) and (4.2). The phase noise of the architecture is defined in equation (4.6). To design a good SOL, the phase noise of the electronics (amplifiers and filters) must be less than the intrinsic phase noise of the resonator. In a SOL, an incompressible time is needed to establish the oscillations. This time depends on the quality factor of the resonator. The higher the quality factor is, the faster the oscillations start. A second time corresponds to the time of change of frequency and in general is fast (few µs to ms).

To design an FLL architecture around the resonator, it is necessary to design a VCO, a phase detector (PFD), a loop filter and a transimpedance amplifier. The phase noise of the architecture is defined by equation (4.18). To have FLL electronics with low phase noise, it is necessary to minimize the phase noise of the PFD and the VCO. In addition, during the design it is necessary to guarantee the convergence of the loop. For this purpose, the stability of the open loop system is calculated with the defined transfer function (4.13). The PLL convergence time depends on the bandwidth of the loop filter. The higher this bandwidth is, the faster the PLL converges.

An optomechanical resonator can be read in open loop using an LIA architecture. For this, it is necessary to design an ultra-stable oscillator, a low-pass filter, and a TIA. The noise of this architecture is defined in equations (4.26) and (4.27). The LIA is an architecture that has an excellent frequency resolution due to the ultra-stable oscillator that allows the sweep, however it converges slowly. Indeed, the convergence time depends on the accuracy. When accuracy is required to be high the bandwidth of the filters is reduced and therefore the architecture takes more time to converge. Precision and convergence time must be adjusted to find the right compromise.

4.3.1 Figure of Merit (FoM)

For a given resonator, it is difficult to know which architecture is relevant compared to another. To evaluate an architecture, we introduce a Figure of Merit (FoM). To have a relevant comparison, we must first look at the frequency operating range of the architecture. This frequency range is often imposed by the resonance frequency of the resonator. Then we compare the performance of the architectures, in terms of frequency stability defined by the Allan deviation and convergence time, which respectively characterize the stability of the frequency and the time needed to reach this stability. Considering these criteria, the FoM is written:

	Closed-Loop Architecture		Open-Loop Architecture
	Self-oscillating loop (SOL)	Frequency locked loop (FLL)	Lock-in-amplifier (LIA)
Operating Principle	The sensor is placed in a loop that guarantees its self-oscillation according to the Barkhausen's phase and gain conditions.	The sensor is place inside a loop that exploits the phase difference between the resonator and VCO.	Using a frequency sweep, the output signal of the resonator (low amplitude and narrow band) is extracted and then reconstructedwith I and Q.
Output Phase	$\varphi_{out} = \frac{1}{H_d}\varphi_{G_{lim}} + \frac{1}{H_d}\varphi_{HP} + \frac{H_{HP}^{ph}}{H_d}\varphi_{BP} + \frac{H_{HP}^{ph}H_{BP}^{ph}}{H_d}\varphi_{TIA} + \frac{H_{HP}^{ph}H_{BP}^{ph}}{H_d}\varphi_{G_{PD}} + \frac{H_{HP}^{ph}H_{BP}^{ph}}{H_d}\varphi_{res}$ With $H_d = 1 - H_{HP}^{ph}H_{BP}^{ph}H_{res}^{phase}$	$\varphi_{out} = \frac{1}{1 - H_{res}^{ph}H_{PLL}^{ph}}\varphi_{PLL} + \frac{H_{PLL}^{ph}}{1 - H_{res}^{ph}H_{PLL}^{ph}}(\varphi_{res} + \varphi_{TIA} + \varphi_{PD})$	$I = \frac{AB}{2}\cos(\varphi_x - \varphi_{LO})$ and $Q = \frac{AB}{2}\sin(\varphi_x - \varphi_{LO})$ With $\varphi_x = \varphi_{TIA} + \varphi_{PD} + \varphi_{res} + H_{res}^{ph}\varphi_{in}$
Output Phase Noise (PSD)	$S_{\varphi_{out}} = \left\|\frac{1}{H_d}\right\|^2 S_{\varphi_{G_{lim}}} + \left\|\frac{1}{H_d}\right\|^2 S_{\varphi_{HP}} + \left\|\frac{H_{HP}^{ph}}{H_d}\right\|^2 S_{\varphi_{BP}} + \left\|\frac{H_{HP}^{ph}H_{BP}^{ph}}{H_d}\right\|^2 S_{\varphi_{TIA}} + \left\|\frac{H_{HP}^{ph}H_{BP}^{ph}}{H_d}\right\|^2 S_{\varphi_{PD}} + \left\|\frac{H_{HP}^{ph}H_{BP}^{ph}}{H_d}\right\|^2 S_{\varphi_{res}}$	$S_{\varphi_{out}} = \left\|\frac{1}{1 - H_{res}^{ph}H_{PLL}^{ph}}\right\|^2 S_{\varphi_{PLL}} + \left\|\frac{H_{PLL}^{ph}}{1 - H_{res}^{ph}H_{PLL}^{ph}}\right\|^2 (S_{\varphi_{res}} + S_{\varphi_{TIA}} + S_{\varphi_{PD}})$	$S_I(f) = \|H_{LPF}(f)\|^2 S_{I'}(f)$ and $S_Q(f) = \|H_{LPF}(f)\|^2 S_{Q'}(f)$
AVAR/ADEV	$\sigma_{SOL}^2(\tau) = \sigma_{elec}^2(\tau) + \sigma_{res}^2(\tau) + \sigma_{PD}^2(\tau)$ With $\sigma_{elec}^2(\tau) = \sigma_{G_{lim}}^2(\tau) + \sigma_{HP}^2(\tau) + \sigma_{TIA}^2(\tau) + \sigma_{BP}^2(\tau)$	$\sigma_{FLL}^2(\tau) = \sigma_{elec}^2(\tau) + \sigma_{res}^2(\tau) + \sigma_{PD}^2(\tau)$ With $\sigma_{elec}^2(\tau) = \sigma_{VCO}^2(\tau) + \sigma_{LPF}^2(\tau) + \sigma_{PFD}^2(\tau) + \sigma_{TIA}^2(\tau)$	$\sigma_I^2(\tau) = \int_0^\infty \left(\frac{f}{f_0}\right)^2 \left(\|H_{LPF}(f)\|^2 S_{I'}(f)\right) \|H_A(jf)\|^2 df$ and $\sigma_Q^2(\tau) = \int_0^\infty \left(\frac{f}{f_0}\right)^2 \left(\|H_{LPF}(f)\|^2 S_{Q'}(f)\right) \|H_A(jf)\|^2 df$
Mass resolution	$\sigma_m = 2M_{res}\,\sigma_{SOL,min}(\tau)$ M_{res} the resonator's mass and $\sigma_{SOL,min}$ the frequency resolution	$\sigma_m = 2M_{res}\,\sigma_{FLL,min}(\tau)$ M_{res} the resonator's mass and $\sigma_{FLL,min}$ the frequency resolution	$\sigma_m = 2M_{res}\,\sigma_{LIA,min}(\tau)$ M_{res} the resonator's mass and $\sigma_{FLL,min}$ the frequency resolution
Open-loop Analysis	$H_{SOL-OL} = H_{res}\,H_{BP}H_{HP}G_{TIA}G_{lim}\,G_{PD}$	$H_{FLL\_OL}(s) = H_{res}^{ph}(s)H_{PLL}^{ph}(s)$	Open-Loop analysis not required
Convergence time (Single device)	Time to establish the oscillation (Fast)	VCO convergence time (Very Fast)	For an excellent resolution, the frequency step of the sweep must be very small . (Very Slow)
Implementation complexity	Amplifiers + Passive Filters	Requires a VCO , phase- detector, amplifier and passive filters	Requires an oscillator, amplifier and passive filters

Table 4.1: Comparative summary of different readout architectures that can be applied to the optomechanical sensors

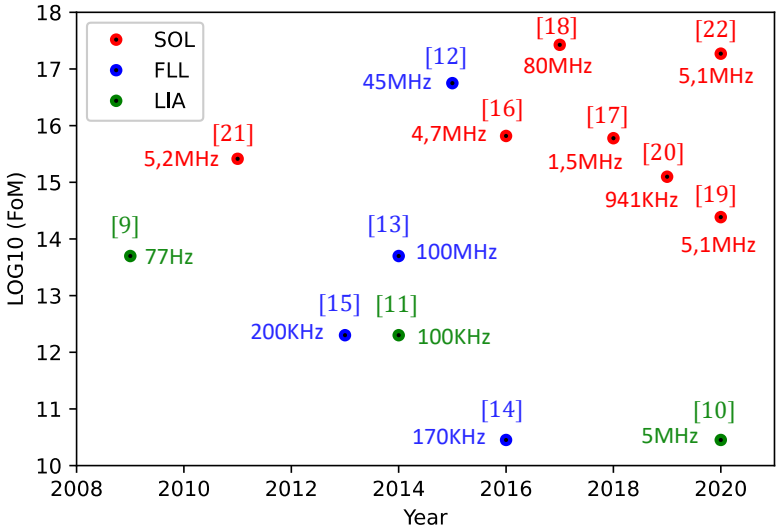

Figure 4.9: State of the art of readout architectures for a resonant sensor.

$$FoM = f_{res}[Hz] \cdot \frac{1}{\sigma_{archi}\tau[s]} \tag{4.35}$$

where $f_{res}$is the frequency of the resonator in Hz, σ_{archi} is the standard deviation of the architecture and τ is the convergence time in s. The FoM has been used to compare the state of the art of the resonant sensor architectures.

Figure 4.9 shows the comparison based on the FoM defined in equation (4.35) of the reading architectures used to read a single resonant sensor. To read low frequency resonators [9], [11], in the state of the art, the authors tend to design the LIA type architecture. This can be explained by the fact that the LIA has an excellent frequency resolution. In this frequency range, the convergence time is not a fundamental criterion. The authors prefer to read the resonance frequency with greater precision. At low frequencies, closed-loop architectures of the FLL type [14] and [15] can also be used.

For high-frequency resonators (10-100 MHz), the authors tend to choose closed-loop architectures such as FLL [12] or SOL [18]. In this frequency range, the authors prefer to design electronics that can read the resonator quickly (from µs to ms) at the expense of precision. Therefore, they concentrate on closed loop architectures such as FLL or SOL with a rather fast convergence time. For very high frequency resonators above 100 MHz, the preferred architecture in the state of the art is FLL architecture [13]. This choice of architecture is relevant because it is the architecture that presents the fastest convergence.

4.3.2 Matrix configuration

Chapter 3 present the matrix configuration chosen for the optomechanical resonators. As a reminder, this matrix is to be read sequentially column by column. The objective in this section is to choose, according to the comparisons already made, the appropriate architecture for reading such a matrix.

As our optomechanical matrix will be read sequentially, the first selection criteria is the convergence time. This corresponds to the time that the architecture takes to read a single optomechanical resonator. The higher this time is, the more consequent the total reading time of the matrix will be. From this point of view, we can already eliminate the LIA type architecture which presents the slowest convergence time for a given frequency stability.

Closed-loop architectures, thanks to their fast convergence time, are more suitable for reading such a matrix. However, an SOL architecture is complex to realize in the context of a matrix. Indeed, due to manufacturing dispersions, it is difficult to design an SOL electronics that can guarantee the same oscillation condition on all resonators of the matrix. A preliminary step to identify the resonance frequencies of the disks can solve this problem. This step will allow to pre-set the oscillation conditions of the electronics. However, for very large matrices this becomes fastidious. That is why, to read a matrix, we generally prefer to use an FLL type architecture. This architecture has a fast convergence time and is robust to parasitics.

4.4. AH-FLL architecture for optomechanical sensors

As previously discussed, to read our optomechanical resonators we have opted for a FLL based architecture. This type of architecture can have good frequency stability if we design a TIA, PFD and VCO with low phase noise. Generally, within a classical FLL, the frequency range is limited by the frequency of the VCO. However, the resonance frequencies of our resonators spread over a wide range of frequencies from 200 to 350 MHz depending on their dimensions. In this context, it could be interesting to develop a reading architecture compatible with a wide variety of resonance frequency without having to redesign a new architecture.

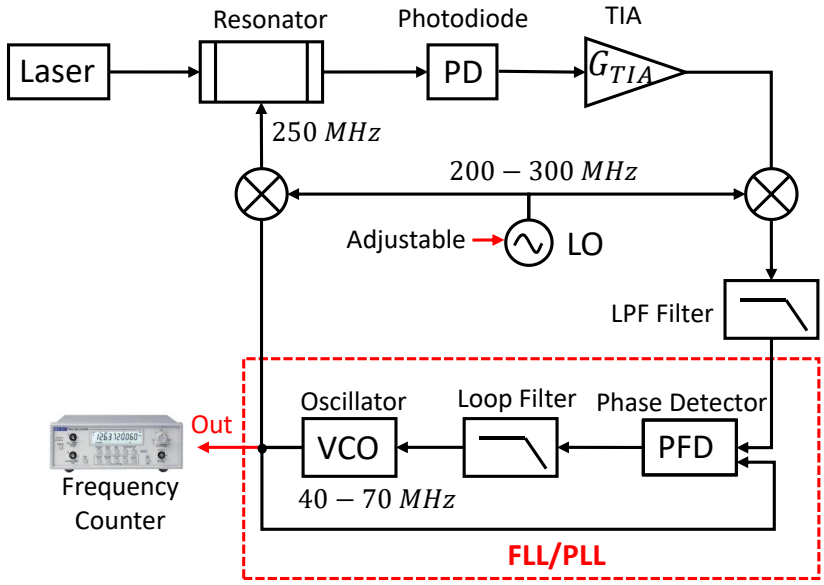

Figure 4.10: AH-FLL architecture for reading optomechanical resonators

For that purpose, we introduce for that the concept of AH-FLL for adjustable frequency locked loop, depicted on Figure 4.10. The principle is to downconvert the resonator signal to lower frequency values with the help of an auxiliary oscillator. The downconverted signal is tracked by the PLL and then upconverted close to the sensor resonance frequency using the same auxiliary oscillator. This configuration makes it possible to adjust the working frequency of the AH-FLL by changing the center frequency of the auxiliary oscillator only, without having to recalculate the stability of the PLL loop. Moreover, with the double mixing, the PLL block could work at a much lower frequency than in classical FLL loop which simplifies the realization of the PCB (track length, impedance matching,…).

The AH-FLL architecture contains a TIA, a down-conversion mixer, a local oscillator, a PLL module and an up-conversion mixer driven by the same local oscillator. The PLL module includes a PFD, a loop filter and a VCO. The VCO locks on the frequency at the output of the LPF. AH-FLL works in the same way as a classic FLL. This means that we exploit the phase shift between the resonator and a VCO. The heterodyne block (2 mixers with same adjustable oscillator) allows to have a low frequency signal in order that the PLL module locks. Once locked, the VCO signal is up mixed with the oscillator signal to drive the resonator. At the output of the mixer, the resonator receives the two components of the mixed signal. The image rejection is ensured by the high-quality factor provided by the resonator.

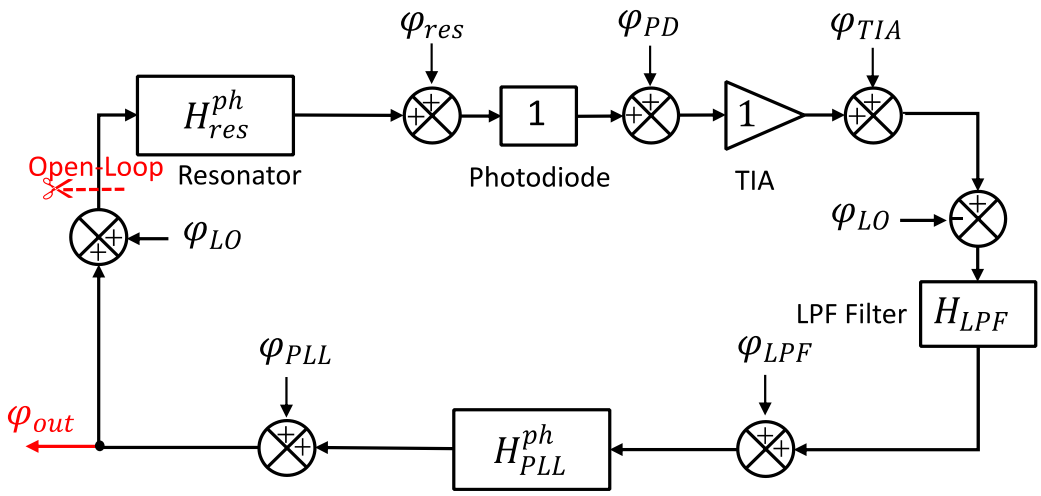

Figure 4.11: Phase noise model of the AH-FLL architecture to read the optomechanical resonator

4.4.1 Open-Loop Analysis

Figure 4.11 shows the linear time-invariant model of the AH-FLL in the phase domain. This model describes the transfer functions and phase noise of each of the blocks forming the AH-FLL. In terms of transfer function, the resonator corresponds to a 1st order filter. The photodiode and the transimpedance amplifier a unity gain. The LPF low-pass filter is of order greater than 2 to keep only the low frequency component. The open-loop transfer function is therefore written as follows :

$$H_{AH-FLL\_OL}(s) = H_{res}^{ph}(s)H_{LPF}(s)H_{PLL}^{ph}(s) \tag{4.36}$$

where H_{LPF} is the transfer function of the low-pass filter placed at the output of the mixer. H_{res}^{ph} and H_{PLL}^{ph} are respectively the transfer function of the resonator and the PLL as seen previously in section 4.1.2.1. Stability analysis of the AH-FLL defined in equation (4.36) can be reduced to the evaluation of the PLL stability. Indeed, in the phase domain, the transfer function of the resonator $H_{res}^{ph}(s)$ is a 1st order low pass. The cut-off frequency of the filter corresponds to the resonator frequency. Thus, the resonator introduces a pole at very high frequency which has no consequence on the stability. The same conclusion applies to the LPF low-pass filter placed at the output of the mixer which introduces a high frequency pole that has no effect on stability. Therefore equation (4.36) becomes (see Appendix E):

$$H_{AH-FLL\_OL}(s) = H_{PLL}^{ph}(s) \tag{4.37}$$

We will see in more detail the calculation of the stability equation (4.37) in the next chapter. This chapter will be dedicated to the design and testing of the readout circuit for the optomechanical sensor. This circuit is based on the AH-FLL architecture illustrated in Figure 4.10.

4.4.2 Phase noise Analysis

Referring to Figure 4.11, the output phase of the AH-FLL is expressed as follows :

$$\varphi_{out} = \frac{1}{H_d}\varphi_{PLL} + \frac{H_{PLL}^{ph}}{H_d}\varphi_{LPF} + \frac{H_k}{H_d}\varphi_{LO} + \frac{H_i}{H_d}\varphi_i \tag{4.38}$$

where, $H_d = 1 - H_{res}^{ph} H_{LPF} H_{PLL}^{ph}$ and $H_k = H_{LPF} H_{PLL}^{ph}(H_{res}^{ph} - 1)$ and $H_i = H_{LPF} H_{PLL}^{ph}$. The phase $\varphi_i = \varphi_{TIA} + \varphi_{PD} + \varphi_{res}$. We can calculate, from the output phase φ_{out}, the phase noise of the AH-FLL architecture. For this it is sufficient to calculate the spectral density of noise which is written as follows (see Appendix E) :

$$S_{\varphi_{out}} = \left|\frac{1}{H_d}\right|^2 S_{\varphi_{PLL}} + \left|\frac{H_{PLL}^{ph}}{H_d}\right|^2 S_{\varphi_{LPF}} + \left|\frac{H_k}{H_d}\right|^2 S_{\varphi_{LO}} + \left|\frac{H_i}{H_d}\right|^2 S_{\varphi_i} \tag{4.39}$$

According to equation (4.39), the overall phase noise of the AH-FLL architecture depends on the phase noise of all the components that compose it. The transimpedance amplifier, the photodiode and the filters generally have a lower phase noise than the oscillators. When designing the circuit, we must pay attention to the intrinsic phase noise of each block in order to minimize the overall AH-FLL phase noise.

4.4.3 Allan Deviation and AH-FLL specification

To evaluate the frequency stability of the AH-FLL architecture in a relevant way we calculate the Allan variance defined in section 4.1.1.3. We inject the spectral density equation (4.39) to the definition of the AVAR equation (4.7). In a simplified way, the Allan variance of the AH-FLL architecture is thus expressed as follows (see Appendix E):

$$\sigma_{AH-FLL}^2(\tau) = \sigma_{elec}^2(\tau) + \sigma_{res}^2(\tau) + \sigma_{PD}^2(\tau) \tag{4.40}$$

with,

$$\sigma_{elec}^2(\tau) = \sigma_{PLL}^2(\tau) + \sigma_{LPF}^2(\tau) + \sigma_{LO}^2(\tau) + \sigma_{TIA}^2(\tau) \tag{4.41}$$

where the AVAR of the resonator and photodiode are respectively noted $\sigma_{res}^2(\tau)$ and $\sigma_{PD}^2(\tau)$. $\sigma_{elec}^2(\tau)$ is the Allan variance of the electronics (PLL block, transimpedance amplifier, low-pass filter, and local oscillator). A properly designed AH-FLL architecture should not degrade the frequency stability $\sigma_{res}^2(\tau)$ of the resonator. Therefore, we must respect the condition:

$$\sigma_{elec}^2(\tau) + \sigma_{PD}^2(\tau) \leq \sigma_{res}^2(\tau) \tag{4.42}$$

To satisfy the condition equation (4.42), we must first know the frequency stability of our optomechanical resonator. Figure 4.12.a shows the measurement result in air of the Allan deviation for an optomechanical disk resonator.

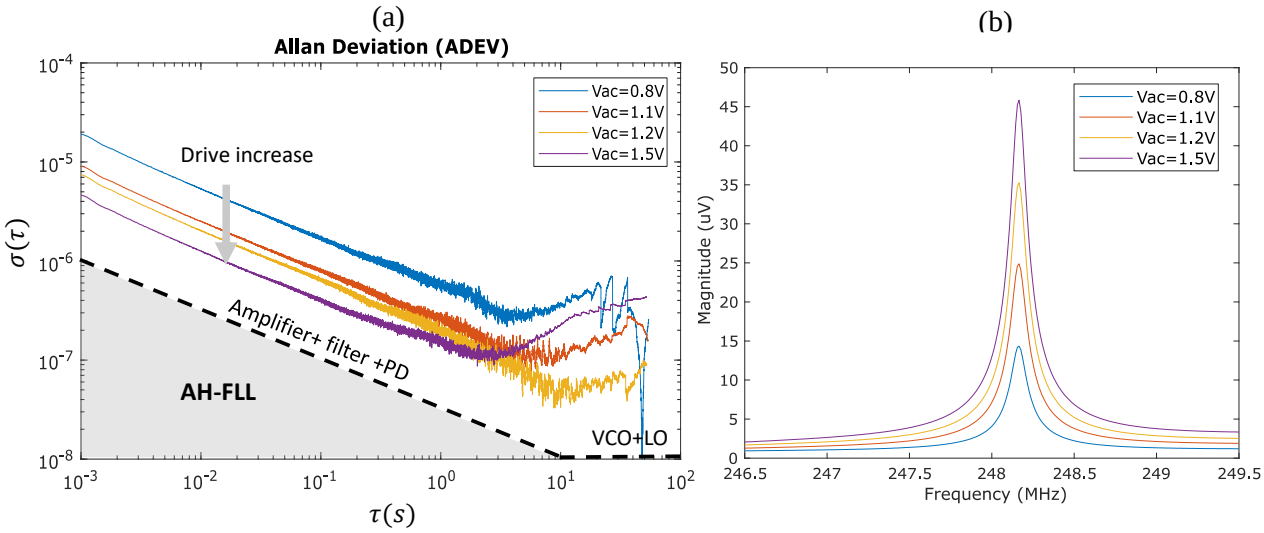

Figure 4.12: (a) Allan deviation measurement of an optomechanical resonator for different drive voltages (b) Measurement of the mechanical signal for different drive voltages.

Based on Figure 4.12.a, for a drive of 1.2 V, the frequency resolution of the optomechanical resonator $\sigma_{res_{min}} = 10^{-7}$ (100 ppb). To fully exploit the intrinsic frequency stability of the resonator it is necessary to specify the AH-FLL electronics in a way that does not exceed 100 ppb. To respect this resolution, we propose the specification illustrated in the gray area of Figure 4.12.a. For an integration time greater than 10s, the phase noise of the AH-FLL is limited by the phase noise of the oscillators. In the specification we therefore impose that $\sigma_{VCO} < 10^{-8}$ and $\sigma_{LO} < 10^{-8}$. This condition is not restrictive. There are many commercial oscillators with stability below 10 ppb, such as the oscillator from Crystek.

For an integration time of less than 10s, the AH-FLL phase noise is limited by the noise of the transimpedance amplifier, the photodiode, and the filters. In this regime the white phase noise dominates, the Allan deviation of the AH-FLL becomes [23]:

$$\sigma_{AH-FLL}(\tau) \cong \frac{1}{2Q}\frac{N_v}{S_{max}}\sqrt{\frac{1}{2\pi\tau}} \tag{4.43}$$

where, τ and Q are respectively the integration time and mechanical quality factor of the resonator. N_v is the noise spectral density in $V/\sqrt{Hz}$ and S_{max} is the maximum amplitude of the mechanical signal expressed in V. To respect our specification, we consider that $\sigma_{AH-FLL}(10^{-3}) = 10^{-6}$. For a resonator driven at 1.2 V, if we observe Figure 4.12.b, the maximum amplitude and the quality factor are respectively $S_{max} = 35\ \mu V$ and Q=2600.

By injecting these numerical values into equation (4.43), we obtain $N_v \approx 14\ nV/\sqrt{Hz}$. When designing the electronics, the noise level of the amplifiers, photodiode and filters must be less than N_v. This specification is not restrictive, if we consider the realization of passive filters. The noise of the photodiode and transimpedance amplifier must also be less than $14\ nV/\sqrt{Hz}$.

4.5 Conclusion

In this chapter we have presented the different architectures that can be applied to the reading of our optomechanical resonator. There are two types of architecture. The open-loop architectures (LIA) which only allow to read the frequency of the resonator. The closed-loop architectures (SOL and FLL) which allow both the reading and the excitation of the resonator. In the first part, for each architecture we have studied a theoretical analysis of phase noise, mass resolution and loop stability.

In the second part, we have summarized in a table all the essential information to know about each of the architectures. In this table we have reminded the operating principle, as well as all the theoretical analyses developed in the previous part. To improve the comparison, we have added the convergence time criterion and the implementation complexity. We have introduced a Figure of Merit (FoM) allowing us to compare the architectures between them. And based on this FoM, we have realized a state-of-the-art of architectures allowing to read resonant sensors. According to this analysis, for low-frequency resonators we noticed that the authors tended to design an LIA architecture. While for high-frequency resonators, they tended to realize a closed-loop architecture of type SOL or FLL especially because of their fast convergence time. In the context of a matrix of high frequency resonators, it is preferable to use an FLL architecture. The latter is more robust and converges faster than the SOL architecture.

To read our optomechanical resonator, we naturally chose an FLL-based architecture. In an FLL architecture, the frequency range is limited by the VCO. However, our optomechanical resonators do not have the same resonance frequency (between 200 and 300 MHz), depending on their dimensions. To be able to read all of our resonators, we introduce the AH-FLL architecture. The idea is to increase the frequency range by mixing with an adjustable local oscillator. This allows us to adjust the frequency range according to the resonator to be read. Thus, we avoid changing the VCO and the stability calculation of the FLL loop remains valid. Before starting the circuit design, we specify the different blocks that compose the AH-FLL. In order to exploit the frequency resolution of our sensor, the local oscillator and the VCO must have a stability of 10 ppb. The amplifiers, photodiode and filters must have a noise floor below $14\ nV/\sqrt{Hz}$.

References

[1] V. Singh, « Discussion on Barkhausen and Nyquist stability criteria », Analog Integr Circ Sig Process, vol. 62, no 3, p. 327-332, mars 2010, doi: 10.1007/s10470-009-9360-4.

[2] P. Wardkien et K. Kittipute, « Discussion on The Physic of The Barkhausen Criteria Based on The Second Order Differential Equation », in 2019 7th International Electrical Engineering Congress (iEECON), mars 2019, p. 1-4. doi: 10.1109/iEECON45304.2019.8938934.

[3] E. Rubiola, Phase Noise and Frequency Stability in Oscillators. Cambridge: Cambridge University Press, 2008. doi: 10.1017/CBO9780511812798.

[4] J. Gronicz, L. Aaltonen, N. Chekurov, M. Kosunen, et K. Halonen, « A 1.8 MHz MEMS-based oscillator with synchronous amplitude limiter », in 2013 European Conference on Circuit Theory and Design (ECCTD), sept. 2013, p. 1-4. doi: 10.1109/ECCTD.2013.6662225.

[5] G. Gourlat, "Conception de circuit intégré pour les applications gravimétriques basées sur l'utilisation de résonateurs mécaniques arrangés en réseau," These de doctorat, Université Grenoble Alpes (ComUE), 2017.

[6] D. B. Leeson, "A simple model of feedback oscillator noise spectrum," Proceedings of the IEEE, vol. 54, no. 2, pp. 329–330, Feb. 1966, doi: 10.1109/PROC.1966.4682.

[7] M. Sansa et al., « Optomechanical mass spectrometry », Nat Commun, vol. 11, no 1, Art. no 1, juill. 2020, doi: 10.1038/s41467-020-17592-9.

[8] G. B. Lee, P. K. Chan, et L. Siek, « A CMOS phase frequency detector for charge pump phase-locked loop », in 42nd Midwest Symposium on Circuits and Systems (Cat. No.99CH36356), août 1999, vol. 2, p. 601-604 vol. 2. doi: 10.1109/MWSCAS.1999.867710.

[9] A. D'Amico and al., « Low-voltage low-power integrated analog lock-in amplifier for gas sensor applications », Sens. Actuators B Chem., vol. 144, no 2, p. 400-406, févr. 2010, doi: 10.1016/j.snb.2009.01.045.

[10] A. A. Zope, J.-H. Chang, T.-Y. Liu, and S.-S. Li, « A CMOS-MEMS Thermal-Piezoresistive Oscillator for Mass Sensing Applications », IEEE Trans. Electron Devices, vol. 67, no 3, p. 1183-1191, mars 2020, doi: 10.1109/TED.2020.2969967.

[11] G. Gervasoni and al., « A 12-channel dual-lock-in platform for magneto-resistive DNA detection with ppm resolution », in 2014 IEEE Biomedical Circuits and Systems Conference (BioCAS) Proceedings, oct. 2014, p. 316-319. doi: 10.1109/BioCAS.2014.6981726.

[12] N. Delorme and al., « 16.5 A NEMS-array control IC for sub-attogram gravimetric sensing applications in 28nm CMOS technology », in 2015 IEEE International Solid-State Circuits Conference - (ISSCC) Digest of Technical Papers, févr. 2015, p. 1-3. doi: 10.1109/ISSCC.2015.7063044.

[13] J. Arcamone and al., « VHF NEMS-CMOS piezoresistive resonators for advanced sensing applications », Nanotechnology, vol. 25, no 43, p. 435501, oct. 2014, doi: 10.1088/0957-4484/25/43/435501.

[14] Y.-K. Liao, C.-H. Chiang, and M. S.-C. Lu, « Automated Resonance Matching for CMOS MEMS Micro-Resonators », IEEE Sens. J., vol. 16, no 21, p. 7685-7692, nov. 2016, doi: 10.1109/JSEN.2016.2605663.

[15] G.-C. Wei and M. S.-C. Lu, « A CMOS MEMS capacitive resonant sensor array utilizing a PLL-based oscillator loop », in 2013 Transducers Eurosensors XXVII: The 17th International Conference on Solid-State Sensors, Actuators and Microsystems (TRANSDUCERS EUROSENSORS XXVII), juin 2013, p. 82-85. doi: 10.1109/Transducers.2013.6626706.

[16] E.-C. Chang, C.-C. Chen, and S.-S. Li, « Real-time mass sensing and dynamic impact monitoring of printed pico-liter droplets realized by a thermal-piezoresistive self-sustained oscillator », in 2016 IEEE 29th International Conference on Micro Electro Mechanical Systems (MEMS), janv. 2016, p. 1078-1081. doi: 10.1109/MEMSYS.2016.7421821.

[17] C.-C. Chu, S. Dey, T.-Y. Liu, C.-C. Chen, and S.-S. Li, « Thermal-Piezoresistive SOI-MEMS Oscillators Based on a Fully Differential Mechanically Coupled Resonator Array for Mass Sensing Applications », J. Microelectromechanical Syst., vol. 27, no 1, p. 59-72, févr. 2018, doi: 10.1109/JMEMS.2017.2778307.

[18] G. Gourlat and al., « A 30-to-80MHz simultaneous dual-mode heterodyne oscillator targeting NEMS array gravimetric sensing applications with a 300zg mass resolution », in 2017 IEEE International Solid- State Circuits Conference - (ISSCC), San Francisco, United States, févr. 2017, p. 266-267.

[19] A. A. Zope, J.-H. Chang, T.-Y. Liu, and S.-S. Li, « A CMOS-MEMS Thermal-Piezoresistive Oscillator for Mass Sensing Applications », IEEE Trans. Electron Devices, vol. 67, no 3, p. 1183-1191, mars 2020, doi: 10.1109/TED.2020.2969967.

[20] C.-A. Sung, T.-Y. Liu, A. A. Zope, M.-H. Li, and S.-S. Li, « Interface Circuit Design to Enable Miniaturization of Thermal-Piezoresistive Oscillators for Mass Sensing Applications », in 2019 IEEE 32nd International Conference on Micro Electro Mechanical Systems (MEMS), janv. 2019, p. 899-902. doi: 10.1109/MEMSYS.2019.8870785.

[21] M. Konno and al. « Novel MEMS oscillator using in-plane disk resonator with sensing platform and its mass sensing characteristics », in 2011 16th International Solid-State Sensors, Actuators and Microsystems Conference, juin 2011, p. 518-521. doi: 10.1109/TRANSDUCERS.2011.5969670.

[22] C.-H. Weng, G. Pillai, and S.-S. Li, « A Thin-Film Piezoelectric-on-Silicon MEMS Oscillator for Mass Sensing Applications », IEEE Sens. J., vol. 20, no 13, p. 7001-7009, juill. 2020, doi: 10.1109/JSEN.2020.2979283.

[23] M. Sansa et al., « Frequency fluctuations in silicon nanoresonators », Nature Nanotech, vol. 11, no 6, Art. no 6, juin 2016, doi: 10.1038/nnano.2016.19.

Chapter 5

Practical realization and experimental validation

Contents

In this chapter we will see the practical implementation of an AH-FLL using discrete components off-the-shelf (COTS) for optomechanical sensor readout. First, we will present the AH-FLL complete architecture. Then we validate this architecture by stability studies and electrical simulations. In the second part, we illustrate the design steps of the PCB. We explain the different constraints of design including the adaptation of transmission lines. In the third part we present the debug and functionality test of the circuit board. And in the last part, the demonstration of the circuit with an optomechanical sensor. During this demonstration we have succeeded in reading and in self-actuating the optomechanical disk with our circuit. In terms of performance the system (sensor + circuit) reaches a resolution of 500 ppb.

5.1. Circuit design and simulation results

In the previous chapter, we have presented a state of the art of architectures that can be applied to the reading of optomechanical resonator arrays for mass detection. As a reminder, we identified two types of architectures: closed-loop and open-loop. In the closed loop architectures (self-oscillating loop [1]-[3] or phase locked loop [4]-[6]), the idea is to read the resonator and then reinject the reading signal to stimulate the mechanical resonance. For open loop architectures (lock-in-amplifier [7]-[8]), the electronics is only used for the reading. It is necessary to provide separate excitation electronics to adequately drive the resonance.

For the reading of our optomechanical resonators, we have chosen an architecture based on FLL. Indeed, this architecture presents a low phase noise if we choose a stable VCO and a very fast convergence time which is very useful in the perspective of optomechanical resonator array. And, once locked, as a feedback system, the loop is robust to disturbances. Due to the high resonance frequencies of the optomechanical sensors and to ease the design of the PCB, the Adjustable Heterodyne Frequency Locked Loop (AH-FLL) architecture has been introduced. The idea is to work at low frequency using a heterodyne frequency conversion.

In this section, we will present the complete AH-FLL architecture. We will describe the different blocks that compose the architecture. Then the design steps, the choice of the components, the stability analysis of the loop are detailed. Finally, the simulation results and the expected theoretical performances in terms of phase noise are presented.

5.1.1 Presentation of the AH-FLL complete architecture

Figure 5.1 below shows the architecture of the circuit for reading optomechanical sensors. The circuit is composed of multiple modules: an input module, a heterodyne module, a PLL module and a drive module. The principle of operation is as follows. As seen in chapter 2, the optomechanical sensor modulates an optical power with its mechanical resonance. So at the input of the circuit, we have an optical power modulated at the frequency $f_m$of the resonator.

The input module transforms this optical power into a voltage that can be used by the heterodyne module. The heterodyne module allows to lower the signal frequency in order to address the PLL. When the PLL is locked, at the output of the VCO, frequency is read. Using this frequency and the sensitivity of the resonator, we can estimate the mass on the resonator. The Drive module allows us to reinject the signal that was previously mixed to stimulate the mechanical resonance of the disk. We will explain the different modules in more detail.

5.1.1.1 Input Module

The input module allows the conversion of optical power into voltage. It is composed of a photodiode, a transimpedance amplifier (TIA), a high pass filter and a second amplifier. The photodiode chosen is the FCI-InGaAs-120L-FC with a fiber optic type connector. It has a peak responsivity of $0.95\,A/W$ at $1550\,nm$. The noise equivalent power (NEP) noise is $4.50\,fW/\sqrt{Hz}$.

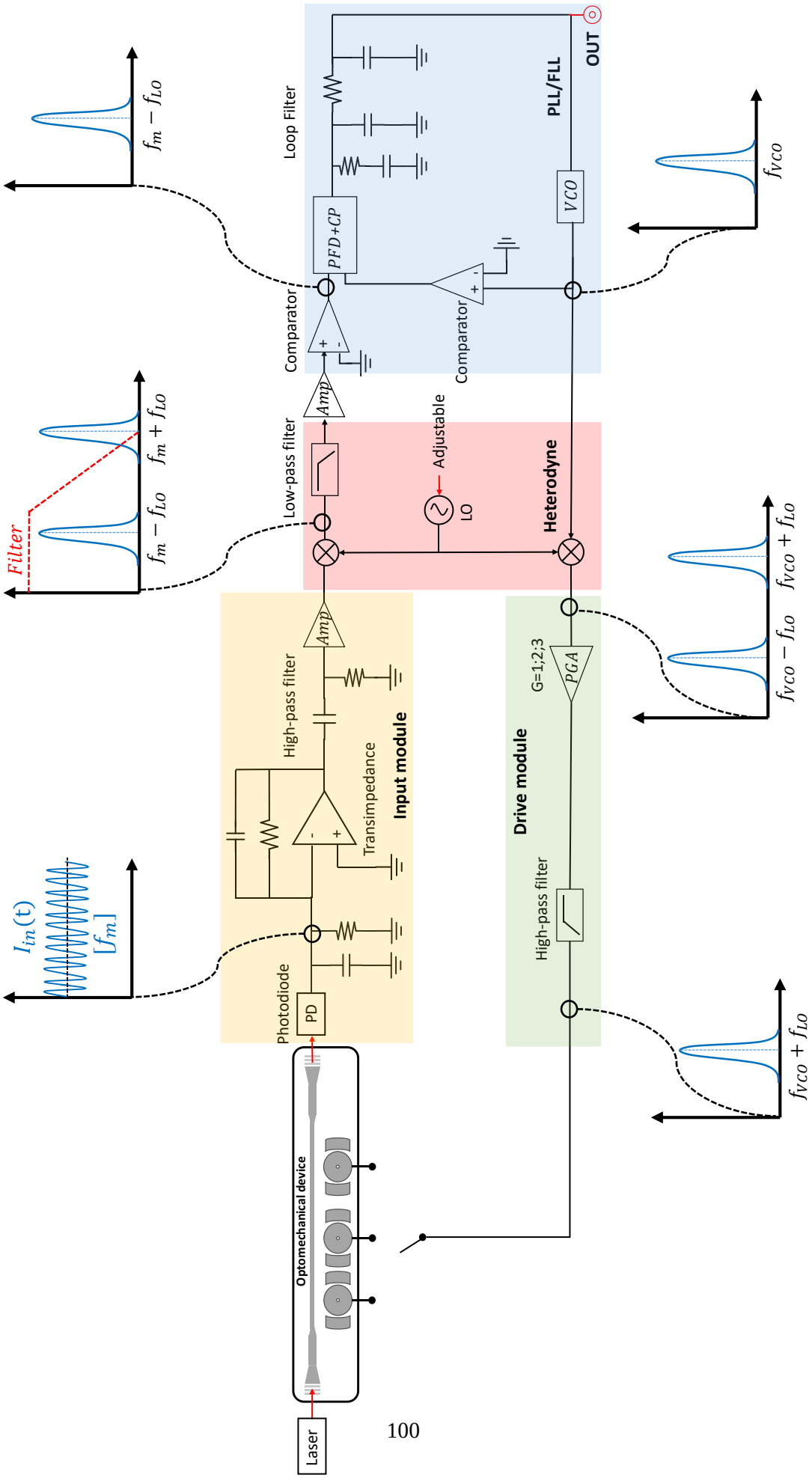

Figure 5.1: Complete AH-FLL circuit for reading optomechanical sensors

The transimpedance amplifier converts the current from the photodiode into voltage. It is a resistive feedback TIA based on the OPA2846 with a gain of about 50 dBOhms. Then we have a high pass filter to eliminate the DC component. A second amplifier is necessary because the signal level is too low ($\sim 2\ nV/\sqrt{Hz}$).

5.1.1.2 Heterodyne Module

The heterodyne module is used to down convert the signal to lower frequencies. With the help of a passive RF mixer, here the ADE-1+ we mix our f_m frequency signal at the output of the input module with a signal from an oscillator. We choose here as local oscillator, the voltage-controlled oscillator CVCO55CL-0150-0200 from Crystek [9]. Once mixed we have the low frequency $(f_m - f_{LO})$ and high frequency $(f_m + f_{LO})$ components. Efficient filtering is required to remove the higher frequency from the image. For this purpose, we have implemented a low-pass filter of order 4.

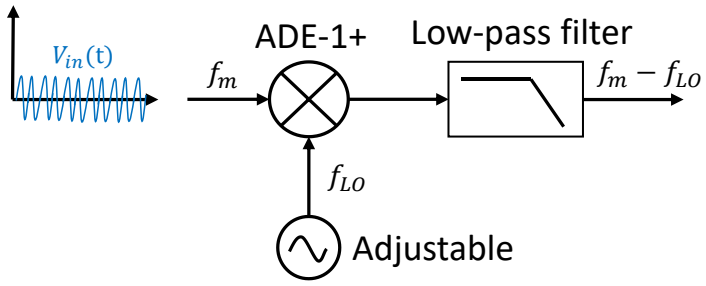

Figure 5.2: Operating principle of the heterodyne module

5.1.1.3 PLL/FLL Module

The PLL module is the most important module of the architecture presented in Figure 5.1. It is composed of two comparators, a phase frequency detector (PFD), a charge pump, a loop filter and a VCO. The operating principle is as follows. At the input, the PFD compares the frequency and phase of the signals from the heterodyne module (reference) and the VCO. As long as the two signals do not have the same frequency and phase, the PFD generates a voltage that drives the switches of the charge pump as illustrated in figure 5.3. Depending on the up or down configuration, the charge pump current drives the loop filter and changes the VCO frequency to reduce the phase error at PFD inputs. When the PLL converges, the phase difference at the PFD inputs is zero, resulting in equal frequencies of the VCO and the PLL reference input.

The LTC6752 comparators are used here to convert the sinusoidal outputs of the VCO and the reference into square signals with steep edges. The HMC1031 from Analog Device [10] is composed of a PFD and a charge pump and operates up to 140 MHz. It also has a charge pump current of about 50 µA. The loop filter chosen here is a 3rd order filter, which allows better filtering of the PFD spurious tones at reference frequency. And finally, a VCO here the CVCO55CL-0045-0070 from Crystek [11]. This VCO operates between 40 to 70 MHz and has a very low phase noise $-95\ dBc/Hz$ at 1 Hz and $-136\ dBc/Hz$ at 100 KHz.

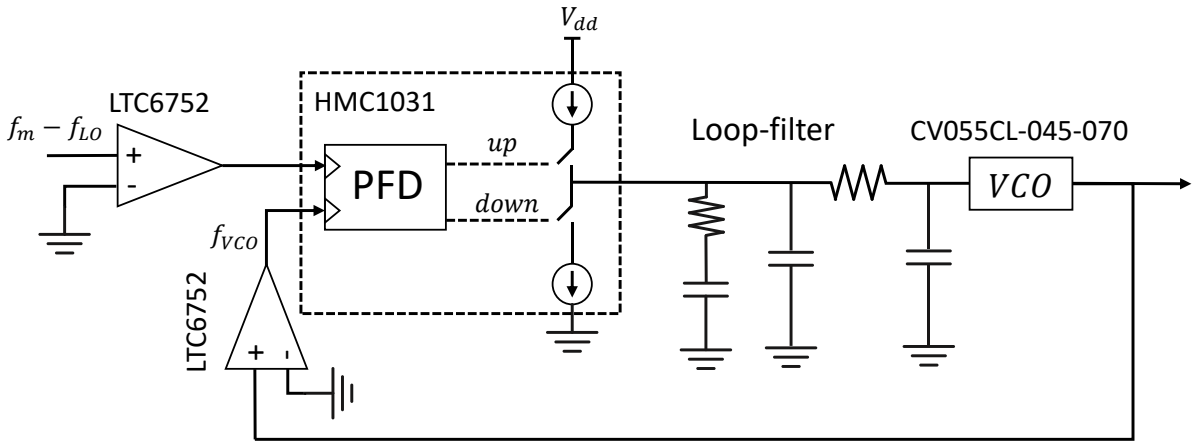

Figure 5.3: Operating principle of the PLL module

5.1.1.4 Drive Module

The last module is the drive module which allows to feed-back the measured signal in order to stimulate optomechanical disks. For this purpose, the VCO signal is up-mixed with the signal of the adjustable oscillator. A high-pass filter is used to filter out the low frequency image at the up-mixer output.

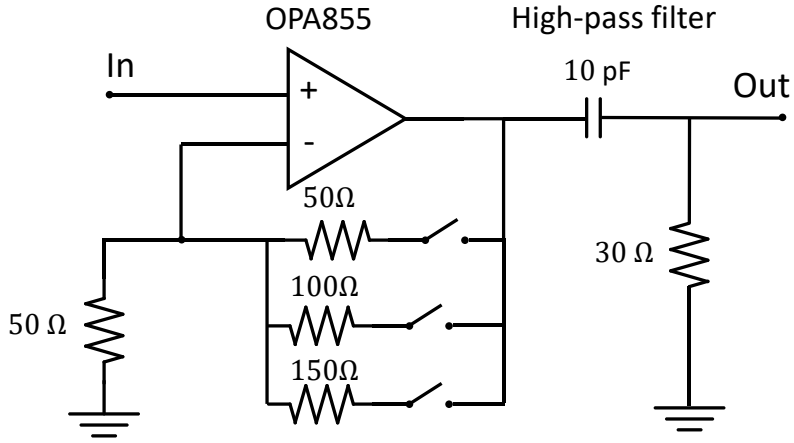

Figure 5.4: Complete schematic of the drive module (PGA + High-pass filter)

The addition of this filter is optional because the resonator behaves like a band-pass around its excitation frequency. By default, it removes the low-frequency component. We have added a programmable gain amplifier (PGA) to give us the possibility to amplify the signal before driving the disks. Here we are working with OPA855 amplifier from Texas Instrument [12] with a gain bandwidth product of 8 GHz. As shown in Figure 5.4, the PGA can have a gain G=1; 2; 3.

5.1.2 AH-FLL loop stability analysis

To design the circuit in Figure 5.1, we need to ensure that the AH-FLL architecture is stable in the phase domain so that the loop can converge. As seen in chapiter 4, the stability study of the AH-FLL architecture can be boiled down to the stability study of the PLL module. With respect to the components chosen in the previous section, we propose here to estimate the stability of the circuit to be designed.

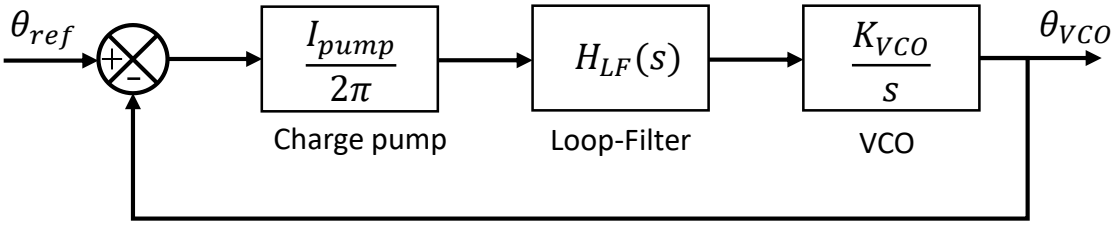

Figure 5.5: PLL block diagram with transfer functions of charge pump, loop filter and VCO

To study the stability of PLL, it is necessary to calculate the open loop transfer function and determine the phase margin. Figure 5.5 above shows a block diagram with the transfer functions of the charge pump, the loop filter and the VCO. For the PLL to be stable, the open-loop transfer function must be written as (see chapiter 4):

$$H_{AH-FLL,OL}(s) = H_{PLL,OL}(s) = \frac{I_{pump}}{2\pi}\frac{K_{VCO}}{s}H_{LF}(s) \tag{5.1}$$

where I_{pump} is the current of the charge pump (50 µA), K_{VCO} is the VCO gain (4 MHz/V) and $H_{LF}(s)$ the transfer of the loop-filter. This filter can be of order 2 or order 3 according to the configurations presented in Figure 5.6. The transfer functions $H_{LF_{2nd}}(s)$ for the second order filter and $H_{LF_{3rd}}(s)$for the third order filter are expressed as follows:

$$H_{LF_{2nd}}(s) = \frac{1}{C_0 + C_1}\frac{1 + R_1C_0}{s\left(1 + R_1\frac{C_0C_1}{C_0 + C_1}s\right)} \text{ and } H_{LF_{3rd}}(s) = \frac{1}{C_0 + C_1}\frac{1}{1 + R_2C_2s}\frac{1 + R_1C_0}{s\left(1 + R_1\frac{C_0C_1}{C_0 + C_1}s\right)} \tag{5.2}$$

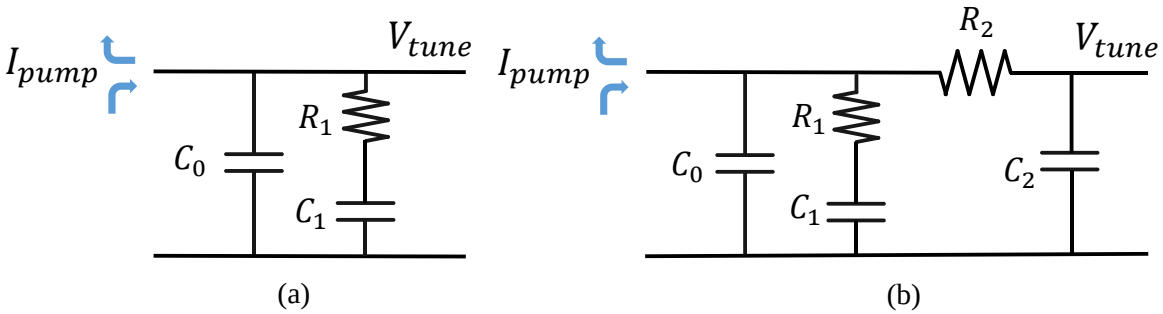

(a) (b)

Figure 5.6: PLL Loop-filter configuration (a) second order filter (b) third order filter

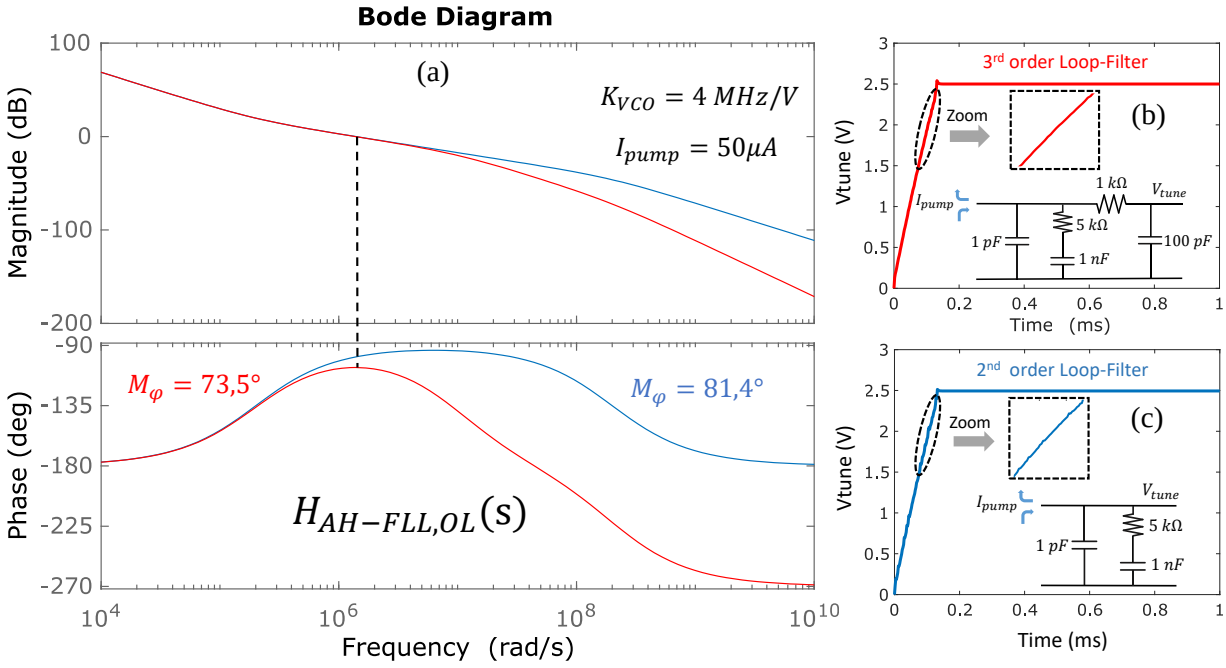

Figure 5.7: (a) Bode diagram of the $H_{AH-FLL,OL}(s)$ transfer function defined in equation (5.1) for a second and third order filters. (b) Simulation of the VCO control voltage for the case of an 3^{rd} order filter (b) Simulation of the VCO control voltage for the case of an 2^{nd} order filter.

Figure 5.7.a shows the bode diagram of the $H_{AH-FLL,OL}(s)$ transfer function defined in equation (5.1) for the two loop-filter configurations. In both cases the system is stable with a phase margin of $M_\varphi = 81{,}4°$ for the second order filter and a phase margin of $M_\varphi = 73{,}5°$ for the third order filter.

Figures 5.7.b and 5.7.c illustrate the transient simulation of the VCO control voltage for the two filter configurations. We can observe a ripple on the VCO control voltage at a frequency equal to the PFD reference frequency coming from the downconverter mixer. It is due to the mismatch of the charge pump current sources which is responsible for the injection of noise at the harmonics of the reference frequency. We observe that the third-order filter provides better filtering of the high frequency components. As a result, the PLL output, here the VCO frequency has a better stability. There is therefore a trade-off between PLL stability and PLL output noise that is linked to the frequency resolution and thus the mass resolution of the sensor. As presented in Section 5.1.1.3, in the AH-FLL circuit we consider a third-order loop filter. It is possible to increase the order of the filter to have better frequency resolution, but this will be at the expense of stability (phase margin degradation).

5.1.3 Transient Simulation Results

Before starting the design of the PCB, it is necessary to be sure that the AH-FLL architecture is stable and converges well in transient simulation. In the Virtuoso Cadence environment, we have at our disposition a complete model of the optomechanical sensor that can simulate a mass deposition in transient regime, see chapter 2 for more details. The idea here is to simulate the whole system (sensor + reading electronics). To do this, we used the SPICE models of the

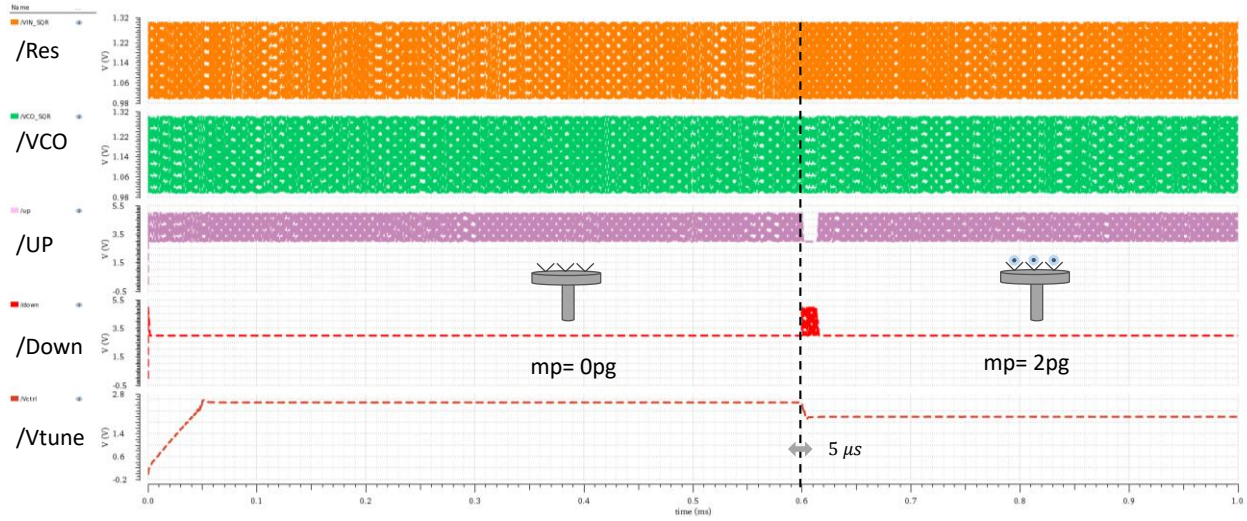

Figure 5.8: Transient simulation of the AH-FLL architecture when simulating a 2 pg mass deposition on the Verilog A model of the optomechanical sensor.

amplifiers extracted from the manufacturer's website. For all the other components for which manufacturer models don't exist, we use generic Verilog A models, e.g., for mixers, comparators, PFD + charge pump and VCO already existing in the Cadence Analog library. AH-FLL stability has been verified through transient simulation. First by verifying the AH-FLL locking process at power on and second by simulating a mass deposition.

Figure 5.8 above represents the results of simulations when a mass of 2 pg is deposited. In this figure the output of the optomechanical resonator, the output of the VCO, the up and down outputs of the charge pump and the tuning voltage V_{tune} of the VCO are represented. Between 0 and 600 µs, no mass is deposited, the resonator resonates at over 250 MHz. As shown in Figure 5.8, the voltage of the VCO converges at 2.5 V, which corresponds to 50 MHz. This is coherent since we have mixed the signal of the resonator with an oscillator at 200 MHz. The convergence time here is about 50 µs.

At 600 µs we simulate a deposit of 2 pg of mass on the resonator. Consequently, the frequency of the sensor changes from 250 to 248 MHz and the PLL loop adapts the V_{tune} voltage in order that the VCO converges to 48 MHz. The convergence time is very fast, about 5 µs. This simulation confirms that the choice of components is adequate, and that the stability calculation presented in section 5.1.2 is correct.

5.1.4 Application of the theory to the proposed design

In this part, we will check whether the components that we have chosen to design the AH-FLL circuit are consistent with the specification done in chapter 4 section 4.4.3. As a reminder, this specification was to get an ADEV of 10^{-8} at 0.1s.

In chapiter 4, we saw that the most important contributor to the phase noise was the VCO of the PLL. The local oscillator allowing the heterodyne does not contribute since the noise introduced during down-mixing is canceled during up-mixing. The amplifiers, the photodiode and the PFD also contribute but in a lesser extent [13].

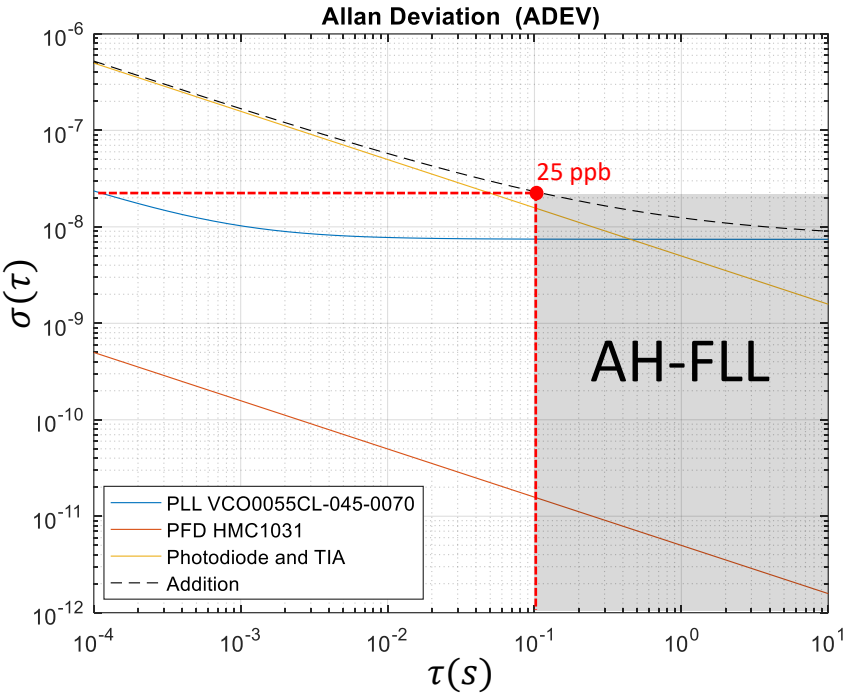

Figure 5.9: Theoretical prediction of the different noise sources of the AH-FLL architecture.

Figure 5.9 shows the theoretically calculated Allan deviation from the phase noise given in the component data sheet. For an integration time of less than 1 s the dominant phase noise is the noise of the photodiode and the TIA. Beyond 1 s it is the phase noise of the VCO.

For an integration time of 0.1 s, with the chosen elements we obtain an ADEV of 25 ppb. This is slightly above the 10 ppb value expected in the specification. Mainly because of our choice of photodiode (FCI-InGaAs-120L-FC) and TIA to amplify the weak signal at the output of the resonator.

5.2. AH-FLL PCB design schematic and Layout

In the previous section, we have validated the implementation of the AH-FLL through simulations. First, we performed stability simulations to guarantee the stability of the architecture to be designed. Then, transient simulations using the optomechanical sensor model developed in chapter 2. This section is dedicated to the development of a PCB including all the functionalities of the architecture as presented in Figure 5.1.

5.2.1 Schematic view of the AH-FLL circuit

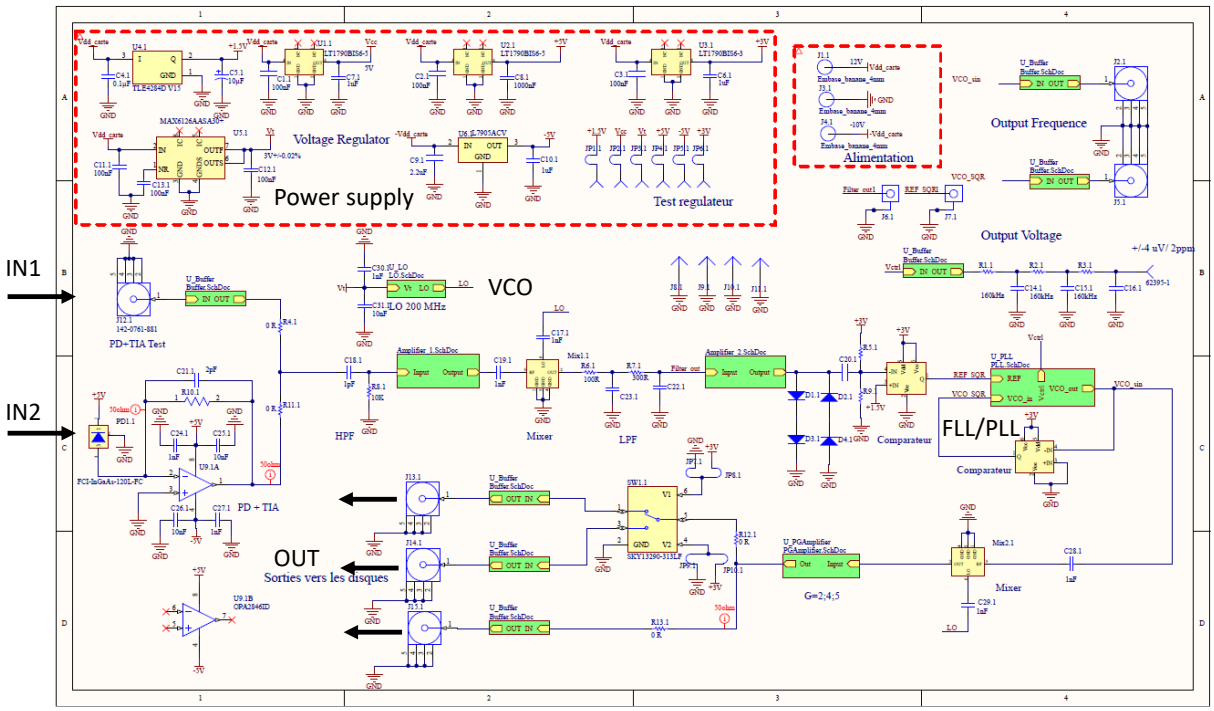

Figure 5.10: Altium schematic view of the AH-FLL circuit for reading optomechanical sensors.

Figure 5.10 shows the complete schematic of the AH-FLL circuit. The board integrates a photodiode and a TIA to ensure compatibility with the optical output of the optomechanical sensor. The board also incorporates an electrical input that bypasses the photodiode and TIA for debugging purposes. In terms of outputs, we have provided, as shown in Figure 5.1, three outputs with SMA connectors. A first output allows the reading of a single optomechanical resonator. Two other outputs, which can be selected using switches, have been implemented to demonstrate the ability of AH-FLL to sequentially reading of matrix of optomechanical sensors. Particular attention has been paid to reduce noise coupling, for example by implementing dedicated power supplies for the different oscillators using linear voltage regulators.

5.2.2 Presentation of the PCB board

Figure 5.11 shows the pictures of the board for reading of the optomechanical sensors. In terms of dimensions the board is 15 cm long with a width of 11.5 cm. In the board we can see the two input channels IN1 and IN2 and the three output channels (Out1, Out2 and Out3) for

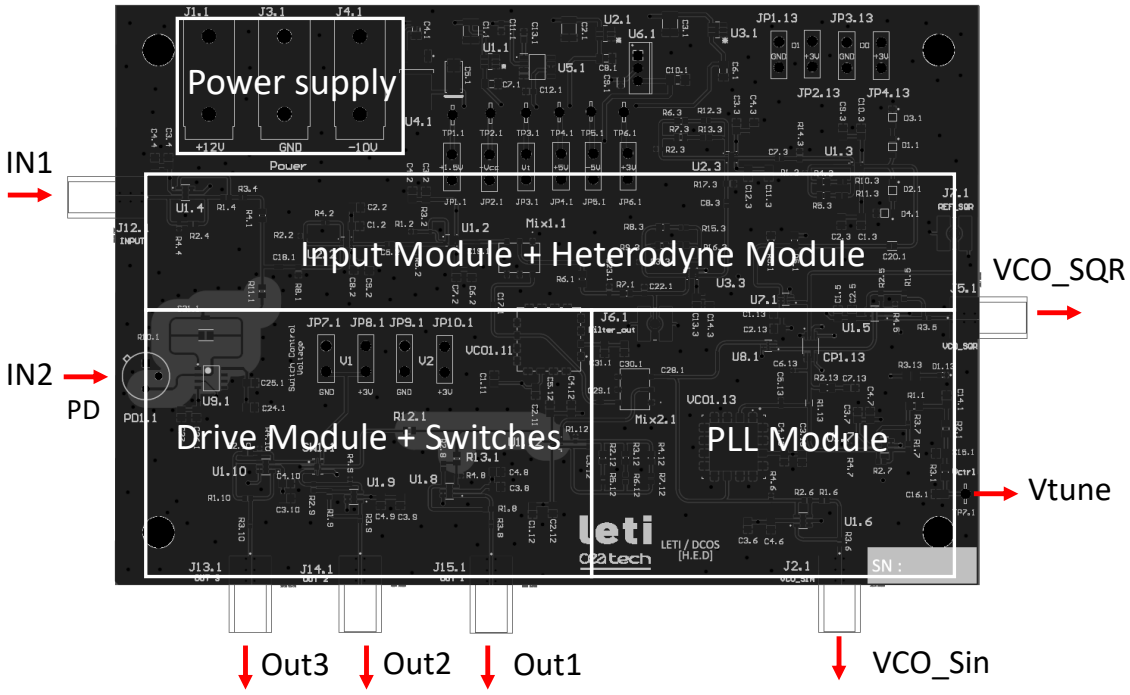

Figure 5.11: Presentation of the PCB board corresponding to the AH-FLL architecture.

driving the optomechanical disks. To facilitate the tests, there are also test points such as the input and output of the VCO (Vtune, and VCO_SQR or VCO_Sin).

Once manufactured, the circuit board in Figure 5.11 did not work properly. During the debug phases, the board worked module by module but never all the modules at the same time. The problem came from the heterodyne module. To realize the mixing, we took as oscillator the VCO0055CL-0150-0200. This VCO has the disadvantage to present a strong second harmonic at -10dBc. As a result, the PLL module could not be locked.

It was therefore necessary to design a second circuit by correcting the errors of the first. However, due to the shortage of components and the time constraint, application boards have been ordered to reproduce the AH-FLL architecture. Figure 5.12 below shows the assembled boards. There is a RF mixer board. We have two comparator boards that are positioned at the input of the PLL. A board where the frequency detector, the charge pump and the loop filter are mounted. In order to complete the architecture, we have designed by ourselves application boards for some functions such as passive filter, RF mixer and VCO when no application board was available.

All the experimental results that we are going to present from here, come from the demonstration carried out with the assembly of the application boards.

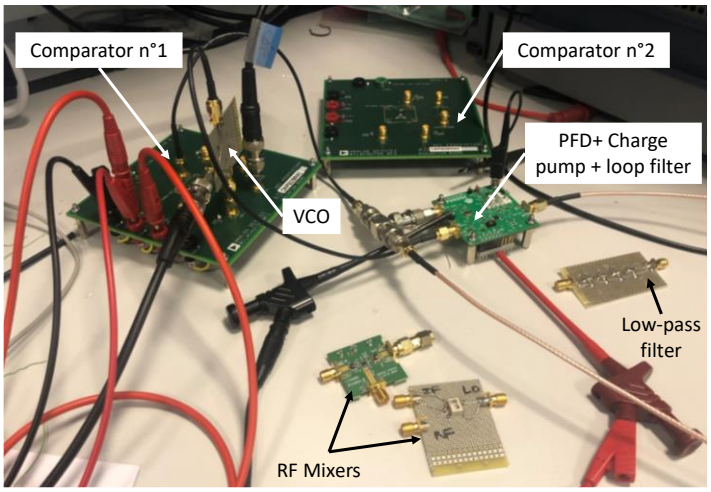

Figure 5.12: Presentation of the assembled boards used to implement the AH-FLL architecture

5.3. Experimental test and validation results

We have presented in the previous section the application board assembly to realize the AH-FLL architecture. The assembled circuit should allow us to experimentally validate our concept of frequency-adjustable architecture. In this section, we propose to carry out several experimental tests to validate the functionality of the assembled circuit before proceeding to the demonstration with the optomechanical sensor. To do so, we will first present the experimental setup and then we will see the different functionality measurements.

5.3.1 Experimental test setup

Figure 5.13 represents the test bench on which we worked. The high frequency signals are visualized with the help of a 1 GHz-bandwidth digital oscilloscope or with the help a spectrum analyzer able to measure the phase noise of the different signals. Long term stability is measured with the help of a very accurate frequency meter that operates up to 350 MHz. A 1 GHz bandwidth signal generator is used to emulate the optomechanical sensor at the down converter input. A second signal generator was used to provide the reference frequency for the down converter and up converter mixers.

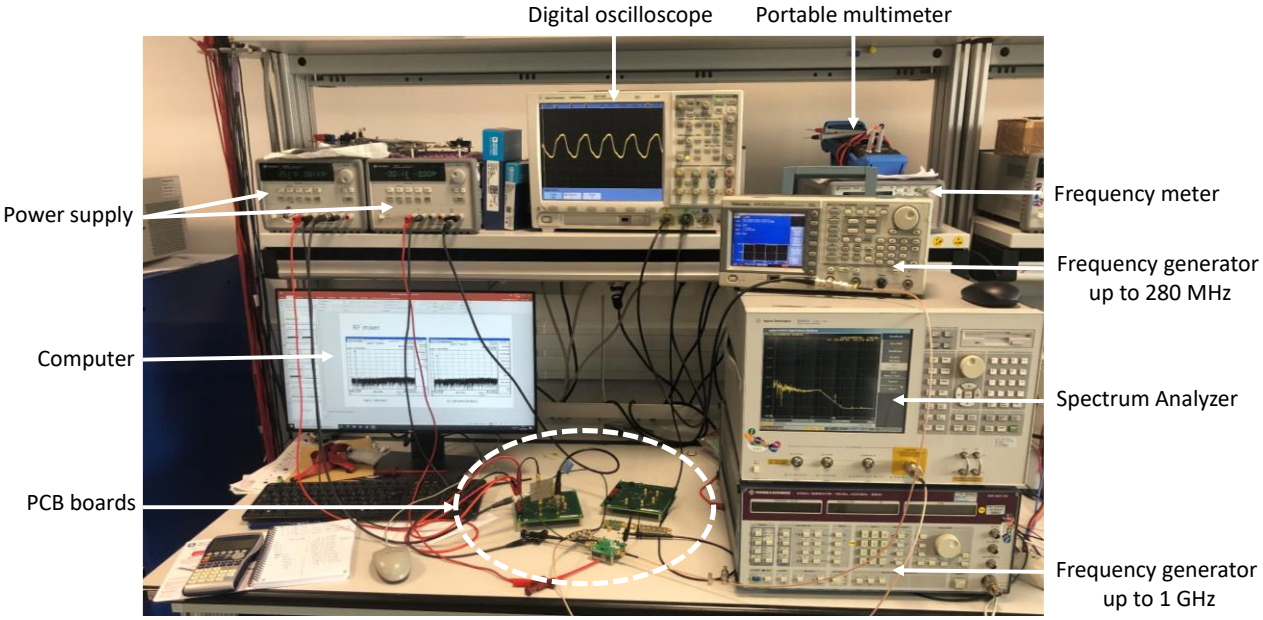

Figure 5.13: Overview of the experimental test setup in the laboratory.

We can also see on Figure 5.13 the montage boards once assembled. We suggest for the continuation of the experimental work to validate the different blocks (heterodyne, PLL, ...) of the AH-FLL architecture.

5.3.2 Heterodyne block test

We will first check the functionality of our heterodyne module. This module is realized with two frequency generators as shown in Figure 5.13 and an active RF mixer as illustrated in Figure 5.12. One generator can go up to 1 GHz to emulate the resonance frequency of optomechanical disks. Indeed, the disks according to their dimensions can go until 500 MHz (disk of radius 5 µm) of resonance frequency. To accomplish a relevant experiment, the frequency of the first generator is set to 290 MHz (which corresponds to a resonator of radius 8-9 µm) and the second generator to 240 MHz.

Once the two signals are mixed, we have two signals of the same magnitude. A frequency signal at 50 MHz and a frequency signal at 530 MHz. As our PLL works between 40 and 70 MHz, we must filter this signal to keep only the useful signal (50 MHz). For this we implemented a 4th order low-pass filter with a cutoff frequency at 53 MHz which filters out the 530 MHz image frequency.

Figure 5.14.a shows the spectrum of the signal at the output of the filter. We can observe an attenuation of the signal amplitude at 530 MHz compared to the useful signal of 50 MHz. The conversion gain of the mixer makes that the useful signal is also slightly attenuated. Figure 5.14.b shows the oscilloscope view of the signal at the output of the low pass filter. The signal is very clean and can be transformed into a logic signal with a comparator in order to be injected into the PLL block.

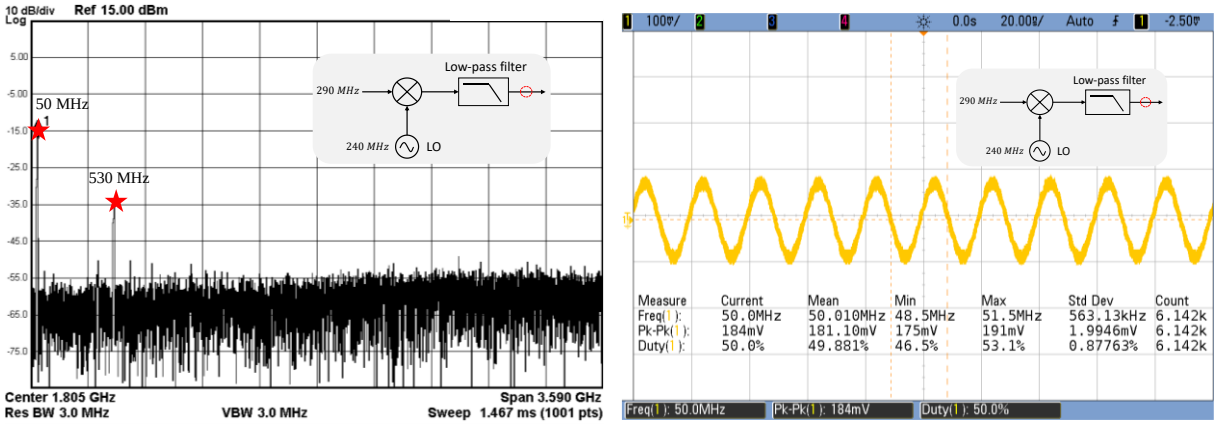

(a) (b)

Figure 5.14: (a) Frequency spectrum of the heterodyne block output signal (b) Oscilloscope view of the heterodyne block output.

5.3.3 PLL functionality validation

The second step consists in validating the functionality of the PLL. As a reminder the PLL block was presented in section 5.1.1.3 and is composed of two comparators, a PFD with charge pump, a loop filter and a VCO. We apply the signal of 50 MHz coming from the low-pass filter after the downconverter mixer presented in Figure 5.14.b to the input of the comparator. With a threshold voltage of 0V, this comparator transforms the sinusoidal 50 MHz signal into a full-scale logic signal as shown in Figure 5.15.a.

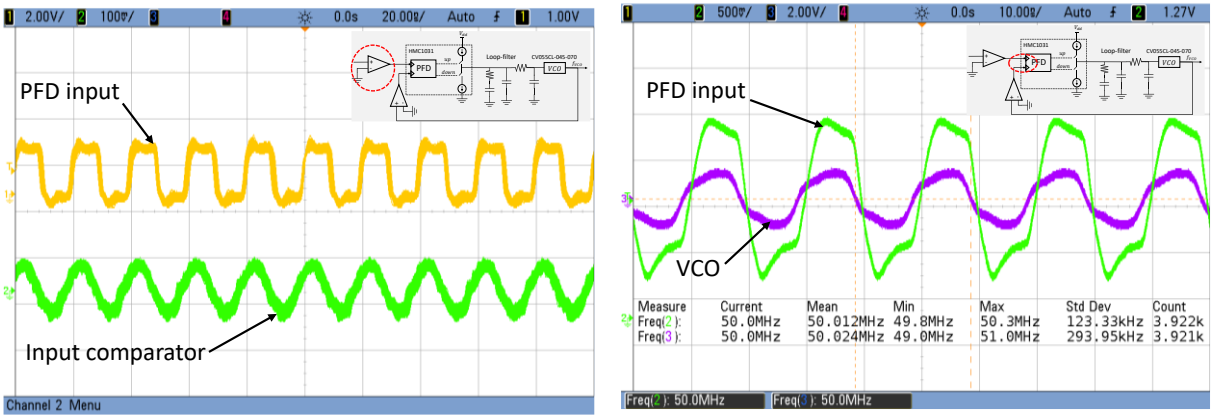

(a) (b)

Figure 5.15: (a) Oscilloscope view of the comparator input and output (b) Oscilloscope view of the PLL input with the useful or reference signal and the VCO signal.

As illustrated, this logic signal is clean and can therefore be used as a reference signal by the PLL. Subsequently, this signal is injected to the PFD and charge pump component to be compared to the logic signal from the VCO. Alone and without control voltages applied (0V), the VCO has a frequency of 40 MHz with a gain $K_{VCO} = 4\,MHz/V$. The loop adjusts the frequency of the VCO compared to the useful signal. The frequency of the VCO is increased from 40 MHz to 50 MHz. Figure 5.15.b shows the result of the PLL when the VCO signal is locked to the useful signal frequency.

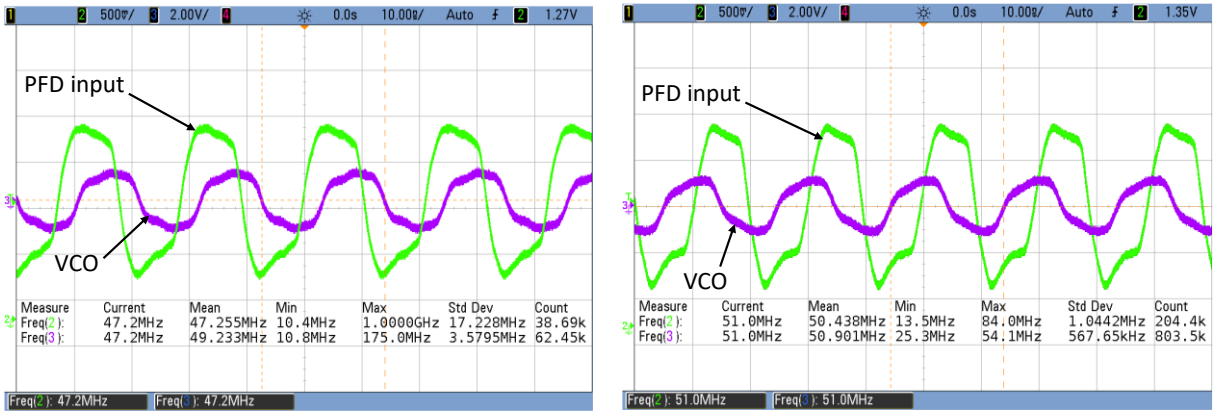

(a) (b)

Figure 5.16: Oscilloscope view of the PLL input (a) case where the useful signal is at 47.2 MHz (b) case where the useful signal is at 51 MHz.

We repeated this operation, to see the frequency locking range of the PLL. Figure 5.16.a represents the case where the useful signal is placed at 47 MHz and the Figure 5.16.b represents the case where the useful signal is placed at 51 MHz. In both configurations the VCO converges to the frequency of the useful signal. The measured locking range of the PLL is 7 MHz (46 to 53 MHz).

5.3.4 Phase Noise measurements

Measuring the phase noise of our circuit is important. It allows us to identify the main contributors to the overall noise. We carry out a first manipulation in which we evaluate the phase noise of the VCO alone. Then in a second experiment, we measure the noise of the PLL module (Comparators, PFD, Loop filter and VCO). And in a last experiment, we measure the complete AH-FLL circuit (PLL and Heterodyne).

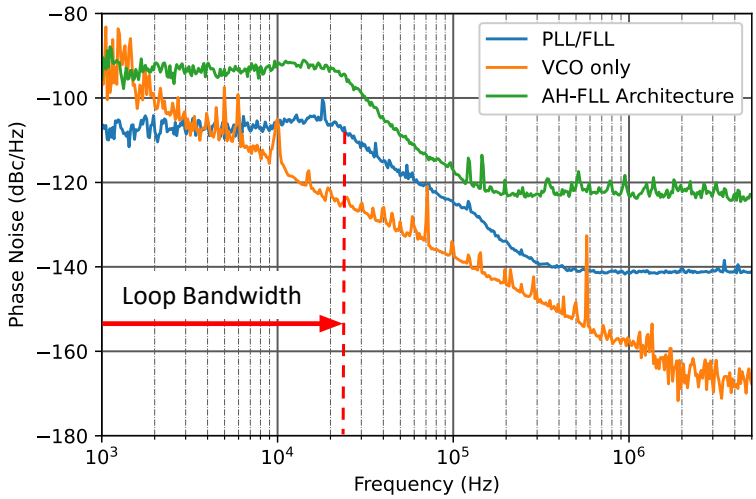

Figure 5.17: Phase noise measurements of VCO alone, PLL block and AH-FLL global circuit.

Figure 5.17 illustrates the performed phase noise measurements. The phase noise of the VCO alone is in accordance with the datasheet given by the manufacturer. As expected, it has a phase noise of around $-105\ dBc/Hz$ at $10\ KHz$. The phase noise in blue corresponds to the phase noise of the PLL module. We measure a loop bandwidth of about $23\ KHz$. This corresponds approximately to the theoretical bandwidth of $20\ KHz$. The small difference is explained by incertitudes on the value of the capacitors and resistors used to realize the loop filter.

We also note that outside the PLL bandwidth the noise does not match the VCO noise as expected. A hypothesis on the origin of this noise could be the charge pump which must deteriorate the global phase noise. But in the absence of a noise model associated with this discrete component, it is difficult to determine accurately the origin of this noise degradation. The phase noise in green corresponds to the overall phase noise of the circuit (PLL block and heterodyne). The circuit has a phase noise of about $-95\ dBc/Hz$ at $10\ KHz$.

5.4. Demonstration with optomechanical sensor

We have seen in the previous section that the PLL of the circuit works on a frequency range of 7 MHz (between 46 to 53 MHz). This could be sufficient to read our optomechanical sensors. Figure 5.18 shows the optomechanical test bench on which we add the test bench of the circuit to read the resonator. The optomechanical bench is composed of Fiber polarization Controller (FPC) to adjust the polarization of the light. Photodetectors (photodiode and transimpedance) with 1 GHz bandwidth. A lock-in-amplifier (LIA) and a tunable wavelength laser for optical actuation of our resonator disk.

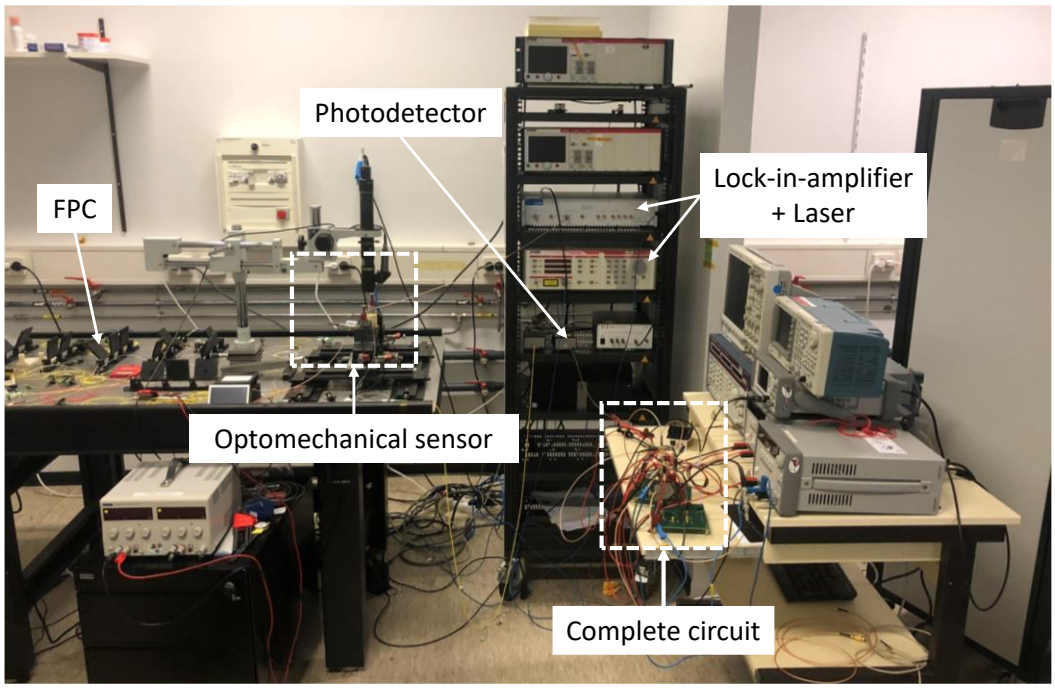

Figure 5.18: Overview of the optomechanical sensor test bench and the complete circuit.

For the demonstration, we worked on actuated devices. They have a better SNR, and they also allow us to verify with our assembled circuit the reading and self-actuation of an optomechanical resonator. The simple fact of reading and driving the sensor with our electronics is considered as a first in the state of the art.

As a reminder, the circuit presented in Figure 5.1 has a drive module that allows to reinject the measured signal to stimulate the disk mechanical resonance. The optomechanical resonators on which we worked had a resonance frequency of 316 MHz.

Figure 5.19 shows the complete circuit that allows both the reading and the self-actuation of the optomechanical sensor. To the best of our knowledge, for the first time in the state of the art we successfully read with our assembled circuit the resonance frequency of the sensor. The experimentation took place in the following way, at the output of the photodetector we have a 30 mV signal modulated at 316 MHz. Then we have amplified this signal with a 30 dB amplifier (see Figure 5.19). We then down mixed (with a signal of 268 MHz) and filtered to keep only the low frequency component. The signal is then injected into the PLL which locks.

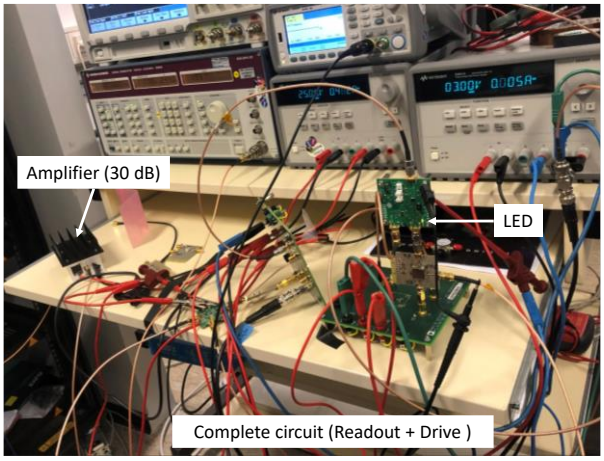

Figure 5.19: Circuit assembly for the reading and self-actuation of the optomechanical sensors.

Once the PLL is locked we measure the VCO frequency as the image of the resonator frequency. Then with an up-mixing we raise the frequency of the VCO to stimulate the disk mechanical resonance. To start the loop, the phase of the system must be adjusted. To do this, we used a voltage-controlled phase shifter placed between the up-mixer and the VCO input. At startup, the circuit cannot start on the thermomechanical noise of the sensor alone. An external clean signal must first be injected into the resonator so that the PLL converges. Once the PLL converges, the external stimulation is stopped and the VCO output is connected into the resonator. In this way, the system (sensor and circuit) is self-acting, and the electronics tracks the resonator frequency.

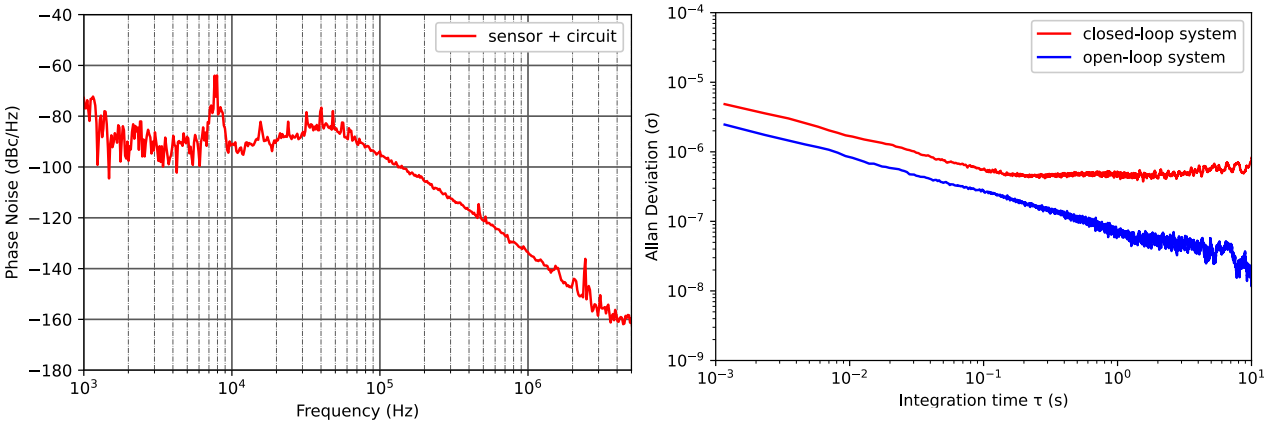

(a) (b)

Figure 5.20: (a) Phase noise measurement of the optomechanical sensor + circuit (b) Measurement of the Allan deviation in open-loop and closed-loop.

Figure 5.20.a illustrates the phase noise of the signal at the output of the circuit when reading the optomechanical sensor. We have seen previously in the Figure 5.17, the phase noise of each block of our circuits. In comparison the system (circuit with sensor) has a little more phase noise, it is -91 dBc at 10 KHz. Figure 5.20.b shows the frequency stability of the system in open and closed loop. If we analyze this figure, in closed loop the resolution reached is 500 ppb. For a sensor with a resonance frequency of 316 MHz this corresponds to a frequency resolution of 158 Hz.

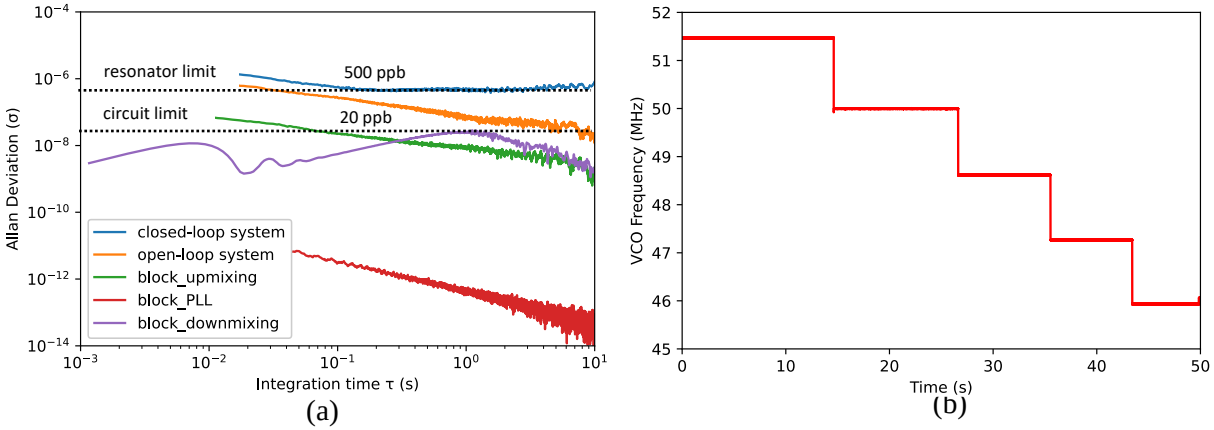

Figure 5.21: (a) Block by block measurement of the Allan deviation (b) Measurement of the VCO frequency during a simulation of mass deposition.

Considering the sensitivity of our optomechanical sensor which is 1 Hz/ag it corresponds to a resolution in mass of 158 ag.

Once the stability of the complete system has been evaluated, we are interested in analyzing the contribution of our circuit to the global stability. The purpose is to identify whether it is the electronics or the optomechanical resonator which limits the performance of the system in closed loop. Figure 5.21.a shows the measurement of the Allan deviation made individually on each block of the circuit. As can be seen in the AH-FLL circuit, the most stable block is the PLL block. Indeed, this block integrates the very low-phase noise VCO CV005CL-0045-0070 form Crystek. The heterodyne block (up-mixing and downmixing) is the block that currently limits the stability of the circuit to 20 ppb.

To improve the frequency resolution of the circuit, work must be done on the design of the heterodyne block. When demonstrated with the optomechanical sensor, the closed-loop resolution is 500 ppb. Since the circuit has a limit of 20 ppb, we can conclude that it is the optomechanical resonator that limits the frequency stability. This is consistent, disk resonators depending on their drive voltage have a resolution between 100 ppb to 1ppm (see Figure 4.10).

To validate the proof of concept, it is necessary to see if the assembled circuit can track the resonance frequency during a mass deposition. Experimentally, such process was not possible with the optomechanical sensor available. Nevertheless, the mass deposition could be emulated by slightly modifying the frequency of the oscillator driving the heterodyne stage. Figure 5.21.b shows the measurement of the VCO frequency when we change the oscillator frequency. For each change of frequency, we observe that the circuit converges. The circuit is thus able to read a mass deposition.

5.5 Conclusion

In this chapter we have presented for the first time the design of a circuit for the reading of optomechanical resonators. The first part of the chapter shows the complete AH-FLL architecture. The circuit consists of several blocks. An input block which allows to transform the optical power into an electrical signal. A heterodyne block allowing us to reduce the frequency to facilitate the design of the PCB. A PLL block which is the core of the circuit. It allows us to track the resonance frequency. And a drive block that loops the system to inject the VCO signal to drive the optomechanical resonators.

Once the AH-FLL architecture has been validated by the electrical simulations, we move on to the design of the board. We presented the schematic view and the layout of the board. Once manufactured, the PCB showed some functional failures. Therefore, we moved to application boards in order to realize the AH-FLL architecture and validate our concept of a frequency-adjustable circuit.

In the third part, we have shown the test bench. We presented the experimental results corresponding to the different blocks that compose the AH-FLL architecture. In terms of phase noise, the assembled boards have a phase noise of about $-95\ dBc/Hz$ at $10\ KHz$. This gives us hope to read the optomechanical sensor.

Finally, we realized the demonstration of the proposed AH-FLL architecture with the optomechanical sensor. The resonator chosen for the demonstration is an electrostatically actuated resonator with 316 MHz resonance frequency. We succeeded for the first time in the state of the art to read and self-actuate an optomechanical resonator with our circuit. The reading is done with the VCO frequency which is an image of the resonance frequency. Then this signal is reinjected into the sensor to amplify the mechanical resonance. To start the loop self-actuation, it is necessary to adjust the phase of the closed loop. To do this, we used a phase shifter in the loop. At startup, it is required to stimulate the resonator by an external signal to allow the PLL to converge. Once the PLL converges, the external stimulation is stopped and the VCO output is connected into the resonator. In this way, the system (sensor and circuit) is self-acting. In terms of performance the system reaches a resolution of 500 ppb which corresponds to a frequency of 158 Hz for a resonance at 316 MHz. In terms of mass resolution, if we assume the sensitivity of our resonator is $1Hz/10^{-18}g$, the minimum mass detected is 158 ag.

References

[1] A. A. Zope, J.-H. Chang, T.-Y. Liu, et S.-S. Li, « A CMOS-MEMS Thermal-Piezoresistive Oscillator for Mass Sensing Applications », IEEE Transactions on Electron Devices, vol. 67, no 3, p. 1183-1191, mars 2020, doi: 10.1109/TED.2020.2969967.

[2] C.-A. Sung, T.-Y. Liu, A. A. Zope, M.-H. Li, et S.-S. Li, « Interface Circuit Design to Enable Miniaturization of Thermal-Piezoresistive Oscillators for Mass Sensing Applications », in 2019 IEEE 32nd International Conference on Micro Electro Mechanical Systems (MEMS), janv. 2019, p. 899-902. doi: 10.1109/MEMSYS.2019.8870785.

[3] M. Konno et al., « Novel MEMS oscillator using in-plane disk resonator with sensing platform and its mass sensing characteristics », in 2011 16th International Solid-State Sensors, Actuators and Microsystems Conference, juin 2011, p. 518-521. doi: 10.1109/TRANSDUCERS.2011.5969670.

[4] N. Delorme et al., « 16.5 A NEMS-array control IC for sub-attogram gravimetric sensing applications in 28nm CMOS technology », in 2015 IEEE International Solid-State Circuits Conference - (ISSCC) Digest of Technical Papers, févr. 2015, p. 1-3. doi: 10.1109/ISSCC.2015.7063044.

[5] J. Arcamone et al., « VHF NEMS-CMOS piezoresistive resonators for advanced sensing applications », Nanotechnology, vol. 25, no 43, p. 435501, oct. 2014, doi: 10.1088/0957-4484/25/43/435501.

[6] G. B. Lee, P. K. Chan, et L. Siek, « A CMOS phase frequency detector for charge pump phase-locked loop », in 42nd Midwest Symposium on Circuits and Systems (Cat. No.99CH36356), août 1999, vol. 2, p. 601-604 vol. 2. doi: 10.1109/MWSCAS.1999.867710.

[7] A. D'Amico et al., « Low-voltage low-power integrated analog lock-in amplifier for gas sensor applications », Sensors and Actuators B: Chemical, vol. 144, no 2, p. 400-406, févr. 2010, doi: 10.1016/j.snb.2009.01.045.

[8] G. Gervasoni et al., « A 12-channel dual-lock-in platform for magneto-resistive DNA detection with ppm resolution », in 2014 IEEE Biomedical Circuits and Systems Conference (BioCAS) Proceedings, oct. 2014, p. 316-319. doi: 10.1109/BioCAS.2014.6981726.

[9] https://www.crystek.com/microwave/admin/webapps/welcome/files/vco/CVCO55CL-0150-0200.pdf

[10]"HMC1031 Datasheet and Product Info | Analog Devices." https://www.analog.com/en/products/hmc1031.html.

[11] https://www.crystek.com/microwave/admin/webapps/welcome/files/vco/CVCO55CL-0045-0070.pdf

[12]"OPA855 data sheet, product information and support | TI.com." https://www.ti.com/product/OPA855.

[13] M. Sansa et al., « Optomechanical mass spectrometry », Nat Commun, vol. 11, no 1, p. 3781, déc. 2020, doi: 10.1038/s41467-020-17592-9.

Conclusion and perspectives

The research work presented in this thesis is part of the development of a compact mass measurement system based on optomechanical resonators. The main objective of this thesis was to design a circuit to achieve a mass sensor demonstrator with readout electronics. To reach this final objective, we followed several milestones.

A first milestone was the development of a compact analytical model of the optomechanical resonators. This model was necessary to understand the physical principles and to facilitate the development of a circuit. The work resulting from this part has been published in a conference (IEEE MEMS) and a journal (Transactions Electron Devices). As our goal was to design a circuit compatible with matrix reading, a second milestone was the consideration of the organization of optomechanical resonators in matrix form. A patent has been filed following the results of this reflection. Finally, a third milestone consisted in the research of an architecture adapted to the reading of optomechanical resonators. From this research, we proposed a frequency-flexible readout architecture to read optomechanical resonators. Afterwards, we specified and designed the electronics based on this architecture to realize the final demonstration with the optomechanical sensor. The result of this work has been published in a conference (IEEE Sensors).

This manuscript respects the same work plan. Chapter 1 is devoted to the state of the art of optomechanical resonators. We first presented the history of optomechanical cavities from the very first experiments to the present day. Then we reviewed the different resonators and their fields of application (detection of force, acceleration, magnetic field, mass, acoustic wave, ...). For sensing applications, we distinguish two main families of optomechanical resonators: the photonic Crystal and the circular WGM cavities. Regarding mass detection applications, the resonators developed by CEA-Leti are based on WGM circular cavities.

Chapter 2 describes the operating principles of the optomechanical disk resonator. It behaves like an optical resonator in which the light propagates by successive reflection in WGM mode. It also acts as a mechanical resonator, expanding radially in the RBM mode. An optomechanical coupling connects the mechanical cavity to the optical cavity. In this chapter we have developed the equations describing these physical principles. Based on these equations we have elaborated a compact Verilog A model of the optomechanical resonator. The presented model includes the mechanical, optical, optomechanical coupling and the thermal behavior of the sensor.

We have proposed in Chapter 3 a matrix configuration appropriate for mass detection. The array is organized in rows and columns. On each row is placed several optomechanical resonators sharing the same optical waveguide. A readout electronics is placed at the output of the waveguide to read sequentially the disks located on the same waveguide. To avoid overlapping mechanical responses of the disks, we enable or disable them. A p-n junction injects current to heat locally the disk in order to shift the optical resonance with respect to the laser wavelength. Consequently, only the disk to be read is visible compared to the other disks positioned on the same waveguide. To estimate the complexity of such a structure, we have also detailed the fabrication process.

Following this, we studied in chapter 4, the architectures which are potentially applicable to the reading of optomechanical resonators. We have presented closed loop architectures of type SOL and FLL and the open loop architectures of type LIA. For each architecture, we have detailed the theoretical equations in terms of phase noise, mass resolution and loop stability. A summary table shows all the equations developed. To read the optomechanical resonators, we have chosen an architecture based on the FLL. This architecture is robust and has a fast convergence time. However, since our optomechanical resonators have different resonance frequencies (between 200 and 300 MHz), depending on their dimensions. We introduce the concept of AH-FLL architecture.

Chapter 5 is dedicated to the demonstration. Based on the specifications done in the previous chapter and electrical simulations, we presented the AH-FLL circuit to be designed. Once the circuit assembly is completed, we moved to the demonstration with the optomechanical sensor. To the best of our knowledge, we have succeeded for the first time to read an optomechanical sensor with our circuit setup. In terms of performance the system (sensor and readout circuit) reaches a resolution of 500 ppb which corresponds to a frequency of 158 Hz for a resonance at 316 MHz. Considering , the resonator sensitivity ($1Hz/10^{-18}g$), the mass resolution is 158 ag.

Perspectives

These research works lead to a few perspectives. A first perspective is to complete the developed model by integrating the optical nonlinearities effects (bistability) of the optomechanical resonators. These effects manifest themselves only in specific cases where the injected power is very high. A second perspective is to experimentally validate the model during a mass deposition. We could not carry out this experiment even if the result obtained in simulation seems coherent. A third perspective would be to implement, based on the work already done, a model of the matrix configuration proposed in the framework of the thesis. It would consist in cascading the model already developed by adding the possibility of activating or deactivating the optical resonators.

The demonstration of the sensor and readout circuit was carried out with a PCB circuit assembly, to make the circuit more compact, it is necessary to develop an integrated circuit based on this work. The final perspective would be to realize with the designed circuit a real mass deposition.

Résumé en Français

Introduction

Ces dernières années, les résonateurs nano-électromécaniques (NEMS) ou micro-électromécanique (MEMS) ont démontré leur énorme potentiel pour les applications de détections de masses. Grâce à leur couplage électrique-mécanique, ils présentent une excellente sensibilité. C'est ce qui leur permet d'être utilisés dans applications de précision comme la spectrométrie de masse. Aujourd'hui ces technologies apparaissent comme matures et sont capables de détecter des atomes dans le vide. La résolution en masse d'un résonateur nano et micro-mécanique est proportionnelle à sa masse effective. Plus la masse des résonateurs est faible et meilleure est la résolution atteinte. Par conséquent, les résonateurs ont fait l'objet d'une campagne de miniaturisation pour atteindre la meilleure résolution possible. Néanmoins, cela fragilise leur structure et ils sont moins résistants. De tels dispositifs ne sont utilisés uniquement que dans des milieux non contraignants comme le vide ou l'air. Dans un milieu contraignant comme le liquide, la viscosité fait que les dispositifs micro et nano mécaniques à base de poutres ont tendance à casser et ne résonnent pas.

Dans l'état de l'art, il existe des dispositifs plus résistants tels que les disques optomécaniques. Ce type de résonateur héberge deux modes de résonance : optique et mécanique. Un couplage appelé "couplage optomécanique" relie ces deux modes, ce qui permet l'interaction entre la lumière et un résonateur mécanique à disque au niveau de la basse énergie. Un résonateur optomécanique est un dispositif dans lequel la propagation de la lumière est modifiée (modulée) par son mouvement mécanique. Le CEA-Leti développe ce type de résonateurs à disque pour des applications de détection de masse. Les dispositifs sont à base de silicium, il présente une excellente sensibilité de masse de $1\ Hz/10^{-18} g$. Cette thèse s'inscrit dans le cadre du développement d'un système de mesure de masse à base de résonateurs optomécaniques. L'objectif du projet de thèse est de développer une électronique compacte pour la lecture d'un résonateur optomécanique. L'électronique à concevoir doit aussi être avec la lecture matricielle du capteur.

Chapitre 1 : Introduction à l'optomécanique

Le chapitre 1 introduit les cavités optomécaniques. Dans la première partie du chapitre, nous avons réalisé l'historique et le développement des cavités optomécaniques. Les toutes premières expériences recensées datent du XVII -ème siècle avec Kepler qui remarque que la poussière d'une comète se déforme à cause de la force d'attraction terrestre. Nichols et Hull ont montré que la lumière exerçait une force de pression radiale. La Figure 1.1 présente le dispositif expérimental de Nichols et Hull. Nous avons aussi décrit le principe de fonctionnement d'un système optomécanique (OM). En analysant le couplage optomécanique entre la résonance optique et la résonance mécanique. Pour les applications capteurs, on distingue en général

deux grandes familles de résonateurs : les résonateurs à cristaux photoniques (voir Figure 1.6) et les résonateurs à cavité circulaire WGM (voir Figure 1.7).

Dans la deuxième partie du chapitre, nous avons fait un état de l'art des résonateurs optomécaniques et de leurs applications. Aujourd'hui, les dispositifs optomécaniques sont utilisés dans plusieurs domaines d'application (voir Figure 1.8). Par exemple, pour détecter une force avec un résonateur à disque ou une cavité Fabry-Pérot (voir Figure 1.9), pour mesurer une accélération avec des cristaux photoniques (voir Figure 1.11), pour mesurer un champ magnétique avec un micro-toroïdal ou une microsphère (voir Figure 1.13 et Figure 1.14). Les résonateurs sont également capables de mesurer avec une très grande précision une masse avec un résonateur à microsphère (voir Figure 1.15) ou un nano-bélier (voir Figure 1.16) ou un micro-toroïdal (voir Figure 1.17). Grâce à leur haute sensibilité optique, les résonateurs optomécaniques peuvent également être utilisés pour détecter une onde acoustique (voir Figure 1.18 et Figure 1.19).

Dans la dernière partie du chapitre, nous avons expliqué le contexte du projet de thèse. Au CEA-Leti, précisément au département composant silicium, deux types de résonateurs optomécaniques ont été développés. Les résonateurs à actionnement optique et des résonateurs à actionnement électrostatique. Au cours de cette thèse, nous avons travaillé sur ces deux configurations pour réaliser la modélisation compacte et la conception du circuit de lecture.

Chapitre 2 : Capteur optomécanique : Théorie et modélisation

Ce chapitre est consacré la compréhension théorique du comportement d'un capteur optomécanique. Dans la première partie du chapitre, nous avons expliqué que le micro-disque se comporte comme un résonateur optique. En effet, à l'intérieur de la cavité optique, la lumière se déplace par réflexion successive, c'est le mode de propagation optique WGM (voir Figure 2.2). Suivant l'équation (2.1) le disque résonne à chaque fois que la lumière se déplace par réflexion successive. Le facteur de qualité optique du micro-disque est très élevé de l'ordre de 10^5. Le disque résonateur se comporte aussi comme un résonateur mécanique. Lors de la résonnance le disque se dilate de manière radiale, c'est le mode RBM (voir Figure 2.5). Un gain dit « couplage optomécanique » relie la cavité mécanique à la cavité optique. L'expression de ce couplage est définie par l'équation (2.8).

Dans la deuxième partie, nous avons présenté le capteur optomécanique à actionnement optique. Le mouvement mécanique de ce type de capteur est stimulé par une excitation optique. En effet, lorsqu'une puissance optique est injectée dans le disque, les photons se propagent par réflexion successive sur la paroi en mode WGM. On dit que les photons exercent une force de pression radiale. En général, le déplacement radial généré par cette force de pression est faible. Dans cette section, nous avons développé les équations analytiques décrivant le comportement optique, mécanique et thermique.

Dans la troisième partie, nous avons présenté le capteur optomécanique à actionnement électrostatique. C'est-à-dire que cette fois-ci le mouvement mécanique est stimulé de manière électrostatique avec des électrodes externe (voir Figure 2.15). Le déplacement radial provoqué par la stimulation externe est beaucoup plus important que dans le cas d'un dispositif avec actionnement optique. En général pour la détection de particule microscopique nous préférons utiliser un résonateur à cause du bon SNR. Dans cette section, nous avons développé un modèle compact en Verilog A. Ce modèle décrit l'ensemble des comportements physique du capteur optomécanique. Les résultats des simulations issus du modèle sont en accord par rapport aux mesures réelles.

Chapitre 3 : Vers une intégration matricielle des résonateurs optomécaniques

L'objectif de ce chapitre est d'étudier les possibilités d'intégration de résonateurs optomécaniques sous forme de matrice. Dans la première partie, nous nous sommes intéressés aux différents principes de lecture applicables à la matrice. On distingue deux principes de lecture : la lecture séquentielle et la lecture simultanée. La lecture séquentielle consiste à lire la matrice disque par disque (voir la Figure 3.3). Alors que pour la lecture simultanée, tous les résonateurs de la matrice sont lus en même temps (voir Figure 3.4). Pour lire notre matrice de capteurs optomécaniques, nous choisissons finalement une lecture séquentielle. En effet ce type de lecture est simple à réaliser d'un point de vue électronique. Notamment parce qu'il est possible de discriminer correctement les résonances mécaniques. Ce principe de lecture permet également de connaître en temps réel la position de la particule dans la matrice.

Dans la deuxième partie du chapitre, nous avons présenté l'intérêt de ce type de matrice dans le contexte liquide. En effet, en milieu liquide, en raison de la viscosité et de l'inertie, les particules mettent un certain temps à se déposer sur le disque. Comme ce temps ne peut être réduit, l'idée est d'augmenter la surface de détection afin de détecter le plus de particules possibles. Une façon d'augmenter cette surface tout en préservant les performances (sensibilité, bruit...) est de réaliser une matrice de résonateurs optomécaniques. Nous avons présenté quelques configurations de matrice envisageables. Il y a la configuration multiplexée (voir Figure 3.5), dans laquelle plusieurs disques sont placés autour d'un même guide d'onde optique. Il existe une autre configuration de matrice possible qui consiste à placer des résonateurs mécaniques à béliers autour d'un seul résonateur optique (voir Figure 3.8).

Dans les deux dernières parties du chapitre, nous avons présenté les différentes techniques d'activation et de désactivation des disques optomécaniques. Nous avons précédemment opté pour une lecture séquentielle. Pour appliquer ce principe, il faut que l'on soit capable d'activer le disque à lire pendant que les disques alentour sont désactivés. Pour activer et désactiver un disque on peut le faire soit de manière optique en exploitant l'effet thermo-optique. Cela permet de rendre invisible la résonance mécanique (voir Figure 3.10). A la suite de cette réflexion, nous proposons la configuration idéale de matrice de résonateur optomécanique présentée sur la Figure 3.15.

Chapitre 4 : Les architectures de lecture à suivi de fréquence

Ce chapitre détaille l'étude des différentes architectures qui peuvent être appliquées à la lecture de notre résonateur optomécanique. Il existe deux grandes familles d'architecture : les architectures de lecture en boucle ouverte de type Lock-in Amplifier (LIA) et les architectures en boucle fermées de type oscillateur ou boucle à verrouillage de fréquence (SOL et FLL). Pour chaque type d'architecture (SOL, FLL, LIA), nous avons réalisé une analyse théorique du bruit de phase, la résolution en masse et la stabilité de la boucle.

Nous avons résumé dans un tableau toutes les informations essentielles à connaître sur chacune des architectures. Dans ce tableau (voir Table 4.1), nous avons rappelé le principe de fonctionnement, ainsi que toutes les analyses théoriques développées dans la partie précédente. Pour améliorer la comparaison, nous avons ajouté le critère de temps de convergence et la complexité d'implémentation. Nous avons introduit une figure de mérite (voir équation 4.30) permettant de comparer les architectures entre elles. Et sur la base de cette figure de mérite nous avons réalisé un état de l'art des architectures permettant de lire les capteurs résonnants (voir Figure 4.9).

Si l'on observe la Figure 4.9, pour les résonateurs basse fréquence, nous avons remarqué que les auteurs avaient tendance à concevoir une architecture de type LIA. En effet cette architecture présente une excellente résolution en fréquence malgré un temps de convergence lent. Alors que pour les résonateurs haute fréquence (au-delà de 10 MHz), ils ont tendance à réaliser une architecture en boucle fermée de type SOL ou FLL. Notamment en raison de leur temps de convergence rapide. Dans le contexte d'une matrice de résonateurs hautes fréquences, il est préférable d'utiliser une architecture FLL. Cette dernière converge plus rapidement qu'une l'architecture SOL. Et elle est beaucoup plus robuste aux parasites.

Pour lire notre résonateur optomécanique, nous avons naturellement choisi une architecture à base de FLL. Dans une architecture FLL, la gamme de fréquence est limitée par le VCO. Cependant, nos résonateurs optomécaniques, en fonction de leurs dimensions n'ont pas la même fréquence de résonance (entre 200 et 300 MHz). Pour espérer lire tous nos résonateurs, nous introduisons l'architecture AH-FLL (voir Figure 4.10). L'idée est d'augmenter la plage de fréquence en réalisant un mélange RF avec un oscillateur local ajustable. Cela nous permet d'ajuster la gamme de fréquence en fonction du résonateur à lire. Ainsi, nous évitons de changer le VCO et le calcul de stabilité de la boucle FLL reste valide. Avant de commencer la conception du circuit, nous spécifions les différents blocs qui composent la AH-FLL. Pour respecter les conditions définies par la Figure 4.12, il faut que l'oscillateur local et le VCO aient une stabilité de 10 ppb. Les amplificateurs, la photodiode et les filtres doivent avoir un plancher de bruit inférieur à 14 $nV/\sqrt{Hz}$.

Chapitre 5 : Conception du circuit et validation expérimentale

Dans ce chapitre, nous avons présenté pour la première fois la conception d'un circuit pour lire les résonateurs optomécaniques. Le circuit AH-FLL complet (voir Figure 5.1) est constitué de plusieurs blocs. Un bloc d'entrée qui permet de transformer la puissance optique en un signal électrique. Un bloc hétérodyne nous permettant de transformer le signal en un signal basse fréquence. Un bloc PLL qui correspond au cœur du circuit. Il nous permet de suivre la fréquence

de résonance du disque. Et un bloc d'actionnement qui reboucle le système dans le but de stimuler la résonance mécanique.

Par la suite, nous proposons le dimensionnement de ses blocs avec des simulations électriques. Nous avons présenté la vue schématique et le layout de la carte (voir Figure 5.10 et Figure 5.11). Nous avons expliqué nos contraintes de conception telles que l'adaptation des lignes de transmission.

Dans la troisième partie, nous avons présenté le banc d'essai (voir Figure 5.13). Dans ce banc, l'idée était de valider la fonctionnalité de la carte conçue précédemment. Malheureusement cette carte n'a pas fonctionné à 100% à cause du module hétérodyne. Par manque de temps et d'apprivoisements incertains des composants, nous avons réalisé la même architecture avec des cartes d'application du commerce et quelques circuits que nous avons faits à la main (voir Figure 5.12). Les résultats des cartes assemblées en matière de performance sont excellents.

Enfin, nous avons réalisé la démonstration avec le capteur optomécanique (voir Figure 5.18 et Figure 5.19). Le résonateur choisi pour la démonstration est un résonateur actionné de manière électrostatique avec une fréquence de résonance de 316 MHz. Nous avons réussi pour la première fois dans l'état de l'art à lire et à auto-actionner un résonateur optomécanique avec notre circuit. La lecture se fait en mesurant la fréquence du VCO qui est une image de la fréquence de résonance. Ce signal est ensuite réinjecté dans le capteur pour amplifier la résonance mécanique. Le système (capteur et montage circuit) ne fonctionne que lorsque nous ajustons la phase de la boucle fermée. Il est également nécessaire de commencer par un actionnement externe afin que la PLL converge, puis on arrête et la boucle s'auto régule elle-même. Concernant la performance, le système atteint une résolution de 500 ppb ce qui correspond à une fréquence de 158 Hz pour une résonance à 316 MHz. Si nous supposons la sensibilité de notre résonateur est de $1Hz/10^{-18}g$, la masse minimale détectée est de 158 ag.

Conclusion

Les travaux de recherches présentés dans cette thèse s'inscrivent dans le cadre plus général de développement d'un système de mesure de masse compacte basée sur des résonateurs optomécaniques. L'objectif principal de cette thèse était de concevoir un circuit afin de réaliser un démonstrateur capteur de masse et circuit électronique de lecture. Pour arriver à cet objectif final, nous sommes passés par plusieurs jalons.

Un premier jalon était le développement d'un modèle analytique compact des résonateurs optomécanique. Le développement d'un tel modèle était nécessaire non seulement pour la compréhension des principes physiques, mais aussi pour faciliter le développement d'un circuit. Les travaux qui découlent de cette partie ont fait l'objet de publications dans une conférence (IEEE MEMS) et un journal (Transactions Electron Devices). Notre objectif étant de concevoir un circuit compatible aussi à la lecture matricielle, un second jalon était la réflexion sur l'organisation sous forme de matrice des résonateurs optomécaniques. Nous avons suggéré dans ce manuscrit une configuration de matrice dite « idéale ». Les résultats qui découlent de cette réflexion ont fait l'objet d'un dépôt de brevet. Un troisième jalon consistait à la recherche d'une architecture adaptée à lecture des résonateurs optomécaniques. Sur la base de cette recherche

nous avons proposé une architecture de lecture flexible en fréquence capable de lire des résonateurs optomécaniques. Par la suite nous avons spécifié, puis conçu une électronique basée sur cette architecture afin de réaliser la démonstration finale avec le résonateur optomécanique. Le résultat de ce travail a fait l'objet d'une publication dans une conférence (IEEE Sensors).

De ce projet de thèse, découlent un certain nombre de perspectives. Une première perspective serait de compléter le modèle développé en intégrant les effets de non-linéarités optique (bistabilité) des résonateurs optomécaniques. Une seconde perspective est de valider expérimentalement le modèle lors d'un dépôt de masse. Nous n'avons pas pu effectuer cette étape même si le résultat obtenu en simulation nous semble cohérent. Une troisième perspective serait de développer, sur la base du travail déjà effectuer un modèle de la configuration matrice qu'on a proposé dans le cadre de thèse. La démonstration capteur et circuit de lecture a été effectuée avec un montage de circuit PCB, il serait nécessaire à terme de développer sur les bases de ses travaux un circuit intégré. Une dernière perspective serait de réaliser avec le circuit réalisé un vrai dépôt de masse.

Appendix A

Self-oscillating loop (SOL): Extensive Analysis.

This appendix presents in detail the theoretical calculations introduced in Chapter 4 section 4.1.1. As a reminder, the SOL architecture applied to the mechanical resonator is shown in Figure A.1.a. The phase noise model is illustrated in Figure A.1.b.

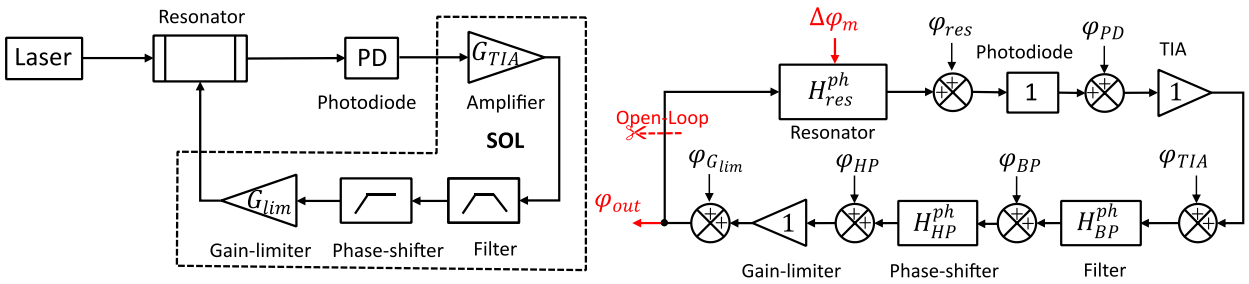

(a) (b)

Figure A.1: (a) SOL architecture applied to the optomechanical resonator (b) Phase noise model

- Phase noise Analysis

The SOL output phase noise noted φ_{out} is determined from the phase noise model depicted in Figure A.1.b. The output phase φ_{out} is written as follows:

$$\varphi_{out} = \frac{1}{H_d}\left(\varphi_{G_{lim}} + \varphi_{HP}\right) + \frac{H_{HP}^{ph}}{H_d}\varphi_{BP} + \frac{H_{HP}^{ph}H_{BP}^{ph}}{H_d}\left(\varphi_{TIA} + \varphi_{PD} + \varphi_{res}\right) \quad \text{(A.1)}$$

where,

$$H_d = 1 - H_{HP}^{ph}H_{BP}^{ph}H_{res}^{ph} \quad \text{(A.2)}$$

$H_{res}^{ph}(s) = 1/\left(1 + 2\frac{Q_{res}}{w_{res}}s\right)$ is the phase transfer function of the resonator where Q_{res} and w_{res} are the quality factor and the resonance frequency respectively. H_{HP}^{ph} and H_{BP}^{ph} are the respective phase transfer functions of the phase-shifter and the band-pass filter.

- Phase noise expressed in Power Spectral Density (PSD):

As the noise is a random process, it is better to write it as Power Spectral Density. Equation (A.1) becomes :

$$S_{\varphi_{out}} = \left|\frac{1}{H_d}\right|^2 (S_{\varphi_{G_{lim}}} + S_{\varphi_{HP}}) + \left|\frac{H_{HP}^{ph}}{H_d}\right|^2 S_{\varphi_{BP}} + \left|\frac{H_{HP}^{ph} H_{BP}^{ph}}{H_d}\right|^2 (S_{\varphi_{TIA}} + S_{\varphi_{PD}} + S_{\varphi_{res}}) \quad \text{(A.3)}$$

where, $S_{\varphi_{G_{lim}}}, S_{\varphi_{HP}}, S_{\varphi_{BP}}, S_{\varphi_{TIA}}, S_{\varphi_{PD}}, S_{\varphi_{res}}$ are respectively the phase noise spectral density of the gain limiter, high-pass filter, band-pass filter, transimpedance amplifier, photodiode and optomechanical resonator.

- Allan Variance (AVAR) and Mass resolution :

The phase noise for the resonant sensor is evaluated using the Allan Variance. The AVAR is defined as follows :

$$\sigma^2(\tau) = \int_0^\infty S_y(f) |H_A(jf)|^2 df \quad \text{(A.4)}$$

where, $S_y(f) = \left(\frac{f}{f_0}\right)^2 S_{\varphi_{out}}(f)$ is the power spectral density of a fractional frequency deviation and $|H_A(jf)|^2$ is the filter transfer function expressed as :

$$|H_A(jf)|^2 = 2\frac{sin^4 \pi\tau f}{(\pi\tau f)^2} \quad \text{(A.5)}$$

τ is the integration time where the AVAR is calculated. The phase noise density $S_{\varphi_{out}}$ can be injected into equation (A.5). The AVAR of the SOL architecture is written :

$$\sigma_{SOL}^2(\tau) = \int_0^\infty \left(\frac{f}{f_0}\right)^2 \left[S_{\varphi_{elec}}(f) + \left|\frac{H_{HP}^{ph} H_{BP}^{ph}}{H_d}\right|^2 \left(S_{\varphi_{PD}}(f) + S_{\varphi_{res}}(f)\right) \right] |H_A(jf)|^2 df \quad \text{(A.6)}$$

where,

$$S_{\varphi_{elec}}(f) = \left|\frac{1}{H_d}\right|^2 \left(S_{\varphi_{G_{lim}}}(f) + S_{\varphi_{HP}}(f)\right) + \left|\frac{H_{HP}^{ph}}{H_d}\right|^2 S_{\varphi_{BP}}(f) + \left|\frac{H_{HP}^{ph} H_{BP}^{ph}}{H_d}\right|^2 S_{\varphi_{TIA}}(f) \quad \text{(A.7)}$$

If we inject equation (A.7) into (A.6), $\sigma_{SOL}^2(\tau)$ becomes :

$$\sigma_{SOL}^2(\tau) = \int_0^\infty \left(\frac{f}{f_0}\right)^2 \left[\left|\frac{1}{H_d}\right|^2 \left(S_{\varphi_{G_{lim}}}(f) + S_{\varphi_{HP}}(f)\right)\right] |H_A(jf)|^2 df + \int_0^\infty \left(\frac{f}{f_0}\right)^2 \left[\left|\frac{H_{HP}^{ph}}{H_d}\right|^2 S_{\varphi_{BP}}(f)\right] |H_A(jf)|^2 df + \int_0^\infty \left(\frac{f}{f_0}\right)^2 \left[\left|\frac{H_{HP}^{ph} H_{BP}^{ph}}{H_d}\right|^2 S_{\varphi_{TIA}}(f)\right] |H_A(jf)|^2 df + \int_0^\infty \left(\frac{f}{f_0}\right)^2 \left[\left|\frac{H_{HP}^{ph} H_{BP}^{ph}}{H_d}\right|^2 \left(S_{\varphi_{PD}}(f) + S_{\varphi_{res}}(f)\right)\right] |H_A(jf)|^2 df \quad \text{(A.8)}$$

To simplify, equation (A.8) becomes :

$$\sigma_{SOL}^2(\tau) = \sigma_{G_{lim}}^2(\tau) + \sigma_{HP}^2(\tau) + \sigma_{BP}^2(\tau) + \sigma_{TIA}^2(\tau) + \sigma_{PD}^2(\tau) + \sigma_{res}^2(\tau) \quad \text{(A.9)}$$

$\sigma_{SOL}(\tau)$ corresponds to the Allan frequency deviation of the SOL architecture. The mass resolution σ_m depends on the minimum frequency resolution $\sigma_{SOL,min}$ and the mass of the resonator M_{res}. It is expressed as follows :

$$\sigma_m = 2M_{res}\sigma_{SOL,min}(\tau) \quad \text{(A.10)}$$

- Open-Loop Analysis :

The oscillation conditions of a self-oscillating loop are calculated from the open-loop transfer function. At start-up, the Barkhausen criterion in amplitude and phase is defined as follows :

$$\left|H_{SOL\_OL}(\omega_0)\right| > 1 \quad \text{(A.11)}$$

and

$$\arg\left(H_{SOL\_OL}(\omega_0)\right) = 0\ [2\pi] \quad \text{(A.12)}$$

Equation (A.11) is the gain condition and equation (A.12) the phase condition of the Barkhausen criterion. Once the desired amplitude is reached, the gain condition equation (A.11) becomes :

$$\left|H_{SOL\_OL}(\omega_0)\right| = 1 \quad \text{(A.13)}$$

Appendix B

Frequency locked loop (FLL) : Extensive Analysis.

This appendix presents in detail the theoretical calculations introduced in Chapter 4 section 4.1.2. As a reminder, the FLL architecture applied to the mechanical resonator is shown in Figure B.1.a. The phase noise model is depicted in Figure B.1.b.

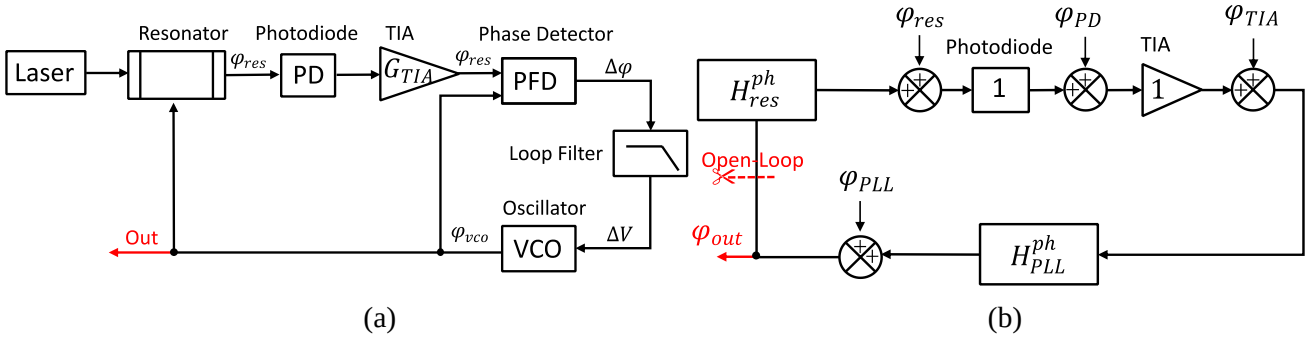

Figure B.1: (a) FLL architecture applied to the optomechanical resonator (b) Phase noise model

- Phase noise Analysis

The FLL output phase noise noted φ_{out} is determined from the phase noise model. If we consider Figure B.1.b, φ_{out} is written as follows:

$$\varphi_{out} = \frac{1}{1 - H_{res}^{ph} H_{PLL}^{ph}} \varphi_{PLL} + \frac{H_{PLL}^{ph}}{1 - H_{res}^{ph} H_{PLL}^{ph}} (\varphi_{res} + \varphi_{TIA} + \varphi_{PD}) \tag{B.1}$$

where,

$$H_{res}^{ph}(s) = \frac{1}{1 + 2\frac{Q_{res}}{w_{res}} s} \quad \text{and} \quad H_{PLL}^{ph}(s) = \frac{H_{VCO}(s) H_{LF}(s) H_{PFD}(s)}{1 + H_{VCO}(s) H_{LF}(s) H_{PFD}(s)} \tag{B.2}$$

H_{res}^{ph} and H_{PLL}^{ph} the phase transfer function of the resonator and the PLL block respectively. $H_{VCO}(s) = \frac{K_{VCO}}{s}$ is the transfer function of the VCO with K_{VCO} the gain. $H_{PFD}(s) = \frac{I_{pump}}{2\pi}$ and $H_{LF}(s)$ are respectively the transfer function of the charge pump and the loop filter.

- Phase noise expressed in Power Spectral Density (PSD):

As the noise is a random process, it is better to write it as Power Spectral Density. Equation (B.1) becomes :

$$S_{\varphi_{out}} = \left|\frac{1}{1 - H_{res}^{ph}H_{PLL}^{ph}}\right|^2 S_{\varphi_{PLL}} + \left|\frac{H_{PLL}^{ph}}{1 - H_{res}^{ph}H_{PLL}^{ph}}\right|^2 \left(S_{\varphi_{res}} + S_{\varphi_{TIA}} + S_{\varphi_{PD}}\right) \quad \text{(B.3)}$$

where, $S_{\varphi_{PLL}}$ is the spectral density of the PLL block , $S_{\varphi_{TIA}}$ is the spectral density of the transimpedance amplifier, $S_{\varphi_{res}}$ and $S_{\varphi_{PD}}$ are the spectral density of the resonator and photodiode respectively.

- Allan Variance (AVAR) and Mass resolution :

The phase noise for the resonant sensor is evaluated using the Allan Variance. The AVAR is defined as follows :

$$\sigma^2(\tau) = \int_0^\infty S_y(f)|H_A(jf)|^2 df \quad \text{(B.4)}$$

where, $S_y(f) = \left(\frac{f}{f_0}\right)^2 S_{\varphi_{out}}(f)$ is the power spectral density of a fractional frequency deviation and $|H_A(jf)|^2$ is the filter transfer function expressed as :

$$|H_A(jf)|^2 = 2\frac{sin^4\pi\tau f}{(\pi\tau f)^2} \quad \text{(B.5)}$$

τ is the integration time where the AVAR is calculated. The phase noise density $S_{\varphi_{out}}$ can be injected into equation (B.5). The AVAR of the FLL architecture is written :

$$\sigma_{FLL}^2(\tau) = \int_0^\infty \left(\frac{f}{f_0}\right)^2 \left[S_{\varphi_{elec}}(f) + \left|\frac{H_{PLL}^{ph}}{1 - H_{res}^{ph}H_{PLL}^{ph}}\right|^2 \left(S_{\varphi_{PD}}(f) + S_{\varphi_{res}}(f)\right)\right] |H_A(jf)|^2 df \quad \text{(B.6)}$$

where,

$$S_{\varphi_{elec}}(f) = \left|\frac{1}{1 - H_{res}^{ph}H_{PLL}^{ph}}\right|^2 S_{\varphi_{PLL}}(f) + \left|\frac{H_{PLL}^{ph}}{1 - H_{res}^{ph}H_{PLL}^{ph}}\right|^2 S_{\varphi_{TIA}}(f) \quad \text{(B.7)}$$

$$\sigma_{FLL}^2(\tau) = \int_0^\infty \left(\frac{f}{f_0}\right)^2 \left[\left|\frac{1}{1 - H_{res}^{ph} H_{PLL}^{ph}}\right|^2 S_{\varphi_{PLL}}(f)\right] |H_A(jf)|^2 df + \int_0^\infty \left(\frac{f}{f_0}\right)^2 \left[\left|\frac{H_{PLL}^{ph}}{1 - H_{res}^{ph} H_{PLL}^{ph}}\right|^2 \left(S_{\varphi_{res}}(f) + S_{\varphi_{TIA}}(f) + S_{\varphi_{PD}}(f)\right)\right] |H_A(jf)|^2 df \quad \text{(B.8)}$$

To simplify, equation (B.9) becomes :

$$\sigma_{FLL}^2(\tau) = \sigma_{PLL}^2(\tau) + \sigma_{TIA}^2(\tau) + \sigma_{PD}^2(\tau) + \sigma_{res}^2(\tau) \quad \text{(B.9)}$$

$\sigma_{FLL}(\tau)$ corresponds to the Allan frequency deviation of the FLL architecture. Therefore, the mass resolution depends on the minimum frequency resolution $\sigma_{FLL,min}$ and the mass of the resonator M_{res} :

$$\sigma_m = 2M_{res}\sigma_{FLL,min}(\tau) \quad \text{(B.11)}$$

- Open-Loop Analysis :

The FLL architecture is a closed loop architecture, so it is necessary to ensure the stability of the loop. For this, we need to calculate the transfer function in open loop which expression is as follows:

$$H_{FLL\_OL}(s) = H_{res}^{ph}(s) H_{PLL}^{ph}(s) \quad \text{(B.12)}$$

To achieve a stable architecture, the PLL block component such as the gain K_{VCO}, I_{pump}, and the loop filter must be calculated to have a phase margin M_φ greater than 45° and a gain margin M_G greater than 10 dB.

$$M_\varphi = \arg\left(H_{FLL\_OL}(jw_{0dB})\right) + \pi \quad \text{(B.13)}$$

and

$$M_G = -20\mathrm{Log}_{10}\left|H_{FLL\_OL}(jw_{-\pi})\right| \quad \text{(B.14)}$$

Appendix C

Amplitude & Phase tracking

During this thesis, to read our optomechanical resonator we have studied different architectures other than those presented in chapter 4. We benefit from this appendix to present another reading technique. The method consists in monitoring either the amplitude or the phase of the resonator. Indeed during a deposition the mechanical resonance shifts and the amplitude or the phase at the output of the resonator is modified. In this technique, we want to read this amplitude or phase variation in order to estimate the mass deposited.

C.1 Operating Principle

The amplitude or phase tracking is an open loop technique allowing the tracking of the resonance frequency. Indeed, if a mass Δm is deposited on the optomechanical disk, its resonance frequency shifts to the left as shown in Figure C.1.a. The same observation applies to the phase as illustrated in Figure C.2.b. If we place at output, a band-pass filter with a high quality factor and a cutoff frequency corresponding to the resonance frequency of the disk. Each mass deposit will correspond to an amplitude and phase variation. And from this amplitude or phase variation we can estimate the quantity of particles deposited on the resonator disk. Figure C.1 below details this method for frequency tracking.

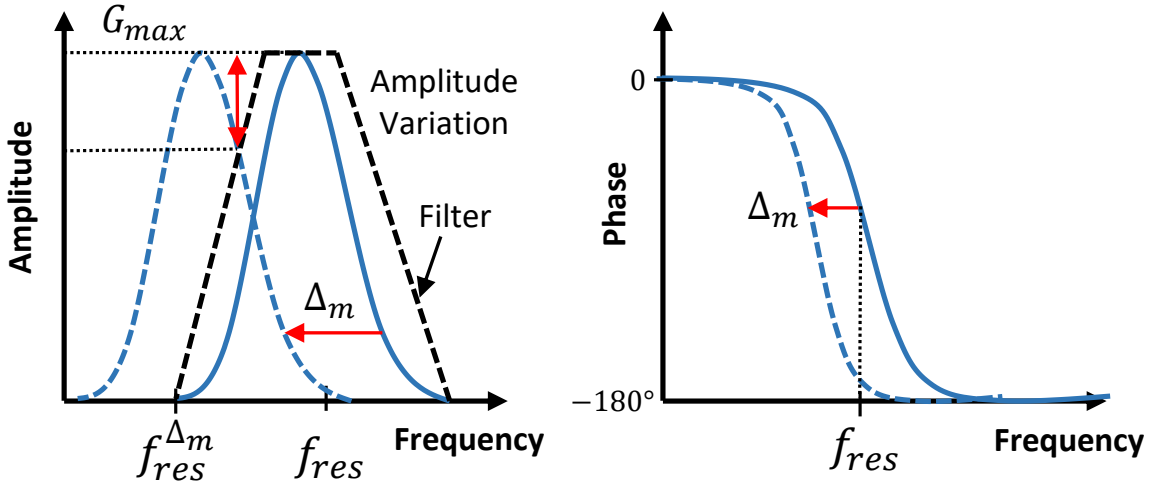

Figure C.1: (a) Operating principle of the amplitude variation tracking during a mass deposition (b) Operating principle of the amplitude variation during a mass deposition.

C.2 Transfer function of the resonator

To implement the amplitude and phase tracking technique, we must first know the transfer function of the resonator. This will allow us to identify the maximum gain, from which we will calculate the variation. As described in Chapter 2, the optomechanical resonator has a mechanical transfer function H_{mec} and optical transfer function H_{opt}. The resonator is actuated and therefore has an actuation gain G_{act}. There is also the gain of the photodiode G_{PD} and the TIA noted G_{TIA}. The transfer function of the resonator is written:

$$H_{opto+PD+TIA} = G_{act} H_{mec} H_{opt} G_{PD} G_{TIA} \tag{C.1}$$

where the mechanical transfer function is expressed as:

$$H_{mec}(jw) = \frac{1}{mw_0^2} \frac{1}{1 + j\frac{w}{Qw_0} - \left(\frac{w}{w_0}\right)^2} \tag{C.2}$$

To simplify, we assume that the modulation is done on the linear zone of the optical resonance as shown in Figure C.3. The transfer function of the optical resonator is considered as a gain:

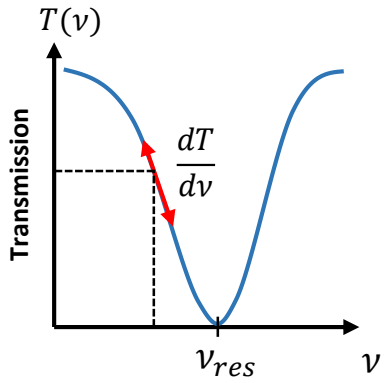

$$H_{opt} = \frac{dT}{d\nu}\frac{g_{om}}{2\pi} \tag{C.3}$$

where $\nu = \frac{2\pi c}{\lambda}$ and optical transmission $T(\nu)$:

$$T(\nu) = P_{in}\left(1 - C_r \frac{(k_{in} + k_{ex})^2}{4\Delta^2 + (k_{in} + k_{ex})^2}\right) \tag{C.4}$$

Figure C.3: Optical Transmission

We derived the expression of the optical transmission equation (C.4) as follow:

$$T'(\nu) = 8P_{in}C_r(k_{in} + k_{ext})^2 \frac{\Delta}{(4\Delta^2 + (k_{in} + k_{ext})^2)^2} \tag{C.5}$$

One more time we derived equation (C.5):

$$T''(\nu) = -8P_{in}C_r(k_{in} + k_{ext})^2 \frac{12\Delta^2 - (k_{in} + k_{ext})^2}{(\Delta^2 + (k_{in} + k_{ext})^2)^3} \tag{C.6}$$

We can inject the derivative expression of the optical transmission defined in equation (C.5) into (C.3). But we preferred to derive a second time (C.5) to be able to determine the maximum ($T''(\nu) = 0$) of the equation then we inject them into (C.3).

After calculation, the transfer function of the resonator (C.3) is written:

$$H_{opt} = \frac{3\sqrt{3}}{4}\frac{P_{in}C_r Q_{opt}\lambda_{res}}{4\pi^2 c} g_{om} \tag{C.7}$$

where $Q_{opt} = \frac{\nu_{res}}{k_{in}+k_{ext}}$ is the optical quality factor, C_r is the contrast, g_{om} the optomechanical coupling, c the light speed and P_{in} the optical power. The transfer function of the opto-mechanical sensor + PD + TIA is expressed as:

$$H_{opto+PD+TIA}(jw) = \frac{1}{mw_0^2}\frac{G_{act}G_{PD}G_{TIA}\frac{3\sqrt{3}}{4}\frac{P_{in}C_r Q_{opt}\lambda_{res}}{4\pi^2 c} g_{om}}{1 + j\frac{w}{Qw_0} - \left(\frac{w}{w_0}\right)^2} \tag{C.8}$$

From the transfer function of the resonator equation (C.8), we can determine the maximum gain G_{max}. This gain is used as an amplitude reference to follow the resonance. Written as:

$$G_{max} = \frac{1}{mw_0^2} G_{act}G_{PD}G_{TIA}\frac{3\sqrt{3}}{4}\frac{P_{in}C_r Q_{opt}\lambda_{res}}{4\pi^2 c} g_{om} \tag{C.9}$$

From the equation (C.8), the expression of the phase is:

$$\psi_{opto+PD+TIA} = \arg\left(H_{opto+PD+TIA}(jw)\right) = -\arctan\left(\frac{\frac{w}{Qw_0}}{1-\left(\frac{w}{w_0}\right)^2}\right) \tag{C.10}$$

C.3 Amplitude & Phase tracking architecture: Example

Figure C.4 below shows an example of an amplitude tracking architecture. The resonator has an initial frequency f_{res}. When a mass deposition is performed its frequency becomes $f_{res}^{\Delta m}$. The output signal is converted into voltage by a photodiode and TIA. A band-pass filter of central frequency f_{res} allows to change the amplitude of the signal with its attenuation. And then with an envelope detector and an integrator we average this amplitude level ΔV to estimate the resonator frequency. This architecture requires a perfect dimensioning of the quality factor and resonance frequency of the band-pass filter.

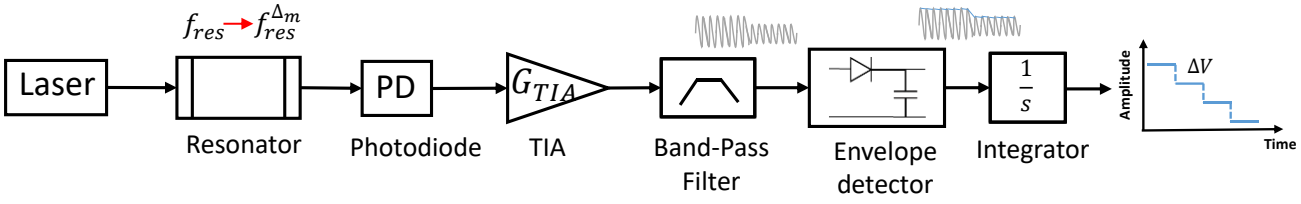

Figure C.4: Example of Amplitude tracking architecture

Appendix D

Closed-loop I/Q architecture

In this appendix we will present a second architecture that we could not present in chapter 4. This architecture is a closed-loop architecture that combines part of a lock-in-amplifier I/Q demodulation type architecture and a Phase locked-loop architecture. In this architecture, the idea is to control the direction of the phase in the loop in order that the error between the I and the Q channels is zero. We called this architecture the closed-loop I/Q architecture.

D.1 Operating Principle

Figure D.1 below represents the complete schematic of the I/Q closed-loop architecture. Within this architecture we have our optomechanical resonator. At the output of the resonator is placed a photodiode and a transimpedance amplifier (TIA). Then we have the two channels I / Q. Each channel is composed of two mixers, a low-pass filter, a gain and a derivation. Then we compare the two channels between them at the level of ε_r. Then we integrate this error to drive a voltage controlled oscillator (VCO). At the output of the VCO, the I channel corresponds to the signal of the VCO and the Q channel the signal of the VCO phase shifted by 90° .

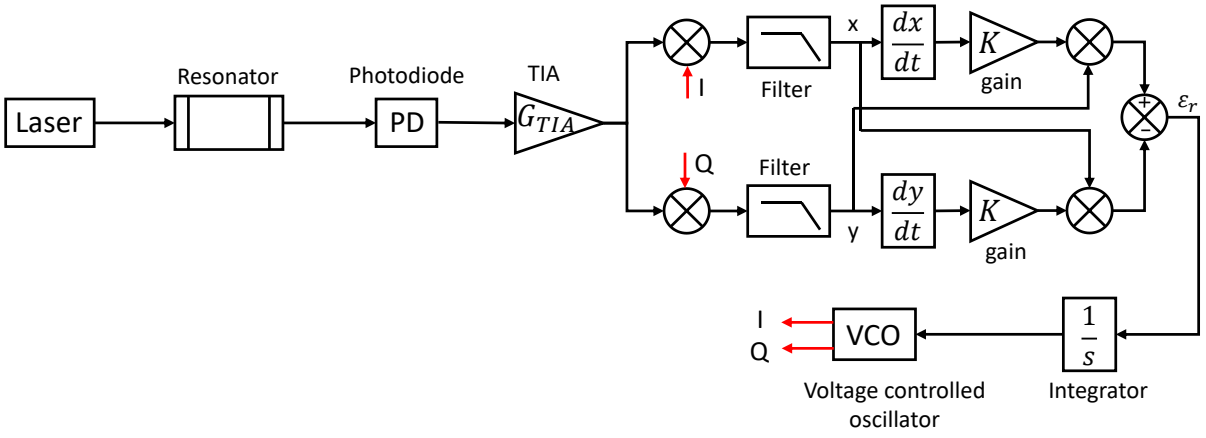

Figure D.1: General schematic of a closed-loop I/Q architecture

The operating principle is as follows. The signal at the output of the TIA is demodulated in the I/Q way and then low-pass filtered. At the point x and y the I and Q channel signals are derived with respect to time. Then we multiply each signal by the derivative of the opposite channel to compare them. The expression of the error ε_r is presented by the equations (D.1) and (D.2). When ε_r respects the condition D.1, on the trigonometric circle the phase of the VCO is

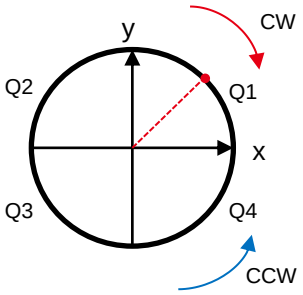

$$\text{(CW)} \qquad \varepsilon_r = y.\frac{dx}{dt} - x.\frac{dy}{dt} > 0 \qquad \text{(D.1)}$$

$$\text{(CCW)} \qquad \varepsilon_r = y.\frac{dx}{dt} - x.\frac{dy}{dt} < 0 \qquad \text{(D.2)}$$

adjusted in clockwise direction (CW). When ε_r meets the condition D.2, the VCO phase is set counterclockwise (CCW). In this way the phase of the VCO is adjusted to match the phase of the resonator. To test the validity and suitability of the architecture shown in Figure D.1, we performed a block simulation on Simulink. Figure D.2 shows the Simulink schematic of the closed-loop I/Q architecture. To emulate the resonator signal at the TIA, we considered a sinusoidal source of frequency 300 MHz. The Dechrip blocks are mixers. The low-pass filters correspond to a Butterworth of order 2 and two continuous-time VCO.

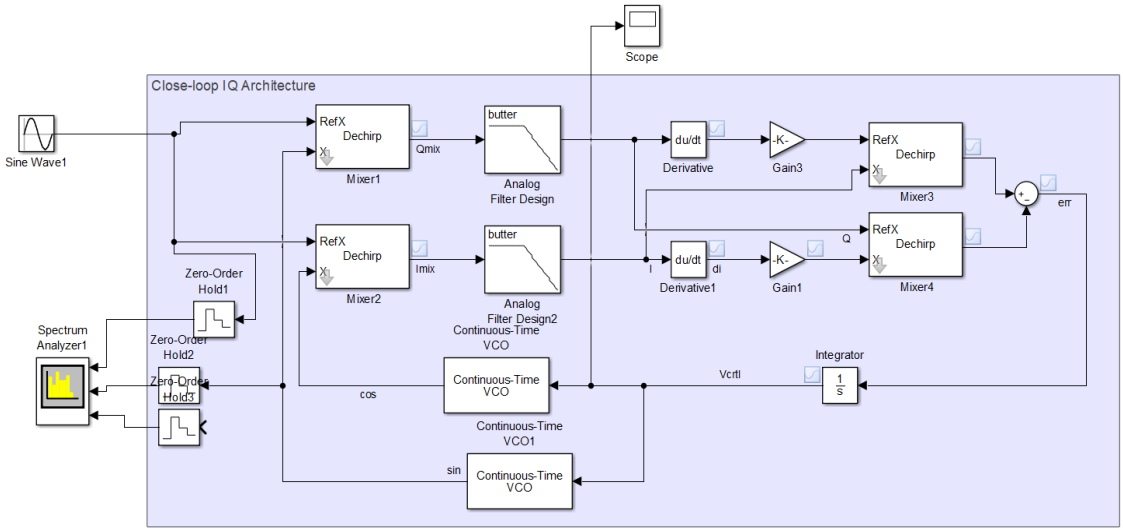

Figure D.2: Simulink (Matlab) schematic of a closed-loop I/Q architecture

The simulation results are shown in Figure D.3. At the initial state, the VCO frequency is 250 MHz and the resonator is 300 MHz as shown in Figure D.3.a. The VCO gain is 50 MHz/V. Figure D.3.b shows the control voltage of the VCO as a function of time. As can be seen the frequency of the VCO converges at 300 MHz since its control voltage converges to 1 V.

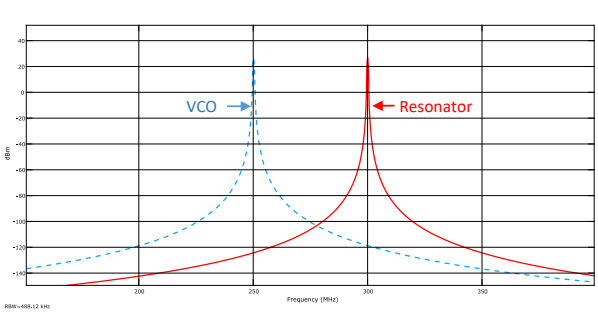

(a)

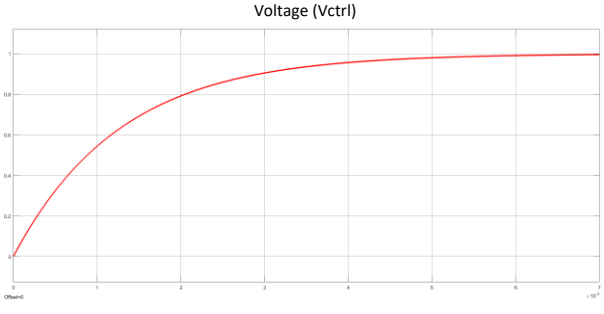

(b)

Figure D.3: (a) Initial state of the Simulink simulation with the VCO frequency at 250 MHz and the resonator at 300 MHz. (b) Control voltage of the VCO (gain 50 MHz/V) which converges to 1 V.

Appendix E

Adjustable Heterodyne Frequency Locked Loop (AH-FLL): Extensive Analysis.

This appendix presents in detail the theoretical approach introduced in chapter 4 section 4.4. As a reminder, to read our optomechanical resonators we have chosen an AH-FLL architecture. Figure E.1.a represents the block diagram of the AH-FLL. The phase noise model is illustrated in figure E.1.b.

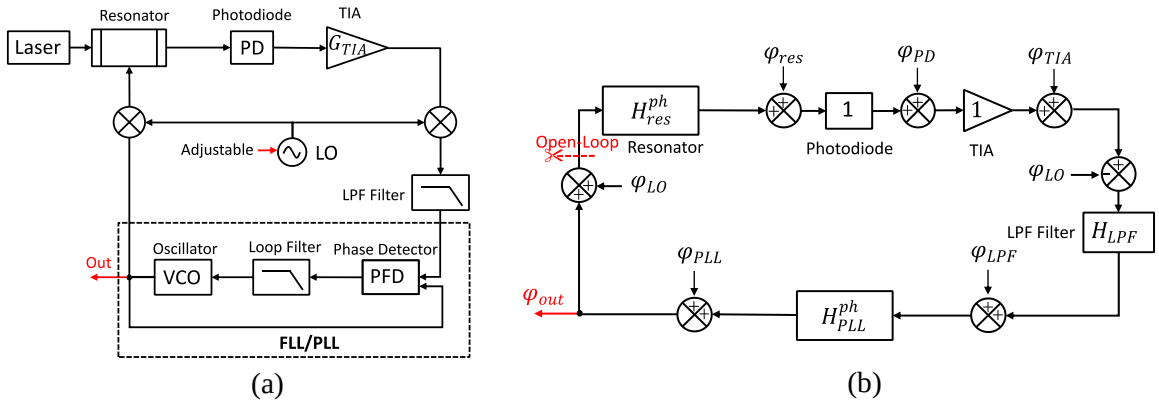

(a) (b)

Figure E.1: (a) AH-FLL architecture applied to the optomechanical resonator (b) Phase noise model

- Phase noise Analysis

The AH-FLL output phase noise noted φ_{out} is determined from the phase noise model. If we consider Figure E.1.b, φ_{out} is written as follows:

$$\varphi_{out} = \frac{1}{H_d}\varphi_{PLL} + \frac{H_{PLL}^{ph}}{H_d}\varphi_{LPF} + \frac{H_k}{H_d}\varphi_{LO} + \frac{H_i}{H_d}\varphi_i \tag{E.1}$$

where,

$$H_d = 1 - H_{res}^{ph} H_{LPF} H_{PLL}^{ph} \tag{E.2}$$

with $H_k = H_{LPF}H_{PLL}^{ph}(H_{res}^{ph} - 1)$ and $H_i = H_{LPF}H_{PLL}^{ph}$. The phase φ_i is written as :

$$\varphi_i = \varphi_{TIA} + \varphi_{PD} + \varphi_{res} \tag{E.3}$$

where, $H_{res}^{ph}(s) = 1/\left(1 + 2\frac{Q_{res}}{w_{res}}s\right)$ is the transfer function of the resonator where Q_{res} and w_{res} are the quality factor and the resonance frequency respectively.

- Phase noise expressed in Power Spectral Density (PSD):

As the noise is a random process, it is better to write it as Power Spectral Density. Equation (E.1) becomes :

$$S_{\varphi_{out}} = \left|\frac{1}{H_d}\right|^2 S_{\varphi_{PLL}} + \left|\frac{H_{PLL}^{ph}}{H_d}\right|^2 S_{\varphi_{LPF}} + \left|\frac{H_k}{H_d}\right|^2 S_{\varphi_{LO}} + \left|\frac{H_i}{H_d}\right|^2 S_{\varphi_i} \tag{E.4}$$

where,

$$S_{\varphi_i} = S_{\varphi_{TIA}} + S_{\varphi_{PD}} + S_{\varphi_{res}} \tag{E.5}$$

$S_{\varphi_{PLL}}$, $S_{\varphi_{LPF}}$, $S_{\varphi_{TIA}}$, $S_{\varphi_{PD}}$, $S_{\varphi_{res}}$, $S_{\varphi_{LO}}$ are respectively the spectral noise density in phase of the PLL, low-pass filter, TIA, photodiode, resonator, and local oscillator.

- Allan Variance (AVAR) and Mass resolution :

The phase noise for the resonant sensor is evaluated using the Allan Variance. The AVAR is defined as follows :

$$\sigma^2(\tau) = \int_0^\infty S_y(f)|H_A(jf)|^2 df \tag{E.6}$$

where, $S_y(f) = \left(\frac{f}{f_0}\right)^2 S_{\varphi_{out}}(f)$ is the power spectral density of a fractional frequency deviation and $|H_A(jf)|^2$ is the filter transfer function expressed as :

$$|H_A(jf)|^2 = 2\frac{sin^4\pi\tau f}{(\pi\tau f)^2} \tag{E.7}$$

τ is the integration time where the AVAR is calculated. The phase noise density $S_{\varphi_{out}}$ can be injected into equation (E.4). The AVAR of the FLL architecture is written :

$$\sigma_{FLL}^2(\tau) = \int_0^\infty \left(\frac{f}{f_0}\right)^2 \left[\left|\frac{1}{H_d}\right|^2 S_{\varphi_{PLL}} + \left|\frac{H_{PLL}^{ph}}{H_d}\right|^2 S_{\varphi_{LPF}} + \left|\frac{H_k}{H_d}\right|^2 S_{\varphi_{LO}} + \left|\frac{H_i}{H_d}\right|^2 S_{\varphi_i}\right] |H_A(jf)|^2 \tag{E.8}$$

$$= \int_0^\infty \left(\frac{f}{f_0}\right)^2 \left[\left|\frac{1}{H_d}\right|^2 S_{\varphi_{PLL}}\right] |H_A(jf)|^2 df + \int_0^\infty \left(\frac{f}{f_0}\right)^2 \left[\left|\frac{H_{PLL}^{ph}}{H_d}\right|^2 S_{\varphi_{LPF}}\right] |H_A(jf)|^2 df$$
$$+ \int_0^\infty \left(\frac{f}{f_0}\right)^2 \left[\left|\frac{H_k}{H_d}\right|^2 S_{\varphi_{LO}}\right] |H_A(jf)|^2 df$$
$$+ \int_0^\infty \left(\frac{f}{f_0}\right)^2 \left[\left|\frac{H_i}{H_d}\right|^2 \left(S_{\varphi_{TIA}}(f) + S_{\varphi_{PD}}(f) + S_{\varphi_{res}}(f)\right)\right] |H_A(jf)|^2 df$$

To simplify, equation (E.9) becomes :

$$\sigma_{AH-FLL}^2(\tau) = \sigma_{elec}^2(\tau) + \sigma_{res}^2(\tau) + \sigma_{PD}^2(\tau) \quad \text{(E.9)}$$

where $\sigma_{elec}^2(\tau) = \sigma_{PLL}^2(\tau) + \sigma_{LPF}^2(\tau) + \sigma_{LO}^2(\tau) + \sigma_{TIA}^2(\tau)$ is the AVAR of electronics. $\sigma_{res}^2(\tau)$ and $\sigma_{PD}^2(\tau)$ are respectively the AVAR of the resonator and the photodiode.
$\sigma_{AH-FLL}(\tau)$ corresponds to the Allan frequency deviation of the AH-FLL architecture. The mass resolution σ_m depends on the minimum frequency resolution $\sigma_{AH-FLL,min}$ and the mass of the resonator M_{res}. It is expressed as follows :

$$\sigma_m = 2M_{res}\sigma_{AH-FLL,min}(\tau) \quad \text{(E.10)}$$

- Open-Loop Analysis :

The AH-FLL architecture is a closed loop architecture, so it is necessary to ensure the stability of the loop. For this, we need to calculate the transfer function in open loop which expression is as follows:

$$H_{AH-FLL\_OL}(s) = H_{res}^{ph}(s) H_{LPF}(s) H_{PLL}^{ph}(s) \quad \text{(E.11)}$$

The resonator and low-pass filter introduce high-frequency poles that have no effect on stability, so the equation (E.11) simplifies:

$$H_{AH-FLL\_OL}(s) = H_{PLL}^{ph}(s)$$
$$= \frac{K_{VCO}}{s} \frac{I_{pump}}{2\pi} \frac{1}{C_1 + C_2} \frac{(1 + RC_1 s)}{s(1 + R\frac{C_1 C_2}{C_1 + C_2} s)} \quad \text{(E.12)}$$

The equation (E.12) is the case where we consider a 2nd order loop filter (two capacitors in parallel with a resistor). To achieve a stable architecture, the gain K_{VCO}, I_{pump}, and the loop filter must be calculated to have a phase margin M_φ greater than 45° and a gain margin M_G greater than 10 dB.

$$M_\varphi = \arg\left(H_{AH-FLL\_OL}(jw_{0dB})\right) + \pi \quad \text{(E.13)}$$

and

$$M_G = -20\text{Log}_{10}\left|H_{AH-FLL\_OL}(jw_{-\pi})\right| \quad \text{(E.14)}$$

List of Publications

Articles published in international conferences.

- **H. E. Dawale**, S. Regord, T. Fourcatte, M. Sansa, P. Villard, G. Jourdan, and F. Badets, " A 20 ppb Resolution Readout Circuit Dedicated to Optomechanical Mass Sensors," in Oct. 2022 *IEEE SENSORS*, doi: 10.1109/SENSORS52175.2022.9967328.
- Q. Schmidt, A. Morel, Y. Moursy, **H. E. Dawale**, G. Billiot, and F. Badets, "Exploring the analytical boundaries of capacitive feedback transimpedance amplifiers," in *2021 28th IEEE International Conference on Electronics, Circuits, and Systems (ICECS)*, Nov. 2021, pp. 1–4. doi: 10.1109/ICECS53924.2021.9665553.
- **H. E. Dawale**, G. Jourdan, L. Sibeud, F. Lamberti, S. Hentz, and F. Badets, "Analytical Compact Model for Opto-Mechanical Sensor," in *2020 IEEE 33rd International Conference on Micro Electro Mechanical Systems (MEMS)*, Jan. 2020, pp. 869–872. doi: 10.1109/MEMS46641.2020.9056258.

Article published in a refereed journal

- **H. E. Dawale**, L. Sibeud, S. Regord, G. Jourdan, S. Hentz, and F. Badets, "Compact Modeling and Behavioral Simulation of an Optomechanical Sensor in Verilog A," *IEEE Transactions on Electron Devices*, vol. 67, no. 11, pp. 4677–4681, Nov. 2020, doi: 10.1109/TED.2020.3024477.

Patent

- **H. E. Dawale**, L. Sibeud, F. Badets, G. Jourdan, M. Sansa, and S. Hentz, " Dispositif et procédé de détection d'espèces chimiques ou biologiques," N° de dépôt: FR2110087, 2021

Résumé

Titre : Interface électronique compacte pour capteur optomécanique

Grâce à leurs extrêmes sensibilités, les résonateurs optomécaniques ont montré ces dernières années leur potentiel pour les applications capteurs, en particulier pour la détection de masse. Comparés aux autres résonateurs mécaniques, ils présentent une surface de détection plus importante (quelques µm de diamètre). Ils sont aussi beaucoup plus robustes, ce qui leur permet de résonner dans différents milieux (air, vide, liquide, …). Les résonateurs optomécaniques développés par les équipes du CEA, sont à base de micro-disque en silicium. Un tel dispositif, présente une sensibilité de $1Hz/10^{-18}g$. Cela nous permet d'envisager la détection de particule infime quels que soient les types applications envisagées : détection de particule chimique, détection biologique….

Les travaux de cette thèse s'inscrivent dans le cadre du développement d'un système de mesures de masse compacte à base de résonateur optomécanique. L'objectif de la thèse consiste à développer une électronique suffisamment compacte permettant de lire ses capteurs de masse optomécanique. Pour parvenir à cet objectif, nous avons d'abord développé un modèle compact en Verilog A des résonateurs optomécaniques. Cela facilite la conception des circuits en permettant de réaliser des simulations réalistes, conjointes capteur-électronique. Ensuite, nous avons mené une réflexion sur les configurations matricielles des résonateurs optomécaniques. Un tel système permet d'avoir une surface de détection plus importante tout en préservant la sensibilité d'un seul résonateur optomécanique. A moyen terme, le système de mesure de masse que l'on souhaite réaliser doit être à base de cette matrice. Aujourd'hui, une telle matrice n'existe pas encore, mais il faut anticiper et concevoir un circuit de lecture compatible. Finalement, pour lire les résonateurs optomécaniques, nous proposons un circuit de lecture modulable en fréquence. En termes de performance le système de mesure réalisé (capteur et circuit de lecture) atteint une résolution de 500 ppb, c'est qui correspond à une fréquence de 158 Hz pour un résonateur de 316 MHz de fréquence. Si l'on considère la sensibilité des disques optomécaniques cela correspond à une résolution de masse de 158 ag.

Mots clés :

Détection de masse, résonateur optomécanique, matrice de capteur, modélisation compacte, électronique de lecture pour capteur, architecture de lecture boucle ouverte, architecture de lecture boucle fermée.

Abstract

Title : Compact electronic interface for optomechanical sensor

Thanks to their high sensitivity, optomechanical resonators have shown in recent years their potential for sensor applications, in particular for mass detection. Compared to other mechanical resonators , they exhibit a larger detection area (a few µm in diameter). They are much more robust, which allows them to resonate in different environments (air, vacuum, liquid, ...). The optomechanical resonators developed by the CEA teams are based on a silicon microdisk. The sensitivity of such a device is $1Hz/10^{-18}g$. This enables us to consider the detection of tiny particles for any type of applications : chemical detection, biological detection.

The work of this thesis is part of the development of a compact mass measurement system based on optomechanical resonator. The objective of the thesis project is to develop suitably compact electronics to read optomechanical mass sensors. To achieve this purpose, we first developed a compact Verilog A model of optomechanical resonators. This helped us to design the circuit allowing us to perform realistic and complete simulations. Then, we moved on to the reflection of a matrix configuration of optomechanical resonators. Such system allows to have a larger detection surface while preserving the sensitivity of a single optomechanical resonator. In the mid-term, the mass measurement system that we wish to realize must be based on matrices of optomechanical sensors. At present, such a matrix does not yet exist, but we must anticipate and design a compatible readout circuit. Finally, to read the optomechanical resonators, we propose a modulable reading circuit in frequency. The performance of the measurement system (sensor and reading circuit) reaches a resolution of 500 ppb, which corresponds to a frequency of 158 Hz for a resonator of 316 MHz frequency. Considering the sensitivity of optomechanical disks, this corresponds to a mass resolution of 158 ag.

Key words :

Mass detection, optomechanical resonator, sensor matrix, compact modeling, readout electronics for sensor, open loop readout architecture, closed loop readout architecture.